ALMA MATER STUDIORUM
UNIVERSITÀ DI BOLOGNA

DOTTORATO DI RICERCA IN

NANOSCIENZE PER LA MEDICINA E PER L'AMBIENTE

Ciclo 38

Settore Concorsuale: 03/B1 - FONDAMENTI DELLE SCIENZE CHIMICHE E SISTEMI INORGANICI

Settore Scientifico Disciplinare: CHIM/03 - CHIMICA GENERALE E INORGANICA

CAPACITIVE–FLOW HYBRID SYSTEMS: ELECTROCHEMICAL SOLUTIONS FOR CLEAN ENERGY AND CLIMATE APPLICATIONS

Presentata da: Monica Giovannucci

Coordinatore Dottorato

Matteo Calvaresi

Supervisore

Francesca Soavi

Co-supervisore

Alexander Forse

Esame finale anno 2026

General Index

Abstract

In order to mitigate the effects of climate change, the European Green Deal established ambitious objectives for reducing CO_2 emissions. Achieving these goals requires a profound transformation of the energy production, harvesting, and storage . From this perspective, electrochemical energy storage systems (EESSs) play a crucial role in this transition by enabling the storage of variable and intermittent energy derived from renewable sources. Redox Flow Batteries (RFBs) and Supercapacitors (SCs) are two types of EESSs that differ significantly in energy and power performance but share design flexibility. The integration of RFBs and SCs leads to an innovative Hybrid Energy Storage System (HESS) that allows various configurations suitable for multiple applications. In parallel, SCs can readily store energy from energy harvesters with a variable (not programmable) operation, like piezoelectric systems. In addition, the flow architecture of batteries and SCs can be exploited to design novel technologies, like the high specific energy, flow Li/O_2 battery or the Flow SCs developed for CO_2 capture.

Hence, this study investigates different approaches to hybridising a flow system through capacitive effects at both laboratory and up-scaled levels, with particular attention to system sustainability.

Chapter 1 provides a background on the effects of climate change, the countermeasures defined by international agreements, and introduces the importance of energy storage systems in climate mitigation. Chapter 2 presents EESSs and offers the technical background on Flow Systems and Supercapacitors, identifying the key components and fundamental operating principles. Chapters 3, 4 and 5 constitute the core of the thesis, describing the research activities and results achieved during my PhD. Chapter 3 reports about the integration of a Vanadium Redox Flow Cell (VRFC) and a Supercapacitor at cell level to form a HESS based on a passive configuration that avoids DC–DC converters (Section 3.1). The study combines experimental activities, modelling, life cycle assessment (LCA), and economic evaluation. Tests demonstrated that capacitance enhances the system's overall performance by increasing its short-term deliverable energy. Two models are presented: a mathematical model that provides a tool to size the capacitance according to the desired energy output, and a semi-empirical one

showing that capacitance can act as a current peak filter, improving the efficiency of the VRFC. The LCA and economic analyses revealed that the passive configuration, together with the adoption of a water-based SC, represents the most sustainable and cost-effective solution. Within Chapter 3 (Section 3.2), a model developed to simulate the charging of a supercapacitor through piezoelectric devices is reported. This work enables forecasting of the voltage profile during charging and estimation of the time required for a supercapacitor to reach full charge under mechanical stress, with a relative voltage error of 9.4%. Chapter 4 discusses my contribution to the development of a new upscaled Semisolid Lithium Air Flow Battery (SLAFB) aimed at simplifying its design. Specifically, a critical component of the cell, the 3D current collector (reticulated vitreous carbon – RVC), features high cost, exhibits fragility and induces agglomeration of the catholyte which consists of a carbon suspension. The objective was to assess the feasibility of removing the RVC component by increasing the carbon content in the semi-solid slurry. The new formulation demonstrated lower but comparable performance while maintaining a more stable current signal, probably due to the absence of agglomerates. Chapter 5 presents a study on the design of an Electrochemical Flow Capacitor circuit aimed at capturing CO_2 through the Supercapacitive Swing Adsorption phenomenon, which enables CO_2 uptake during the charging and discharging of a gas-exposed SC. The system provided a tool for analysing the governing mechanisms of SSA and achieved promising results in terms of CO_2 adsorption: approximately 45 mmol kg^{-1} of CO_2 was captured using a 30–70% CO_2–N_2 gas stream, which is a notable outcome compared with 100% CO_2-exposed SSA systems (up to 60 mmol kg^{-1}). Chapter 6 contains the conclusions of the thesis, while Chapter 7 summarises the projects in which I participated.

The activities conducted during my PhD resulted from a multidisciplinary approach combining engineering and chemistry to demonstrate the outcomes of mixed knowledge. Indeed the findings include both experimental data and modelling or numerical analyses results. This research demonstrates that the HESS concept can be implemented at different levels, providing promising results and adaptability for various applications. Moreover, particular attention should be paid to the LCA, which offers valuable insights into the environmental impact of system components and identifies those requiring further research focus.

These activities were carried out within national and international collaborative projects involving several research groups. Specifically, external collaborations included the Energieinstitut at the Johannes Kepler University Linz (Eva-Maria Heigl, Andreas Zauner), Epic Power Converters S.L. (Prof. Estanis Oyarbide), University of West Bohemia (Jiří Charvát), University of Perugia (Prof. Linda Barelli), and University of Cambridge (Prof. Alexander Forse, Dr. Malina Seyffertitz, Dr. Jack Taylor). Internal collaborations within the University of Bologna involved the Department of Chemistry "Giacomo Ciamician" (Dr. Elisabetta Petri, Dr. Michele Zanoni, Dr. Federico Poli, Prof. Chiara Gualandi), the Department of Electrical, Electronic, and Information Engineering "Guglielmo Marconi" (Dr. Leonardo Gasperini, Dr. Giacomo Selleri, Prof. Davide Fabiani), and Bettery s.r.l. (Dr. Alessandro Brilloni). These highly productive collaborations were developed under different national and international projects, namely: (i) HyFlow H2020-LC-BAT-2020 / HyFlow: Development of a suitable hybrid storage system based on high-power vanadium redox flow battery and supercapacitor technology (ID 963550), coordinated by Professor Karl-Heinz Pettinger, and (ii) Piano Triennale 2025–2027 della Ricerca di Sistema Elettrico (ENEA 2025) – issued by D.M. MASE n. 388 of 06/11/2024, titled LA1.26 Approfondimento: Elettroliti redox a base di metalli multivalenti per nuove generazioni di sistemi di accumulo (CUP I53C24003300001).

Chapter 1: Introduction

1.1 Climate change, decarbonisation and efforts

In 2000, atmospheric chemist Paul Crutzen introduced the term *Anthropocene* to describe the present geological epoch [1]. The proposal of defining a new geological epoch emerges from the recognition that human activities are significantly altering the interactions between living organisms and the biosphere. Global processes such as ecosystem transformation, the increasing frequency of catastrophic events, and large-scale modifications of the biosphere are creating a worldwide imbalance [2]. Among all the effects of human activity, it is essential to discuss climate change. Heat waves, heavy rainfall, and agricultural and ecological drought are frequent topics in the news and, as explained below, they are related to global warming. Indeed, these events have both direct and indirect effects on human life, especially on water availability, food production, health, wellbeing, cities, settlements, and infrastructure. Naturally, the Global South is more likely to be affected, bearing disproportionate burdens despite lower historical emissions. [3-4] According to the results reported by the Intergovernmental Panel on Climate Change (IPCC), the frequency of calamitous events has increased since the 1950s, and this is likely due to human influence. In fact, emissions of GreenHouse Gases (GHGs), which contribute to the warming greenhouse effect, have risen rapidly since 1850. Following a similar trend, the global surface temperature has increased by 1.1 °C compared to the 1850–1900 period (the pre-industrial reference) as depicted in Figure 1.1.1 that is showing the world annual temperature anomalies relative to the pre-industrial period (1850) [4] Among the greenhouse gases (GHGs), the most relevant is carbon dioxide (CO_2), which has reached its highest level in the past two million years. CO_2 is the main cause of global warming due to its ability to remain in the atmosphere for a long time. The concentration of carbon dioxide increased from about 278 ppm in 1750 to 430 ppm measured at Mauna Loa Observatory during May 2025. [5] Initially, this rise was mainly caused by deforestation and land use change while since around 1950, the primary driver has been the burning of fossil fuels showing a clear increasing trend as depicted in Figure 1.1.2 [6].

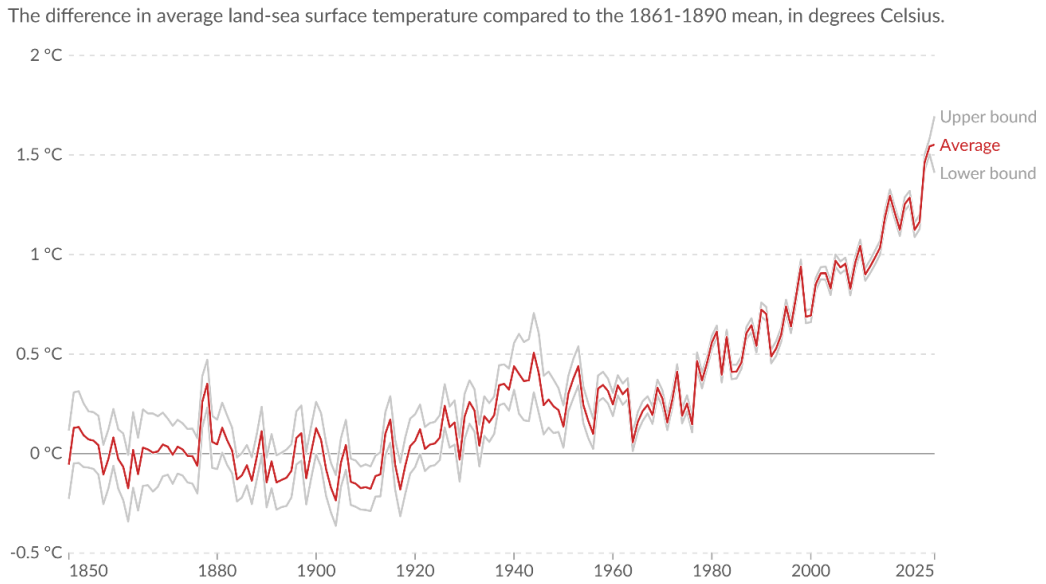

Figure 1.1.1 World annual temperature anomalies relative to the pre-industrial period [7]

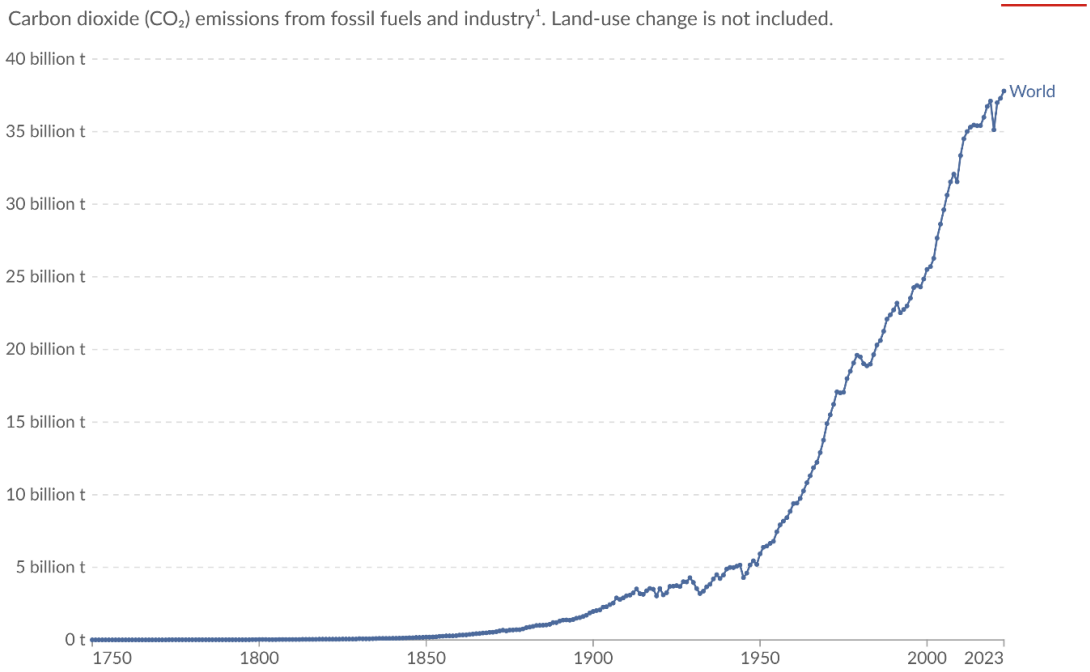

Figure 1.1.2 Historical global emissions from fossil fuel and industry of CO_2 over time. Trends reflect the cumulative impact of human activities from 1850 to the present. [7]

To mitigate climate change and reduce CO_2 emissions, countries initiated cooperative efforts to develop international agreements. The first significant one was the Kyoto Protocol, which came into force in 2005 and involved most of the considered developed nations of that period. The objective of this agreement was to achieve at least a 5% reduction in greenhouse

gas emissions compared with 1990 levels during 2008–2012, representing a goal that was not particularly ambitious [8]. In 2015, with the intention of overcoming the limitations of the Kyoto Protocol, the Paris Agreement was established, including all countries and setting a more ambitious objective to mitigate climate change, as it states that the global temperature rise must remain below 1.5°C above pre-industrial levels. Furthermore, the agreement encourages each country to develop its own targets to contribute and to promote international cooperation aimed at sharing financial and technological resources. [9]. In parallel with the climate change agreement, in 2015 the United Nations established 17 Sustainable Development Goals (UN SDGs) to promote peace, prosperity, and environmental protection by 2030 that are summarised in Figure 1.1.3. These goals are closely linked to climate change as Goal 7 emphasizes the importance of ensuring that energy is accessible, affordable, and reliable for all; Goal 9 encourages industry to invest in the development of sustainable technologies that reduce environmental impact; Goal 11 focuses on the need for cities to become more environmentally sustainable and resilient to climate-related challenges; Goal 12 promotes sustainable and efficient production systems, encouraging long-term responsibility in resource use; Goal 13 calls for coordinated action to mitigate the effects of climate change; finally, Goal 15 highlights the crucial role of protecting forests, soil, and biodiversity, which are all significantly affected by climate change [10].

Figure 1.1.3 UN Sustainable Development Goals.

The Paris Agreement led to the creation of the European Green Deal (EGD) in 2019, which represents a strategy to make Europe the first climate-neutral continent by 2050 implying that European emissions must decrease by at least 55% by 2030 compared to 1990 levels. In 2025, the EU expanded the EGD by introducing new targets, including a 90% reduction in emissions by 2040. Regulations concerning clean industries were also implemented under the name Clean Industrial Deal, aiming to make the economy more sustainable with an emphasis on the environment and human well-being [11-12].

From a practical point of view, to achieve the goal of reducing CO_2 in the atmosphere, two main strategies can be applied simultaneously: decreasing emissions by minimizing the use of fossil fuels and capturing CO_2. Next Sections will address the potential to reduce CO_2 emissions by exploiting sustainable energy sources, enabled by the development of tailored energy storage systems and the capture of CO_2 from gas streams generated by fuel combustion, employing analogous technologies.

1.2 Role of Energy Storage Systems in the decarbonization process

To accomplish the climate goals, energy sources need to shift from fossil fuels and natural gas to renewable alternatives, such as wind, solar, tidal, and geothermal sources [13]. With the aim of maximizing the use of energy from renewable sources, storage systems are becoming increasingly important in future scenarios [14]. Since intermittent renewable energy is not always available, it is necessary to store it when it is generated. In addition, Intermittent Renewable Energy Sources (RESs), like sun and wind, can create challenges for the stability of the electric grid. Both the need for storage and for grid stabilization can be addressed through the implementation of Energy Storage Systems (ESSs) [15]. The stored energy can then be utilized when required, contributing to system flexibility. Furthermore, electricity should progressively become the primary energy carrier across sectors such as transport and industry, in order to support a more sustainable and decarbonized energy system [16,17]. Thus, ESSs play a key role in the electric transition and, consequently, in the reduction of CO_2 emissions.

Various ESS technologies are available on the market and are classified into five categories: chemical, mechanical, thermal, electrochemical, and electrical. These systems can

be characterized by their energy storage capacity and storage duration, as shown in Figure 1.1.4; in detail, a typical way to group ESSs is to split them in two categories: "power-oriented" and "energy-oriented". Chemical and thermal ESSs include hydrogen, synthetic fuels, and warm water. Flywheels, compressed air, and pumped hydro storage are categorized as mechanical systems. The electrochemical energy storage system (EESS) group includes batteries and supercapacitors [14].

The most energy performing batteries are the Lithium-ion batteries (LIBs), which include a wide range of chemistries. This diversity allows the technology to be flexible, ranging from energy-oriented to power-oriented cells. However, transition metals present in LIBs, along with lithium, are generally classified as a critical raw material (CRM) due to both geological scarcity and geopolitical concerns [18]. One of the most promising technologies beyond LIBs is the redox flow battery (RFB). RFBs represent a combination of intelligent design and operational flexibility. Indeed, their key feature is their ability to decouple energy from power, allowing systems to be tailored to specific needs. In addition, RFBs operated with various redox species are under development, which offers the potential to reduce the reliance on CRMs [19]. Researchers are investigating alternative chemistries to exploit RFB technology, and one of the most promising options involves implementing metal–air systems as the redox couple. Metal–Air Batteries (MABs) represent an innovative technology because they employ the lightest available cathode material, namely oxygen, combined with solid metal foils such as Li, Na, K, Zn, Mg, Al, or Fe. Integrating MAB chemistry into RFBs leads to Metal–Air Flow Batteries (MAFBs), which combine the high energy density of MABs with the design flexibility of RFBs [14]. Supercapacitors (SCs) are of great interest for high power demand applications: they operate through a different mechanism compared to batteries, which will be explained in the Chapter 2. It is important to note that this mechanism allows SCs to be the fastest devices among ESSs, although they are limited by low energy density [20]. This PhD dissertation focuses primarily on RFBs and SCs, which are gaining visibility due to their design flexibility. Chapter 2 will deeply describe the functionality of RFBs and SCs under a technological point of view detailing their key components across different configurations and also the possible interactions between the two technologies.

Beside EESSs energy and power performance, regulations have been introduced to ensure that new generation systems are sustainable throughout their entire life cycle.

Specifically, the European Battery Regulation (Regulation EU 2023/1542) states that batteries must remain sustainable from the materials used to the recycling phase [21]. In addition, the regulation requires a carbon footprint declaration for each battery. As mentioned above, the United Nations has established several sustainability goals, and battery development and use are essential for achieving Goals 7, 9, 11, and 13. The Life Cycle Assessment (LCA) methodology is a crucial tool for evaluating the environmental challenges of modern battery technologies. Indeed a cradle-to-cradle approach provides a comprehensive understanding of sustainability across different types of energy storage systems [22].

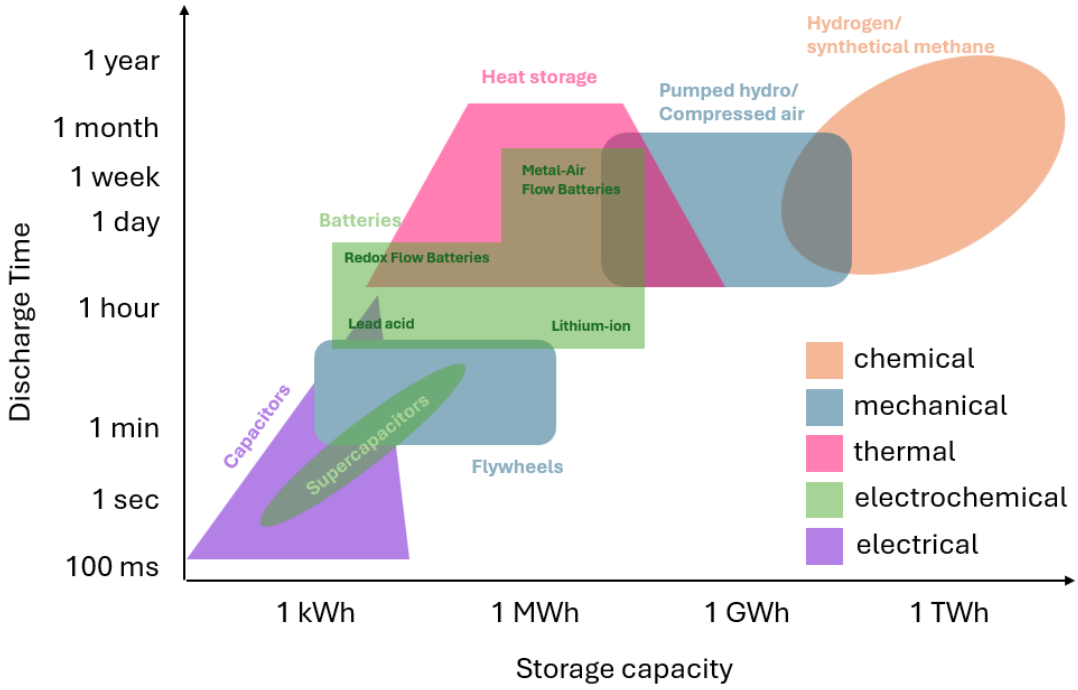

Figure 1.1.4. Classification of storage technologies based on storage size and discharge time. Inspired from [14]

One method to design more sustainable and customized storage systems is hybridization. Hybrid Energy Storage Systems (HESSs) consist of two or more different storage technologies integrated into a single system. Since different ESSs have distinct characteristics, combining them into a single system makes it possible to take advantage of their specific strengths and adapt to a wide range of applications, from micro to macro scale, and from stationary to mobile uses [23]. Typically, *power-oriented* technologies are combined with *energy-oriented* ones to create a complementary configuration [24]. However, as will be discussed in the next Chapters, it is essential to consider additional key characteristics such as

sustainability and lifespan when designing a HESS. By taking all these parameters into account, it is possible to develop a system with reduced environmental impact when conducting a LCA [25].

The integration of different energy storage systems can occur at multiple levels: at system, cell or materials level. In the latter case, electrode materials can feature simultaneously an electrochemical behaviour that is typical of batteries or SCs or, in general, of different technologies. This work analyses various levels of integration of the capacitive effect with battery systems.

1.3 Carbon Capture through Supercapacitor Flow Cell

An approach to integrate flow technology with the capacitive effect involves employing supercapacitor flow cells to capture CO_2. According to several studies, achieving the net-zero emissions objective is not possible without carbon capture [26]. Carbon dioxide can be captured either directly from the atmosphere (Direct Air Capture – DAC) or from industrial emissions (point source capture). The captured gas can be stored or used in industrial applications or pilot-scale plants [27]. In 2019, researchers estimated that industrial and manufacturing plants generated over 60% of the total CO_2 emissions. Point sources generally contain a higher concentration of CO_2 than ambient air, thus enabling a more efficient local capture compared to DAC. [28] Indeed the composition of flue gases consists mostly of N_2 with a fraction of 15% CO_2 and other minor components [29]. Among post-combustion capture techniques, the most conventional is the amine-based adsorption method which consists in employing a sorbent (typically monoethanolamine) to capture the CO_2. This method is costly in terms of both financial and energy resources requiring regeneration of the sorbent by heating, corrosion issues and it also generates environmental impact during disposal [30]. To address this limitation, researchers have developed alternative technologies since the 1960s–70s, with electrochemical carbon capture and concentration (eCCC) methods emerging as one of the most extensively studied approaches [28]. More recently, in 2014, a novel method gained attention in carbon capture research: supercapacitive swing adsorption (SSA), which operates by exploiting the capacitive effect. In this context, electrochemical technologies—particularly hybrid capacitive–flow systems—offer innovative solutions to reduce greenhouse gas

emissions and improve energy storage sustainability. Chapter 2 provides a comprehensive overview of these technologies and examine their performance, efficiency, and role in sustainable energy systems.

Chapter 1 References

[1] Trischler, H. (2016). The Anthropocene: A challenge for the history of science, technology, and the environment. N.T.M. – Zeitschrift für Geschichte der Wissenschaften, Technik und Medizin, 24, 309–335. https://doi.org/10.1007/s00048-016-0146-3

[2] Miles, S. H., & Craddock, S. (2018). Ethics for the Anthropocene Epoch. In D. A. DellaSala & M. I. Goldstein (Eds.), Encyclopedia of the Anthropocene (Vol. 1, pp. 21–27). Elsevier. https://doi.org/10.1016/B978-0-12-809665-9.10444-6

[3] Hase, V., Mahl, D., Schäfer, M. S., & Keller, T. R. (2021). Climate change in news media across the globe: An automated analysis of issue attention and themes in climate change coverage in 10 countries (2006–2018). Global Environmental Change, 70, 102353. https://doi.org/10.1016/j.gloenvcha.2021.102353

[4] Intergovernmental Panel on Climate Change. (2022). Climate Change 2022: Mitigation of Climate Change. Contribution of Working Group III to the Sixth Assessment Report of the Intergovernmental Panel on Climate Change (P. R. Shukla, J. Skea, R. Slade, A. Al Khourdajie, R. van Diemen, D. McCollum, et al., Eds.). Cambridge University Press. https://doi.org/10.1017/9781009157926

[5] Monroe, R. (2025, 5 giugno). Annual carbon dioxide peak passes another milestone. UC San Diego Today. https://today.ucsd.edu/story/annual-carbon-dioxide-peak-passes-another-milestone

[6] Friedlingstein, P., O'Sullivan, M., Jones, M. W., Andrew, R. M., Bakker, D. C. E., Hauck, J., Landschützer, P., Le Quéré, C., Luijkx, I. T., Peters, G. P., Peters, W., Pongratz, J., Schwingshackl, C., Sitch, S., Canadell, J. G., Ciais, P., Jackson, R. B., Alin, S. R., Anthoni, P., Barbero, L., … Zheng, B. (2023). Global carbon budget 2023. Earth System Science Data, 15, 5301–5369. https://doi.org/10.5194/essd-15-5301-2023

[7] Our World in Data. (2025). HadCRUT5 dataset [Data visualization]. Based on data from Met Office Hadley Centre (HadCRUT5, 2025). https://ourworldindata.org

[8] United Nations Framework Convention on Climate Change. (1997). Kyoto Protocol to the United Nations Framework Convention on Climate Change. United Nations. https://unfccc.int/kyoto_protocol

[9] United Nations Framework Convention on Climate Change. (2015). Paris Agreement. United Nations. https://unfccc.int/process-and-meetings/the-paris-agreement

[10] United Nations. (2015). Transforming our world: The 2030 Agenda for Sustainable Development. United Nations. https://sdgs.un.org/2030agenda

[11] European Commission. (2019). The European Green Deal. European Commission. https://ec.europa.eu/info/strategy/priorities-2019-2024/european-green-deal_en

[12] European Commission. (2025). Clean Industrial Deal: integrating industrial policy and climate ambitions [Documento della Commissione]. In 2040 Climate Target Proposal: reducing EU net GHG emissions by 90 % (relative to 1990). https://climate.ec.europa.eu/eu-action/climate-strategies-targets/2040-climate-target_en

[13] Gür, T. M. (2018). Review of electrical energy storage technologies, materials and systems: Challenges and prospects for large-scale grid storage. Energy & Environmental Science, 11, 2696–2767. https://doi.org/10.1039/c8ee01419a

[14] Passerini, S., Barelli, L., Baumann, M., Peters, J., & Weil, M. (Eds.). (2024). Emerging battery technologies to boost the clean energy transition: Cost, sustainability, and performance analysis. Springer Nature. https://doi.org/10.1007/978-3-031-48359-2

[15] Horzela-Miś, A., & Semrau, J. (2025). The role of renewable energy and storage technologies in sustainable development: Simulation in the construction industry. Frontiers in Energy Research, 13, 1540423. https://doi.org/10.3389/fenrg.2025.1540423

[16] International Energy Agency. (n.d.). Electrification. IEA. Retrieved October 10, 2025, from https://www.iea.org/energy-system/electricity/electrification

[17] Thomaßen, G., Kavvadias, K., & Jiménez Navarro, J. P. (2021). The decarbonisation of the EU heating sector through electrification: A parametric analysis. Energy Policy, 148, 111929. https://doi.org/10.1016/j.enpol.2020.111929

[18] Gardiner, N. J., Jowitt, S. M., & Sykes, J. P. (2024). Lithium: Critical, or not so critical? Geoenergy, 2, Article geoenergy2023-045. https://doi.org/10.1144/geoenergy2023-045

[19] Weber, A. Z., Mench, M. M., Meyers, J. P., Ross, P. N., Gostick, J. T., & Liu, Q. (2011). Redox flow batteries: A review. Journal of Applied Electrochemistry, 41(10), 1137–1164. https://doi.org/10.1007/s10800-011-0348-2

[20] Béguin, F., Presser, V., Balducci, A., & Frackowiak, E. (2014). Carbons and electrolytes for advanced supercapacitors. Advanced Materials, 26(14), 2219–2251. https://doi.org/10.1002/adma.201304137

[21] European Parliament & Council of the European Union. (2023). Regulation (EU) 2023/1542 of 12 July 2023 concerning batteries and waste batteries, amending Directive 2008/98/EC and Regulation (EU) 2019/1020, and repealing Directive 2006/66/EC (Batteries Regulation). Official Journal of the European Union, L191, 1–156. Retrieved July 4, 2024, from https://eur-lex.europa.eu/eli/reg/2023/1542/oj

[22] Zubi, G., Dufo-López, R., Carvalho, M., & Pasaoglu, G. (2018). The lithium-ion battery: State of the art and future perspectives. Renewable and Sustainable Energy Reviews, 89, 292–308. https://doi.org/10.1016/j.rser.2018.03.002

[23] Scipioni, R., Gil Bardají, M. E., Barelli, L., Baumann, M., & Passerini, S. (Eds.). (2026). Hybrid energy storage: Case studies for the energy transition (Vol. 47). Springer Nature Switzerland AG. https://doi.org/10.1007/978-3-031-97755-8

[24] Bocklisch, T. (2016). Hybrid energy storage approach for renewable energy applications. Journal of Energy Storage, 8, 311–319. https://doi.org/10.1016/j.est.2016.01.004

[25] Vangari, M., Pryor, T., & Jiang, L. (2023). An overview of sodium-ion batteries as an alternative to lithium-ion batteries: From materials to cell performance and applications. Batteries, 9(8), 211. https://doi.org/10.3390/batteries9080211

[26] Pye, S., Li, F. G. N., Price, J., & Fais, B. (2017). Achieving net-zero emissions through the reframing of UK national targets in the post-Paris Agreement era. Nature Energy, 2, 17024. https://doi.org/10.1038/nenergy.2017.24

[27] Fu, L., Ren, Z., Si, W., Ma, Q., Huang, W., Liao, K., Huang, Z., Wang, Y., Li, J., & Xu, P. (2022). Research progress on CO_2 capture and utilization technology. Journal of CO_2 Utilization, 66, 102260. https://doi.org/10.1016/j.jcou.2022.102260

[28] Zito, A. M., Clarke, L. E., Barlow, J. M., Bím, D., Zhang, Z., Ripley, K. M., Li, C. J., Kummeth, A., Leonard, M. E., Alexandrova, A. N., Brushett, F. R., & Yang, J. Y. (2023). Electrochemical carbon dioxide capture and concentration. Chemical Reviews, 123(13), 8069–8098. https://doi.org/10.1021/acs.chemrev.2c00681

[29] Zhu, S., Ma, K., & Landskron, K. (2018). Relationships between the charge–discharge methods and the performance of a supercapacitive swing adsorption module for CO_2 separation. The Journal of Physical Chemistry C, 122(32), 18476–18483. https://doi.org/10.1021/acs.jpcc.8b03968

[30] Raganati, F., Miccio, F., & Ammendola, P. (2021). Adsorption of carbon dioxide for post-combustion capture: A review. Energy & Fuels, 35(16), 12845–12868. https://doi.org/10.1021/acs.energyfuels.1c01618

Chapter 2: Technological Background

2.1 Electrochemical Energy Storage systems and their classification

Section 1.2 presented, among all the ESSs, the category of Electrochemical Energy Storage Systems (EESSs). The technologies included in this group demonstrate significant diversity, but two subgroups can be distinguished based on their operating principle: Electrical Double Layer Capacitors (EDLCs) and Electrochemical Batteries. EDLCs operate through a non-Faradaic process, in which charging occurs by electrostatic charge separation, generating an electrical double layer at the electrode–electrolyte interface. In contrast, Batteries function through Faradaic processes involving redox reactions. Researchers generally refer to EDLCs as Supercapacitors, a category that also comprises Hybrid and Pseudo-Capacitors, which exhibit similar power and energy characteristics but also depend partly on Faradaic processes. In this study, the term Supercapacitors will specifically denote EDLCs, which represent the only type of SC device examined.

Electrochemical Batteries can be further divided into two categories: closed batteries and open batteries. Closed batteries contain active species in solid form within the electrodes. Among closed batteries, Lithium-ion batteries are the most extensively studied and commercially available. Typically, Lithium-ion batteries employ graphite as the anode and a metal oxide (or phosphate) as the cathode. During recent years, research efforts have focused on developing Metal–Air open batteries featuring metallic anodes, such as lithium, due to their promising high energy densities. Flow batteries are also considered as “open” systems because redox species are dissolved in the electrolyte that in turn is stored in tanks outside of the cell. The most widely deployed flow battery is the Vanadium Redox Flow Battery (VRFB). [1,2]

2.2 The capacitive effect and Supercapacitors

In 1957, engineer Howard I. Becker obtained a patent for developing the first low-voltage, high-capacity capacitor. The device comprised a container with two porous carbon electrodes and a water-based electrolyte. Although Becker was unable to define the mechanism underlying the system's charging process, experimental results confirmed its effective performance [3]. Previous investigations, particularly those conducted by Helmholtz, Gouy-Chapman, and Stern, provided the theoretical foundation for understanding how a device like Becker's operates. Professor Brian Evan Conway integrated this knowledge and identified such devices as supercapacitors [4].

As illustrated in Figure 2.2.1, a modern supercapacitor typically consists of two current collectors and two electrodes—one positive and one negative—separated by a membrane that prevents short circuits. A highly conductive electrolyte permeates both the separator and the internal volume of the cell. The electrodes are usually composed of highly conductive carbon materials with a large specific surface area. These characteristics are crucial to achieve a high-power device with significant capacitance. [5].

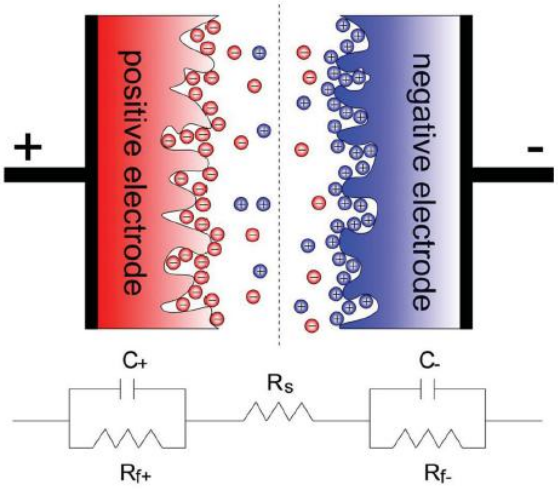

Figure 2.2.1 Representation of a charged Supercapacitor and its corresponding equivalent circuit adopted from [5].

As previously discussed, supercapacitors are classified as an electrochemical energy storage system. In fact, the storage mechanism is based on charge separation driven by electrostatic processes. When a voltage is applied, the two electrodes become polarized with

opposite charges, attracting electrolyte ions of opposite polarity. This charge separation takes place at the electrode/electrolyte interface. More specifically, energy storage results from the electrostatic accumulation of ions on the surface of each electrode, through ion adsorption into the porous carbon-based material. Cations are attracted to the negatively polarized electrode, while anions migrate toward the positive one, forming a symmetrical configuration. This mechanism, known as the Electrical Double Layer, gives the device its name.

The performance of a Supercapacitor is usually evaluated through its capacitance, which represents the amount of charge q stored by the device at a given potential V, according to the Equation $C=q/V$. The unit of capacitance is the Farad (F). In a supercapacitor, each charged electrode forms a double layer, which behaves as a capacitance. According to the Helmholtz model proposed in 1879, the capacitance is related to the electrode surface area A, the average thickness of the double-layer structure d_H, and the effective dielectric constant ε_r, together with ε_0, the vacuum permittivity. This relationship follows Equation 2.2.1 [4]:

$$C = \frac{\varepsilon_r \varepsilon_0}{d_H} A \qquad 2.2.1$$

This formula shows the relationship between C and A: capacitance increases when the electrode surface area increases. Thus, electrodes usually consist of a porous material such as carbons with high specific surface area A_s (typically A_s>1500 $m^2\ g^{-1}$). Also, the dielectric constant of the solvent is strongly related to the capacitance: the higher the dielectric constant is, the higher the capacitance, as in the case of aqueous electrolytes. The two charged electrodes act like two capacitors in series (Figure 2.2.1), and the equivalent capacitance can be evaluated through Equation 2.2.2:

$$\frac{1}{C} = \frac{1}{C^+} + \frac{1}{C^-} \qquad 2.2.2$$

considering $C+$ as the capacitance of the positive electrode and $C-$ as that of the negative one. The cell presents three main types of resistance: the ionic resistance of the electrolyte, the electronic resistance of the electrodes, and the electrode/electrolyte interface resistance. The overall resistance of the device, which includes all these contributions, is called Equivalent Series Resistance (ESR). Resistance has a significant impact on the power performance of supercapacitors. In fact, the maximum specific power can be extrapolated using the following Equation 2.2.3:

$$P = \frac{U_{max}^2}{4\ ESR\ m} \quad 2.2.3$$

where m is the mass of the cell and U_{max} refers to the maximum EDL cell voltage, that is mainly limited by the electrochemical stability of the electrolyte. The EDL mechanism does not involve any redox reactions, allowing fast energy storage and delivery. From an energetic point of view, we must consider that the EDL mechanism is confined to a layer of only a few nanometers (dH~1–2 nm), which is several orders of magnitude smaller than the total cell volume and results in a low energy density for the device [6]. Combining the effects of the EDL on the device, we can say that SCs are characterized by very high specific power, attaining values around 10 kW kg^{-1}, and by relatively modest specific energy, typically lower than 10 Wh kg^{-1}. As for the capacitance, present commercial supercapacitors have sizes ranging from a few millifarads to 100 kilofarads [7].

One of the disadvantages of supercapacitors is their high energy storage cost, which can exceed 4500 EUR kWh^{-1}, even though they are considered inexpensive in terms of power capability (less than 1 EUR kW^{-1}). Currently, in order to significantly enter the market, a storage technology should typically reach a cost < 100 EUR kWh^{-1}, depending on the specific use case. The production cost of supercapacitors is divided into four main categories, as shown in Figure 2.2.2: electrolyte, separator, electrodes, and cell parts/production. The electrolyte is typically an organic solution that includes a solvent and a conductive salt; the separator is usually made of microporous polymers or glass fiber foils (the latter are more expensive and mainly used in research); the electrodes consist of the current collector, a carbonaceous high surface area material, a binder, and often a conductive agent; the final group includes all mechanical and electrical components of the device. As illustrated in the pie charts, the organic electrolyte accounts for 27% of the total cost, and this value can be further divided into the contributions from the solvent and the salt, with the salt being the most influential cost factor. The electrode accounts for 28% of the overall device cost. The current collector foil represents the most expensive component (58.8%), followed by the carbonaceous material (39.2%). Reducing the cost of both the carbon-based material and the electrolyte could significantly decrease the total cost of supercapacitors, thus enhancing their potential for large-scale market adoption [8].

This work will focus on more cost-effective and sustainable solutions for both the electrolyte and the carbon material. For this reason, the next Section will examine these aspects in greater detail.

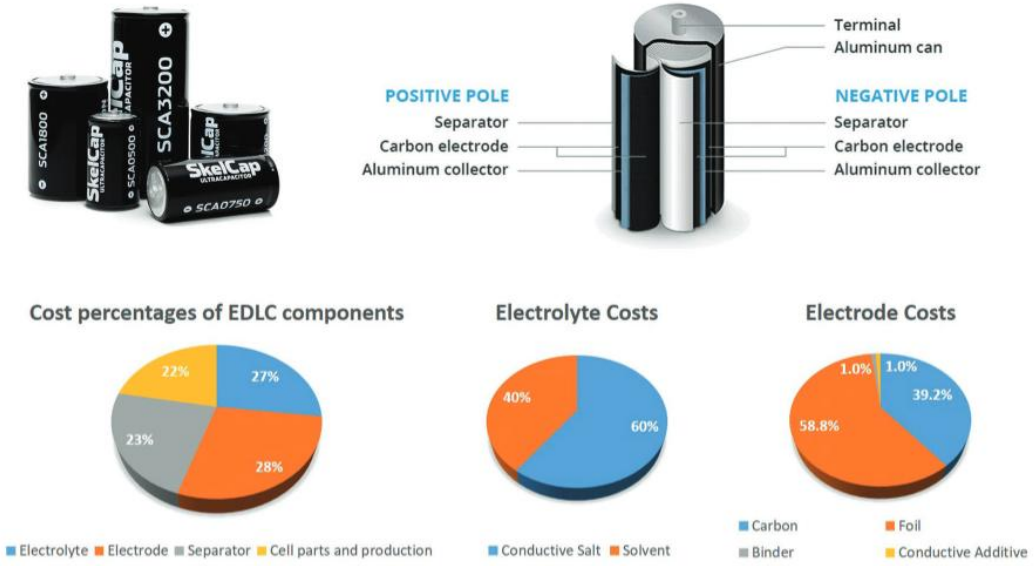

Figure 2.2.2 Picture of an actual SC cell with an exploded view and cost distribution of its components adapted from [8]

2.2.1 Electrolyte

The electrolyte is a conductive solution consisting of a salt dissolved in a solvent. The properties of the electrolyte influence several characteristics of the supercapacitor. Electrolyte ions are essential for the formation of the electrical double layer during the charge and discharge cycles. The capacitance is influenced by the interaction between ions and pores; therefore, the ratio between ion size and pore size plays a key role. As previously discussed, the energy density is directly related to the voltage window. Different combinations of current collectors and electrolytes provide different electrochemical stability window, affecting the operating EDL voltage. A wider voltage window results in higher energy. The resistance of the electrolyte to decomposition is critical for ensuring long cycle life. The electrolyte's conductivity affects the overall ESR of the cell, and thus the power performance. Finally,

electrolyte properties such as boiling point, freezing point, flash point, and salt solubility determine the operating temperature range and safety use of the supercapacitor.

Electrolytes are typically classified based on the type of solvent and they can be classified into two main groups: organic electrolytes and aqueous electrolytes. Some examples of the most employed in SCs are reported in Table 2.2.1.1 which summarizes their ionic conductivity, the electrochemical stability window (ESW) and the estimated cost. Organic electrolytes offer a wider voltage stability window, and supercapacitor cells using them can operate at voltages even higher than 3 V. However, organic electrolytes—such as the widely used 1 M triethyl ammonium tetrafluoro borate (Et_4NBF_4) in acetonitrile (ACN)—are commonly considered flammable, toxic, carcinogenic, and expensive. In contrast, aqueous electrolytes exhibit higher ionic conductivity and provide several advantages in terms of cost and safety. The main limitation of water-based supercapacitors is the narrower voltage window, caused by water electrolysis, which restricts the operating voltage to a maximum of approximately 1.8 V. Water-based electrolytes can also be categorized according to their pH: acidic, basic, or neutral. Among the acidic electrolytes, the most widely investigated is sulfuric acid (H_2SO_4), which displays high ionic conductivity (around 850 mS cm^{-1} at 1 M) but suffers from a limited potential window due to its strong corrosive nature [9]. 6 M KOH (potassium hydroxide) is one of the most widely employed basic electrolytes in supercapacitors due to its high ionic conductivity (around 600 mS cm^{-1} at 6 M). However, current collectors are still subject to corrosion when in contact with the electrolyte, especially near the limits of the electrochemical stability window. To reduce the corrosion of current collectors, neutral water-based electrolytes are currently being investigated in the literature. One of the most commonly used is the aqueous solution of sodium sulfate (Na_2SO_4), which enables a relatively wide potential window [10]. In recent years, a new class of electrolytes has emerged in the literature: water-in-salt electrolytes (WiSE). In these systems, the high salt-to-water ratio causes the salt to behave as the solvent, while water acts as the solute. The salt ions strongly coordinate the water molecules, thereby reducing water activity and suppressing electrolysis reactions. As a result, a wider electrochemical stability window can be achieved. Among the various WiSE formulations, high concentration solutions of potassium acetate (KOAC) is one of the most widely studied, allowing a stability window of approximately 1.7 V .[11] Generally, in addition to the high conductivity and the low sustainability impact, water-based electrolytes

exhibit a low price as reported in Table 2.2.1.1. Another significant category of alternative, organic electrolytes for supercapacitors is the class of ionic liquids (e.g., 1-Butyl-1-methylpyrrolidinium bis(trifluoromethanesulfonyl)imide, $PYR_{14}TFSI$), which exhibit high electrochemical stability and are regarded as safe due to their low flammability. However, they are not considered environmentally sustainable and are known to be toxic.

Table 2.2.1.1 Ionic conductivity (κ), Electrochemical Stability Window (ESW) at room temperature, and commercial cost of various electrolyte solutions and components used in supercapacitors, adapted from [12] and supplemented with data from [9]

Electrolyte solution components and composition		**Concentration**	**κ**	**ESW**	**Cost**
			mS cm^{-1}	*V*	*\$ g^{-1}*
Conventional Organic electrolytes					
Tetraethylammonium tetrafluoroborate in Acetonitrile	$ACN/TEABF_4$	1 mol L^{-1}	56	6.1	3.69
Water based					
Sulfuric Acid	H_2SO_4	1 mol L^{-1}	850	1.2	0.07
Potassium Hydroxide	KOH	6 mol L^{-1}	600	1.2	0.07
Sodium Sulphate	Na_2SO_4	1 mol L^{-1}	50	1.6	0.04
Ionic liquids					
1-Butyl-1-methylpyrrolidinium bis(trifluoromethanesulfonyl)imide	$PYR_{14}TFSI$	6 mol L^{-1}	2.8	6.6	22
Salts used in WiSE					
Potassium acetate	KOAC	30 mol kg^{-1}	25	3.2	0.35
Ammonium acetate	AmAc	26.4 mol kg^{-1}	49	2.9 – 3.3	1.2

2.2.2 Electrodes

As seen above, the most important property of supercapacitor electrodes is the surface area. For this reason, the most commonly used material for their production is activated carbon powder, which offers both high electrical conductivity and a large specific surface area. Additional advantages of carbon-based materials include corrosion resistance, high thermal stability, and low cost, which is also related to the possibility of producing them from organic waste. Most carbonaceous materials are classified based on the precursor, such as biomass, coals, or petroleum coke. The characteristics of the precursor strongly influence the properties of the resulting carbonaceous material. The precursor is typically subjected to high-temperature treatment to initiate the carbonization process, which involves thermal decomposition—known as pyrolysis—that removes volatile components from the material.

Different carbonization and pyrolysis temperatures lead to various structural modifications in the carbon, such as the formation of graphite-like microcrystals or sheets, which alter both the orientation and the size of the crystallites. These features have a significant impact on the electrical conductivity of the carbonaceous material. . Carbon materials are generally classified as graphitizing or non-graphitizing, with the latter category including biomass-derived precursors. Since the carbonization process affects the carbon structure, it becomes a strategic step in tuning the electronic conductivity. A high degree of graphitization is scientifically correlated with enhanced conductivity. On the other hand, highly ordered graphitic carbons typically display lower specific surface area [13].

2.3 Flow electrochemical storage systems

A flow electrochemical storage system (Figure 2.3.1) is generally composed of four main components: the tanks, the reactor, the membrane, and the pumps. The tanks contain the electrolyte, which is circulated by the pumps into the reactor, where the electrochemical reactions take place. The membrane separates the two sides of the reactor, preventing short circuits and allowing the selective passage of ions. The key advantage of a flow system is its ability to decouple energy and power. Specifically, the amount of energy depends on the volume of electrolyte stored in the tanks, while the power is determined by the number of cells in the stack. This configuration can be applied to both supercapacitors and batteries, depending on the desired application. The following paragraphs will present different approaches to implementing this technology by varying its components.

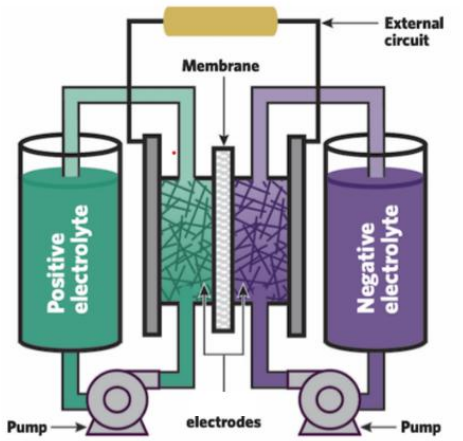

Figure 2.3.1 Flow electrochemical cell essential components. Picture from [14]

2.3.1 Redox Flow Batteries

Usually, when referring to a flow electrochemical system, we mean a redox flow battery (RFB), also known as an open battery [15]. In fact, this technology was initially developed by NASA during the 1970s, exploring various types of redox chemistries such as Fe/Cr and Zn/Br systems. However, it was only in 1985, through the work of Maria Skyllas-Kazacos [16], that a fully stable, reversible, and scalable redox cell was demonstrated, employing vanadium in four oxidation states (V^{2+}, V^{3+}, V^{4+}, V^{5+}).

As shown in Figure 2.3.1.1, the scheme of a Vanadium Redox Flow Battery (VRFB) is similar to the one presented in Figure 2.3.1; however, in this case, the specific materials employed must be identified. As previously stated, this type of cell takes advantage of vanadium's ability to exist in four different oxidation states. In fact RFBs operate with redox couples, and for this reason, they rely on Faradaic processes involving electron transfer. In the catholyte (i.e., the positive side of the cell), vanadium is present as VO_2^+ (V^{5+}) when the cell is charged and is reduced to VO^{2+} (V^{4+}) during discharge. On the anolyte side (i.e., the negative half-cell), vanadium exists as V^{2+} and is oxidized to V^{3+} during discharge. As illustrated by the corresponding half-cell reactions, protons (H^+) participate in the redox processes. For this reason, the membrane used in a VRFB is a proton-exchange membrane, which selectively permits the transport of protons while minimizing the crossover of vanadium species. The standard cell voltage associated with these reactions is 1.26 V at 25 °C with 50% state of charge (SOC), while the practical open-circuit voltage of a fully charged cell reaches approximately 1.4 V [17].

As reported in the previous Section, the amount of energy storable in a RFB is strictly related to the size of the tanks, while the power output depends on the stack size. The ability to decouple energy and power is one of the most attractive advantages of RFBs. This feature makes RFBs particularly suitable for large-scale applications that require high energy storage capacity. RFBs also offer high round-trip efficiency (RTE), high depth of discharge (DOD), and long calendar and cycle life, typically ranging from 15 000 to 20 000 charge/discharge cycles. In terms of performance, the energy density of RFBs is relatively low (approximately 20–35 Wh L^{-1}), as is the power density (40–100 W L^{-1}). The low power density of RFBs—especially when

compared to that of supercapacitors—is directly linked to the slow Faradaic processes on which they rely [19].

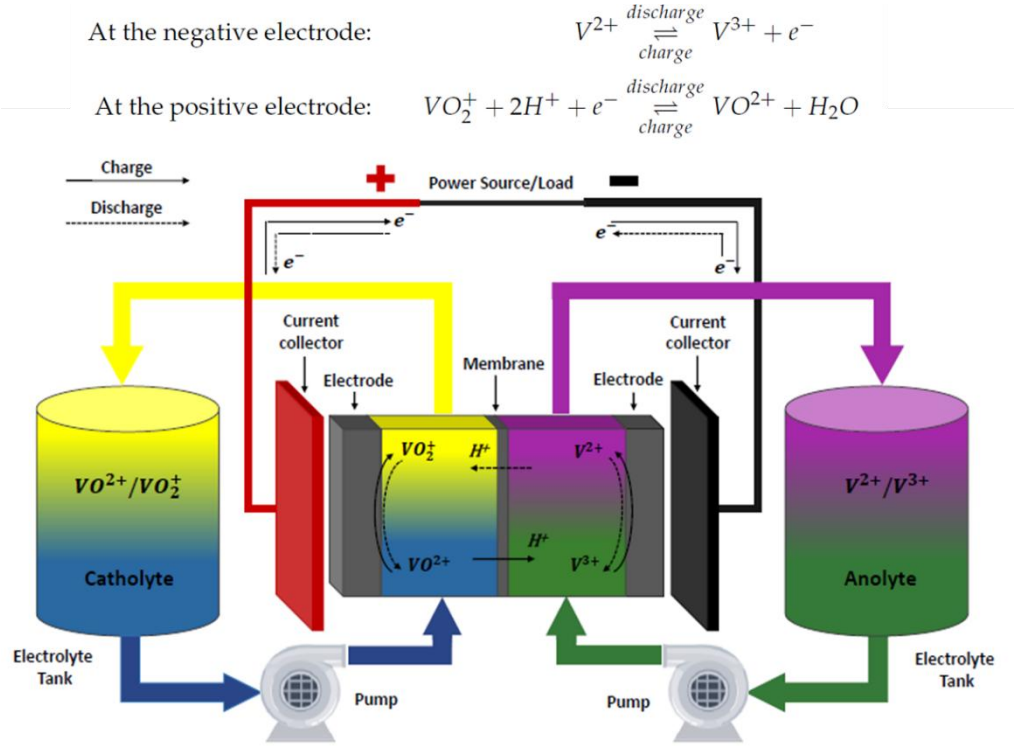

Figure 2.3.1.1 General scheme of a VRFB and its main redox reactions. Picture from [18]

Currently, several large-scale plants employing VRFBs are in operation worldwide, particularly in Asia and the United States. The largest installation, with a capacity of 175 MW and 700 MWh, began operation in December 2024 in Xinjiang, China. It is designed to support the integration of renewable energy into the grid by providing peak shaving and frequency regulation services [20].

Unfortunately, vanadium is currently classified as a Critical Raw Material (CRM). In particular, the European Union included it in the official CRM list in 2023 [21]. For this reason, new chemistries are currently under investigation in the literature to identify a suitable substitute for vanadium. Among the redox couples being studied, the zinc-based systems are the most extensively investigated. In particular, the Zn–Br_2 couple is approaching commercialisation, with companies such as Redflow in Australia leading its development, although certain issues concerning toxicity and corrosion are associated with the formation of Br_2 gas [22,23].

2.3.2 Semi-Solid Lithium-Air Flow Batteries

As stated earlier, RFBs are considered a well-suited technology for stationary energy storage, particularly due to their ability to decouple power from energy. However, they suffer from low energy density, typically around 20–35 Wh/L. Among the strategies investigated to improve this limitation, one promising approach is to consider metallic lithium and oxygen as a redox couple. Specifically, F. Soavi et al patented Semi-Solid Lithium–Air Flow Battery (SLAFB), in which metallic lithium serves as the anode, while oxygen is continuously supplied to the catholyte from an external tank [24]. This configuration can be considered a half-flow battery, since only the cathode side is flowable. As shown in Figure 2.3.2.1a, the cell operates in flow mode exclusively on the cathode side, where an O_2-saturated electrolyte is pumped through a porous current collector within the reactor. A key feature of the proposed configuration is the dispersion of conductive carbon particles into the catholyte, forming a slurry. These particles should not be considered "active" species, as in Semi-Solid Redox Flow Batteries (SRFBs), because their main function is to facilitate the Oxygen Reduction and Evolution Reactions (ORR/OER) according to Equation 2.3.2.1:

$$O_2\,(sol) + 2\,Li^+ + carbon \leftrightarrow carbon/Li_2O_2(s) \qquad 2.3.2.1$$

Indeed, the carbon particles act as a dispersed electrode, providing the surface where the electrochemical reactions occur. One advantage of this configuration is that the formation of Li_2O_2 — which typically deposits on the electrode surface and increases the cell's overpotential—takes place on the carbon particles instead. This reduces the passivation of the current collector. Additionally, the carbon percolating network offers multiple active sites for the redox reactions, thereby enhancing the current rate response of the system. As stated in the current opinion [25], the University of Bologna spin-off Bettery Srl developed the first scaled-up SLAFB prototype, named NESSOX (NEw Semi-Solid Flow Lithium OXygen Battery), as illustrated in Figure 2.3.2.1b–c. The upscaling of this innovative system requires comprehensive optimisation of all components, including the separator, catholyte formulation, cell design, and management. Figure 2.3.2.1d displays the cell management system unit, which encloses a peristaltic pump used to circulate the catholyte, together with an O_2 flow meter and pressure sensors that monitor the circuit pressure. Figure 2.3.2.1e–f illustrates the most representative charging and discharging results obtained with the

prototype at room temperature. The cell operated at a discharge current of 24 mA, and the graph demonstrates a flat plateau at 2.5 V, whereas the charging profile, which occurred at 12 mA, shows a plateau at 3.5 V. Based on these results, the energy density and specific energy can reasonably be estimated at approximately 950 Wh L^{-1} and 800 Wh kg^{-1}, respectively (excluding the case and control units).

Unfortunately, this system currently presents several disadvantages due to its high carbon content. These include a significant increase in the viscosity and ionic resistance of the catholyte, as well as clogging issues within the porous current collector. These issues will be addressed in Chapter 4, which is dedicated to the improvement of this activity.

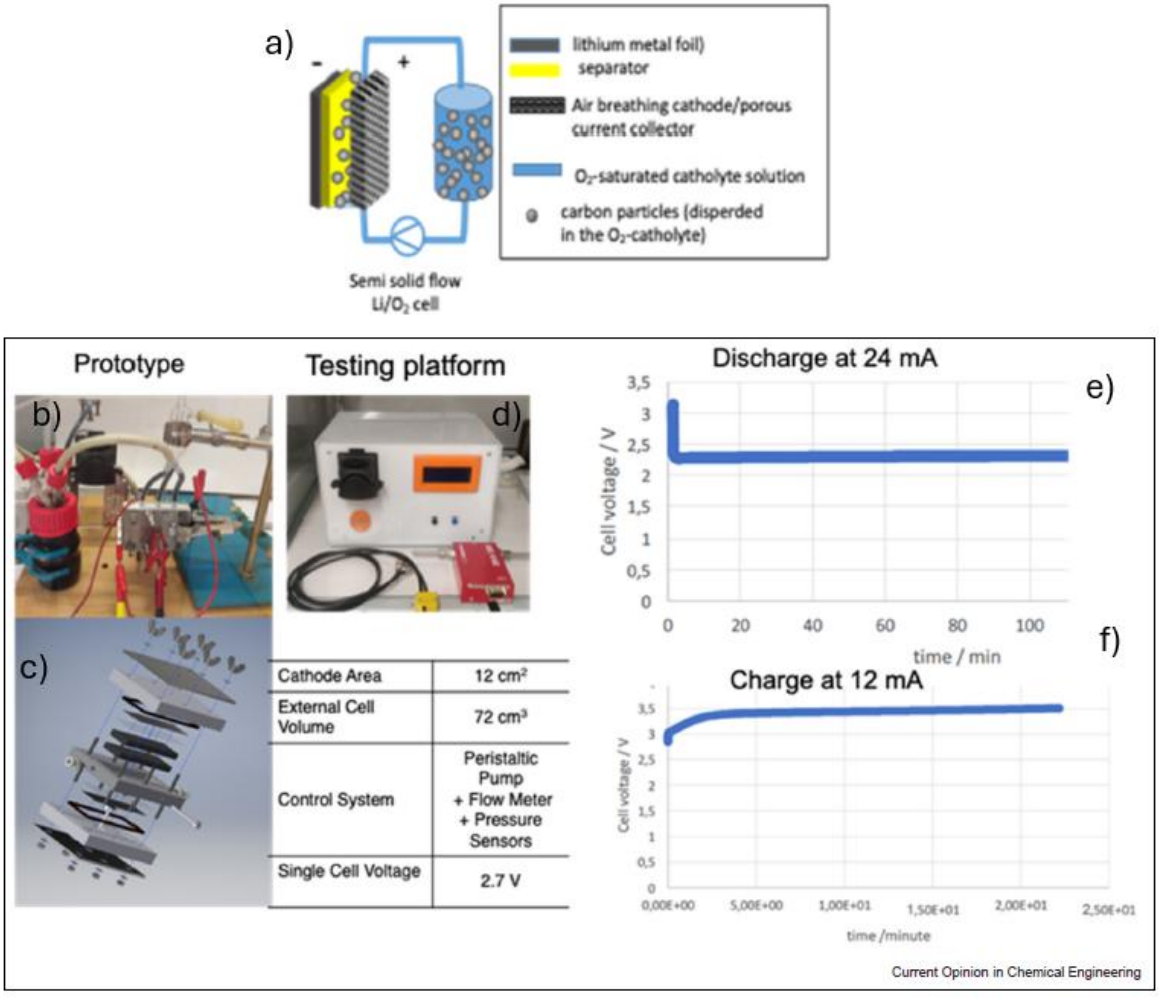

Figure 2.3.2.1 a) Schematic of the Semi-Solid Lithium–Air Flow Battery (SLAFB); b–c) NESSOX prototype developed by Bettery Srl.; d) Cell management system with peristaltic pump, O_2 flow meter, and pressure sensors; e-f) Representative charge and discharge profiles of the SLAFB at room temperature. [25]

2.3.3 Electrochemical Flow Capacitors

As described in Section 2.2, supercapacitors (SCs) are characterized by extremely fast charge/discharge times, due to the electrostatically induced adsorption of ions, which avoids slower Faradaic reactions. In contrast, RFBs, as explained in Section 2.3.1, rely on Faradaic processes, which inherently limit their charge/discharge speed and contribute to their lower power density. However, the main advantage of RFBs—the decoupling of power and energy—is not strictly linked to the redox couple used, but rather to the flow-based architecture, as discussed in Section 2.3. Combining these aspects, a new concept for dynamic energy storage has recently emerged: the Electrochemical Flow Capacitor (EFC). This hybrid technology is designed to merge the benefits of flow systems and supercapacitors, offering the high-power density and long lifetime of supercapacitors along with the high energy capacity of flow batteries [26]. In the literature, only a few studies have been published on EFCs, and they generally adopt an architecture similar to the one shown in Figure 2.3.3.1 (a). Specifically, they incorporate carbon particles directly into the electrolyte, forming a slurry, rather than using layered carbon electrodes. In this configuration, ions are adsorbed onto the porous surface of the carbon particles (b), and the charged electrolyte can be stored in separate tanks (c) [27].

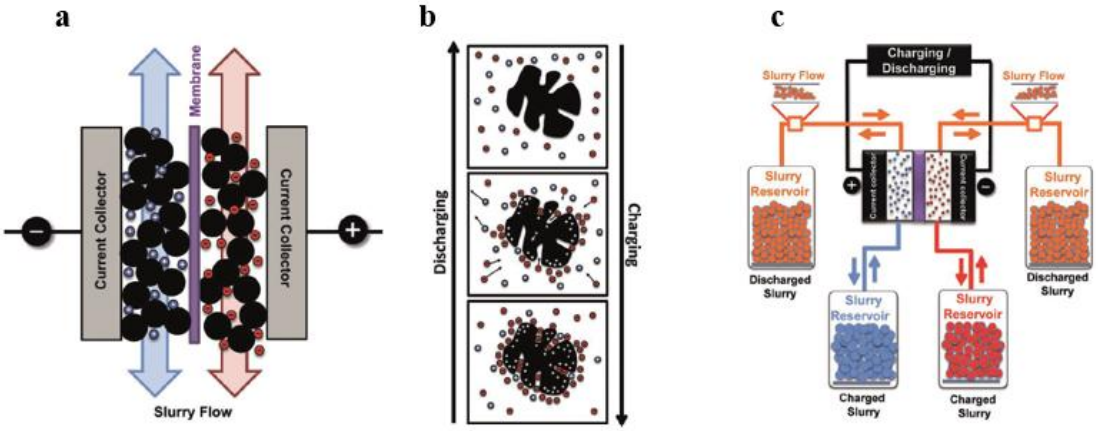

Figure 2.3.3.1 a) Schematic representation of an Electrochemical Flow Capacitor (EFC); b) Ion adsorption on porous carbon particles; c) Complete system with charged slurry reservoirs. [27]

Instead of using slurries, an EFCs can also employ solid carbonaceous electrodes, such as carbon cloths and a flowable electrolyte. In this case, it is possible to exploit the capacitive

effect of the cell without separating the charged and discharged electrolyte. This type of configuration is generally suitable for power-oriented applications or for auxiliary uses, such as Supercapacitive Swing Adsorption (SSA) of carbon dioxide. The application of EFCs in SSA will be discussed in Section 2.4 and Chapter 5.

2.4 Supercapacitive Swing Adsorption

The first paper introducing Supercapacitive Swing Adsorption (SSA) was published in 2014 by the Landskron Group at Lehigh University. For the first time, it was demonstrated that CO_2 can be adsorbed and released by charging and discharging a supercapacitor equipped with gas-exposed porous electrodes and a water-based electrolyte. [28] The mechanism that governs carbon dioxide adsorption through supercapacitors is not yet fully understood, and three possible pathways are proposed in the literature (Figure 2.4.1): i) the gas–solid mechanism, which assumes that CO_2 molecules are adsorbed into the non-wetted pores of the electrodes; ii) the molecular liquid–solid mechanism, in which CO_2 dissolves into the aqueous electrolyte and is captured within the electrical double layer near the electrode surface; both these mechanisms are considered symmetrical since neutral CO_2 can be adsorbed similarly at the positive and negative electrodes; iii) the ionic liquid–solid mechanism, which suggests that CO_2 dissolves in the electrolyte forming ions (HCO_3^-) that migrate from one electrode to the other under the influence of an electric field. This last mechanism is the only one that exhibits asymmetrical behaviour, as the bicarbonate ion (HCO_3^-) migrates toward the positive electrode driven by the electric field, leading to adsorption taking place exclusively at the positive electrode. [29]

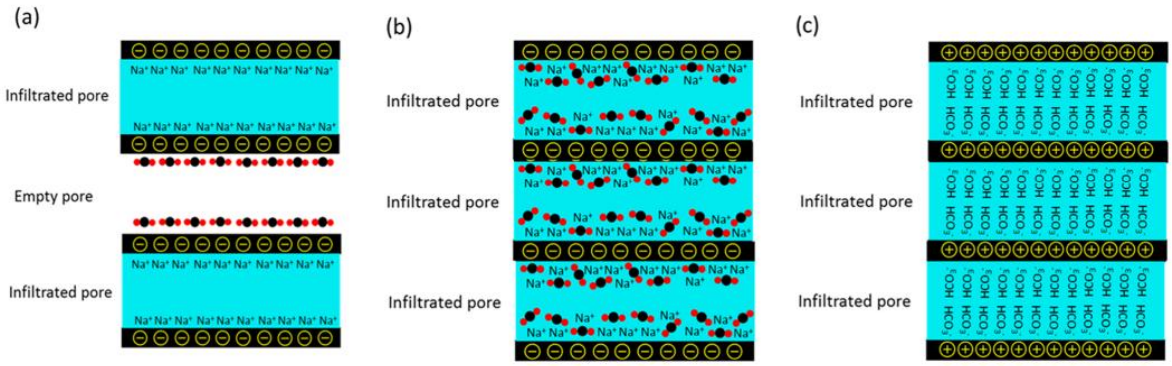

Figure 2.4.1 Schematic representation of CO_2 adsorption mechanisms: (a) gas–solid, (b) molecular liquid–solid, and (c) ionic liquid–solid (occurring only at the positive electrode) [29]

Compared to other CO_2 capture technologies, SSA exhibits a low adsorption capacity. It is approximately eight times lower than that of amine-based systems—the most industrialized approach, that however is highly energy-intensive. In quantitative terms, SSA can typically capture up to 100 mmol of CO_2 kg^{-1}, while amine-based capture (introduced in Section 1.3) exceeds 800 mmol CO_2 kg^{-1}. Moreover, the efficiency of SSA is highly sensitive to several parameters, including the operating protocol, current density, and applied voltage. Further studies, including the present work, aim to improve the understanding and control of these influencing factors. [30-31]

2.5 Battery and Supercapacitors Modelling Techniques

Designing an ESS requires identifying the most suitable technology for a specific application. As discussed in Section 1.2, ESSs are generally classified based on parameters such as power, energy capacity, cycle life, and other performance indicators. In addition, the design process must take into account how demanding the application is for the selected ESS, and how this operational stress may affect the system's lifespan. For instance, it is well known that the cycle life of lithium-ion batteries decreases under high current conditions, as these can cause excessive temperature rise in the cells and other side critical reactions (just to mention lithium plating, solid electrolyte interface damage) [32]. From the perspective of RFBs, high current rates lead to a reduction in battery efficiency [33]. In order to predict the effect of the load on an ESS, engineers commonly model batteries and supercapacitors. This approach allows, for example, to analyse the system's behaviour, predict its operating profile, and determine the optimal management strategy to prevent damage from overcharging or overdischarging, while improving overall efficiency. In addition, modelling supports both system sizing during the design phase and monitoring during operation [34]. Several approaches are available to model batteries and supercapacitors, and they are generally classified into three categories: i) white-box models (e.g., electrochemical models), ii) grey-box models (e.g., circuit-oriented models), and iii) black-box models (e.g., artificial neural networks). White-box models are typically considered the most physically descriptive, while black-box models are the most empirical. Equivalent Circuit Models (ECMs), which belong to the grey-box category, combine physical principles with empirical data and are widely regarded as one of the most suitable methods for modelling ESSs [35].

The simplest way to model a battery, known as the Rint model (Figure 2.5.1a), consists of a resistor representing the internal resistance (R_0) of the battery and a constant voltage source that corresponds to its open-circuit voltage (V_{OC}) [36]. This model is widely used for modelling lead-acid batteries, but it is generally not suitable for fast dynamic estimation. In such cases, to evaluate both the short- and long-term transients of the battery, it is common to add one (Figure 2.5.1b) or two (Figure 2.5.1c) parallel R–C branches. These elements improve the ability to simulate transient behaviour, especially in applications involving Lithium-ion batteries. The R–C blocks require a characterization phase, which is typically carried out through experimental testing in order to empirically determine the resistance (R_n) and capacitance (C_n) parameters. [37].

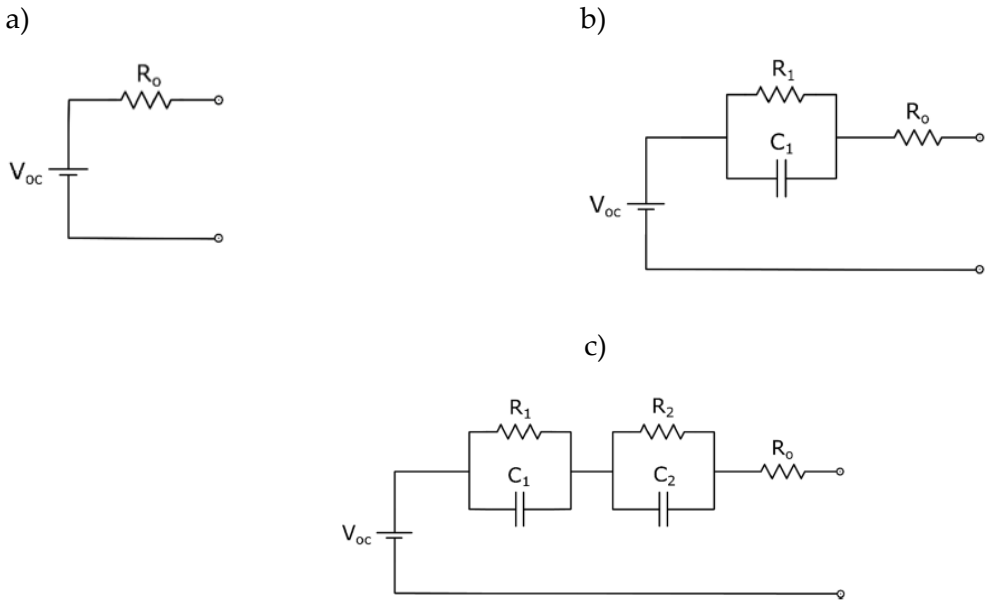

Figure 2.5.1 Three approaches to modelling a battery using an ECM: a) Rint model; b) single R–C block model; c) two R–C block model. Adapted from [37].

The simplest way to model a supercapacitor is by using a branch composed of a resistor, representing the ESR (R), and a capacitor (C) (Figure 2.5.2). This model allows the supercapacitor to be described in terms of energy and storage capacity [38]. As in the case of batteries, to increase the reliability of the model—especially for slow dynamic behaviour—up to two additional R–C blocks can be added. These components must be experimentally characterized to determine the corresponding resistance and capacitance values.

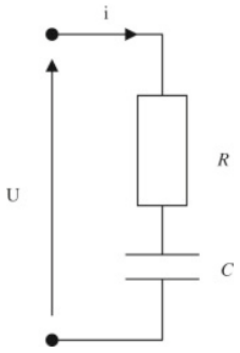

Figure 2.5.2 Modelling approach for Supercapacitors. Adapted from [38]

This thesis work includes modelling studies. Batteries are modelled using the Rint model (Figure 2.5.1a), while supercapacitors are represented through the RC model (Figure 2.5.2). As discussed above, these simplified models present certain limitations, particularly in accurately describing system behaviour under highly dynamic conditions. Nevertheless, the aim of my work is to use modelling primarily as a tool for appropriately sizing batteries and supercapacitors from an energy-oriented perspective. Moreover, incorporating additional R–C blocks would require an experimental characterization phase, making the model highly dependent on empirical data. The use of simple models allows us to rely on input parameters that can also be obtained from datasheets, enabling their application across different scenarios. With this objective, we consider simple modelling a suitable approach to understanding the energetic behaviour of the system during the design phase of a project.

2.6 Topic, Objective and Structure of the Thesis

The main objective of this thesis is to investigate and develop Capacitive–Flow Hybrid Systems as electrochemical solutions for clean energy and climate applications, employing a multidisciplinary and multilevel approach. Indeed, the research addresses the proposed topics from electrochemical, engineering, and sustainability perspectives. In parallel, different levels of integration are considered, ranging from system-level configurations to material-level approaches. This strategy aims to demonstrate that integration enables the design of tailored solutions for specific applications while maintaining a focus on sustainability impacts. Figure 2.6.1 depicts the three main levels of integration considered in the following Chapters. The integration level is defined as low when systems operate independently (System), increases when integration occurs within a single system through materials (Material), and becomes high when integration enables multiple functions to be combined within one system (Functional). At the Material level, integration consists of exploiting new materials derived from different technologies within the same system, whereas at the Functional level integration aims to enable a multipurpose use of the same technology.

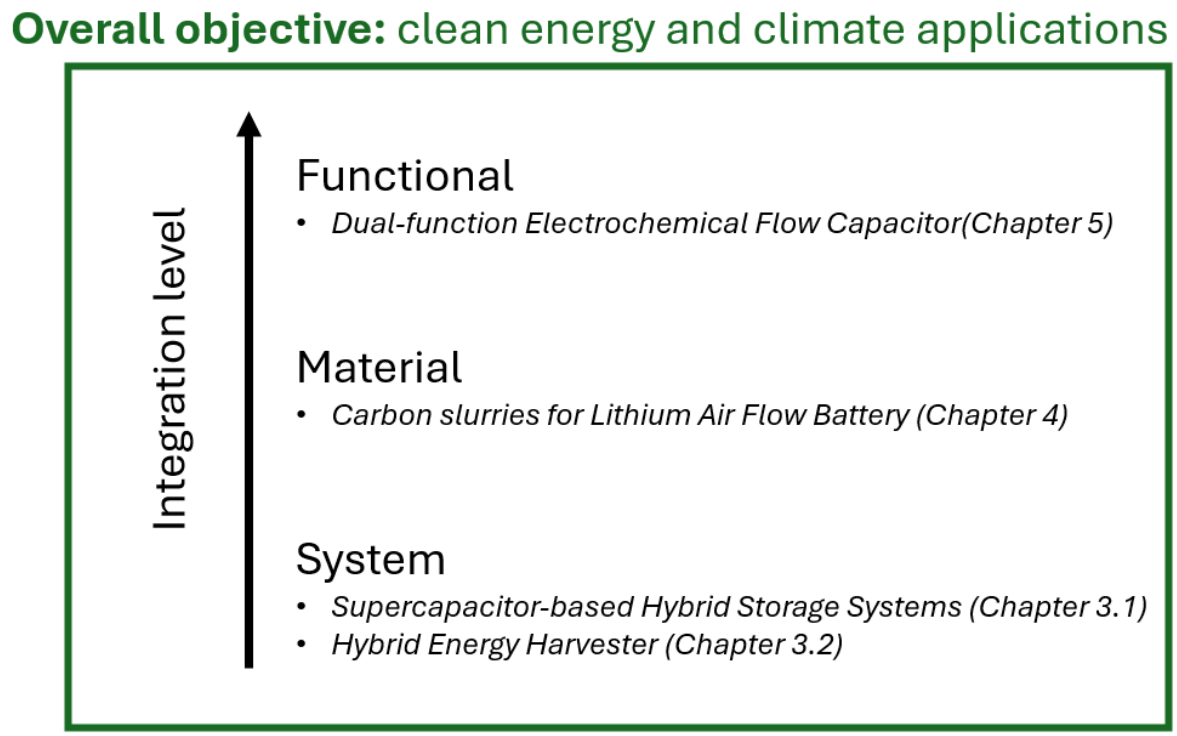

Figure 2.6.1 Schematic overview of the different levels of integration investigated in this thesis for clean energy and climate applications.

Different technologies are considered in this work with a focus on Flow Systems that are increasingly widespread in the ESS market due to the flexibility enabled by their inherent design. Unfortunately, RFBs generally exhibit low power performance, which restricts their implementation in certain applications. SCs, when coupled with RFBs in hybrid EESs, extend the potential applications of the system by improving its overall power response. In parallel, piezoelectric energy harvesters represent an innovative approach to harvest mechanical energy from the environment and convert it into electrical energy. Integrating piezoelectric devices with SCs enables the rapid storage of energy generated by the piezoelectric unit and the fast release at high power levels. As mentioned above, RFBs are currently considered low energy density batteries compared to other available technologies such as Lithium-ion batteries. Furthermore, lithium–air flow batteries are a novel solution that employs carbonaceous, flowing slurries to enhance performance. An interesting way to exploit the flow system and the capacitive phenomena is to employ them for the carbon dioxide capture, as CO_2 capture is also considered, as outlined in Chapter 1, a mandatory technology to address climate challenges.

All the above mentioned technologies are considered in this thesis adopting a multidisciplinary approach which includes both electrochemical experiments and modelling. Starting with a System level of integration (with ref. to Figure 2.6.1), Chapter 3 reports results of my investigation on Supercapacitor-based Hybrid Storage Systems and Hybrid Energy Harvester that combines experimental and modelling studies. In the first case, the integration involves two storage systems, whereas in the second case it combines a storage system with a generator. In detail Section 3.1 presents the passive integration of a Vanadium Redox Flow Battery with a Supercapacitor at the cell level, aiming to design a HESS for renewable energy sources (Section 3.1.1) or for electric bus application (Section 3.1.2). This study includes experimental testing, numerical modelling, LCA, and economic evaluation, providing both performance outcomes and sustainability–economic forecasts for the upscaled system. The work reported in Section 3.1.1 was conducted within the framework of the HyFlow project, as the LCA and economic evaluation represent the outcomes of a collaboration with the Energie Institut of Linz. The integration of a supercapacitor with a piezoelectric generator for energy harvesting is described in Section 3.2. The leitmotif of Chapter 3 is the design and validation of models for the different systems through different approaches including a numerical

method described in Section 3.1.1 and a semi-empirical one outlined in Section 3.1.2 which aims at predicting the behaviour of the upscaled HESS under realistic loads. The work presented in Section 3.1.2 results from the Mentoring Programme for PhD students, organised by the StoRIES Project, in which I participated and was mentored by Professor Linda Barelli (Engineering Department - University of Perugia). Another semi-empirical modelling approach is illustrated in Section 3.2, where the investigation of Supercapacitor charging through a piezoelectric device was conducted. In this case, the model simulates the charging process of the Supercapacitor by monitoring the voltage profile. The simulated data are compared and validated with experimental results obtained from a real piezo–SC system. The work presented in Section 3.2 was conducted within the objectives of the THOR project (lighTweight self-cHarging piezO-supercapacitoR systems by nanotechnologies) in collaborations with the groups of Prof. Chiara Gualandi (Dept. Of Chemistry "Giacomo Ciamician") and Prof. Davide Fabiani (Department of Electrical, Electronic, and Information Engineering "Guglielmo Marconi") of University of Bologna.

Moving towards a Material level of integration (with ref. to Figure 2.6.1), Chapter 4 presents my contribution to the upscaling of the Semi-Solid Lithium–Air Flow Battery prototype, NESSOX, developed by the University of Bologna spin-off Bettery srl. In this system, we integrate different concepts by transforming carbon materials used in conventional static Li–air batteries into carbon-based slurry suitable for feeding flow cells. The system integrates a flow configuration employing carbon-based slurries with a solid lithium foil. This research aims to address the technological challenges encountered during the scale-up of NESSOX, which requires careful design and optimisation. In detail, the objective of this work is to test new formulations of carbon slurries that enable the elimination of a problematic component of the system: the reticulated vitreous carbon (RVC), which, in addition to its extremely fragile nature, causes agglomeration inside the cell and increases the overall cost of the system.

Chapter 5 explores flow systems and supercapacitors in the context of CO_2 capture through the innovative Supercapacitive Swing Adsorption exploring a Functional Level of integration (with ref. to Figure 2.6.1). Indeed, we exploit the charge-storage features of a supercapacitor to enable an additional function, namely CO_2 capture. The objective of this work is to develop a flow supercapacitor capable of capturing CO_2 when exposed to the gas simply by means of charge and discharge cycles. This Chapter reports the results of my research activity on this

topic conducted during my abroad period in the Yusuf Hamied Department of Chemistry of the University of Cambridge under the supervision of Professor Alexander Forse.

Finally, Chapter 6 summarises the main achievement of my activities in the different topics while analysing the outcomes under a practical perspective.

Chapter 7 reports the lists of projects in which I was involved.

Chapter 2 References

[1] Abbas, Q., Mirzaeian, M., Hunt, M. R. C., Hall, P., & Raza, R. (2020). Current state and future prospects for electrochemical energy storage and conversion systems. Energies, 13(21), 5847. https://doi.org/10.3390/en13215847

[2] Ramasubramanian, B., Dalapati, G. K., Venkatashamy Reddy, M. V., Zaghib, K., Chellappan, V., & Ramakrishna, S. (2024). Progress and complexities in metal–air battery technology. Energy Technology, 12(5), Article 2301375. https://doi.org/10.1002/ente.202301375

[3] Becker, H. I. (1957). Low voltage electrolytic capacitor (U.S. Patent No. 2,800,616). United States Patent and Trademark Office. https://patents.google.com/patent/US2800616A

[4] Conway, B. E. (1999). Electrochemical Supercapacitors: Scientific Fundamentals and Technological Applications. Springer New York. https://doi.org/10.1007/978-1-4757-3058-6

[5] Béguin, F., Presser, V., Balducci, A., & Frackowiak, E. (2014). Carbons and electrolytes for advanced supercapacitors. Advanced Materials, 26(14), 2219–2251. https://doi.org/10.1002/adma.201304137

[6] Simon, P., Gogotsi, Y., & Dunn, B. (2014). Where do batteries end and supercapacitors begin? Science, 343(6176), 1210–1211. https://doi.org/10.1126/science.1249625

[7] Miller, J. R., & Burke, A. F. (2008). Electrochemical capacitors: Challenges and opportunities for real-world applications. The Electrochemical Society Interface, 17(1), 53–57. https://doi.org/10.1149/2.F08081IF

[8] Schütter, C., Pohlmann, S., & Balducci, A. (2019). Industrial requirements of materials for electrical double layer capacitors: Impact on current and future applications. Advanced Energy Materials, 9(25), Article 1900334. https://doi.org/10.1002/aenm.201900334

[9] Mendhe, A., & Panda, H. S. (2023). A review on electrolytes for supercapacitor device. Discover Materials, 3(1), Article 29. https://doi.org/10.1007/s43939-023-00065-3

[10] Pal, B., Yang, S., Ramesh, S., Thangadurai, V., & Jose, R. (2019). Electrolyte selection for supercapacitive devices: A critical review. Nanoscale Advances, 1(10), 3807–3835. https://doi.org/10.1039/c9na00374f

[11] Tribbia, M., Pianta, N., Brugnetti, G., Lorenzi, R., & Ruffo, R. (2020). A new double layer super-capacitor made by free-standing activated carbon membranes and highly concentrated potassium acetate solutions. Electrochimica Acta, 364, 137323. https://doi.org/10.1016/j.electacta.2020.137323

[12] El Halimi, M. S., Poli, F., Mancuso, N., Olivieri, A., Mattioli, E. J., Calvaresi, M., Chafik, T., Zanelli, A., & Soavi, F. (2021). Circumneutral concentrated ammonium acetate solution as

water-in-salt electrolyte. Electrochimica Acta, 389, 138653. https://doi.org/10.1016/j.electacta.2021.138653

[13] Pandolfo, A. G., & Hollenkamp, A. F. (2006). Carbon properties and their role in supercapacitors. Journal of Power Sources, 157(1), 11–27. https://doi.org/10.1016/j.jpowsour.2006.02.065

[14] Stauffer, N. W. (2023, April 7). Flow batteries for grid-scale energy storage. MIT News. https://news.mit.edu/2023/flow-batteries-grid-scale-energy-storage-0407

[15] Diéz, E. S., Poli, F., & Soavi, F. (2024). Open battery systems. In S. Passerini, L. Barelli, M. Baumann, J. Peters, & M. Weil (Eds.), Emerging battery technologies to boost the clean energy transition (pp. — —). Springer, Cham. https://doi.org/10.1007/978-3-031-48359-2_11

[16] Sum, E., & Skyllas-Kazacos, M. (1985). A study of the V(II)/V(III) redox couple for redox flow cell applications. Journal of Power Sources, 15(2–3), 179–190. https://doi.org/10.1016/0378-7753(85)80071-9

[17] Knehr, K. W., & Kumbur, E. C. (2011). Open circuit voltage of vanadium redox flow batteries: Discrepancy between models and experiments. Electrochemistry Communications, 13(4), 342–345. https://doi.org/10.1016/j.elecom.2011.01.020

[18] Puleston, T., Clemente, A., Costa-Castelló, R., & Serra, M. (2022). Modelling and estimation of vanadium redox flow batteries: A review. Batteries, 8(9), 121. https://doi.org/10.3390/batteries8090121

[19] Paoletti, C., Pozio, A., & Prosini, P. P. (2013, September). Studio preliminare su sistemi redox a flusso (Report No. RdS/2013/252). ENEA – Agenzia nazionale per le nuove tecnologie, l'energia e lo sviluppo economico sostenibile. https://www.ricercasistemaelettrico.enea.it/archivio-documenti.html?task=download.send&id=4232:studio-preliminare-su-sistemi-redox-a-flusso&catid=416

[20] Murray, C. (2024, December 6). Rongke Power completes grid-forming 175MW/700MWh vanadium flow battery in China, world's largest. Energy-Storage.News. https://www.energy-storage.news/rongke-power-completes-grid-forming-175mw-700mwh-vanadium-flow-battery-in-china-worlds-largest

[21] European Commission, Directorate-General for Internal Market, Industry, Entrepreneurship and SMEs. (n.d.). Critical raw materials. Internal Market, Industry, Entrepreneurship and SMEs. Retrieved 11 October 2025, from https://single-market-economy.ec.europa.eu/sectors/raw-materials/areas-specific-interest/critical-raw-materials_en

[22] Zhang, H., Lu, W., & Li, X. (2019). Progress and perspectives of flow battery technologies. Electrochemical Energy Reviews, 2(4), 492–506. https://doi.org/10.1007/s41918-019-00047-1

[23] Mahmood, A., Zheng, Z., & Chen, Y. (2024). Zinc–bromine batteries: Challenges, prospective solutions, and future. Advanced Science, 11, 2305561. https://doi.org/10.1002/advs.202305561

[24] Soavi, F., Arbizzani, C., & Ruggeri, I. (2017). Semi-solid flow Li/O_2 battery (WO2017021840A1). World Intellectual Property Organization.

[25] Soavi, F., Brilloni, A., De Giorgio, F., & Poli, F. (2022). Semi-solid lithium/oxygen flow battery: An emerging, high-energy technology. Current Opinion in Chemical Engineering, 37, 100835. https://doi.org/10.1016/j.coche.2022.100835

[26] Porada, S., Lee, J., Weingarth, D., & Presser, V. (2014). Continuous operation of an electrochemical flow capacitor. Electrochemistry Communications, 48, 178–181. https://doi.org/10.1016/j.elecom.2014.08.023

[27] Presser, V., Dennison, C. R., Campos, J., Knehr, K. W., Kumbur, E. C., & Gogotsi, Y. (2012). The electrochemical flow capacitor: A new concept for rapid energy storage and recovery. Advanced Energy Materials, 2(7), 895–902. https://doi.org/10.1002/aenm.201100768

[28] Kokoszka, B., Jarrah, N. K., Liu, C., Moore, D. T., & Landskron, K. (2014). Supercapacitive swing adsorption of carbon dioxide. Angewandte Chemie International Edition, 53(14), 3698–3701. https://doi.org/10.1002/anie.201310308

[29] Zhu, S., Li, J., Toth, A., & Landskron, K. (2019). Relationships between electrolyte concentration and the supercapacitive swing adsorption of CO_2. ACS Applied Materials & Interfaces, 11(21), 21489–21495. https://doi.org/10.1021/acsami.9b03598

[30] Zito, A. M., Clarke, L. E., Barlow, J. M., Bím, D., Zhang, Z., Ripley, K. M., Li, C. J., Kummeth, A., Leonard, M. E., Alexandrova, A. N., Brushett, F. R., & Yang, J. Y. (2023). Electrochemical carbon dioxide capture and concentration. Chemical Reviews, 123(13), 8069–8098. https://doi.org/10.1021/acs.chemrev.2c00681

[31] Mapstone, T., Ravi, S., & Suss, M. E. (2025). Understanding the mechanism of electrochemical CO_2 capture by supercapacitive swing adsorption. Energy & Environmental Science, 18(1), 123–135. https://doi.org/10.1039/d4ee03055a

[32] Barcellona, S., & Piegari, L. (2020). Effect of current on cycle aging of lithium ion batteries. Journal of Energy Storage, 29, 101310. https://doi.org/10.1016/j.est.2020.101310

[33] Chen, J.-Y., Hsieh, C.-L., Hsu, N.-Y., Chou, Y.-S., & Chen, Y.-S. (2014). Determining the limiting current density of vanadium redox flow batteries. Energies, 7(9), 5863–5873. https://doi.org/10.3390/en7095863

[34] Şahin, M. E., Blaabjerg, F., & Sangwongwanich, A. (2021, March). Modelling of supercapacitors based on simplified equivalent circuit. CPSS Transactions on Power Electronics and Applications, 6(1), 31–39. https://doi.org/10.24295/CPSSTPEA.2021.0000

[35] Tamilselvi, S., Gunasundari, S., Karuppiah, N., Razak R. K., A., Madhusudan, S., Nagarajan, V. M., Sathish, T., Shamim, M. Z. M., Saleel, C. A., & Afzal, A. (2021). A review on battery modelling techniques. Sustainability, 13(18), 10042. https://doi.org/10.3390/su131810042

[36] Zhou, W., Zheng, Y., Pan, Z., & Lu, Q. (2021). Review on the battery model and SOC estimation method. Processes, 9(9), 1685. https://doi.org/10.3390/pr9091685

[37] Arregi, O., Agirrezabala, E., Iraola, U., Milo, A., Yeregui, J., Nogueras, U., Sánchez, R., & Gil, I. (2021). A new equivalent circuit model parametrization methodology based on current pulse tests for different battery technologies. Energies, 14(21), 7255. https://doi.org/10.3390/en14217255

[38] Devillers, N., Jemei, S., Péra, M.-C., Bienaimé, D., & Gustin, F. (2014). Review of characterization methods for supercapacitor modelling. Journal of Power Sources, 246, 596–608. https://doi.org/10.1016/j.jpowsour.2013.07.116

Chapter 3: Supercapacitor-Based Hybrid Storage Systems and Energy Harvesters

This Chapter primarily examines the integration of a VRFC with a SC through various approaches, beginning with experimental tests, followed by modelling and the analysis of results from both economic and sustainable perspectives (Section 3.1). In addition, we include in this Chapter (Section 3.2) a parallel study that focuses on modelling the charging process of a SC via a piezoelectric nanogenerator. Although the two topics share limited overlapping areas, I have included this Chapter to further demonstrate the strength of the modelling procedure adopted in both studies, that followed a similar approach.

3.1 Integration of a Vanadium Redox Flow Cell with Supercapacitors: Evaluation and Applications

As outlined in the introduction, ESSs represent a crucial component of the current energy transition, as they enable the storage of energy derived from sustainable sources such as wind and solar power. A major issue associated with these sources, particularly in microgrid applications, is the intermittent nature of the energy supply. Among all available ESSs, the most attractive are those that demonstrate high efficiency, extended lifespan, and the capacity to manage frequent power fluctuations. However, no single technology currently incorporates all these features. Therefore, one viable approach is to integrate two different technologies with complementary functionalities. This type of electrical integration is commonly referred to as a HESS. At present, RFBs are considered one of the most flexible technologies for stationary applications, primarily due to their capability to store large volumes of energy simply by scaling the size of the electrolyte tanks. A recent study [1] conducted by members of the HyFlow project evaluated several possible configurations of HESSs that include RFBs. Their findings indicate that one of the most effective combinations involves the integration of RFBs with supercapacitors (SCs). This RFB-SC configuration offers a high lifetime, medium energy density, complementary power and the broadest range of storage durations—from minutes to weeks—while maintaining a moderate cost. Additional advantages of this system include design flexibility, improved safety, and reduced environmental impact.

Based on all these aspects, the European Horizon 2020 HyFlow project [2], which partially supported the present research thesis, concentrates on developing a HESS that combines high-power VRFBs with SCs. The project aims to deliver a flexible and scalable energy storage solution, suitable for applications ranging from microgrids to industrial systems, while also emphasizing sustainability.

Within this framework, Section 3.1.1. explores the passive integration of a VRFB with a supercapacitor at the cell level. One of the objectives is to use the high power of the supercapacitor to balance the lower power of the VRFB. A key aspect of this work is the passive connection between the two components, meaning no DC-DC converters are used with the aims to evaluate the system's feasibility, reduce costs, and minimize energy losses.

The study investigates this integration from several perspectives. First, experimental tests were performed to validate the concept. Second, an equivalent circuit model was developed to serve as a practical design tool. Third, a techno-economic evaluation and a Life Cycle Assessment (LCA) were carried out to assess the benefits of excluding the DC-DC converter. All materials, methods, and results related to this work are presented in the article "Hybrid Energy Storage through the Passive Connection of a Vanadium Redox Flow Battery and a Supercapacitor: an Experimental, Modelling, Economic and Environmental Impact Assessment Study" [3] attached in the following Section. The paper resulted from a collaboration between the Energie institut an der JKU Linz (Austria), Pinflow Energy Storage, s.r.o. (Czech Republic), and Epic Power Converters s.l. (Spain). These organizations are part of the HyFlow project. The work reported in Section 3.1.1 has been submitted for publication on Journal of Power Sources and is at present under evaluation

In addition, Section 3.1.2 presents an improved version of the modelling approach described in Section 3.1.1. The first version of the model uses parameters reported in the VRFB and the SC datasheets as input data. The new modelling version, instead, also includes real data to simulate a practical case: the use of the system on an electric city bus. This update helps to give more accurate results about how the devices work with different levels of charge and current loads. However, this model is still at an early stage and needs more tests to confirm its accuracy.

3.1.1 Hybrid Energy Storage through the Passive Connection of a Vanadium Redox Flow Battery and a Supercapacitor: an Experimental, Modelling, Economic and Environmental Impact Assessment Study

This Section corresponds to the paper submitted for publication on Journal of Power Sources, and is co-authored by :

Monica Giovannucci[a], Elisabetta Petri[a], Alessandro Brilloni[a], Eva-Maria Heigl[b], Andreas Zauner[b], Estanis Oyarbide[c,d], Jiří Charvát[e], Francesca Soavi[a,f,*]

[a] *Department of Chemistry "Giacomo Ciamician", Alma Mater Studiorum University of Bologna, via P. Gobetti 85, 40129 Bologna, Italy*

[b] *Energieinstitut an der Johannes Kepler Universität Linz, Altenberger Straße 69, 4040 Linz, Austria*

[c] *Epic Power Converters S.L., Grupo Gregorio Quejido, Calle F Oeste, Nave 93 Polígono Industrial Malpica, 50016 Zaragoza, Spain*

[d] *Aragon Institute of Engineering Research, University of Zaragoza, C/Mariano Esquillor s/n, 50018 Zaragoza, Spain*

[e] *New Technologies – Research Centre, University of West Bohemia, Univerzitní 8, 306 14 Plzeň, Czech Republic*

[f] *Center for the Environment, Energy, and Sea - Interdepartmental Centre for Industrial Research in Renewable Resources, Environment, Sea and Energy (CIRI-FRAME), Alma Mater Studiorum University of Bologna Viale Ciro Menotti, 48 - 48122 Marina di Ravenna (RA), Italy*

*Corresponding author: francesca.soavi@unibo.it

Supplementary Information is in the Appendix.

Abstract

Developing a Hybrid Energy Storage System (HESS) involves integrating technologies with complementary attributes. Coupling Redox Flow Batteries (RFBs) with Supercapacitors (SCs) emerges as one of the most promising options. Feasibility analysis of HESS necessitates considering various specifications, such as energy density, power density, and discharge time. In this study, we present a laboratory-sized HESS comprising a Vanadium Redox Flow Cell (VRFC) and a SC, directly connected in parallel without any power converter. Initially, individual tests were conducted on the standalone VRFB and SC using short discharge protocols (5 s). Subsequently, the two systems were interconnected in parallel and subjected to the same discharge protocol. An equivalent electrical model, resembling a parallel R-C circuit, was developed to elucidate the discharge mechanism of the direct parallel system. The testing and modelling aimed to provide insights into the behaviour and advantages of the VRFB-SC HESS. The tests revealed that the SC mitigates the VRFB's ohmic drop due to the

transient behaviour of the R-C circuit. Furthermore, the hybrid system demonstrated enhanced energy delivery at higher currents compared to the standalone VRFB, a phenomenon elucidated by our proposed model. Additionally, the model facilitates appropriate sizing of the SC relative to VRFB performance. In addition to technical findings, this article provides a comprehensive economic analysis and life cycle assessment (LCA) of the proposed system. These assessments highlight the potential cost-effectiveness and reduced global warming potential of the passively connected VRFB-SC HESS, underscoring its viability as a sustainable energy storage solution.

3.1.1.1 Introduction

Redox-flow batteries (RFBs) are among the most interesting technologies in the energy storage scenario. The design flexibility and the possibility to separately scale power and energy make them extremely attractive for the energy stakeholders. [4].

RFBs have been proposed with different chemistries. Among them, Vanadium Redox Flow Batteries (VRFBs) are the most widespread and marketed. VRFBs feature an energy density of 25–35 Wh L^{-1} and a long cycle life of 15 000–20 000 charge/discharge cycles. Power performance, that can be controlled by regulating the electrolyte flow, still need improvements being in the order of 100 mW cm^{-2} of electrode. Increasing energy and power performance of VRFBs is extremely important, because it will decrease the Levelized Costs of Storage (LCOS) of this technology that today is indicated in 0.18 € kWh^{-1} $cycle^{-1}$, 3 times higher than the 2023 European Commission target of 0.05 € kWh^{-1} $cycle^{-1}$ (10 000 cycles) [5-6].

An emerging approach to enhance performance, efficiency, and lifespan is by integrating VRFBs with diverse energy storage technologies within the so-called Hybrid Energy Storage Systems (HESSs). Shubert et al. conducted a comprehensive review of the technologies currently available on the market, including Supercapacitors (SCs) and RFBs. They concluded that combining RFBs with SCs represents the most appropriate solution for HESS in terms of cycle and calendar lifetime, design flexibility, ecological impact, and safety. In addition, when comparing hybrid configurations in terms of self-discharge, systems combining RFB and SC demonstrates clear advantages due to low RFB daily self-discharge rate of 0.13% and high durability, with average cycle lives of 10^6 cycles for SC and 10^5 cycles for RFB. This combination also supports the widest range of storage durations, from milliseconds to several weeks. This makes it particularly suitable for complex applications where energy systems must manage both rapid power fluctuations and longer-term energy balancing across multiple temporal scales. [1]. An example is the HESS developed in the HyFlow project [2], that combined VRFB and supercapacitor technologies. This system ensures rapid and adaptable electricity availability by addressing peak demands from both private and public loads, as well as renewable energy production. Specifically, the HyFlow project aimed to design a storage solution suitable for applications ranging from microgrid level (5 kW) to industrial scale (300 kW). [2]. SCs are, indeed, distinguished by their high specific power (500–30 000 W kg^{-1}) and

outstanding cycle-life (up to millions of cycles) [7-8]. The most commercialized SC technology, i.e. the electrochemical double-layer capacitor (EDLC), stores energy by a very fast and reversible electrostatic charge separation at the electrode surface/electrolyte interphase, without involving faradic reactions. However, the specific energy of SCs is one order of magnitude lower than that of batteries (2–8 Wh kg^{-1}) [7-8]. Hence, SCs are considered an expensive technology in terms of energy storage capability (>4500 € kWh^{-1}), but inexpensive in terms of power capability (<1 € kW^{-1}) [7]. Commercial SCs commonly employ expensive organic electrolyte solutions containing alkylammonium salts (e.g. tetraethylammonium tetrafluoroborate) in organic solvents (e.g. acetonitrile or propylene carbonate) that enable to achieve $V_{SC,max}$ up to 3 V but that contribute up to 27% of the overall SC cost [7]. Hence, alternative electrolytes are being investigated to meet performance and safety requirements. Aqueous electrolytes appear promising due to their non-flammability, cost-effectiveness, and environmental friendliness. However, water electrolysis in conventional aqueous solutions (acidic, alkaline or neutral) limits $V_{SC,max}$ below 2 V [9]. An interesting option is represented by water-in-salt electrolytes (WiSE) that offer a wide electrochemical stability window and high conductivity [10]. Notably, a solution with a concentration of 30 mol kg^{-1} of ammonium acetate can yield an electrochemical stability window of 3.2 V and a conductivity of 25 mS cm^{-1} [11].

The most common scheme of linking batteries and supercapacitors typically employs a bidirectional power converter [1]. This converter facilitates bidirectional power flow management within the system [12]. However, in literature, few studies report about the direct connection between batteries and supercapacitors. This type of connection is termed "passive" [13, 14] and consists in the parallel connection between different storage systems that does not employ a power converter. While an active topology, such as that of the HyFlow project, can be used in microgrids and industrial applications, according to the literature a passive topology can be implemented in diverse applications, including pulsed current [15] and vehicle applications [16].

In ref. [13], it is shown that the power converter-based (or "active") connection offers several advantages over the passive one, such as battery current peaks reduction and DC bus voltage control. In ref. [17] it is shown that the autonomy of a device powered by a HESS based on a battery and a parallel connected supercapacitor bank, is improved because the supercapacitor decreases the HESS internal resistance. Furthermore, the connection of the battery to the

supercapacitor by a DC-DC converter enables the use of lower voltage supercapacitor banks, hence a lower number of SC cells. Therefore, the use of a DC-DC converter appears to be a cost-effective option, since it allows the use of reduced number of EDLC cells while maintaining a comparable performance. However, power converters decrease HESS efficiency and hence might impact on power cost. Indeed, the power converters might cause 50% of power losses [13]. Ref. [18] compares efficiencies of 26 types of DC/DC converters and shows that most of them exhibit efficiencies between 92% and 98.5%.

The studies discussed above were carried out by considering "closed" battery (e.g. lithium-ion batteries) and supercapacitor packs, as separate elements, each one of them made of different stacks embedded in different cases. To date, there are no studies focusing on the passive connection of emerging technologies such as RFBs and SCs, as well as detailed LCA (life cycle assessment) and economic analyses of HESSs based on these storage units are not available.

Hence the aim of this study is to investigate and model the electrical behaviour of a HESS based on the passive, parallel connection of a Vanadium Redox Flow cell (VRFC) and an SC cell, while providing an assessment of the economics and environmental impacts of a hypothetical upscaled system. We report about the electrochemical tests carried out on the single VRFC and SC cells units and of the VFRC-SC HESS. We tested the integration of the VRFC and Supercapacitors at cell level and laboratory scale. The standalone VRFC and SCs served as control groups. Such monolithically integrated system has been evaluated by short-galvanostatic discharges to assess energy and capacitance performance. The pulsed test validates the system for applications characterised by power peaks on a timescale of seconds, such as the load profile of an electric city bus. In addition, we propose a simple methodology and a semi-empirical model that enables to design the VRFC-SC HESS by taking into account relevant VRFC and SC cell parameters (e.g. sizes, current rate, ESR, capacitance). The literature offers various methodologies for modelling VRFC and SC [19-20], but an equivalent circuit that models the passive connected VRFC-SC system is not available yet. Here, we propose a simple equivalent model, while being aware of the potential increased error compared to more complex models. Our aim is, indeed, to propose a simple tool that allows sizing the hybrid VRFC-SC system based on common parameters that can be easily derived from the VRFC and SC datasheets.

In addition to experimental characterization and modelling, this work incorporates the assessment of economic and environmental impacts of the proposed HESS with passive connection compared to a HESS with converter-based connection. These evaluations aim to provide a comprehensive understanding of the system's feasibility and sustainability. The economic assessment considers key cost drivers, such as the components' capital expenses and operational requirements, whereas the LCA conducted in this study focuses on quantifying environmental impacts of the system's production and use phase. Indeed, environmental aspects are essential when rating and selecting new energy storage technologies. Energy storage systems can play an important future role for renewables balancing and electricity grid stabilizing. They can increase the utilization factors of renewable electricity sources and thus advance the decarbonization of our energy system; however, these storage technologies must be sustainable themselves. The European Battery Regulation (Regulation EU 2023/1542) [21] aims to ensure that "batteries remain sustainable throughout their entire lifecycle – from material sourcing to collection, recycling, and repurposing." Thus, it supports the UN's Sustainable Development Goals (SDGs) [22] and the climate targets set by the Paris Agreement [23]. Among other obligations, the Battery Regulation will require the provision of a carbon footprint declaration for batteries [21]. LCA is an acknowledged method to assess the environmental impacts of a product or a process over its entire lifecycle or in single lifecycle phases. It not only determines the well-known global warming potential (GWP), but can also comprise a multitude of other indicators, such as the fossil depletion potential, water consumption potential or primary energy demand. Data used for the LCA presented in this study were to a large extent developed in HyFlow and adapted to the new system specifications.

Overall, the aim of our experimental and modelling work is to demonstrate that the parallel passive connection at cell level of the VRFC with a SC: i) is a simple approach that enables to boost energy and current rate response under short discharge pulses, ii) does not require high-voltage SCs, such as the commercial ones that feature organic electrolytes, iii) needs an equivalent electric model as a tool to forecast the behaviour of the system varying the SC size, and iv) is superior to a comparable system with converter-based connection regarding costs and environmental impacts (specifically for GWP).

We would like to clarify that the objective of this study is not to provide a complete design of a HESS based on VRFB and SC. Instead, we present an exploratory investigation aimed at assessing the potential to combine these two technologies in a passive configuration. This preliminary analysis intends to offer insights that may support future research and development in this area.

3.1.1.2 Materials and Methods

This Section reports the specifications of the devices under examination, along with their corresponding characterization, electrochemical techniques, modelling, LCA and Economic materials and methods. The devices involved in the study comprise a VRFC (discussed in Section 3.1.1.2.1), and different commercially available SCs (outlined in Section 3.1.1.2.2). Section 3.1.1.2.3 describes the test protocols and Section 3.1.1.2.4 elaborates the proposed equivalent electric model. Section 3.1.1.2.5 and Section 3.1.1.2.6 report respectively the LCA and Economic assessment database and hypothesis.

3.1.1.2.1 Vanadium Redox Flow Cell nominal characteristics and assembly

The company Pinflow provided the cell used during the test. This cell possesses an exchange (electrode) surface area of 4 cm^2, operates within a voltage range of 1.65 V to 0.8 V, and supports a maximum discharging current of 2 A. A total of 100 mL electrolyte (50 mL for the anolyte and 50 mL for the catholyte) was contained in two tanks. The theoretical calculated capacity of the cell is 2144 mAh. Further specifications are detailed in Table 3.1.1.2.1.1.

Table 3.1.1.2.1.1 Nominal values of exchange surface, cell voltage range, theoretical capacity (50 mL tanks), and maximum discharging current of the Pinflow VRF Cell

Surface	**Cell voltage range**	**Theoretical Capacity**	**Maximum discharging current**
cm^2	*V*	*mAh*	*A*
4	0.8-1.65	2 144	2

The assembly of the cell is shown in the exploded view drawing in Figure S1 (Supplementary information). Table S1 reports the coulombic, energy and voltage efficiency of the cell varying the current density. The structure of both sides of the cell comprises layers arranged as follows: an end plate with an insulating plane, a copper current collector, a carbon-polymer composite plate, a seal, the flow frame with fittings, a membrane seal, and a felt electrode; in the middle between the two sides there is the membrane positioned centrally. After the assembly, the cell was operated with the electrolyte which consisted of 1.6 mol dm^{-3} of vanadium (equimolar mixture of vanadium in oxidation states III and IV), 2 mol dm^{-3} of H_2SO_4 and 0.3% of H_3PO_4. Two peristaltic pumps, Watson–Marlow 120S/DV, operate at 40 to 60 rpm, ensuring a catholyte and anolyte flow rates within the interval 40–60 mL min^{-1}. This flow rate was set in order to facilitate mass transport, especially at the highest current. Argon was used to purge the cell for 30 minutes before electrochemical tests. Initially, the vanadium electrolyte is equal for both the positive and negative electrodes, featuring an indicative state of charge of a -50%. To activate the electrolyte, the cell went through an activation process. Initially, the cell was charged at 400 mA up to its theoretical capacity (2 144 mAh). Subsequently, the cell underwent cycles of charge and discharge, and when it achieved a coulombic efficiency of at least 95%, the cell was considered prepared to proceed to subsequent testing phases that are described in Section 3.1.1.2.3.

3.1.1.2.2 Commercial Supercapacitors nominal characteristics

Various commercial supercapacitors, purchased from EATON, based on high surface area carbons and organic electrolyte, were considered in this study. We employed commercial supercapacitors because of their availability and reliability. The selection of the SCs was based on ensuring that their operating currents were of the same order of magnitude as the operating currents of the VRFC. The capacitance C, the equivalent series resistance (ESR), the maximum cell voltage ($V_{SC,max}$) and maximum continuous discharge current, and leakage currents derived from the datasheet of the manufacturer, are outlined in Table 3.1.1.2.2.1 along with the maximum energy ($W_{SC,max}$) and the maximum power ($P_{SC,max}$) that were calculated according to the Equations 3.1.1.2.2.1 and 3.1.1.2.2.2.

$$W_{SC,max} = \frac{1}{2} C V_{SC,max}^2 \quad 3.1.1.2.2.1$$

$$P_{SC,max} = \frac{1}{4} \frac{V_{SC,max}^2}{ESR_{SC}} \quad 3.1.1.2.2.2$$

Notably, the primary distinction lies in the nominal capacitance, ranging from 1 F to 100 F. The 9 F SC was built through a parallel direct connection of three distinct supercapacitors: one rated at 1 F, another at 3 F, and a third at 5 F. The related characteristics were deduced from those of the individual supercapacitor units and subsequently confirmed through galvanostatic tests. All commercial supercapacitors can operate up to 2.7 V and exhibit ESRs that diminish with increasing capacitance, ranging from 0.2 Ω to 0.011 Ω as the capacitance moves from 1 F to 100 F.

Table 3.1.1.2.2.1 Commercial Supercapacitors characteristics purchased from Eaton. Data, except for maximum energy and power, are derived from the datasheets of the manufacturer.

Acronym	Capacitance	ESR	$V_{SC,max}$	$W_{SC,max}$	$P_{SC,max}$	Maximum continuous discharging current	Leakage currents
	F	Ω	*V*	*mWh*	*W*	*A*	*μA*
SC1F	1	0.200	2.7	1	9.1	0.8	10
SC3F	3	0.080	2.7	2	23	1.6	15
SC5F	5	0.040	2.7	5.1	46	2.3	20
SC9F[1]	9[1]	0.023[1]	2.7	8.8[1]	46[1]	2.3[1]	23
SC34F	34	0.016	3.0	42.5	141	6.5	75
SC100F	100	0.011	3.0	125	205	11.7	225

[1] values for 9 F supercapacitor were calculated by experimental tests.

3.1.1.2.3 Electrochemical techniques

The electrochemical tests were carried out using a VSP multichannel potentiostat/galvanostat (Bio-Logic Science Instruments) under ambient conditions. Data were analyzed by the Bio-Logic software EC-Lab 10.23. Both the individual VRFC and SC devices and the VRFC-SC underwent similar galvanostatic pulse tests to collect useful data for a comparison, as

described below. The main test conducted on the different charged devices consisted in a pulsed galvanostatic discharge (GCPL) lasting 5 seconds, that was repeated at different current rates. For both the VRFC and the VRFC-SC, the current profile observes a stepwise pattern that was applied after charging the systems at the set cell voltage (ca. 1.5 V): for the initial 5 seconds, neither voltage nor current was applied, maintaining the system in Open Circuit Voltage (OCV); starting from the fifth second, the current load was applied with a discharge time cut-off of 5 seconds and a discharge voltage cut-off of 0.8 V; thereafter, the test was concluded (Figure S2a in the Supplementary Information file). In the case of the SC, an initial charging step was undertaken to attain the maximum voltage. Subsequently, the SC was maintained at this voltage for a duration of 10 seconds, during which it is evident (as depicted in Figure S2b) that the current is not zero. Following this phase, the SC underwent a 5-second pulsed discharge, similarly to the testing procedure conducted on both the VRFC and the VRFC-SC system. Also in this case a voltage cut-off of 0.8 V was applied.

3.1.1.2.4 Equivalent Electric Model

Figure 3.1.1.2.4.1a illustrates the simplified equivalent circuit adopted in this study to model the VRFC-SC parallel connected hybrid system. Given the inherent simplicity of this model, the analysis does not consider influencing factors such as temperature and polarisation effects. A constant voltage source (V_b) in series with a resistance R_b represents the equivalent circuit branch of the VRFC battery according to the Rint Model for batteries [24]. A capacitance (C) in series with the equivalent series resistance R_{SC} describes the SC [25]. The two blocks are connected in parallel, mirroring the VRFC-SC system. The VRFC-SC block is then connected to the external load that is configured to emulate the constant current discharge, denoted as i_L. The currents flowing in the SC and VRFC branches are named respectively i_{SC} and i_b. The voltage measured at the two ends of each branch assumes the same value, named as v_L.

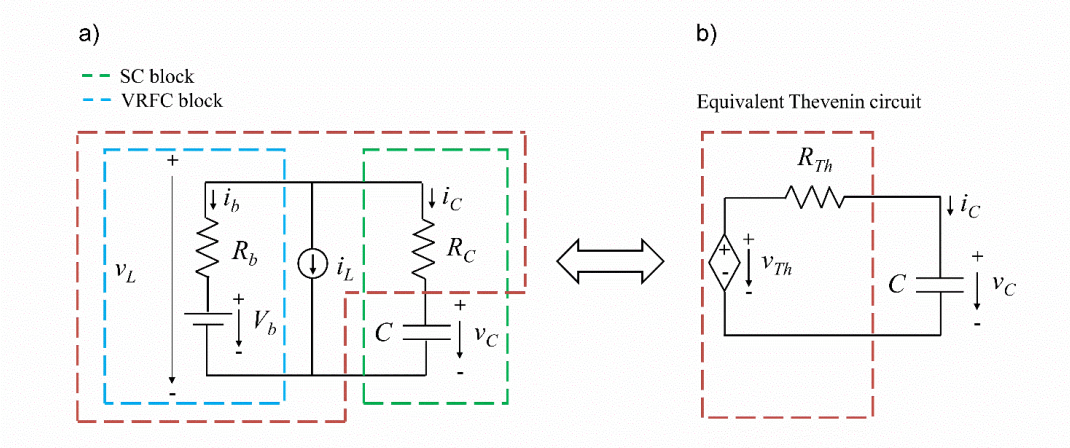

Figure 3.1.1.2.4.1 a) Equivalent Electric Circuit and b) equivalent Thevenin circuit for the VRFC-SC HESS.

The model attempts to achieve various purposes. Firstly, it aims to enhance understanding of the system by elucidating aspects such as how the current flows in the branches and the influence of the devices ESRs and SC capacitance on system behaviour. Secondly, the model should permit the determination of the time-dependent voltage profile during the discharging phase. Indeed, in an R-C circuit like this, it is essential to evaluate the time constant of the system. Finally, this simplified model aims to allow sizing the SC, in terms of capacitance to be combined with the VRFC for improved energy delivery during pulsed discharge. Addressing these objectives necessitates the development of a mathematical model describing the evolution of current and voltage over time. Indeed, due to the presence of capacitance within the system, both current and voltage values vary with time exhibiting transient behaviour. To derive an analytical solution for the circuit, the Thevenin theorem facilitates the transformation of the parallel circuit into the corresponding Thevenin circuit of Figure 3.1.1.2.4.1b, comprising a single loop. Subsequently, Kirchhoff's laws are employed to formulate the Equations. Solving these Equations permits the determination of the system's time constant, while their solutions elucidate the temporal evolution of currents and voltages. The implementation of Thevenin Theorem and Kirchhoff's laws is described in the Supplemental Information Section.

The Thevenin circuit is a simple R-C transient circuit with a well-known solution reported in Equation 3.1.1.2.4.1 with a time constant given by $\tau = R_{th}C$.

$$i_{SC}(t) = I_{SC}(0)\exp(-t/\tau) \qquad 3.1.1.2.4.1$$

Equation 3.1.1.2.4.1 gives the value over time of the current in the SC branch (i_{SC}); the current flows following an exponential behavior from the initial value $I_{SC}(0) = [V_{Th}(0) - V_{SC}(0)]/R_{Th.}$

Once computed the SC current and using the original circuit of Figure 3.1.1.2.4.1a it is straightforward to compute the VRFC current i_b (Eq. 3.1.1.2.4.2) and the measurable load voltage v_L (Eq. 3.1.1.2.4.3).

$$i_b(t) = -i_L(t) - i_{SC}(t) \qquad 3.1.1.2.4.2$$

$$v_L(t) = v_b + i_b(t)R_b \qquad 3.1.1.2.4.3$$

Managing all the Equations from Eq. 3.1.1.2.4.1 to Eq. 3.1.1.2.4.3 it is possible to describe currents and voltages of the whole equivalent circuit. The Equations obtained in this Section have been implemented in the software Matlab to provide a numerical solution for the analysis depicted in the discussion Section.

3.1.1.2.5 Life cycle assessment

This Section reports on the life cycle assessment of a HESS, comparing a converter-based connection between VRFB and SC, to a passive connection. The LCA was conducted following the ISO 14040/14044 LCA standards [26-27]. In the goal and scope definition, the study's purpose was outlined and in the life cycle inventory (LCI) analysis, data on process inputs and outputs (masses, energy) were collected. Subsequently, LCI results were translated into environmental impacts in the life cycle impact assessment phase (LCIA), applying a harmonized LCIA methodology. LCIA results were then discussed and further investigated in a sensitivity analysis. This was complemented by a discussion of the limitations of the study and an outlook regarding potential further research needs. The LCA process was iterative, ensuring its continuous improvement and alignment between the different phases. For a deeper understanding of LCA methodologies, please refer to the works of Frischknecht et al. (2020) [28] Guinee et al. (Ed.) (2002) [29], Curran (Ed.) (2014) [30] and Klöpffer and Grahl (2014) [31]. Data used for the LCA presented in this study were to a large extent developed in HyFlow and adapted to the new system specifications.[32]

Goal, scope and functional unit

The goal of this LCA study was to compare the environmental impacts of the production and use phase of a HESS with a converter-based connection between a VRFB and a SC, to a HESS with a direct connection. In case of a direct connection, no bidirectional DC-DC converters are required, but a higher number of SC cells than for a converter-based connection.

Table 3.1.1.2.5.1 HESS parameters for the base case and for the sensitivity analysis

	VRFB			**SC[1)]**			**AC-DC[2)]**			**DC-DC[3)]**	**EMS[4)]**	**Cabling[5)]**
Converter-based (A)	**x**			**x**			**x**			**x**	**x**	**x**
Passive (B)	**x**			**x**			**x**				**x**	**x**
Configuration	Power [MW]	Energy	Mass [t]	Power [MW]	Mass a[1)] [t]	Mass b[1)] [t]	Power [MW]	Mass [t]	Power [MW]	Mass [t]	Mass [t]	Mass [t]
Base case	1	4	299	2.5	2.2	6.5	3.5	21	1+2.5	5.5	0.4	0.3
Sensitivity 1				5	4.3	12.9	6	36	1+5	9.4	0.4	0.4
Sensitivity 2				10	6.5	19.4	11	66	1+10	17	0.4	0.5
Sensitivity 3				20	8.6	25.9	21	126	1+20	33	0.8	0.6
Sensitivity 4				40	10.8	32.4	41	246	1+40	64	1.5	0.7
Sensitivity 5				80	12.9	38.8	81	486	1+80	127	3	0.8

[1)] Mass a = SC for converter-based connection, mass b = SC for passive connection (3x number of cells of SC for converter-based connection) - SC5F cell specifications, Table 3.1.1.2.2.1

[2)] AC-DC Inverter. LCI dataset: "GLO: market for inverter, 500kW ecoinvent 3.8" [31] linearly upscaled by inversion power

[3)] DC-DC converters NOT included in HESS with direct connection between VRFB and SC

[4)] approximated with LCI datasets for control cabinet (1 piece / 10 MW SC assumed) and 1 computer: "GLO: market for control cabinet, heat and power co-generation unit, 160kW electrical ecoinvent 3.8" AND "GLO: market for computer, desktop, without screen ecoinvent 3.8" [31]

[5)] estimated values

To obtain results of practical interest, we projected the SC and VRFB to a realistic MW-scale. In the base case, we investigated a HESS integrating a 1 MW/4 MWh VRFB with a 2.5 MW SC, with either a converter-based or a direct connection (Table 3.1.1.2.5.1). In case of the direct connection, it has been considered that SC cells are charged only up to 1.65 V of the maximum value of 2.7 V. Consequently, as for Equation 3.1.1.2.2.2, the deliverable maximum power is approximately one third of the nominal power. Hence, to achieve the target power of the different HESS configurations listed in Table 3.1.1.2.5.1, the number of SC cells connected in parallel must triplicate.

In addition to the VRFB and SC, and the DC-DC converters in case of a converter-based connection, the HESS also employs an AC-DC inverter for connection to the energy source/sink, an energy management system (EMS) and power and data cabling. Foundations or housing were not accounted for in the LCA. The LCA of the production phase started from basic processes such as raw materials mining or energy generation, followed by parts production and final HESS assembly, including all transport steps. The use phase was modelled for a system lifetime of 20 years and 20 000 full cycles of charging/discharging, respectively. The production and use of the HESS were assumed to take place in Europe. The end-of-life phase of the HESS was not accounted for. The functional unit of this study was 1 kWh of energy discharged by the HESS over its lifetime.

Life cycle inventory

This LCA partly builds on data from a previous HyFlow publication [32], which were adapted to the new system specifications. The LCI of the SC, however, was not derived from HyFlow, as a different kind of SC was employed there. Instead, we used an activated carbon-acetonitrile SC, as published by Jiao et al. (2023) [33]. All underlying inventories are reported in the Supplementary Information (SI). Moreover, we expect that substituting the acetonitrile electrolyte by an aqueous electrolyte could further reduce the SC's environmental impacts. Therefore, we conducted an LCA comparing 1 kg of acetonitrile with 1 kg of WiSE ammonium acetate electrolyte (30 mol/kg) [11]. We assume that a 1:1 mass substitution of these two electrolyte types in the current SC design would be valid, a point that still requires experimental confirmation. The use phase of an energy storage system is shaped by the energy

losses that occur during charging and discharging. These losses depend on the specific use case of the HESS and the individual energy efficiencies of its single components. In our preceding study [32], we showed that the theoretical round-trip efficiency of the HESS with active connection can range from 43% to 79%, depending on the storage pathway. The same methodology was now applied to a HESS with passive connection, resulting in a theoretical round-trip efficiency between 64% and 89%. Potential losses specifically arising from the passive connection are not included here but are addressed in a sensitivity analysis. For this study, we considered a simplified use case in which all electricity is charged through the VRFB and then discharged through the SC. This results in a round-trip efficiency of 51% for an active connection and of 67% for a passive connection (Table S6, SI). Based on these considerations, the lifetime discharged energy, and the energy losses of the HESS, were determined as 54 040 MWh and 51 921 MWh in case of the active (converter-based) connection, and as 64 192 MWh and 31 617 MWh in case of the passive connection. For LCA modelling and LCI background datasets, the LCA for Experts 10.7 software and professional database by Sphera [34] and the ecoinvent 3.8 database [35] were used. European LCI background datasets were applied, if available. The use phase was modelled for a HESS cycle life of 20 000 full charging and discharging cycles over 20 years, following Blume et al. (2022) [36].

Moreover, the transport of the finalized HESS to a user in Europe and one exchange of the VRFB-stack [37], of the SC and of the AC-DC inverter after 10 years of operation, were accounted for [32]. The HESS was modelled to be charged with European photovoltaic power.

Life cycle impact assessment and sensitivity analysis

To translate the results of the LCI analysis into environmental impacts, we employed the acknowledged ReCiPe 2016 q(H) v1.1 methodology [38]. ReCiPe 2016 investigates environmental impacts in 18 midpoint categories, such as climate change, ozone depletion, and ecotoxicity. In this article, we focused on climate change with its indicator global warming potential (GWP). Moreover, the primary energy demand (PED) was assessed based on the cumulative energy approach [39-40]. A full list of investigated indicators, and all LCIA results, are provided in the SI. In a sensitivity analysis, we increased the SC size in five steps by 100%,

300%, 700%, 1 500% and 3 100% up to 80 MW, while leaving the VRFB specifications the same (Table 3.1.1.2.5.1). Thus, we assessed for both connection types, how a change of the system's power influenced its environmental impacts. Another sensitivity analysis was performed on the base configuration of the passively connected HESS, altering its roundtrip-efficiency from 67% to 62, 57 and 52%. In this way, we investigated how potential losses arising from the passive connection might impact the environmental performance of this type of HESS. The impact of varying the round-trip efficiency of the converter-based HESS was already examined through sensitivity analysis in our previous publication [32].

3.1.1.2.6 Economic assessment

Accurate forecasting of total project costs is pivotal for the planning and implementation of complex systems such as HESS. In contrast to simple cost aggregation approaches, total project costs cannot be derived solely from the costs of the main components (VRFB, SC, and PCS), but must also include additional and indirect cost elements, such as engineering, civil works, component assembly, and commissioning, which significantly influence overall cost of the system. In industrial plant engineering, total project costs are commonly estimated using surcharge factor methods, such as the Total Factor Method (Lang Factor Method) or Single Factor Methods, which are based on empirical data and historical experience, cf. e.g., [41–44]. As HESS construction differs from conventional industrial plants, these methods, particularly the surcharge factors, cannot be directly transferred and therefore require adaptation. Accordingly, total project costs C_T were calculated as the sum of direct plant costs C_D and indirect plant costs C_I as expressed in the Equation $C_T=C_D+C_I$. Direct plant costs $C_D=C_M+C_A$ comprise the costs of the main components C_M (where C_C is the cost of one main component) and additional plant costs C_A, with the latter estimated by applying surcharge factors for direct costs f_d. Indirect plant costs C_I were derived by applying surcharge factors to the direct plant costs f_{id} (Equations (3.1.1.2.6.1) to (3.1.1.2.6.3)). The applied surcharge factors are summarized in Table S10.

$$C_M = \sum_{i=1}^{x} C_{C_x} \quad 3.1.1.2.6.1$$

$$C_A = \sum_{i=1}^{x} (C_M * f_{d_x}) \quad 3.1.1.2.6.2$$

$$C_I = \sum_{i=1}^{x} (C_D * f_{id_x}) \quad 3.1.1.2.6.3$$

Due to the limited number of realized HESS installations of this kind, no dedicated historical data for surcharge factors are available. Therefore, the factors were estimated based on conventional industrial plant engineering and adjusted to reflect the higher degree of prefabrication of HESS components and their typically containerized delivery, which reduces assembly complexity and structural engineering requirements. Nevertheless, basic civil infrastructure remains necessary. To assess the influence of system size (power and storage capacity) and the power ratio between VRFB and SC, several HESS configurations were analysed. The VRFB size was kept constant, while the SC power was varied (see Section 3.1.1.2.5). Table 3.1.1.2.6.1 presents the CAPEX of the main components (for detail see [45]; the cost estimation for an SC with an aqueous electrolyte was based on the assumption that approximately 40% [7] of the total cost of an SC is attributed to the electrolyte. Given that the cost of an aqueous electrolyte is estimated to be only about one-tenth [11] of that of a conventional organic electrolyte, the total SC cost was adjusted accordingly) which were used to calculate the total project costs. As an illustrative example, the CAPEX for the reference HESS configuration (Base: SC 2.5MW /VRFB 1 MW/4 MWh) is presented for the years 2022 and 2025, considering different connection types (active/passive) and SC types (organic/aqueous).

Table 3.1.1.2.6.1 CAPEX of the main components of the HESS "Base" configuration for the year 2022 and 2025 with different connection types active/passive and SC types organic/aqueous

Year	Configuration	Connection	Component CAPEX [€]				
			SC	**DC-DC converter VRFB**	**DC-DC converter SC**	**AC-DC inverter**	**VRFB**
2022	**Base**	active/organic	127 935	121 500	210 543	253 975	1 676 524
		passive/organic	383 806	0	0		
		passive/aqueous	245 636	0	0		
2050	**Base**	active/organic	67 456	64 570	111 891	134 973	707 871
		passive/organic	202 367	0	0		
		passive/aqueous	129 515	0	0		

3.1.1.3 Results & Discussion

This Section reports about the results obtained performing the pulsed discharging test on the standalone VRFC (Section 3.1.1.3.1), standalone SCs (Section 3.1.1.3.2) and the parallel systems consisting of VRFC and the commercial SCs (Section 3.1.1.3.3). Section 3.1.1.3.4 reports the modelling results showing also some insights comparing test and modelling data. Section 3.1.1.3.5 and Section 3.1.1.3.6 reports respectively the LCA and Economic assessment results.

3.1.1.3.1 VRFC test

The pulsed discharge was configured using the pulse galvanostatic discharge protocol reported in Section 3.1.1.2.3 and depicted in Figure S2a. The VRFC underwent testing across various currents ranging from 100 mA to 4 A, with increments of 100 mA. The discharge voltage cut-off was set at 0.8 V. Figure 3.1.1.3.2.1a displays selected discharge voltage profiles of the VRFC at different current levels. The Figure emphasizes that the maximum practical current for the VRFC is 2 A. Indeed, at currents exceeding 2 A (i.e. 4A), the cell voltage drops below the cut-off threshold in less than 5 seconds of discharge. R_b was calculated at each current using the measured voltage drop (ΔV_b) values according to the Equation $R_b = \Delta V_b/i_L = (V_{OCV}-V)/i_L$ in which i_L is the value of the applied discharging current, V is the potential after the ohmic drop and V_{OCV} the OCV potential value of the cell. The energy delivered over the pulse discharge (W_{pulse}), was quantified at each current by the Equation 3.1.1.3.1.1 (in Wh).

$$W_{pulse} = \frac{1}{3600} i_L \int_0^t v_L(t)dt \qquad 3.1.1.3.1.1$$

Where v_L is the voltage. The discharging curves and the numerical results are respectively reported in Figure 3.1.1.3.2.1a and Table S12. The VRFC delivered energy ranged from 0.4 mWh at 200 mA to 1.3 mWh at 2 A. The ohmic drop increased from 74 mV at 200 mA to 0.65 V at 2 A: this high value limits the discharge because the cut-off voltage (0.8 V) is reached more quickly. The R_b value settles in a range between 0.33 and 0.37 Ω.

3.1.1.3.2 Commercial SC test

As reported in Section 3.1.1.2.3 and depicted in Figure S2b, we subjected the supercapacitors to the following protocol: galvanostatic charging at 1.5 V (selected for comparability with the OCV exhibited by the tested VRFC), followed by a potential step to 1.5 V maintained for few seconds, and subsequent galvanostatic discharge with a cell cut-off voltage of 0.8 V and a cut-off discharge duration of 5 seconds. Discharge ceased upon reaching either of the specified cut-offs. Both charging and discharging steps were conducted at varying currents ranging from 400 mA to 10 A. As an example, Figure 3.1.1.3.2.1b reports the galvanostatic discharge profiles of SC34F. The voltage decreases linearly over time, indicating that the discharge is driven solely by an electrical double layer process. These devices display behaviour similar to that of an ideal capacitor that is in series with a negligible ESR. As expected, the slope (dv_{SC}/dt) of the discharge profile over time increases with the current; this trend is explained by Equation 3.1.1.3.2.1.

$$v_{SC} = \frac{Q}{C} \rightarrow \frac{dv_{SC}}{dt} = \frac{1}{C}\frac{dQ}{dt} = \frac{1}{C} i_{SC} \qquad 3.1.1.3.2.1$$

The ohmic drop ($\Delta v_{SC,Ohmic}$) at the beginning of discharge also increases with the current, following the Equation $\Delta v_{SC,Ohmic} = i_L R_{SC}$.

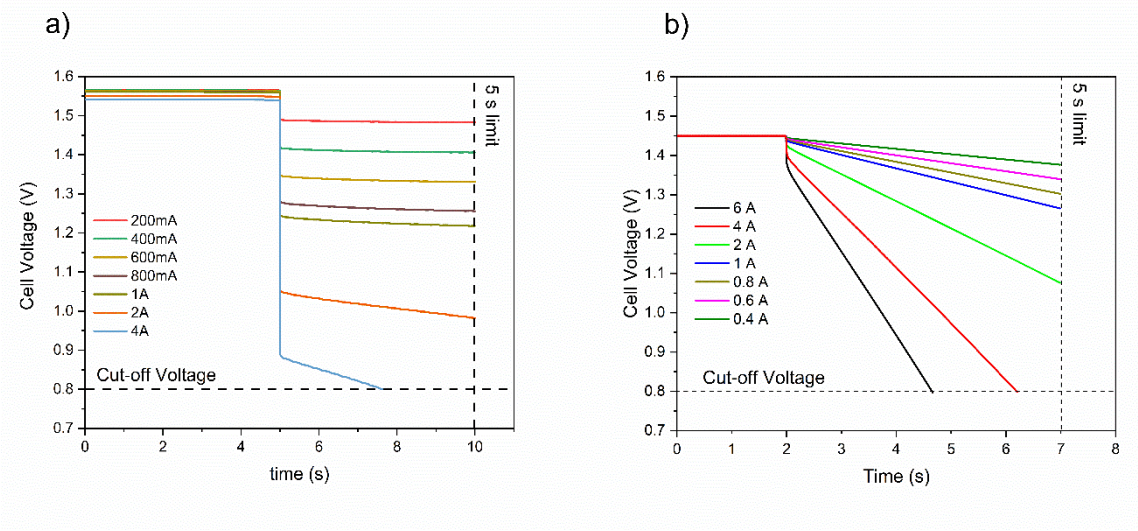

Figure 3.1.1.3.2.1. a) Voltage profile of VRFC during 5s discharge at different currents at RT; b). Voltage profiles of SC34F under pulsed discharge curves of 5 s at different currents. Experimental tests were conducted at RT=25°C. The starting SOC of the VRFC is 100%.

3.1.1.3.3 Hybrid VRFC-SC system test

Four distinct systems were evaluated. All featured the same VRFC, but different SCs of 5 F, 9 F, 34 F, and 100 F. The corresponding acronyms are: VRFC-SC5F, VRFC-SC9F, VRFC-SC34F, and VRFC-SC100F. As outlined in Section 3.1.1.2.3, pulse tests protocol similar to that conducted on the VRFC (Figure S2a), were performed on the VRFC-SC system, with the commercial SC connected in parallel with the vanadium cell. The parallel connection between the VRFC and the SC was established using a four-terminal configuration that was adopted to minimise the influence of external resistances. The initial phase involves charging the VRFC to full capacity at a rate of 600 mA, until reaching the designated cut-off charging voltage of 1.65 V, which is maintained for 5 minutes. Subsequently, the VRFC-SC system is left in open circuit, and the corresponding open circuit voltage of the system is recorded. Following this, a GCPL is executed at a defined current (i_L), with time and discharge voltage cut-offs set at 5 s and 0.8 V, respectively. The discharge profiles of the four tested systems are depicted in Figure 3.1.1.3.3.1 (a, b, c, d). It is worth noting that the value of the capacitance highly impact on the curve trend: the higher is the capacitance, the more linear is the profile. In addition, there is a high reduction of the Ohmic drop. These two effects (more linear profile and ohmic drop reduction) enable the possibility of discharging at higher currents. To deepen the effect of the capacitance on the system, Figure 3.1.1.3.3.1e reports a comparison of the discharge curves at 2 A of the individual VRFC, the single SC34F and the hybrid VRFC-SC34F system.

When the two systems are directly connected in parallel, two phenomena become evident:

- a significant reduction in the ohmic drop compared to that observed with the standalone VRFC.
- the discharge profile exhibits a linear decrease over time, resembling that of the standalone SC but with a smaller slope than the SC (at the same current), suggesting an "apparent" increase in the overall system capacitance relative to the standalone SC. The entity of the reduction in the ohmic drop and the capacitive response depends respectively on the ESR and on the capacitance of the combined SC. These behaviours can be elucidated by referring to the equivalent circuits reported in Section 3.1.1.2.4 and that will be discussed in Section 3.1.1.3.4.

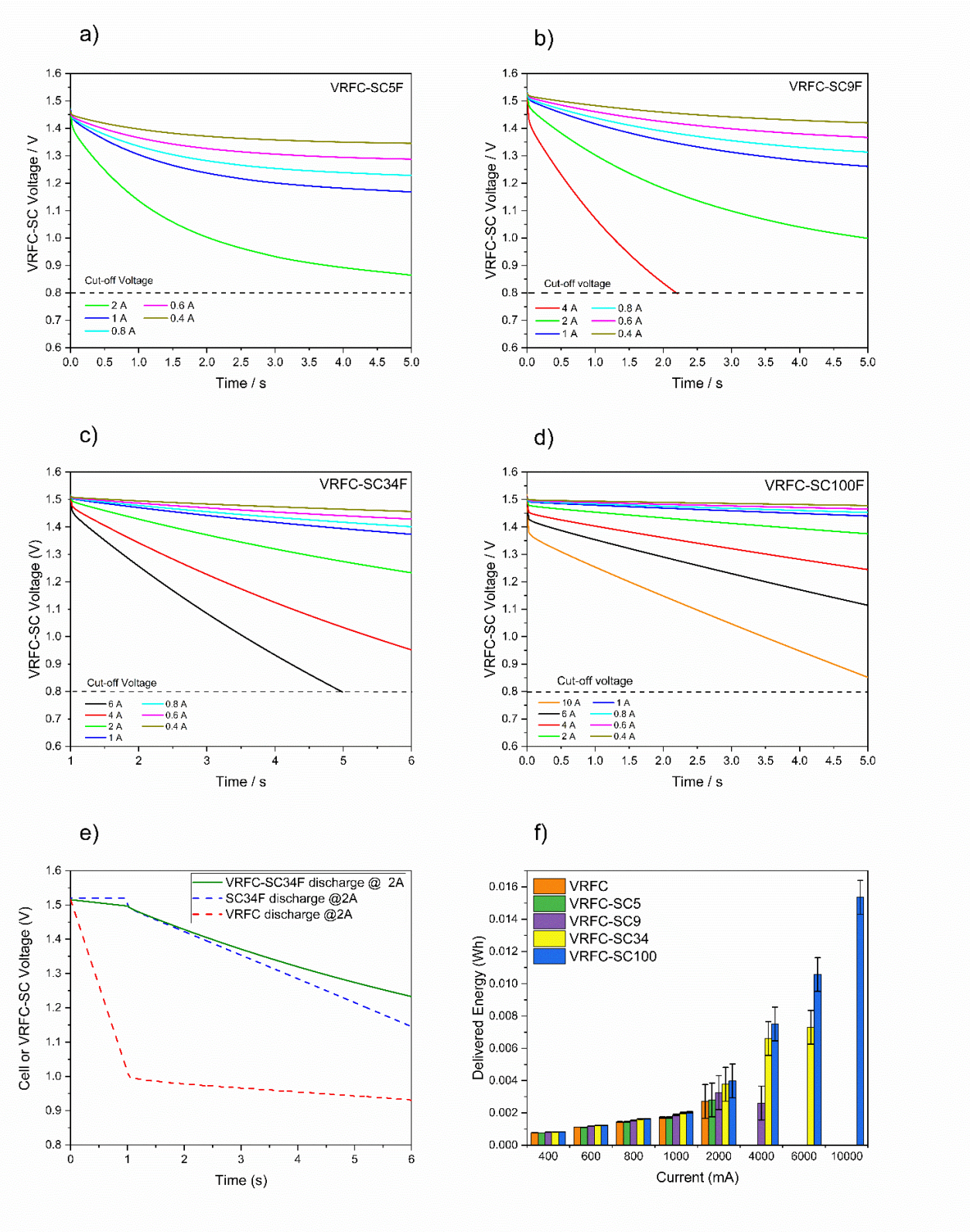

Figure 3.1.1.3.3.1 a), b), c) and d) Discharge profiles of the 4 different VRFC-SC systems during 5s-pulse discharges at different discharging currents. e) Discharge profiles of the single VRFC, the single SC34F and of the hybrid system VRFC-SC34F during 5 s-galvanostatic pulses at 2 A. f) Energy delivered over 5s-pulse discharges at different currents by the single VRFC cell and by the hybrid VRFC-SC systems featuring different commercial SCs. Experimental tests were conducted at RT=25°C. The starting SOC of the VRFC is 100%.

The discharge profiles were analysed to extract significant data such as delivered energy and power. Figure 3.1.1.3.3.1f compares the amount of the energy delivered over 5-second galvanostatic pulses with the increase in currents for the VRFC and VRFC-SC systems featuring different SCs. The Figure clearly illustrates that the reduction in the ohmic drop and the apparent increase in capacitance enhance the energy performance of the hybrid system, which significantly outperforms the standalone VRFC at the highest currents. The energy gain is more pronounced when SCs with higher capacitance are connected. By incorporating the SC100 F, it is possible to conduct 5-second pulse discharges at 10 A, i.e., at a current regime five times greater than that achievable for the standalone VRFC, while delivering approximately 8-10 times more energy.

With regard to efficiency, we would like to emphasize that Table S1 presents the performance of the VRFC cell. Although we did not measure the charge–discharge cycle efficiency, it is important to note that the SC operates only during the initial phase of the discharge. Therefore, we assume that its impact on the overall efficiency is minimal. In addition, reducing the operating voltage of the SCs generates a non-accessible energy amount that can be evaluated through Equation S1; specifically, decreasing the operating voltage from 2.7 to 1.5 V results in a non-accessible energy amount of approximately 70%. As an example, Figure S5 reports examples of the discharge profiles of VRFC-SC systems during discharges longer than 5 s. It shows that after the first seconds the system voltage decreases until it reaches the VRFC voltage. This result indicates that the supercapacitor never fully discharges, as it cannot reach zero voltage because it is connected in parallel with the VRFC. Figure S6 depicts the voltage profile during a continuous pulsed discharge of the VRFC-SC34F system. Each 800 mA pulse is followed by 1 min of rest (I = 0 mA), during which the system voltage returns to the value imposed by the VRFC open-circuit voltage (OCV). In addition, the SC benefit remains evident after several cycles, as the system consistently exhibits the absence of an ohmic drop over more than 30 000 s. In addition, the leakage currents of the SCs investigated in this study are lower than 500 μA (see Table 3.1.1.2.2.1). Hence, we can postulate that during a standby period, the eventual self-discharge of the SC in the VRFC would have a negligible effect.

3.1.1.3.4 Modelling results and test comparison

This Section explores the influence of supercapacitor properties on the performance of a hybrid VRFC-SC system analysing the effect of the supercapacitor's ESR on current distribution and discharge dynamics. An investigation about the impact of capacitance on energy delivery, highlighting the trade-off between performance and system sizing is also reported.

Effect of the Supercapacitor Equivalent Series Resistance on the system

We examine two distinct VRFC-SC systems composed of the same VRFC and two different SCs featuring the same 15 F capacitance and different ESR of 0.02 Ω (SC1) or 0.11 Ω (SC2). The maximum voltage is the same and equal to 1.5 V corresponding to a VRFC SOC of 100%. These values are examples used to numerically assess the effect of the ESR on the system. All the input data implemented in the model for this analysis are reported in Table S13. Utilizing the Equations mentioned in Section 3.1.1.2.4, it is possible to plot the currents flowing in the branches of these two hybrid systems, as exemplified in Figure 3.1.1.3.4.1a. Both systems maintain a constant current of 2 A through the external load. During discharge, while the overall generated current remains constant, the currents in the SC and VRFC branches vary over time. In the SC branch, the current decreases from its maximum value to nearly 0 A within 40 seconds. Conversely, in the VRFC branch, the current initially rises and stabilizes at approximately 2 A after 40 seconds, sustaining the entire current flowing through the external load. At the beginning of the discharge (t = 0 s), the current distribution in the two branches depends on the ESR of the SC branch (R_{SC}). With SC1, most of the total load current (2 A) flows through the SC branch initially, due to the lower internal resistance R_{SC}. Similarly, in the case of SC2, most of the current flows through its branch, although at a lower magnitude than 2 A, because of its higher R_{SC} compared to SC1 (0.11 Ω vs. 0.02 Ω). Despite the different R_{SC} values, the SC capacitance influences the transient duration similarly in both cases, as both SCs possess a capacitance of 15 F. Figure S5 compares the simulated and experimental discharge voltage profiles of VRFC-SC system during discharges at 1 A and 2 A, even longer than 5 s for at 100 % SOC, and for a short pulse at 800 mA and 20% SOC. The simulation agrees well with the experimental profile, showing a maximum relative error below 3% and validating the simplified model for the VRFC-SC system.

Effect of the Supercapacitor Capacitance on the system

To investigate the impact of SC capacitance (SC size) on hybrid system energy performance (5s-pulse discharge), we employed the model, utilizing values measured during the test conducted on the single devices and on the systems. Using the Equations listed in Section 3.1.1.2.4 it is possible to estimate the energy deliverable from the system varying the capacitance and discharging at the same current. The input values used in the model correspond to the VRFC and SCs specifications reported. in Table 3.1.1.2.2.1 and Table S13 while v_L is set at 1.5 V. Figure 3.1.1.3.4.1b depicts the delivered energy values obtained through the model (black points) and compares them with the delivered energy measured during the test of four tested systems. Figure S7 reports the computed and experimental trends for discharge currents of 600 mA, 800 mA and 1 A. It is noticeable that the model provides a good reliability in the evaluation of the pulsed energy. If we increase the value of the combined capacitance to a higher value, such as 300 F, the result given by the model is the one reported in Figure 3.1.1.3.4.1b. It reveals that increasing capacitance enhances delivered energy up to an asymptotic value. This underscores that there is a limit to the deliverable energy by the system also using the highest capacitances.

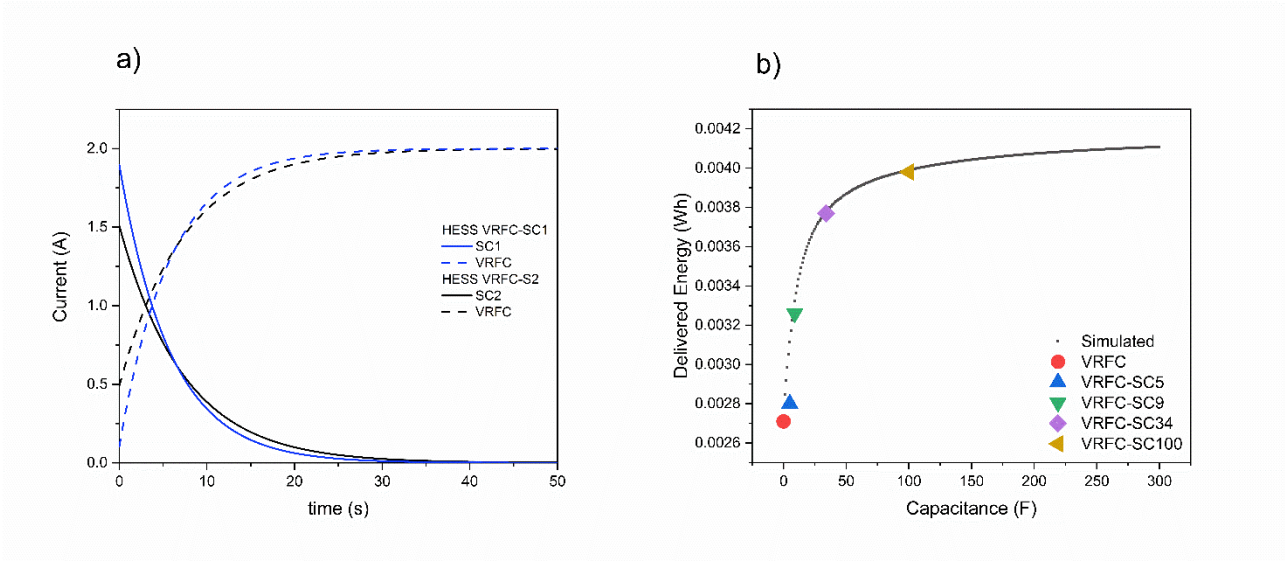

Figure 3.1.1.3.4.1 a) Currents flowing in the separate SC (solid line) and VRFC (dashed line) branches during discharge of two different SC-VRFC hybrid systems discharging at 2 A. The blue lines refer to the HESS with SC1, the black lines refer to the HESS with SC2, b) Energy delivered by the VRFC-SC hybrid system over 5-s pulses at 2 A vs SC Capacitance. The black dots are calculated using the model; coloured markers represent the results obtained during the parallel connection test between the VRFC and the commercial SCs. Experimental tests were conducted at RT=25°C. The starting SOC of the VRFC is 100%.

Rather, the SC capacitance should be tailored to achieve a deliverable energy corresponding to the knee of the curve, which can be extrapolated using different approaches. One possible method to identify the knee point consists in determining the point with the maximum distance from the straight line connecting the first and last points of the delivered energy–capacitance curve. According to this criterion, for the case shown in Figure 3.1.1.3.4.1 b, the knee point is located at approximately 75 F.

3.1.1.3.5 Life cycle assessment and sensitivity analysis

Figure 3.1.1.3.5.1a displays the GWP of the *production* of a HESS with direct connection (A) compared to a HESS with converter-based (B) connection, while Figure 3.1.1.3.5.1b presents the GWP of the *use phase*. In Figure 3.1.1.3.5.1c, both phases were combined. Environmental impacts were determined for the base case and for the five cases of the sensitivity analysis (Sens. 1 – 5), respectively. Indicator values for all other environmental impact categories are provided in the SI. Figure 3.1.1.3.5.1d provides a different depiction of the results of the sensitivity analysis, comparing the effects on all impact indicators investigated.

In the base case, the VRFB clearly caused the major impact on the GWP of the system's production phase (>94%). This was also true for most other impact indicators investigated, as displayed in the SI. The high environmental impacts of a VRFB's production phase are mainly caused by vanadium pentoxide (V_2O_5), which is used as active component in its electrolyte [36, 37, 46]. The GWP of HESS production increased with increasing SC size; however, the VRFB remained the single component with the largest impact. Despite increasing the SC power, the production of the SC continued to play a minor role regarding GWP for all cases investigated and irrespectively of the connection type. The higher GWP of HESS production at larger SC sizes can mainly be attributed to the larger AC-DC inverter and DC-DC converters.

In the base case, the GWP of HESS production with converter-based connection was only 21% higher than with direct connection. However, the sensitivity analysis (Sens. 1 – 5) demonstrated that this relative difference increased with increasing SC size: assuming a SC power of 80 MW (Sens. 5), which would be eighty times the power of the VRFB, the HESS with

direct connection exhibited a GWP of 0.095 kg CO_2-eq kWh^{-1}, while the HESS with converter-based connection showed a 27% higher GWP of 0.140 kg CO_2-eq kWh^{-1}.

Figure 3.1.1.3.5.1b presents the GWP of the use phase. The energy losses during charging and discharging of the HESS caused the majority of the GWP in the base case and for Sens. 1 – 3. However, in Sens 4 and 5, the impact of the AC-DC inverter exchange surpassed that of the energy losses. This applied for both connection types. In contrary to the production phase, the relative difference between the HESS with converter-based connection and passive connection decreased with increasing SC size. This can be attributed to the SC exchange, which showed a stronger increase with increasing SC size in case of the direct connection (triple number of SC cells) than for the converter-based connection. The GWP of the system's energy losses stayed constant with increasing SC size, and the GWP of the inverter exchange was the same for both connection types.

Comparing the results for the production and use phase (Figure 3.1.1.3.5.1c) revealed that the production phase had a higher GWP than the use phase in all cases analysed, for both connection types. However, this only applies when charging the HESS with renewable power, as was modelled here. If applying a conventional electricity mix, the GWP of the use phase would be significantly higher. In the base case, the total GWP of HESS production and use amounted to 0.070 kg CO_2-eq kWh^{-1} for the direct connection and to 0.096 kg CO_2-eq kWh^{-1} for the converter-based connection. The difference between the HESS with direct connection and converter-based connection increased from 37% in the base case to 41% for Sens. 5. Detailed results for the sensitivity analysis of HESS production and use for all impact values are provided in Figure 3.1.1.3.5.1d. A change of the SC power by +3 100% to 80 MW led to a specifically high reaction of up to +2 100% in FETP, HTPnc, METP and TETP. The effects on GWP were less pronounced and amounted to approximately +125% for the passive connection and +132% for the converter-based connection.

Figure 3.1.1.3.5.1e presents the results of the second sensitivity analysis on the round-trip efficiency of the passive HESS. If the efficiency were to drop from 67% to 52%, the GWP for production and use of the passively connected HESS would increase by 32% to 0.093 kg CO2-eq kWh^{-1}. In this case, the GWP benefits of avoiding DC-DC converters would be nearly

cancelled out by added electricity losses, leaving the passive HESS with a specific GWP close to that of the converter based system.

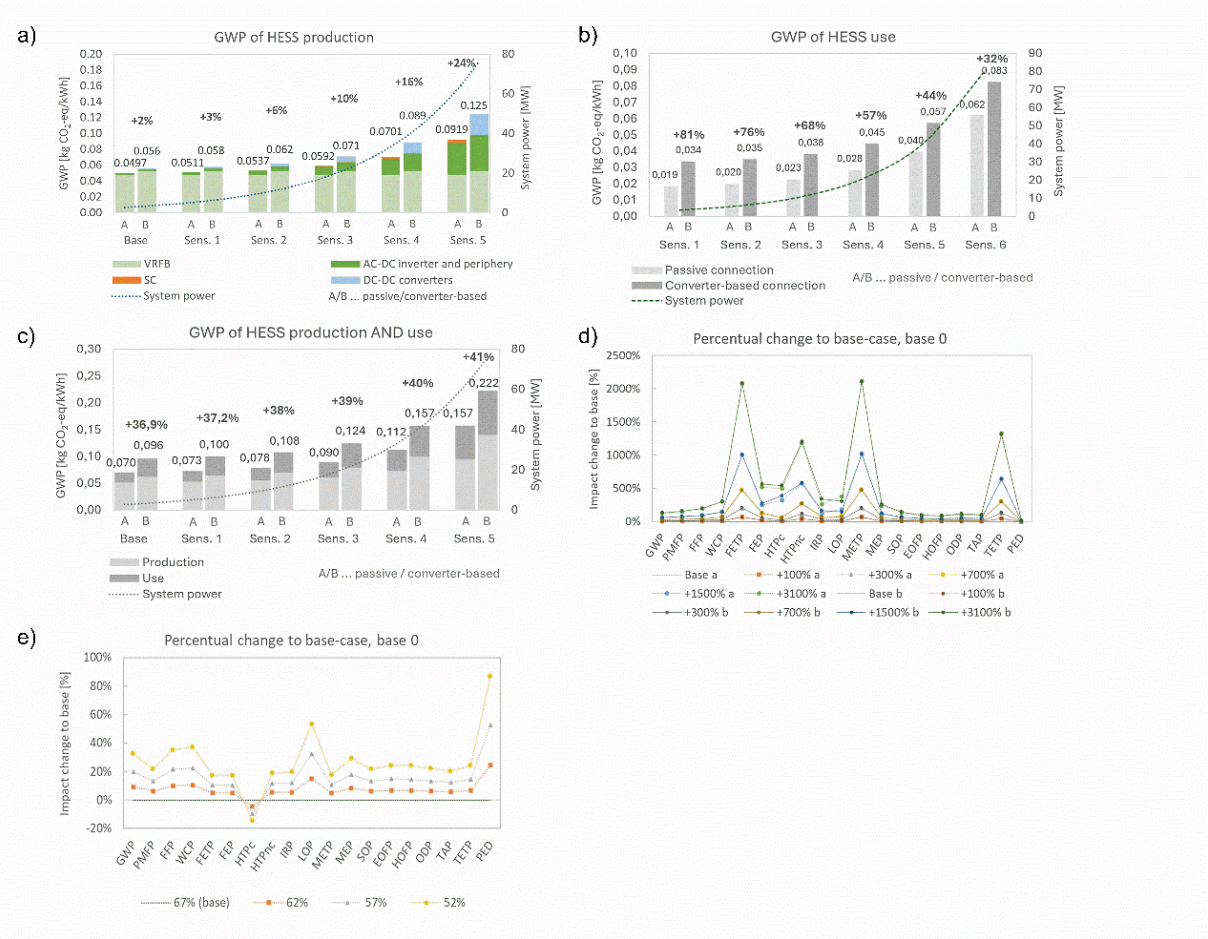

Figure 3.1.1.3.5.1 a) Global warming potential of HESS production, b) global warming potential of HESS use, and c) global warming potential of HESS production AND use, for the base case and for sensitivity cases, respectively. d) Detailed sensitivity analysis results for HESS production AND use (base = 2.5 MW SC, a = passive (direct) connection, b = converter-based connection), d) Results of sensitivity analysis of HESS with passive (a) and converter-based (b) connection, altering HESS power (production and use, base = 2.5 MW SC) e) Results of sensitivity analysis of HESS with passive connection, altering round-trip efficiency from 67% to 62, 57 and 52% (production and use, basic configuration).

The SC architecture assessed in this LCA uses an acetonitrile organic electrolyte. In contrast, aqueous electrolytes typically are not only cheaper and less hazardous but are also expected to reach the required system voltage in a HESS with direct connection. We assume that the acetonitrile electrolyte can be replaced on a 1:1 mass basis by a WiSE ammonium-acetate electrolyte (30 mol kg^{-1}). An LCA comparison showed that the latter exhibits far lower

environmental impacts per kg across all indicators, with a GWP of only about 9% of acetonitrile (Figure S8, SI). This suggests that the GWP contribution of the SC in a directly connected HESS could potentially be reduced further by applying an aqueous SC electrolyte. Still, the use of an aqueous electrolyte in the current SC design, the integration of this "green" SC in the passively connected HESS, and the assumptions described here, remain to be validated experimentally.

3.1.1.3.6 Economic assessment

The total project costs presented for the different HESS configurations represent the investment required for a turnkey facility and include both the costs of the main components and the associated additional and indirect costs. The main cost drivers are the VRFB, the SC, and PCS. For an active connection, the PCS comprises DC/DC converters for both the VRFB and the SC as well as an AC/DC inverter for grid connection, whereas for a passive connection only an AC/DC inverter is required. Additional and indirect costs cover expenditures for civil works, component assembly, process control and electrical engineering (materials and installation), site equipment, safety testing, quality control, engineering, construction and assembly supervision, commissioning, regulatory approvals, and contingencies. The resulting total project costs should be interpreted as indicative benchmarks rather than exact values, as actual costs depend strongly on project-specific conditions (e.g., building requirements or non-containerized implementations). Note that reported component costs in the literature or manufacturer data sheets typically exclude such additional and indirect costs and therefore underestimate the investment required for a fully operational system. Figure 3.1.1.3.6.1 illustrates the calculated CAPEX and cost shares of the main components and additional and indirect costs for the "Base" and "S5" HESS configurations in 2022 and 2050, considering different connection types (active/passive) and SC electrolytes (organic/aqueous).

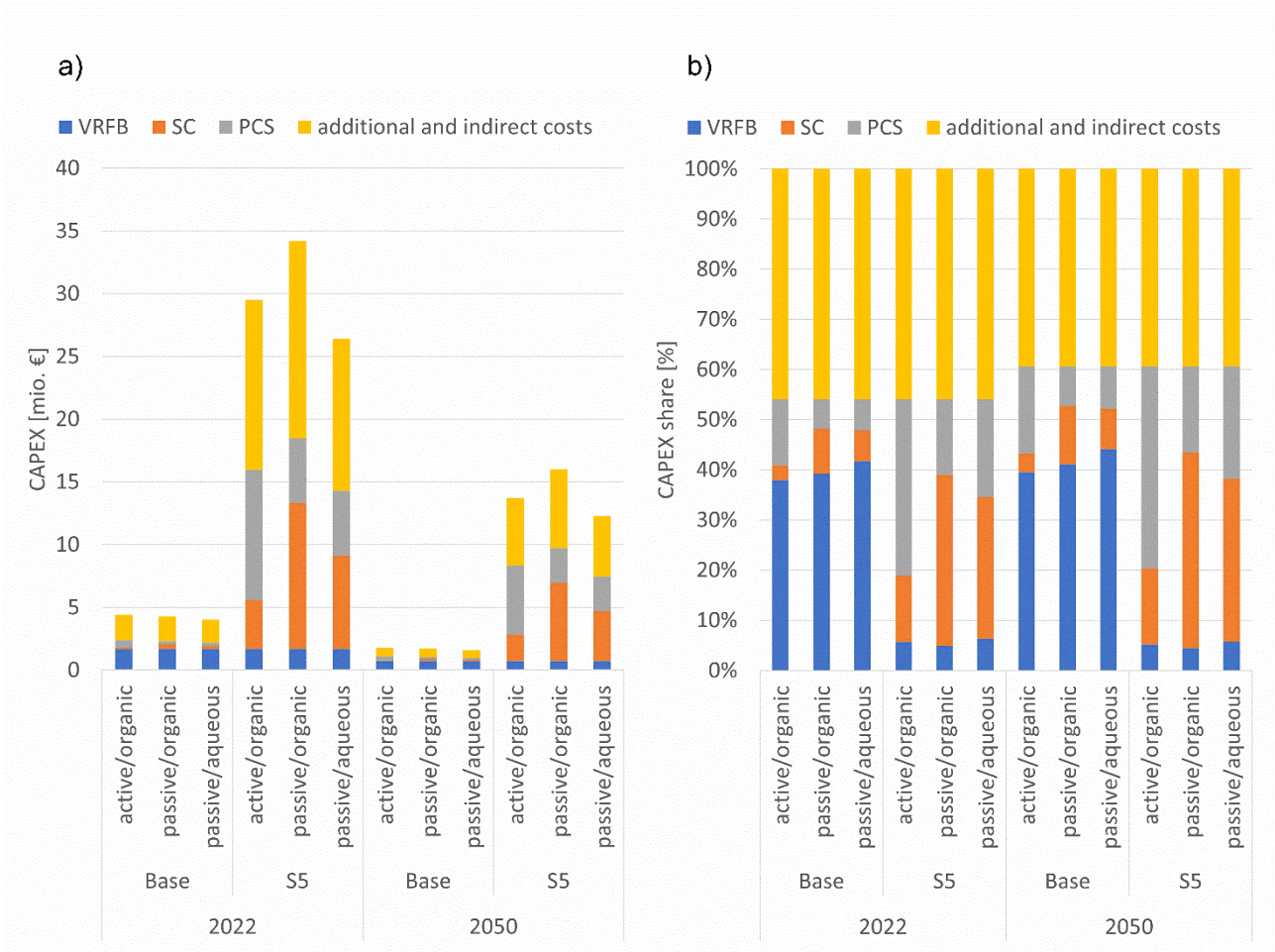

Figure 3.1.1.3.6.1 Cost share a) and Cost share % b) of main components as well as additional and indirect costs for the HESS configurations "Base" and sensitivity "S5" in the years 2022 and 2050 for different connection types (active/passive) and SC types (organic/aqueous)

In 2022, additional and indirect costs account for approximately 46% of total project costs across all configurations, corresponding to a Lang factor of 1.85. By 2050, this share is projected to decrease slightly to approximately 39% (Lang factor 1.65), mainly due to reduced contingencies. These values are substantially lower than typical Lang factors of around 3 for conventional industrial facilities, reflecting the higher degree of prefabrication and reduced assembly complexity of containerized HESS components. The cost structure is primarily influenced by the connection type (active or passive), the system configuration (especially SC power), and the SC electrolyte (organic or aqueous), while temporal effects (until to 2050) play a minor role. In the "Base - active/organic" configuration, the SC contributes only approximately 3% in 2022 to 4% in 2050 of total project costs, the PCS 13 to 17%, and in contrast the VRFB about 38 to 39%. In the high-power "S5 - active/organic" configuration, the overall

cost structure shifts. The SC share increases to 13 to 15% and the PCS to 35 to 40%, while the VRFB share decreases to approximately 6%. For passive configurations, the elimination of DC/DC converters halves PCS costs compared to active connections, but SC costs triple due to the requirement for three times the number of cells. Using an aqueous electrolyte reduces SC costs, making the "passive/aqueous" configuration the lowest-cost option among those analysed. Figure 3.1.1.3.6.2 summarizes the total specific power- and energy-related project CAPEX for all configurations and includes scaling effects, with system sizes varied by factors of 0.1 (indicated by the upper bandwidth error) and 10 (indicated by the lower bandwidth error).

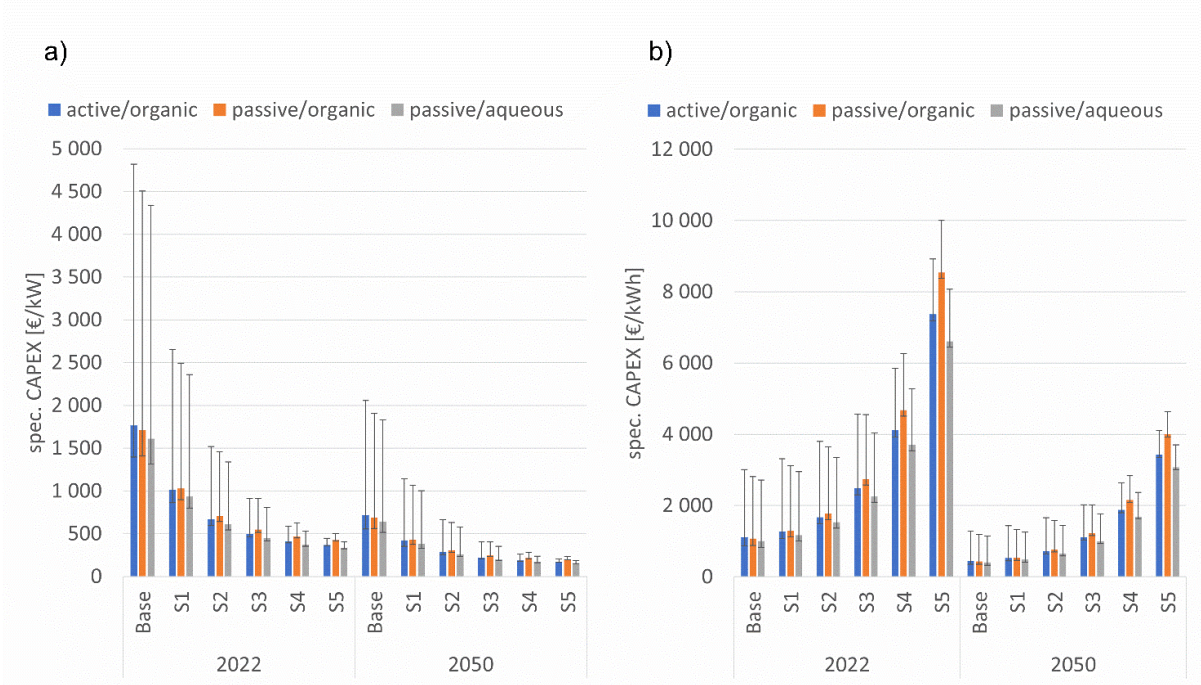

Figure 3.1.1.3.6.2 Total spec. a) power and b) energy-related CAPEX of HESS. Bandwidth error indicator: lower value - reference system size times 10; upper value - reference system size times 0.10. [Base: SC 2.5MW / VRFB 1MW/4MWh; S1: SC 5MW / VRFB 1MW/4MWh; S2: SC 10MW / VRFB 1MW/4MWh, S3: SC 20MW / VRFB 1MW/4MWh, S4: SC 40MW / VRFB 1MW/4MWh, S5: SC 80MW / VRFB 1MW/4MWh]

Five key dependencies were identified: i) the prospective reduction in CAPEX due to technological learning (economies of scale by cumulative production volume), ii) the influence of up- and down-scaling (economies of unit scale), iii) the impact of the HESS configuration (variation in the rated power of the SC, iv) the effect of the connection type ("active" or "passive"), and v) the choice of electrolyte for the SC ("organic" or "aqueous"). Between 2022 and 2050, specific CAPEX decreases by about 60% across all configurations due to

technological learning. Upscaling (by a factor of 10) reduces costs by roughly 20%, while downscaling (by a factor of 10) leads to a cost increase by a factor of 2.8. Increasing SC power strongly reduces power-related CAPEX but significantly increases energy-related CAPEX. Passive connections show slightly lower costs in the base configuration, whereas active connections become more cost-effective at higher SC power levels. Finally, aqueous SC electrolytes reduce specific costs by approximately 6 to 23% compared to organic electrolytes.

The results clearly indicate that the estimated HESS costs are sensitive to several key cost drivers. Additionally, there are uncertainties related to vanadium price volatility, future cost developments of supercapacitors (especially for emerging aqueous electrolyte concepts), converter efficiency improvements, and installation costs can significantly influence total project CAPEX. Further, although passive connection concepts reduce PCS and are therefore commonly associated with lower maintenance requirements, the increased number of SC cells may partially offset this advantage due to a potentially higher probability of cell failures and replacement needs. A comprehensive assessment of operation and maintenance costs, including component reliability and lifetime effects, is therefore identified as an important topic for future research. Consequently, the presented cost estimates should be interpreted as indicative benchmarks rather than precise forecasts, highlighting the importance of project-specific assessments and updated cost data when applying the proposed framework to real-world deployments. Overall, specific CAPEX of the HESS shows strong learning and scaling effects. While the connection type has a moderate influence, SC power and electrolyte choice are decisive cost drivers. Among the analysed configurations, the passive connection with an aqueous SC, results in the lowest costs, although an active connection combined with an aqueous SC may offer further cost reduction potential.

3.1.1.4 Conclusions

This study demonstrates the potential of directly integrating Vanadium Redox Flow Batteries with Supercapacitors to form a Hybrid Energy Storage system. The combination exploits the complementary features of these technologies, with the energy density of VRFBs synergistically paired with the high power density and rapid charge/discharge capabilities of SCs. Through experimental tests and modelling, we showed that the direct parallel connection of VRFB and SC at the cell level significantly enhances the system's ability to deliver energy

during high-power pulses, while reducing the reliance on high-voltage SCs with organic electrolytes. Indeed, the absence of the power converter requires the two HESS branches to feature the same maximum voltages. A full-charged VRFC has an open circuit voltage (OCV) of about 1.5 V; commercial EDLCs, employing conventional organic electrolyte, can reach 3 V maximum voltage. Hence, this EDLC, if directly connected to a VRFC, works in a cell voltage range that is limited by the VRFC OCV. Given that the energy and power performance of the EDLC depends on its cell voltage, reaching half of its cell voltage also means that the EDLC cannot exploit all of its energy and power maximum performance. In turn, this has an impact on the overall system costs. The lower cell voltage opens the possibility of using EDLCs that operate with alternative, more environmentally friendly electrolytes, like aqueous solutions. They are interesting candidates for designing a HESS where the VRFC and SC are directly connected, because they feature maximum voltages that might be compatible with VRFC OCV. Of course, the inherent value of using an aqueous electrolyte is to provide a big improvement in terms of sustainability of the SC and the HESS itself: avoiding the conventional organic electrolytes of SC means avoiding safety issues, such as flammability, toxicity, and teratogenicity. However, water-based supercapacitors, like those employing water-in-salt electrolytes, are still in the development stage and currently exhibit a technology readiness level < 4, as they are available only at laboratory scale. Moreover, our modelling approach provided a practical methodology to size SCs optimally in hybrid configurations, avoiding oversizing and reducing costs. The results highlight the importance of tailoring the SC characteristics to maximize energy delivery while reducing unnecessary economic and environmental impacts.

Indeed, a life cycle assessment and an economic analysis were carried out to evaluate the potential benefits of a passive VRFB-SC connection. The LCA showed that the relative advantages regarding GWP of a HESS with direct connection to a system with converter-based connection increase with increasing system power. There only exist very few LCA studies on SCs in literature [33] [47-49], and those available are based on small cells (2.7 V, 0.005 Wh) that were upscaled. Hence, an LCA of a real SC module in the MW scale based on manufacturer data would be of high interest, to verify the approximations made by means of the small cells. However, the relative impact of the SC on the GWP of the HESS is minor, even at high SC power. By contrast, the impact of the DC-DC converters, in case of the converter-based

connection, and of the AC-DC inverter on the system's GWP is strongly increasing with increasing SC power. Therefore, data verification based on real large-scale units, or an approximation of scaling effects would be interesting for future research.

From an economical point of view the HESS cost depends on connection type (active or passive), system configuration and SC size and type (organic or aqueous). The configuration that achieves the lower project costs is the one featuring a passive connection with aqueous SCs. Overall, the integration of experimental and simulation data with an assessment of economic and environmental impacts confirms the feasibility and potential competitiveness of the VRFB-SC hybrid system. This evaluation underscores the system's relevance as a sustainable and efficient solution for energy storage, particularly for applications requiring short-term high-power outputs combined with long-term energy storage capacity.

Limitations of the study and future developments

One of the limitations of the present study is related to the inherent constraints of laboratory-scale testing. We evaluated only four configurations of the VRFC–SC system, and to enable a more comprehensive assessment, further configurations should be investigated. The benefit of the SC coupling at high currents must be investigated in an upscaled system. Indeed, the obtained results could vary depending on the design and operating parameters, which must be considered during the system design for realistic operating conditions. The research should also explore alternative scenarios, such as comparisons with different connection types, supercapacitor models, system stability assessments, extended discharge experiments, and the influence of varying VRFC cell SOC on dynamic performance outcomes. Further research is in progress to investigate the long-term operation and cycle life of the VRFC, SC, and the integrated passive VRFC–SC system, and to assess their capacity to operate under high current conditions without adjusting the pump rate. Extended cycling tests and accelerated aging studies must be conducted to evaluate long-term performance and reliability. The AC/DC converter regulates the DC bus voltage; however, solutions, such as passive circuits, require evaluation to manage internal balancing currents and reduce the risk of overvoltage during the charging phase, which is outside the scope of the present work.

Moreover, the transition from laboratory-scale systems (4 cm^2) to industrial applications may involve considerable engineering challenges. However, the VRFC provider (Pinflow) has already demonstrated strong transferability between results obtained from a 20 cm^2 single cell and a 608 cm^2 20-cell pilot stack [50]. In addition, in an ideal upscaled system, each supercapacitor should be paired with a single cell in order to minimise the need for balancing circuits. However, from a practical perspective, this configuration presents several challenges. A more detailed evaluation of practical implementation—including system integration and maintenance procedures—is necessary to support real-world application. Furthermore, as outlined in the introduction, the modelling approach remains relatively simple. Although this provides rapid responses, it also introduces a margin of error. Both the experimental and modelling components require deeper analysis, which will likely contribute to the development of a more realistic VRFC-SC system. At this stage, as indicated in the introduction, the research serves as an exploratory effort to understand the operational behaviour of the VRFC system and the modelling process.

From an economic assessment point of view: while this study focused on the assessment of various HESS configurations and connection types with an emphasis on capital expenditure, a comprehensive evaluation of economic performance indicators such as LCOS, NPV, and payback periods remains subject to future research, as such an analysis would require application-specific operational profiles and market assumptions that go beyond the scope of this work. Future work should also address the detailed engineering challenges associated with scaling, integration, and operation of HESS in real-world applications, which go beyond the economic focus of this study. Determining the round-trip efficiency of the HESS in real use cases would be highly relevant for the LCA, as electricity losses account for a significant share of the system's overall GWP. Moreover, the operability of the system with aqueous SC electrolytes needs to be tested, which is a prerequisite for assessing their actual environmental benefits.

Acknowledgements

This project has received funding from the European Union's Horizon 2020 research and innovation programme under grant agreement No. 96355 (HyFlow).

3.1.2 Improvement of the VRFC-SC Modelling and Simulation of Potential Applications

The work presented in this Section results from the Mentoring Programme for PhD students, organised by the StoRIES Project [56], in which I participated and was mentored by Professor Linda Barelli (Department of Engineering - University of Perugia).

The study reported in Section 3.1.1 [3] analyses the modelling of the passive integration between a SC and a VRFC through an electrical equivalent circuit of the system. This circuit comprises two parallel blocks: one represents the VRFC, and the other represents the SC. The first block includes a constant voltage source, which reproduces the OCV, and a resistor that acts as the ESR. Similarly, the SC block includes a resistor as ESR and a capacitor to emulate the capacitance C. It is worth noting that in this model, all parameters of the VRFC and SC (OCV, ESR, and C) are constant values derived from cell datasheets. The applied load consists of a constant pulsed current, which a constant-parameter model can adequately address to emulate reality. However, to extend the applicability of the model to more complex loads, some refinements are required. Indeed, this simplification does not consider critical behaviours of the cells, such as the variation of OCV with the state of charge (SOC) or the dependence of capacitance on current, which are significant for long discharge profiles with variable current. The present Section aims to integrate the empirical characterization of both the VRFC and the SC into the model. This approach enables the simulation and prediction of the behaviour of the passive-connection system under realistic load conditions. A parallel system combining an SC and a VRFC can achieve optimal performance with medium-term loads characterized by frequent positive and negative power peaks. For instance, the hybrid energy storage system could be implemented in stationary or onboard storage for railways, tramways, and electric buses [57]. A distinctive feature of these applications is regenerative braking, which allows energy recovery during braking phases. Moreover, the timing of braking and acceleration in public transport vehicles aligns with the charge and discharge cycles of supercapacitors, which could absorb and release power peaks, consequently smoothing the current delivered to the battery. Specifically, the load scenario used as an example in this study is the absorbed power profile of an electric bus, previously discussed in [58] by L. Barelli et al., and rescaled to match the specifications of the investigated system.

3.1.2.1 Methods

As in the previous study, MATLAB is employed to model and simulate the system. To provide a physical model instead of only a mathematical one, as presented in the previous work [3], this study utilises Simulink and Simscape environments. This approach enables the modelling of the Equivalent Circuit using the physical modelling blocks of Simscape. The electrical blocks, in fact, are derived from the Foundation and Electrical Libraries of Simscape.

VRFC Characteristics and model

The VRFC model resembles the one applied in the previous study, comprising a voltage source in series with a resistor (Section 3.1.1, [3]). The principal distinction is that the voltage source representing the OCV of the cell and the resistor representing the ESR are not assumed to be constant in this refined model. Consequently, the constant voltage source is replaced by a Controlled Voltage Source (CVS) , and the resistor is replaced by a Variable Resistor (VR). In this manner, the OCV and ESR simulated within the system vary according to the current flowing through the VRFC branch. The nominal VRFC cell characteristics, provided by the manufacturer are summarised in Table 3.1.2.1

Table 3.1.2.1 Nominal values of exchange surface, cell voltage range, theoretical capacity (50 mL tanks), and maximum discharging current of the Pinflow VRF Cell

Surface	**Cell voltage range**	**Theoretical Capacity**	**Maximum discharging current**
cm^2	*V*	*mAh*	*A*
4	0.8-1.65	2 144	2

The initial step in converting the previous model into a semi-empirical one involved acquiring characteristic data of the VRFC, including the OCV and ESR values at different SOC levels. In our case, this information was provided by Pinflow Energy Storage [59], the supplier of the cell. The company provided the OCV and ESR values at various SOC levels ranging from 10

to 90%, comprising nine measurements for each parameter, which are illustrated by the markers in Figure 3.1.2.1a showing the OCV ranging from around 1.3 V to 1.50 V and the ESR from 0.28 Ω to 0.38 Ω. These data are incorporated into the model through two Lookup Tables, represented by Simulink blocks that interpolate the experimental results using a linear point-slope method to generate the VRFC characteristic functions $OCV = f(SOC)$ and $ESR = g(SOC)$, as shown in Figure 3.1.2.1a. The interpolation is required to estimate the ESR and OCV values at each current. The Lookup Tables are connected to the two main blocks: the Controlled Voltage Source (CVS) and the Variable Resistor (VR) arranged in series and depicted in Figure 3.1.2.1b. The first simulates the VRFC OCV, whereas the latter represents the empirical VRFC ESR. A current sensor (A in the picture) is attached to this branch to measure the flowing current i_b, which is subsequently used to compute the SOC in a dedicated block (SOC estimator). The SOC is evaluated according to the Equation 3.1.2.1 where Q_{th} is the theoretical capacity of the cell.

$$SOC = 1 - \frac{\int i_b dt}{Q_{th}} \qquad 3.1.2.1$$

The SOC evaluator block output is linked to the two Lookup Tables that evaluate the characteristic values trough the interpolated functions and attribute them to the CVS and VR. The SOC evaluator also includes a Stop Simulation button that, when enabled, terminates the computation once the VRFC remaining charge falls to 10%. The complete VRFC system, including all the mentioned blocks, is illustrated in Figure 3.1.2.1b.

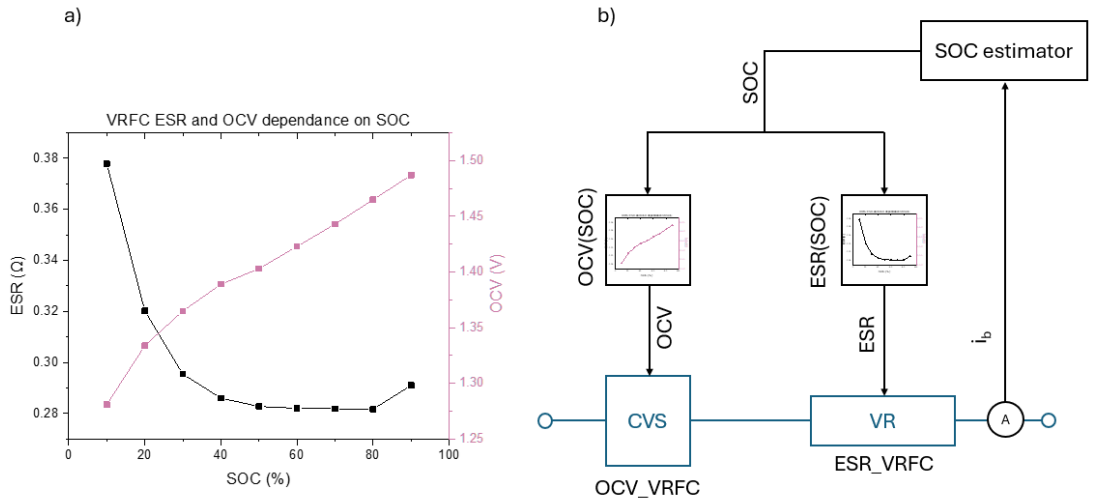

Figure 3.1.2.1 a) Experimental OCV and ESR data at different SOC levels and corresponding interpolated functions implemented in the model through Lookup Tables; b) schematic of the empiric VRFC model

SC Characteristics and model

For this model, we consider two supercapacitors of different sizes (34 F and 100 F) purchased from Eaton, with characteristic values reported in Table 3.1.2.2. The Table reports the nominal capacitance, the ESR, the maximum cell voltage (V_{MAX}) and the maximum continuous discharging current (i_{MAX}) of the two SCs that were derived from the manufacturer's datasheet. The maximum energy U_{MAX} and the maximum power P_{MAX} were derived according respectively to Equation 3.1.2.2 and 3.1.2.3. As reported in the Table the SCs can operate up to 3 V but to pair them in a passive system with the VRFC, as described in [3] they will work with a maximum voltage of 1.5 V.

$$U_{MAX} = \frac{1}{2} C V_{MAX}^2 \qquad 3.1.2.2$$

$$P_{MAX} = \frac{V^2}{4\,ESR} \qquad 3.1.2.3$$

Table 3.1.2.2 Characteristics of the commercial Supercapacitors purchased from Eaton. Data, except for maximum energy and power, are derived from the datasheets of the manufacturer.

Acronym	**Capacitance**	**ESR**	V_{MAX}	U_{MAX}	P_{MAX}	i_{MAX}
	F	Ω	*V*	*mWh*	*W*	*A*
SC34F	34	0.016	3.0	42.5	141	6.5
SC100F	100	0.011	3.0	125	205	11.7

In SC modelling, the focus is on representing the variation of capacitance and ESR with respect to the current flowing through the SC branch i_{SC}. The SC model corresponds to the one outlined in Section 3.1.1 [3], consisting of a capacitance block and a resistor to simulate the ESR. The main distinction is that in this improved scheme, the two blocks are not constant but a Variable Capacitor and a Variable Resistor, which change according to the i_{SC} dependence. The necessary empirical data were obtained by conducting galvanostatic (GCPL) tests using a Biologic Potentiostat at various current levels (0.4, 0.6, 0.8, 1, 2, 4, 6, and 10 A) on each SC, with potential limits between 0 and 3 V. Specifically, the capacitance was evaluated through the Equation $C=i\Delta t/\Delta V$, where i represents the tested current, Δt is the discharge duration, and ΔV is the variation in cell voltage during discharge. Figure 3.1.2.2 illustrates an example of the GCPL curve obtained by applying a 6 A discharge current to the 34 F supercapacitor,

emphasising the ohmic drop and the linear voltage trend during discharge. The ESR was calculated through the Equation $ESR=\Delta V_{Ohm}/(2i)$, where ΔV_{Ohm} denotes the voltage drop (ohmic drop) occurring at the start of the discharge phase. As an example, the extrapolated capacitance and ESR for SC100F are illustrated in Figure 3.1.2.3 a, and it is evident that the capacitance decreases as the current increases, while the ESR remains nearly constant, as anticipated. The evaluation of the ESR from the ohmic drop can be affected by the resolution of the instrument in voltage and time. In this study, only the values obtained at currents higher than 4 A were considered reliable. They are slightly higher than those reported by the manufacturer, presumably because they are also affected by the resistance of the connectors.

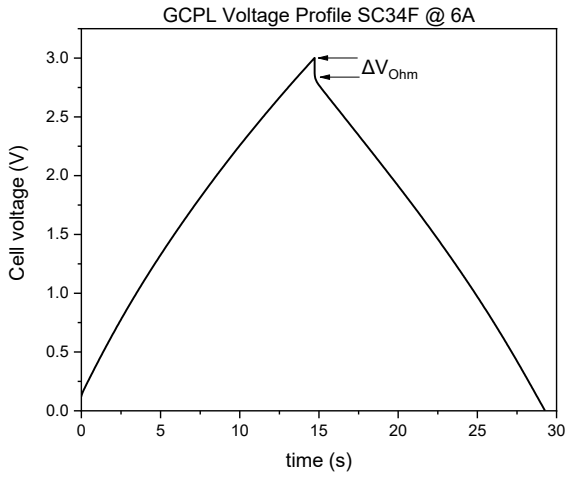

Figure 3.1.2.2 Example of Cell voltage profile obtained conducting a GCPL on SC34F.

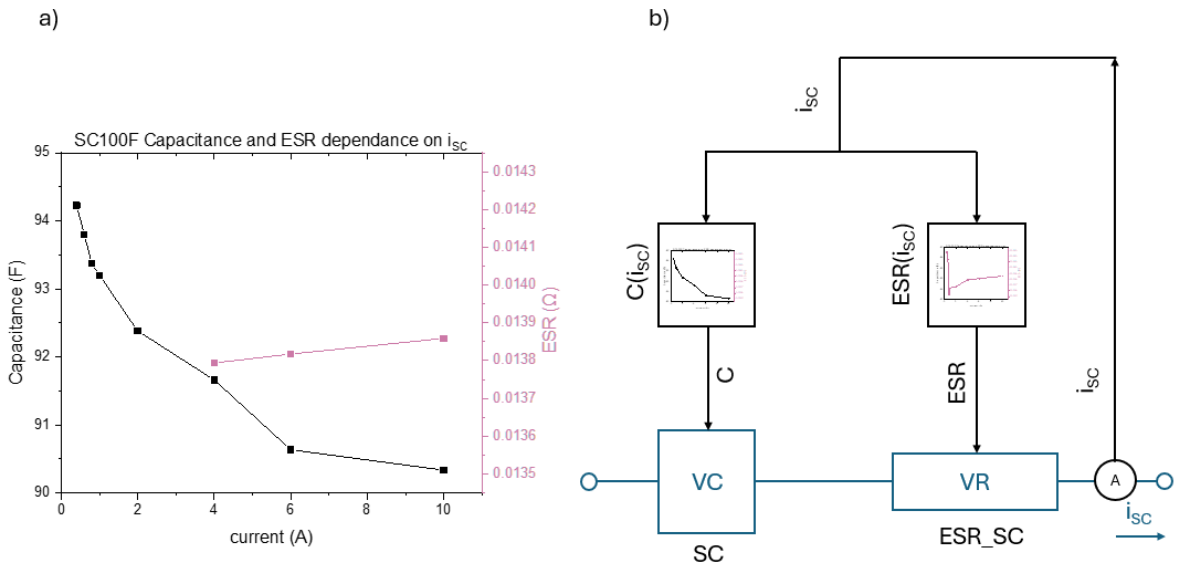

Figure 3.1.2.3 a) Extrapolated Capacitance and ESR values for the SC100F at different current levels; b) schematic of the empiric SC model.

To integrate these empirical data into the model, two Lookup Tables are included as depicted in Figure 3.1.2.3b: one for the characteristic function that relates the ESR to the current in the SC branch, $ESR = h(i_{SC})$, and one for the capacitance, $C = j(i_{SC})$. The ESR and C values derived from these functions are utilised by the two main blocks of the SC model: a Variable Resistor (VR) acting as ESR and a Variable Capacitor (VC) acting as a Capacitance. A current sensor (A in the picture) is connected within the SC branch to measure the current i_{SC}, which is then imported into the Lookup Tables that will extrapolate the C and ESR for the VC and VR blocks.

Current load profile

As previously stated, the purpose of this work is to evaluate the behaviour of the hybrid system when subjected to a realistic load, such as the current consumption profile of an electric city bus. The complete load profile exhibits current peaks of 250 A and requires a capacity of approximately 2700 Ah with a nominal battery voltage of 500 V. Assuming an operating voltage of 1.5 V per VRFC, we estimate 500/1.5 = 333 VRF cells (and 333 SCs) connected in series to satisfy the voltage requirement. We extrapolated the required electrolyte volume using the Equation $V_{TOT}=2Q_{th}/(c_vFn)$, where V_{TOT} denotes the total electrolyte volume, Q_{th} the theoretical capacity required (2700 Ah), c_v the vanadium electrolyte molarity (1.6 mol L^{-1}), F the Faraday constant (26.801 Ah mol^{-1}), and n the number of electrons involved in the redox reaction (1) obtaining V_{TOT}=130 L. The 333 VRFC cells are connected in series (and each cell parallel connected to one SC) to achieve a 500 V voltage, but to allow a 250 A current to flow, the size of the exchanging surface of the VRFC must be increased; assuming a maximum current density of 500 mA cm^{-2}, an exchanging surface of 250/500*1000 = 500 cm^2 must be designed.

Table 3.1.2.3 Proposal of VRFC-SC upscaled system according to the bus load requirements

n. VRFC cells	**Total Electrolyte volume**	**Exchange surface**	**Maximum current**	**Theoretical capacity**	**n SC cells**
	L	*cm^2*	*A*	*Ah*	
333	130	500	250	2700	333

However, this initial design approach is considered a way to conceptualise the upscaled system (summarised in Table 3.1.2.3), whereas the simulation is conducted using the available data from the small laboratory cell with an exchanging surface of 4 cm². Instead of upscaling the simulated model, the load profile is downscaled by dividing the current load by a factor of 250 to keep the peak current below 2 A, which represents the limiting current of the single lab cell. Indeed, the simulation evaluates the behaviour of a single VRFC–SC pairing. The implemented load profile, illustrated in Figure 3.1.2.4a shows peak values below 1 A, while the total load curve extends over approximately 32 hours. By using the Signal Editor Simulink block in combination with a Controlled Current Source, this current can be applied to the equivalent circuit. The complete SC model within the full system is illustrated in Figure 3.1.2.4b.

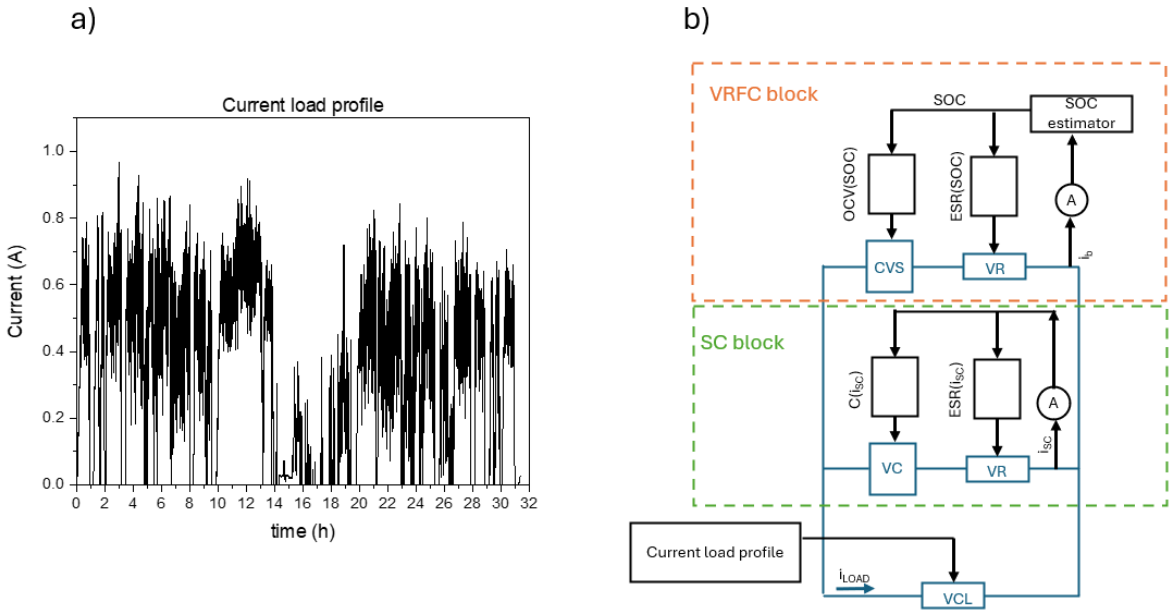

Figure 3.1.2.4 a) Scaled current profile imported into the model to simulate the load of an electric city bus b) Full VRFC-SC system model in the Simulink environment

3.1.2.2 Results and discussion

Two simulations were conducted using the empirical data obtained for SC34F and SC100F, as outlined in Section 3.1.2.1. To emphasise the impact of SC size on the HESS response, the analysis was extended by modelling additional hypothetical capacitances (200 F and 1000 F).

This stage was regarded as an exploratory investigation due to the lack of empirical data. Consequently, the SC200F and SC1000F supercapacitors were modelled under the assumption of a constant capacitance and a constant ESR of 0.010 Ω and 0.002 Ω respectively. Figure 3.1.2.5 displays the outcomes of the four simulations, illustrating the current distribution in the three branches of the VRFC–SC system under varying SC capacitance, while the VRFC model retains identical characteristics. The load current, i_{load} (black in the graphs), remains constant across all four simulations and is considered positive. The VRFC branch current (i_b in orange) is negative throughout since the cell continuously discharges, albeit at different rates. The SC current (i_{SC} in blue) alternates between positive and negative values, indicating that the SC rapidly undergoes charging and discharging phases. For the highest capacitance, for instance in Figure 3.1.2.5d around 4000 s, it is evident that while i_{load} is zero, i_{SC} and i_b exhibit exponential behaviour, implying that the SC is being charged by the VRFC. However, as explained in Section 3.1.2.1, the simulation terminates when SOC reaches 10%. However, in these simulations the discharge lasts less than five hours, not covering the full duration of the city bus load profile (31 h - Figure 3.1.2.4 a). This shorter duration is related to the theoretical capacity entered into the SOC estimator, which corresponds to that of the laboratory cell (2144 mAh), indicating that this capacity is evidently lower than the value required to complete the entire bus route. Furthermore, it is worth noting that the presence of the capacitive SC element influences the impact of the load on the VRFC. In fact, part of the current peaks is absorbed by the SC: the maximum current flowing in the load branch is the same for all the four systems, but the SC capacitance acts as a peak filter that is more effective when the capacitance increases. However, the average of the current is managed by the VRFC, which functions as the main energy reservoir. As reported in [60], operating a VRFB at high currents reduces the system efficiency; therefore, the reduction of current fluctuations thanks to the capacitive effect can enhance the VRFB efficiency. This factor, together with the absence of a DC–DC converter and the considerations assessed by Schubert et al. in [1], could make the combination with SC one of the most efficient solutions.

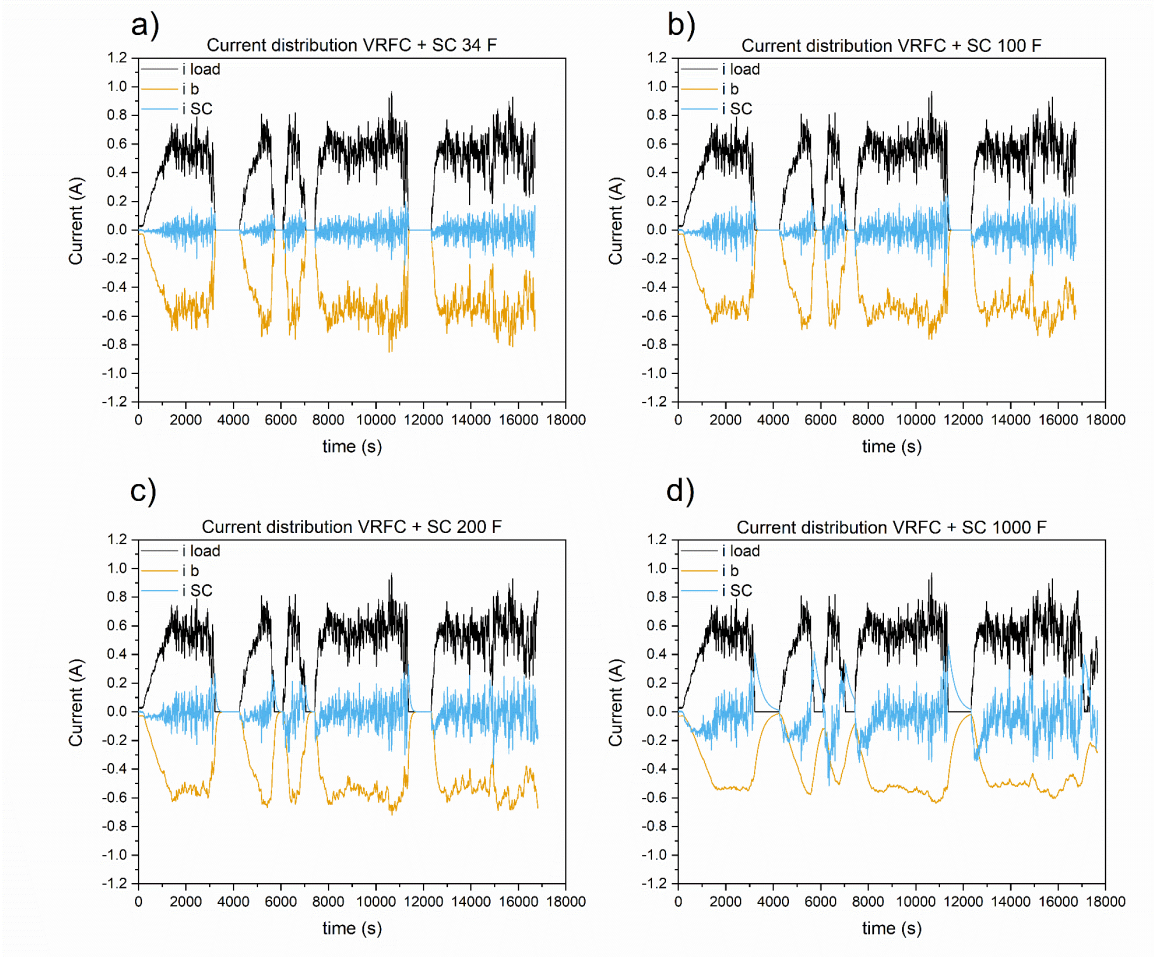

Figure 3.1.2.5 Results of the four simulations showing the current distribution in the three branches of the VRFC–SC system with varying SC capacitance : a) 34 F, b) 100 F, c) 200 F, d) 1000 F.

As explained in the work [3], the passive system requires the two cells to share a compatible voltage. For this reason, up to this point, we have evaluated the connection of one SC with one VRFC, assuming that the SC operates at a maximum voltage comparable to that of the VRFC (1.5–1.6 V). This implies, especially when working with commercial supercapacitors, that the system exploits only about half of the maximum SC voltage (2.7-3.0 V). Therefore, we proposed considering water-based supercapacitors, which have maximum potential voltage of about 1.7 V. In addition, the cost of water-based SCs is lower due to the cheaper electrolyte as reported in Section 2.2.1. Another configuration that we explored was obtained by connecting a series of two VRFC cells in parallel with one acetonitrile-based SC, which operates up to 2.7–3.0 V. Figure 3.1.2.6 reports the results of this investigation compared with the 1 VRFC – 1 SC configuration Specifically, Figure 3.1.2.6a compares the voltage profile of each VRFC cell and indicates that the 2 VRFC configuration seems to achieve greater

advantages than the single-cell setup. Indeed looking at the zoomed graph in Figure 3.1.2.6 b it is possible to notice that the 2 VRFC configuration smooths the voltage peaks and valleys. Indeed, a further reduction in voltage peaks is observed. Figure 3.1.2.6c and Figure 3.1.2.6d show that, in the 2 VRFC – 1 SC system (adopting the same SC100F supercapacitor), the SC is more effective in reducing the current peaks and filtering as the current profile in the VRFC branch (in orange) presents less fluctuations even if paired with just one SC.

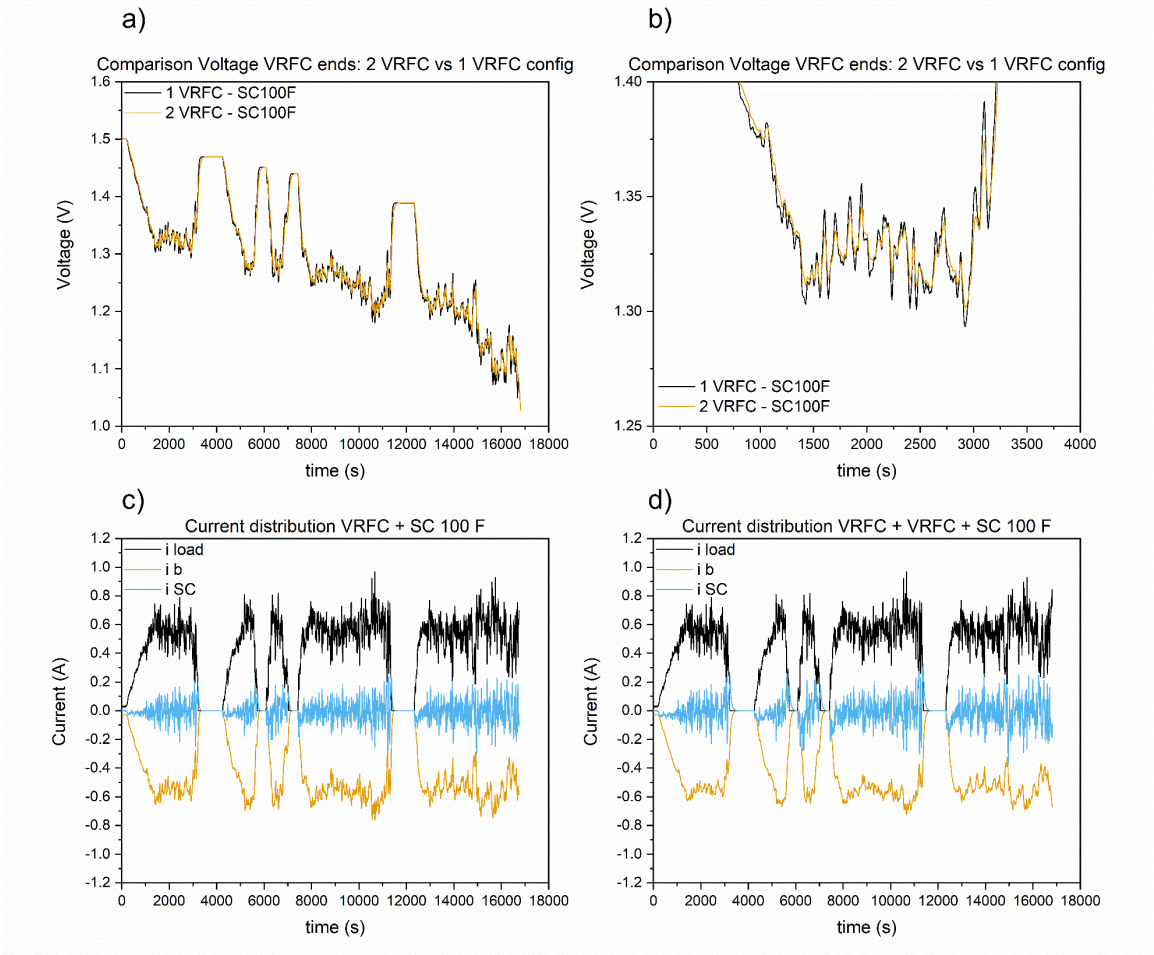

Figure 3.1.2.6 a) Comparison of the voltage profiles at the end of one VRFC with the 2VRFC config and 1 VRFC configuration; b) zoomed view of the compared voltage profile; c) current distribution in the three branches of the VRFC–SC system with the 1 VRFC configuration; d) current distribution in the three branches of the VRFC–SC system with the 2 VRFC configuration.

3.1.2.3 Conclusions

This Section aimed to investigate the behaviour of the passive VRFC-SC system introduced in Section 3.1.1 under actual load conditions. In previous studies, the performance of the system only through the application of a constant current load was analysed. However, as described in the Limitation of the Study paragraph, the appropriate approach to assess the feasibility of such an innovative system is to test it under real load conditions. Since it was not possible to test an entire VRFC stack at that time, the validated model, obtained through comparison with the pulsed-discharge test, was used here to evaluate potential outcomes when applying a dynamic load similar to that of an electric city bus. The monitoring of the current distribution across the three branches of the system demonstrated that the capacitance helps reduce current fluctuations in the VRFC cell, thereby simulating the behaviour of a filter. The reduction in the rapid fluctuation of the current may enhance the efficiency of the VRFC cell. The best results were achieved with the highest capacitance. Furthermore, a new configuration including a parallel connection of two VRFCs in series with one SC was simulated to exploit the full voltage window of an acetonitrile-based SC. This new configuration appeared to provide an additional reduction of current peaks without increasing the SC size. However, this step, which is crucial for the future development of the system, should be supported by experimental tests on a real stack. Future work should involve assembling the stack to assess the design feasibility of several aspects, such as connecting each VRFC cell in parallel with one SC. In addition, cycling stability tests must be carried out to determine whether the VRFC stack performance benefits from the pairing by evaluating efficiency variations.

3.1.3 Conclusions

In the paper "Hybrid energy storage through the passive connection of a vanadium redox flow battery and a supercapacitor: An experimental, modelling, economic and environmental impact assessment study" [3], Section 3.1.1, a HESS composed of a passive parallel configuration between a VRFC and a SC was introduced and analysed. The passive connection did not employ any power converter to interface the two subsystems. This design was evaluated in terms of performance, economic feasibility, and environmental implications, identifying several advantages across all three areas. Specifically, we tested the hybrid configuration under various conditions, demonstrating that it delivered 8–10 times more energy during 5-second high-current pulses (e.g., at 10 A) compared with the standalone VRFC. We also developed a simplified model, based on cell data derived from datasheets, to predict system behaviour and support a preliminary sizing of the SC capacitance, demonstrating that the deliverable energy increases with capacitance up to a limit, thereby indicating that the system can be designed without the necessity of using the highest capacitance values. In the LCA and economic evaluation, we analysed both passive and active configurations across different SC stack sizes. Moreover, we discussed the implementation of a water-based electrolyte for the SC. From an environmental perspective, the GWP of the passive setup was up to 16% lower than that of a converter-based configuration for large-scale scenarios; the vanadium electrolyte significantly affects the sustainability factor; therefore, replacing it with a more sustainable alternative represents an effective approach to enhancing the overall sustainability of the system. Economically, employing aqueous SCs in a passive arrangement achieved the lowest total CAPEX among all evaluated designs.

Section 3.1.2 presents an updated model of the passive system, representing an initial step towards a more accurate framework. Our objective was to integrate empirical cell data into the model, taking into account the influence of current load and SOC on system parameters. The results indicated that the capacitance effectively reduced the current and voltage peaks affecting the VRFC. Indeed, the capacitance appears to function as a filter, reducing the current fluctuations across the VRFC cell. This model enabled the evaluation of different configurations, such as the parallel connection between a series of two VRFCs and one SC,

which demonstrated the most significant reduction in fluctuations without increasing the capacitance.

Nevertheless, the VRFC–SC system and its model require further development, particularly in three key areas: i) conducting extended discharge tests with different configurations while also assessing cycling stability, actual efficiency and dynamic performance; ii) improving the accuracy of the VRFC and SC models under dynamic conditions by incorporating one or two R-C blocks with appropriate characterisation, as discussed in Section 2.5; iii) validating the model through an experimental campaign designed to assess its actual capability to predict system behaviour, particularly under dynamic load conditions.

3.2 Beyond Flow Systems: Charging supercapacitors by nanofibrous and ceramic piezoelectric harvesters: experimental and modelling analysis

This Section corresponds to a paper which is under submission and is co-authored by :

Monica Giovannucci[a], Elisabetta Petri[a], Michele Zanoni[a], Leonardo Gasperini[b], Giacomo Selleri[b], Davide Fabiani[b], Chiara Gualandi [a], Francesca Soavi[a,c]

a Department of Chemistry "Giacomo Ciamician", Alma Mater Studiorum University of Bologna, via P. Gobetti 85, 40129 Bologna, Italy

b Department of Electrical, Electronic, and Information Engineering "Guglielmo Marconi", University of Bologna, Viale Risorgimento 2, 40136 Bologna, Italy

c Center for the Environment, Energy, and Sea - Interdepartmental Centre for Industrial Research in Renewable Resources, Environment, Sea and Energy (CIRI-FRAME), Alma Mater Studiorum University of Bologna Viale Ciro Menotti, 48 - 48122 Marina di Ravenna (RA), Italy

Supplementary Information is in the Appendix.

3.2.1.1 Introduction

Piezoelectric materials can convert energy from body movements (such as walking or breathing), mechanical vibrations, or structural stress (e.g., in bridges and highways) into electrical energy. This is possible because mechanical strain deforms the crystal lattice of the piezoelectric material, generating an electric voltage. The exploitation of the piezoelectric effect is particularly suitable for harvesting ambient energy in environments where conventional power sources are unavailable. Relevant applications include remote sensors and implantable biomedical devices [61].

Among piezoelectric materials, ceramics such as lead zirconate titanate (PZT) and barium titanate (BT) exhibit outstanding piezoelectric responses, which make them highly suitable for energy harvesting applications. However, their intrinsic brittleness significantly limits their integration into flexible devices. Therefore, polymer-based piezoelectric materials are increasingly employed as viable alternatives. Materials such as poly(vinylidene fluoride)

(PVDF) and its copolymer with trifluoroethylene, P(VDF-TrFE), can be easily processed into different morphologies, making them suitable for a wide range of applications, from flexible electronics and wearable devices [62, 63, 64, 65] to the monitoring of structural health of composite materials or civil engineering structures [66, 67, 68, 69]. A well-established fabrication technique of polymeric or composite films is the electrospinning technique, which produces nanofibrous structures. Due to their high porosity, such nanofibers can be embedded into host matrices to create composites with piezoelectric functionality and good mechanical properties [70, 71, 72]. However, the intrinsic piezoelectric response of as-spun nanofibers remains relatively low, highlighting the necessity of a polarization process to align the dipoles of the piezoelectric material within the material crystalline lattice. The highly porous nature of nanofibrous layers and the presence of air voids within the membranes complicate the application of strong electric fields, which are required to enhance macroscopic piezoelectric behaviour. To address this challenge, several poling strategies have been explored, including corona triode poling [73] and direct-current (DC) contact poling within high–dielectric-strength media (e.g., silicone rubber, ester oil). A DC poling technique was proposed, in which a controlled-thickness cell and an ester oil bath were employed to prevent nanofibers collapse during polarization [74]. This approach minimizes the risk of dielectric breakdown, thereby allowing the achievement of high piezoelectric strain coefficients (d_{33}).

Piezoelectric nanogenerators (PENGs) typically produce low-voltage, intermittent power. Therefore, it is essential to couple PENGs with tailored energy storage systems. Thanks to their rapid response and long cycle life, supercapacitors (SCs) are well suited for integration with PENGs, which require a storage device capable of withstanding fast dynamic operating conditions. Supercapacitors, in fact, are a type of electrochemical energy storage in which the mechanism relies on charge separation driven by electrostatic processes. The absence of redox reactions, which are present in batteries, enables supercapacitors to charge and discharge rapidly, achieve higher power densities, and sustain a cycle life of up to millions of cycles. [7] The external connection of PENG and SC units represents a straightforward solution to store energy from motion [75, 76]. In PENG-SC systems it is extremely important that the SC size is set in relation to the PENG generated current. Indeed, large SC charge by PENG might not be effective if SC leakage currents, which in turn affect SC self-discharge, are of the same order of magnitude of PENG generated currents. A strategy to limit leakage currents is the use of SC

featuring stable electrolytes, like ionic liquids (ILs) like N-butyl-N-methylpyrrolidinium bis(trifluoromethanesulfonyl)imide, PYR14TFSI, and 1-Methyl-1-(2-methoxyethyl)pyrrolidinium bis(trifluoromethanesulfonyl)imide, PYR12O1TFSI. [77].

In order to achieve higher system voltages, the two systems (PENG–SC) must be coupled with suitable circuits. For example, the use of bridge rectifiers can transform the both negative and positive current peaks of the piezoelectric output into a full positive response, thereby improving the system's energy conversion efficiency. In our previous work we coupled a piezoelectric energy harvester with a micro-supercapacitor using a full-wave bridge rectifier that converted the transducer's AC output into DC for charging. A parallel array of 15 commercial PZT disks generated sufficient current to charge the ionic-liquid based SC to 3.1 V within 2 h under compressive stimulation (85 N, 2 Hz). The device exhibited stable charge/discharge cycling without structural degradation. Overall, the integrated system stored up to 110 mJ in 2 h, outperforming self-powered supercapacitors (SPSCs) devices with micro-SCs and achieving shorter charge times than commercial SCs [76].

Overall, our previous work highlighted that the design of an efficient PENG–SC calls for a modelling tool that can predict the energy storage behaviour of the SC powered by the PENG. Detailed simulations can predict the duration of the charging phase and the maximum voltage achieved by the charged SC. However, although the literature offers numerous approaches to battery and supercapacitor modelling, only a limited number of papers addresses the modelling of piezoelectric devices as generators. An example of piezoelectric device modelling is reported in [78], although in that case it is not used as a generator. Modelling is generally classified into three categories: i) white-box models (e.g., electrochemical models), ii) grey-box models (e.g., circuit-oriented models), and iii) black-box models (e.g., artificial neural networks). White-box models provide the most physically descriptive representation, whereas black-box models adopt the most empirical approach. Equivalent Circuit Models (ECMs), which fall within the grey-box category, integrate physical principles with empirical data and are widely considered among the most suitable methods for modelling energy storage systems (ESSs) [79].

This study has two principal aims: the first is to demonstrate that an electrospun nanofibrous (NF) PENG represents a viable alternative to PZT nanogenerators, particularly when

integrated with a micro-SC. We compare the energy harvesting/storage performance of NF–SC and PZT-SC. In both systems we adopted micro-SCs that featured IL-electrolytes and carbon electrodes produced by using a green binder like pullulan [80, 81].

The second objective of the present work is to develop a model of the PENG-SC integrated system capable of predicting the charging phase. We propose an ECM that integrates a circuit representation for the piezoelectric generator with one for the supercapacitor. The proposed model aims to facilitate the prediction of the supercapacitor's charging behaviour and to determine the charging time according to a specific application. The intention is to construct this model using characteristics properties values of the piezoelectric device and the SCs, such as resistance and capacitance, which can be determined experimentally or derived from a datasheet. The model is validated by comparing simulated data with experimental measurements from our previous work [76] and the new NF-SC integrated system. Once validated, the integrated system model can be a designing tool that can be employed to predict the performance of analogous systems with different parameter values (e.g., resistance, capacitance, etc.) and/or to simulate an assembly enclosing multiple PENG blocks.

3.2.1.2 Materials and methods

This Section reports the fabrication of piezoelectric devices (Section 3.2.1.2.1) and supercapacitors (Section 3.2.1.2.2), outlines the experimental setup (Section 3.2.1.2.3), and describes the modelling approach (Section 3.2.1.2.4).

3.2.1.2.1 Fabrication of piezoelectric device

P(VDF-TrFE) copolymer with molar composition (VDF:TrFE) 75:25 mol% (Solvene® 250), was kindly provided by Solvay Specialty Polymers. Dimethylformamide (DMF, Sigma-Aldrich, ACS reagent, ≥99.8 %) and acetone (Ac, Sigma-Aldrich, ACS reagent, ≥99.5 %) were used without any further purification. The dielectric ester oil FR3 was supplied by CARGIL and was used after drying in a vacuum oven at 110 °C for 3 h). The piezoelectric transducer employed in the energy harvesting unit consists of a ceramic PZT disk (7BB-20-3 Murata) with a thickness of 100 μm, a diameter of 14 mm and a d33 coefficient equal to 200 pC N^{-1}. One surface of the disk is coated with a silver electrode (12.5 mm in diameter), while the opposite

side is bonded to a brass layer with a thickness of 120 μm and an approximate diameter of 20 mm.

The methodology and treatments for obtaining the polarized P(VDF-TrFE) 75-25 nanofibers are the same as previously reported in [74]. P(VDF-TrFE) 75-25 copolymer was dissolved in a 60:40 v/v Ac:DMF solution at a concentration of 19 % w/v. The solution was stirred for 2 h at room temperature (RT) before being electrospun by using a home-made electrospinning apparatus composed of a SL 50 P10/CE/230 high-voltage power supplier (Spellman, New York, USA), a KDS-200 syringe pump (KDScientific Inc., Massachusetts, USA), a glass syringe containing the polymer solution, a stainless-steel needle (with an inner diameter of 0.5 mm) connected with the power supply electrode set at 22 kV, and a grounded plate collector positioned at a distance of 25 cm from the needle. The polymer solution was dispensed at the rate of 1.08 mL h^{-1}.

Following established procedures, the as spun samples were annealed by placing them in a pre-heated oven for 24 h at 115°C, which is the Curie Temperature of P(VDF-TrFE) 75-25. Afterwards, the annealed samples were placed in the poling cell and soaked in an ester oil bath (FR3 natural ester, Cargil). In a typical procedure, a sample (diameter of 10 cm) was placed between a high-voltage electrode (diameter of 8 cm) and a grounded electrode, separated by a gap of 0.18 mm all soaked in the oil. The poling procedure consisted of heating from room temperature (RT) to 115°C, maintaining this temperature for 30 min, and subsequently cooling back to RT. Following the initial heating ramp, an electric field of 30 kV mm^{-1} was gradually applied using a Fug HCN 35 generator and maintained for 30 min. Once cooling was completed, the electric field was switched off. Following this, the mat was washed in cyclohexane to fully remove the oil. After drying, the portions of the sample extending beyond the electrode-used to prevent electrical breakdown-were carefully trimmed. Finally, both sides of the nanofibrous mats were grounded for 24 hours at room temperature to eliminate any residual electrostatic charges that may have accumulated during electrospinning and poling processes.

Scanning Electron Microscopy (SEM) observations were carried out using a Leica Cambridge Stereoscan 360 at an accelerating voltage of 20 kV. Morphological observations were performed on samples sputtered with gold. The distribution of fiber diameters was

determined through the measurement of about 200 fibers and the results were reported as the average diameter (d) ± standard deviation (SD).

The piezoelectric effect was evaluated by measuring the piezoelectric d_{33} coefficient (pC N^{-1}), using a high-precision piezometer (PiezoMeter System PM300, Piezotest, Singapore). Each sample was placed between two electrodes held together by a screw clamp and the d_{33} was measured by stressing the specimen with a compressive sinusoidal force of 0.25 N at a frequency of 110 Hz with a grip force of 10 N. Each of the 30 P(VDF-TrFE) mats stacked in the device was measured three times on both sides: the one in contact with the live electrode and the one in contact with the grounded electrode. The d_{33} values were reported along with the corresponding standard deviation. The collected data is presented in Table S15 (Supplementary Information Section).

The energy harvesting unit was assembled by stacking 30 nanofibrous layers of P(VDF-TrFE). Between each layer, an aluminium foil was inserted as electrodes to electrically connect them in parallel. To minimize the number of electrodes, the piezoelectric layers were disposed with alternate polarity, as will be shown in Figure 3.2.1.2.3.2. Similarly, the piezoceramic energy harvesting unit consisted of 15 PZT disks, assembles as previously reported [76].

3.2.1.2.2 Supercapacitors assembly

Two similar supercapacitors were considered in this work, one for each piezoelectric generator. They were assembled and tested like reported in [76]. The supercapacitor SC1, assembled for the PZT generator, comprised two symmetric electrodes with a surface area of 0.6 cm^2, fabricated using a mixture of 70 wt% activated carbon YP-80F, 20 wt% Pullulan-Glycerol binder, and 10 wt% SuperC45 carbon coated on aluminium foil. The electrolyte employed was N-butyl-N-methylpyrrolidinium bis(trifluoromethanesulfonyl)imide ($PYR_{14}TFSI$, purity >99.9%, Solvionic), while the separator was a Whatman GF fibreglass membrane. SC2, assembled for the NF generator, differs from SC1 in two main aspects: it uses a different electrolyte, namely 1-Methyl-1-(2-methoxyethyl)pyrrolidinium bis(trifluoromethanesulfonyl)imide ($PYR_{12O1}TFSI$, purity >99%, Merck), in order to reduce the ESR of the device; and it employs positive and negative electrodes with different surface areas

(1.25 cm^2 and 0.5 cm^2, respectively) due to the higher charge storage capability of the negative electrode. The ESR and capacitance of each SC were determined by performing galvanostatic tests, and all these characteristics are summarised in Table 3.2.1.2.2.1.

Table 3.2.1.2.2.1 reports the characteristics of the SCs for each system. Integrated from [76].

		SC1	**SC2**
Paired with	-	**PZT**	**NF**
Electrodes	-	70%wt activated carbon YP-80F, 20%wt Pullulan-Glycerol binder, and 10%wt SuperC45 carbon on aluminum	
Electrolyte	-	PYR14TFSI	PYR12O1TFSI
Separator	-	Whatman GF fiber glass separator	
Surface area	cm^2	0.6	1.25 (+) – 0.5 (-)
ESR	Ω	141 (@ 100 μA)	118 (@ 1 mA)
Capacitance	mF	22.4 (@ 100 μA)	47 (@ 1 mA)

3.2.1.2.3 Experimental Setup

The piezoelectric generator links to a bridge rectifier composed of four Small Signal Schottky Diodes (SD-103-A, Vishay) that directs the output from the generator to the supercapacitor during the charging transforming the alternate current into a direct one. Figure 3.2.1.2.3.1 illustrates the configuration of the coupling circuit used to examine the charge processes of the supercapacitor in connection with the piezoelectric generator.

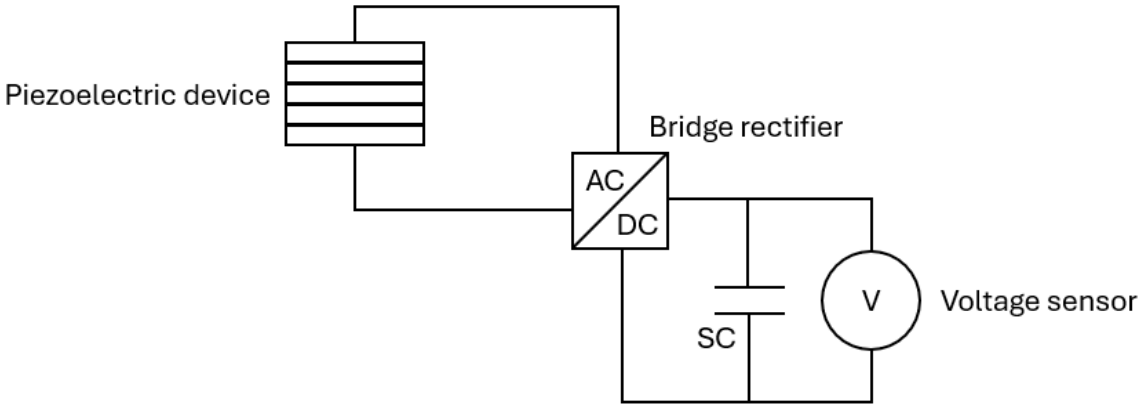

Figure 3.2.1.2.3.1 Piezoelectric generator-supercapacitor coupling system.

During the charging phase, a linear motor (shown in Figure 3.2.1.2.3.2) applies a sinusoidal mechanical compression to the piezoelectric device, with an amplitude of 85 N and a frequency that varies according to the specific characteristics of the tested piezoelectric device. For the PZT-based harvesting unit, a driving frequency of 2 Hz was selected for charging the supercapacitor, whereas the P(VDF-TrFE) unit required a frequency of 10 Hz. Although both frequencies are relevant to wearable device applications, the higher frequency was chosen for the polymer-based unit due to higher output performance reached in terms of both open-circuit voltage and short-circuit current. These enhanced values proved to be more suitable for efficiently charging the manufactured supercapacitor.

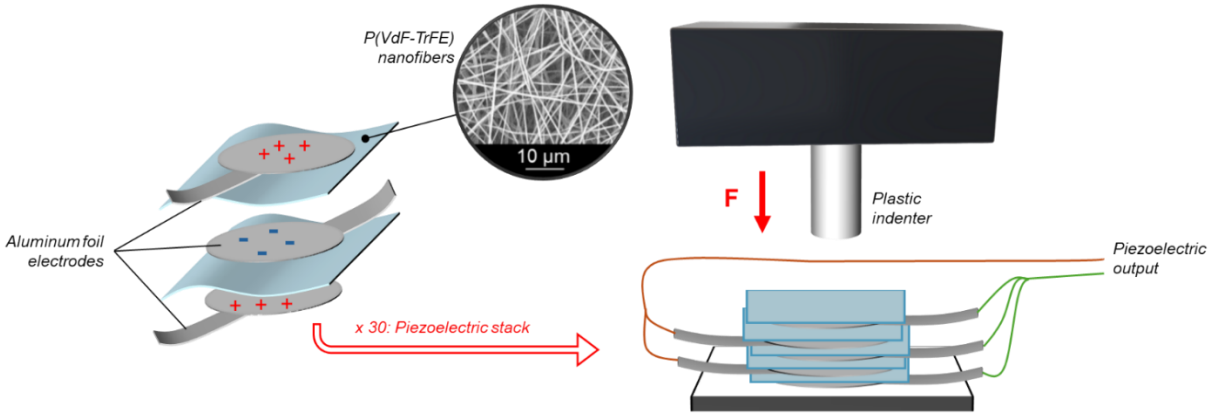

Figure 3.2.1.2.3.2 Energy harvesting unit and schematic representation of the disk arrangement and force application by the linear motor.

3.2.1.2.4 Piezoelectric generator Characterization for modelling and modelling approach

According to the literature, and specifically reference [78], a piezoelectric device can be represented by a voltage source combined with a parallel R–C block, as illustrated in Figure 3.2.1.2.4.1a. We characterised both piezoelectric devices through standalone tests by applying a sinusoidal force of 85 N amplitude at distinct frequencies while simultaneously measuring the open-circuit voltage and the short-circuit current of each device. By applying a sinusoidal force to each generator, the resulting output voltage exhibits a quasi-sinusoidal profile, arising from the continuous compression and release of the applied load, and shows no detectable phase shift relative to the input force. In contrast, the short-circuit piezoelectric current displays a derivative-like behaviour with respect to the applied force, characterized by null plateau regions at the maxima and minima of the applied force F. This relationship can be expressed as:

$$I_p = d_{33}\frac{dF}{dt}$$ 3.2.1.2.4.1

Therefore, to evaluate the effective values of the curve profiles, the root mean square (rms) values are considered, and this value is calculated by applying Equations 3.2.1.2.4.2 and 3.2.1.2.4.3. By knowing the RMS value, it is possible to determine the amplitude of the equivalent sinusoidal curve V_{sin} (Equation 3.2.1.2.4.4).

$$V_{rms} = rms\left[V_{piezo,OCV}(t)\right]$$ 3.2.1.2.4.2

$$i_{rms} = rms\left[i_{piezo,sh}(t)\right]$$ 3.2.1.2.4.3

$$V_{sin} = \sqrt{2}\ V_{rms}$$ 3.2.1.2.4.4

Using the evaluated RMS value, the voltage source can be approximated with a sinusoidal waveform of amplitude V_{sin} and same frequency of the pulsating force according to the Equation: $V_{PZ}(t) = V_{sin}\ sin(8\pi ft)$, where f denotes the operating frequency.

By using the RMS values, it is possible to estimate the impedance Z_{PZ} of the piezoelectric generator according to the Equation $Z_{PZ}=V_{rms}/i_{rms}$ in order to evaluate the resistance and the capacitance of the device. The resistance R_{PZ} corresponds to the device's internal leakage resistance, whereas C_{PZ} represents the piezoelectric capacitance. The capacitance of the single PZT disk was specified in the manufacturer's datasheet, whereas the NF value was extrapolated from the measured capacitance of a 30-disk stack. By knowing C_{PZ} and Z_{PZ}, the resistance R_{PZ} of the PZT device was extrapolated using Equation 3.2.1.2.4.5 expressing the impedance Equation for a parallel R-C circuit. For both PZT and NF devices, the model follows the scheme illustrated in Figure 3.2.1.2.4.1a, using the estimated values of R_{PZ} and C_{PZ} and the $V_{PZ}(t)$ function.

$$|Z_{PZ}| = \frac{R_{PZ}}{\sqrt{1+(\omega R_{PZ} C_{PZ})^2}}$$ 3.2.1.2.4.5

As an initial step, the modelling of the supercapacitors comprised a series connection of a capacitance and a resistance. However, in this system, the currents supplied by the generator are very low, in the range of μA. Therefore, it is considered good practice to include an additional resistor (equivalent parallel resistance, EPR) in the SC model to simulate self-discharge, which mainly originates from device leakage currents of comparable magnitude [82]. The leakage resistances of SC1 and SC2 were extrapolated as be 408 kΩ and 160 kΩ,

respectively assuming 245 kΩ cm² and 80 kΩ cm² [77]. Consequently, the SC is modelled as a parallel connection of a capacitance (C) and a resistance (EPR_{SC}) in series with a resistor (ESR_{SC}), as shown in Figure 3.2.1.2.4.1b.

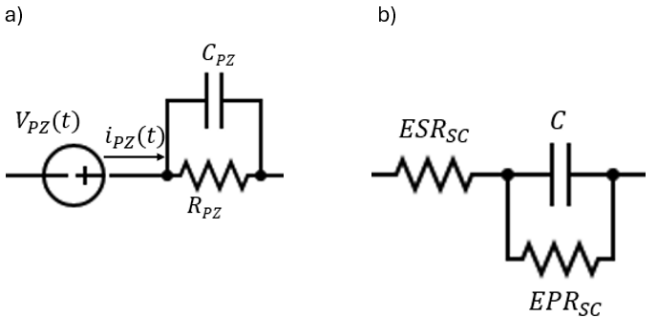

Figure 3.2.1.2.4.1 Proposed model for a) the piezoelectric generator and b) the supercapacitor.

As stated at the beginning of this Section, the objective of the model is to simulate the charging behaviour of the SC and compare it with the data obtained from the charging tests. We implemented both the piezoelectric generator model and the SC model in a Simscape environment, employing the components available in the Foundation Library of Simscape (Electrical Elements). As illustrated in Figure 3.2.1.2.4.2, to replicate the charging layout of the experimental test, we inserted a single-phase rectifier (orange dashed box) downstream of the piezoelectric generator (blue dashed box). The rectifier links the generator to the SC (green dashed box), ensuring that the SC is traversed by a unidirectional current. We extrapolated the forward voltage of the diodes from the Vishay datasheet, considering a temperature of 25°C and a current of 100 μA, and estimated its value to be 0.2 V for the PZT-SC1 system; for the NF-SC2 system currents are lower and the value is set at 0.05 V.

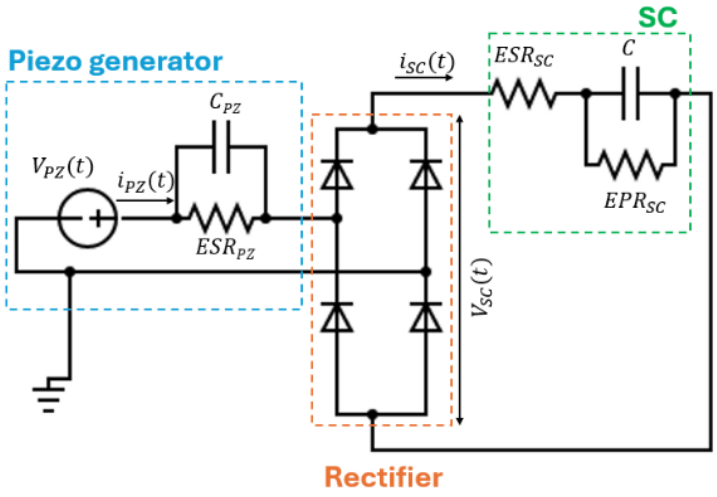

Figure 3.2.1.2.4.2 Schematic of the full modeled circuit.

3.2.1.3 Results

This Section presents the results of charging the supercapacitor through the NF generator and compares them with the findings reported in the previous study [76] (Section 3.2.1.3.1). It also outlines the modelling outcomes for both the NF and PZT energy-harvesting systems (Section 3.2.1.3.2).

3.2.1.3.1 NF devices results

Nanofibrous mats composed of randomly oriented fibers were prepared from polymeric solutions of a P(VDF-TrFE) 75-25 copolymer. The polymer was electrospun to produce as-spun (AS) mats, followed by thermal annealing to obtain annealed (AN) mats. Subsequently, poling was applied to the annealed samples to create annealed-and-poled (AN-P) mats. As described in the experimental Section, both the annealing and poling temperatures were selected based on the Curie temperature (T_C), the ferroelectric-to-paraelectric phase transition, as reported in our previous article [74]. The scanning electron microscopy (SEM) was used to assess the effects of the annealing and poling treatments. SEM images in Figure 3.2.1.3.1.1a and 3.2.1.3.1.1b reveal no significant morphological differences between the AS and AN samples, which exhibit average fiber diameters of 334±100 nm and 325±120 nm, respectively. These results confirm that the thermal annealing treatment did not affect the overall fiber morphology. Following the poling treatment, a slight densification of the fibrous layers was observed, however, the individual fibers remained morphologically similar to those in the annealed sample. Indeed, Figure 3.2.1.3.1.1c and 3.2.1.3.1.1d, which show images of the poled sample's live electrode side and grounded electrode side, respectively, exhibit average fiber diameters of 400±140 nm and 415±135 nm. Table S15 presents the d_{33} measurements for the components of the stack, which comprises 30 layers of PVDF-TrFE. From the Table, it is evident that the average d_{33} for the individual components is −29±2 pC N^{-1}. No significant difference in the d_{33} value was observed between the two sides of the individual components.

The application of the sinusoidal force to the NF stack interconnected with the micro-SC (as illustrated in Figure 3.2.1.2.3.1 and 3.2.1.2.3.2) enabled the accumulation of energy within the storage devices. The black line in Figure 3.2.1.3.2.1b illustrates the voltage profile of the SC during the charging process. Storing an energy of about 211 mJ, the voltage reached a value of

3 V in approximately 20 000 s, which is a similar results if compared with the results obtained in the PZT-SC1 system : indeed, in that case, the voltage of the system reached 3 V in about 7200 s with an extrapolated energy of 110 mJ, as shown by the black line in Figure 3.2.1.3.2.1 a. These results indicate that the NF can charge the SC to a high voltage, although it operates with a lower average power output (around 15 μW for the PZT system and about 11 μW for the NF one).

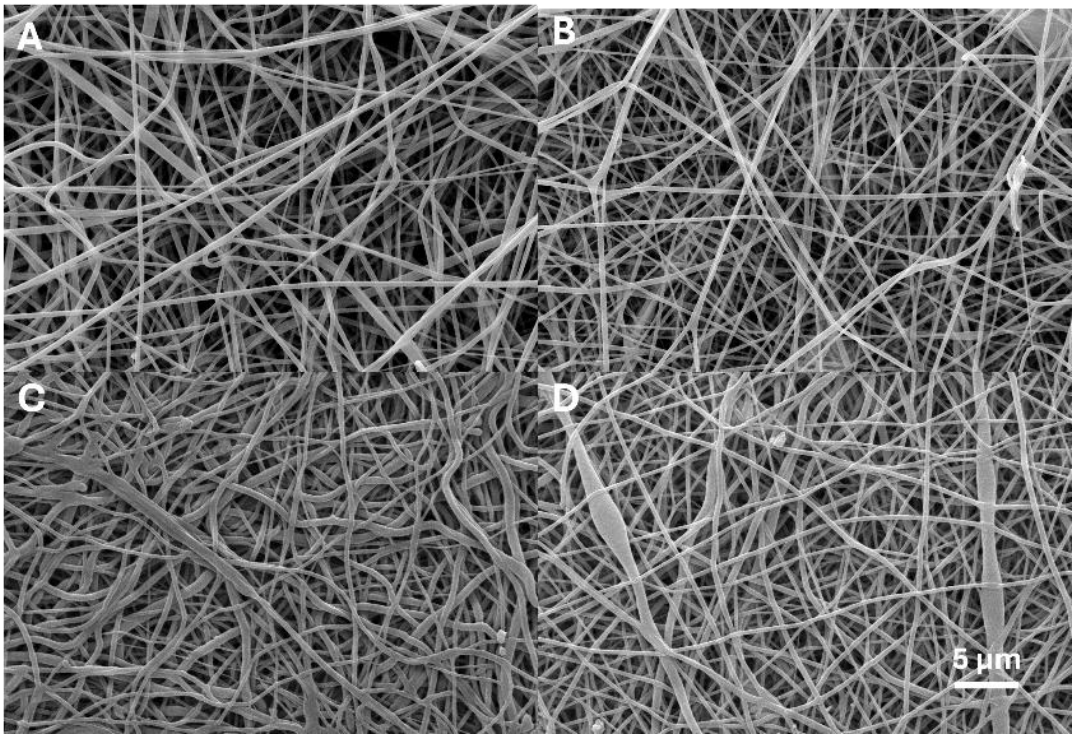

Figure 3.2.1.3.1.1 presents SEM images of the P(VDF-TrFE) 75-25 nanofibrous samples: (A) as-spun sample, (B) sample after annealing, (C) sample after poling (live electrode side), and (D) sample after poling (grounded electrode side).

3.2.1.3.2 Modelling results

To determine all the parameters required for the simulation, the characterisation process followed the procedure described in Section 3.2.1.2. Figure 3.2.1.3.2.1 presents four graphs illustrating the open-circuit voltage (a and c) and the short-circuit current (b and d) for the PZT and NF devices, respectively. As expected, in both cases the voltage operates at frequencies of 2 Hz and 10 Hz, respectively; however, the waveform does not fully correspond to a sinusoidal profile. Conversely, the short-circuit current displays a markedly different waveform, characterised by multiple peaks and a substantial deviation from a sinusoidal function. Table

3.2.1.3.2.1 summarises all the extrapolated data obtained from Equations 3.2.1.2.4.2-3.2.1.2.4.5, together with the measured data for both devices. For the PZT device, the datasheet specifies a capacitance of 21.1 nF for a single disk. As the disks are connected in parallel, the total device capacitance was calculated by multiplying the capacitance of one disk by the number of disks, yielding 316.5 nF. The PZT resistance, derived from Equation 3.2.1.2.4.5, is 214 163 Ω. This value is consistent with the typical resistivity of PZT (3.6×10^{12} Ω·cm) reported in the literature [83]. For the NF device, the resistance was measured directly by volt-amperometric procedure, giving $R_{PZ} = 4.38 \times 10^{8}\ \Omega$, which is several orders of magnitude higher than that of the PZT device. Notably, due to its high deformability, the NF device exhibits variability in the measured parameters depending on its compression state. For example, the capacitance averages 1.6 nF, based on values of 1.77 nF in the compressed state and 1.48 nF in the uncompressed state.

Table 3.2.1.3.2.1 Maximum values and rms values of the open circuit voltage and the short circuit current of the piezoelectric devices. The equivalent sinusoidal amplitude V_{sin} is reported. Some data are adapted from [76]

		PZT (15 disks)	**NF (30 disks)**
$V_{OCV,\,MAX}$	V	6.9	15.1
$V_{OCV,rms}$	V	5.7	11.7
V_{sin}	V	8.1	16.6
$i_{sh,MAX}$	μA	117	3
$i_{sh,\,rms}$	μA	35	1.8
Z_{PZ}	Ω	162 857	9 463 109*
C_{PZ}	nF	316.5	1.6
R_{PZ}	Ω	214 163	4.38 e8 Ω

*Value measured during compression

For the supercapacitor modelling, the parameters reported in Table 3.2.1.2.2.1 were used. The simulation time was set to 7200 s for the PZT–SC1 system and 19 692 s for the NF–SC2 system, matching the durations of the corresponding experimental tests. The maximum simulation step size was fixed at 1×10^{-2}.

By setting the input data as previously described, we obtained the following results. Figure 3.2.1.3.2.2 illustrates the SC voltage profile during charging (V_{SC}) for both systems. The black line represents the experimental curve, whereas the blue line represents the simulated one. For the PZT-SC1 system (Figure 3.2.1.3.2.2a), the voltage during the test reached 3.2 V, while the simulated value was about 3.5 V establishing a relative error of 9,4%. Regarding the energy comparison, Figure 3.2.1.3.2.2c displays the energy transferred to the SC, comparing the

experimental data with the model output. The experimental value is approximately 76.8 μWh (276 mJ), whereas the simulated value is 71.5 μWh (257 mJ), corresponding to a relative error of around 7%.

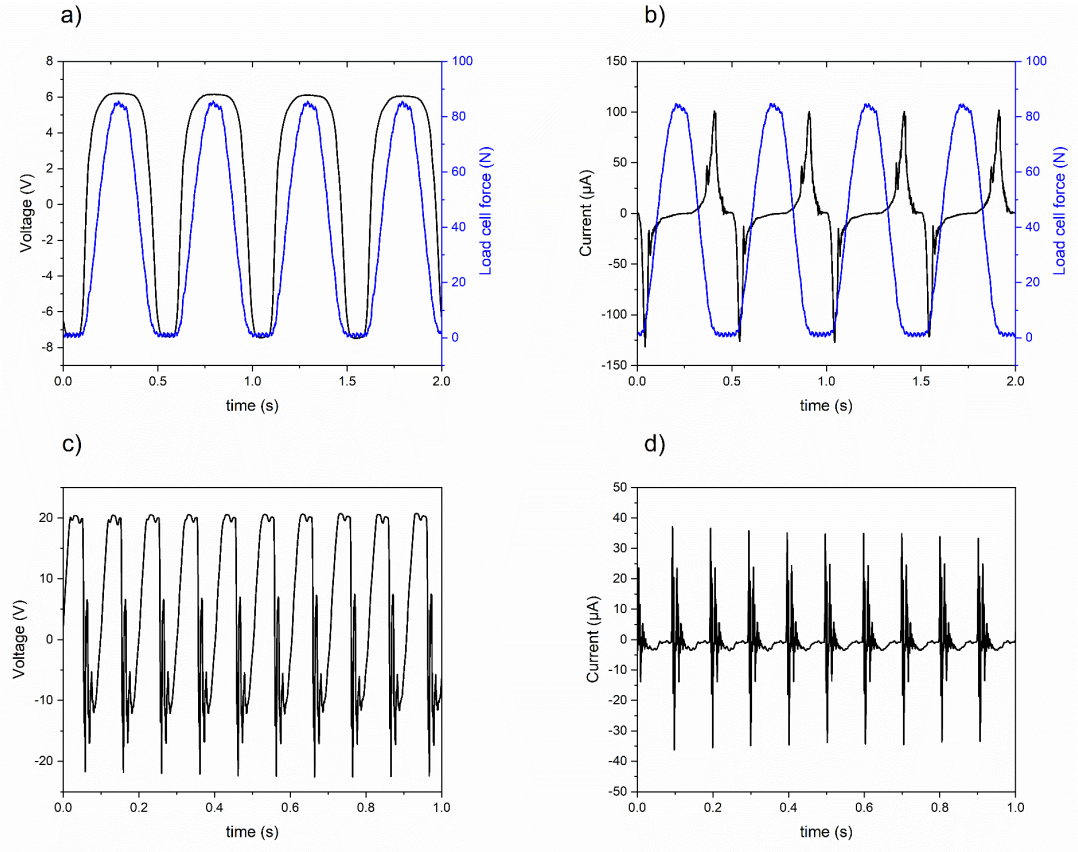

Figure 3.2.1.3.2.1 Open-circuit piezoelectric output voltage and short-circuit piezoelectric output current of the 15-PZT disks (a-b adopted from [76]) and the NF (c-d)

Just as a note, the transferred energy refers to the value immediately after the bridge rectifier, which may differ from the energy stored by the SC due to system losses; indeed, the stored energy of the SC can be estimated using the formula $E = 0.5\ C\ V^2$, which, for SC1, corresponds to 110 mJ, whereas the transferred energy is approximately 276 mJ. For the NF-SC2 system (Figure 3.2.1.3.2.2b), it is evident that the piezoelectric device successfully charged the SC up to 3 V in less than six hours. In this case, unfortunately the model could not replicate the charging behaviour as it is noticeable that the simulated voltage profile in Figure 3.2.1.3.2.2b is really low. Several investigations were conducted, and it is likely that the NF device cannot be characterised in the same manner as the PZT device due to the significant variability in its characteristics depending on the compression state: in detail the ESR of the NF device varies from 4.38 e8 Ω if compressed to 7.00 e9 Ω when uncompressed consisting in one order of

magnitude of difference In addition, the impedance of the NF generator is several orders of magnitude higher than that of the PZT, which may require a different modelling approach for the generator circuit. Furthermore, the error obtained with the PZT-SC1 model could be further diminished by experimentally characterising the EPR resistance of the SC device, since the results are considerably sensitive to this parameter, as we observed this sensitivity without performing an explicit sensitivity analysis.

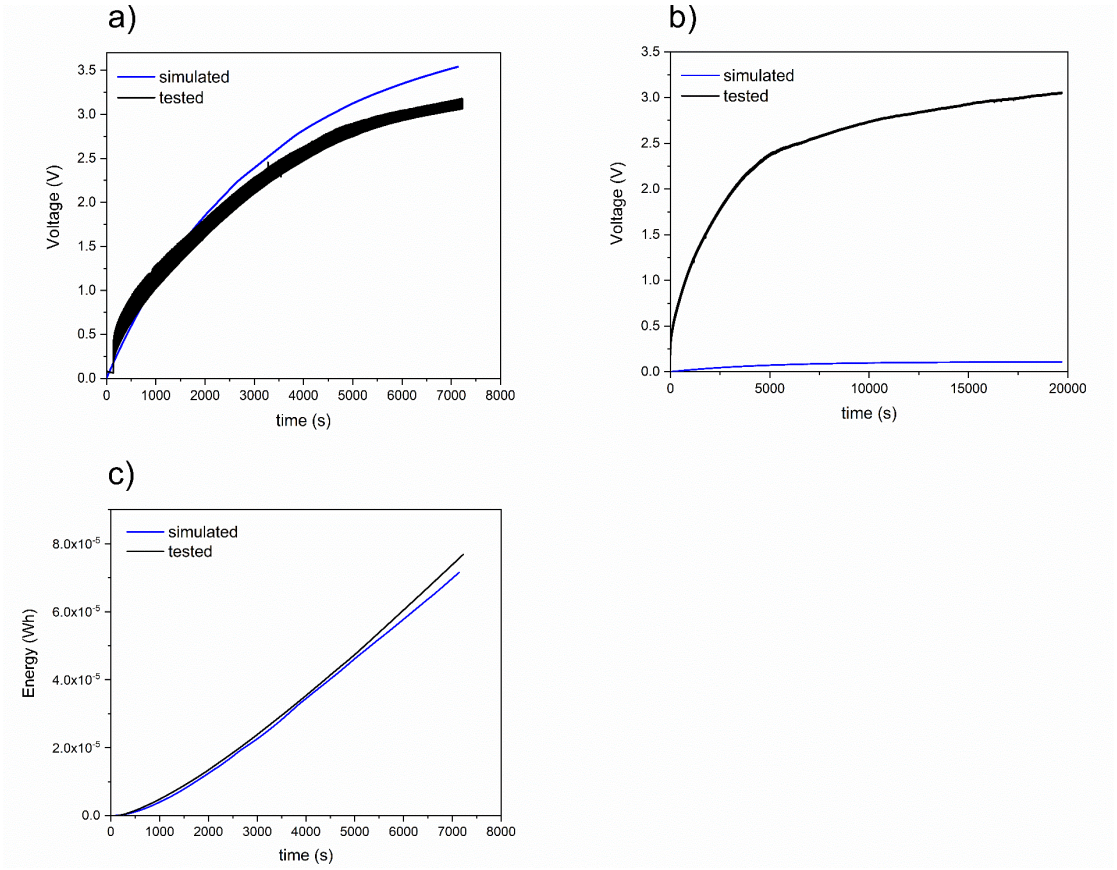

Figure 3.2.1.3.2.2 Comparison between experimental and simulated results for the supercapacitor charging tests. Voltage profiles (V_{SC}) of the a) PZT-SC1 and b) NF-SC2 system. c) Energy transferred to the SC for the PZT-SC1 system.

A stored energy of 110 mJ with a charging time of approximately two hours might appear too long for applied usage. A practical example concerns the delivery of data packages with a Bluetooth Low Energy beacon device [84], which requires about 0.1 mJ (considering a current of 7,1 mA, a voltage of 3 V and 5 ms as duration of the signal) to transmit a small data package. The PZT-SC system, charging the supercapacitor to 110 mJ in two hours (estimated power 15

μW), could enable the delivery of about 1000 signals every around 6 seconds. However, the here proposed model can be used to adapt and size the system even for other applications that demand different power consumption and operation frequencies.

3.2.1.4 Conclusions

This study presents the innovative design, fabrication, and modelling of a high-efficiency energy harvesting unit powered by piezoelectric polymer nanofibers. Exceptional energy conversion capabilities are achieved through an optimized poling protocol and a strategic multilayer configuration of the nanofibrous architecture. In particular, the NF generator consisted of 30 P(VDF-TrFE) nanofibrous layers with a piezoelectric strain coefficient d_{33} equal to −29±2 pC N^{-1}, which generated a maximum open circuit voltage V_{OCV} of 15.1 V and a maximum short circuit current i_{sh} of 3 μA. These results obtained with the NF generator constitute a significant step forward in advancing energy harvesting through flexible and wearable devices.

In addition, this study proposed a new approach to model the charging process of the innovative energy harvesting system comprising a supercapacitor charged by a piezoelectric device. Two types of devices, a PZT and the before mentioned NF generator, were implemented for this purpose. Both devices were initially characterised, then tested and modelled. The proposed model predicts the charging curve profile of the supercapacitor accurately when connected to the PZT device with a relative error of 9,4% and 7% respectively over the voltage profile and the transmitted energy when compared to the experimental data. However, it was not possible to forecast the behaviour of the NF generator. This device presented several challenges during the characterisation phase due to the high sensitivity of its properties to the compression state of the highly porous nanofibrous stack. Moreover, the resistance of the NF generator is significantly higher than that of the PZT, which may require a modified modelling approach to incorporate this factor. Nevertheless, the model proves to be a tool to support the optimization of PENG-SC architecture anticipating the effect of modular upscaling. This feature is particularly relevant for electronic devices application where the harvested energy is sufficient to transmit light data packages. In the case of the PZT-SC system, the model can predict the SC charging by employing as inputs the characteristic

properties of the piezoelectric device and the SC, thereby simulating different PZT devices and SCs guiding parameter choices before the prototyping phase. The model can also be employed to investigate upscaling strategies for specific wearable electronic applications, where multiple PZT-SC units can be connected as modular building blocks.

Acknowledgments

This work was supported by

THOR - lighTweight self-cHarging piezO-supercapacitoR systems by nanotechnologies (PorTable Charges for Soldiers) - NATO Science for Peace and Security Programme, under grant agreement G5772

and

MOST - Sustainable Mobility Centre project, funded by the European Union Next-Generation EU (PIANO NAZIONALE DI RIPRESA E RESILIENZA (PNRR) and MISSIONE 4 COMPONENTE 2, INVESTIMENTO 1.4 e D.D. 1033 June 17, 2022, CN00000023).

Chapter 3 References

[1] Schubert, C., Fekih Hassen, W., Poisl, B., Seitz, S., Schubert, J., Oyarbide Usabiaga, E., Molina Gaudo, P., & Pettinger, K.-H. (2023). Hybrid energy storage systems based on redox-flow batteries: Recent developments, challenges, and future perspectives. Batteries, 9(4), 211. https://doi.org/10.3390/batteries9040211

[2] Pettinger, K. H. (2020). Project HyFlow: Development of a sustainable hybrid storage system based on high power vanadium redox flow battery and supercapacitor—Technology (EU Horizon 2020, Grant No. 963550). European Commission. https://hyflow-h2020.eu/

[3] Giovannucci, M., Petri, E., Brilloni, A., Heigl, E.-M., Zauner, A., Oyarbide, E., Charvát, J., & Soavi, F. (2025). Hybrid Energy Storage through the Passive Connection of a Vanadium Redox Flow Battery and a Supercapacitor: an Experimental, Modelling, Economic and Environmental Impact Assessment Study. Manuscript under review for publication in Journal of Power Sources

[4] Ye, R., Henkensmeier, D., Yoon, S. J., Huang, Z., Kim, D. K., Chang, Z., Kim, S., & Chen, R. (2018). Redox flow batteries for energy storage: A technology review. Journal of Electrochemical Energy Conversion and Storage, 15(1), 010801. https://doi.org/10.1115/1.4037248

[5] Sánchez-Díez, E., Ventosa, E., Guarnieri, M., Trovò, A., Flox, C., Marcilla, R., Soavi, F., Mazur, P., Aranzabe, E., & Ferret, R. (2021). Redox flow batteries: Status and perspective towards sustainable stationary energy storage. Journal of Power Sources, 481, 228804. https://doi.org/10.1016/j.jpowsour.2020.228804

[6] Lourenssen, K., Williams, J., Ahmadpour, F., Clemmer, R., & Tasnim, S. (2019). Vanadium redox flow batteries: A comprehensive review. Journal of Energy Storage, 25, 100844. https://doi.org/10.1016/j.est.2019.100844

[7] Schütter, C., Pohlmann, S., & Balducci, A. (2019). Industrial requirements of materials for electrical double layer capacitors: Impact on current and future applications. Advanced Energy Materials, 9, 1900334. https://doi.org/10.1002/aenm.201900334

[8] Béguin, F., Presser, V., Balducci, A., & Frackowiak, E. (2014). Carbons and electrolytes for advanced supercapacitors. Advanced Materials, 26, 2219–2251. https://doi.org/10.1002/adma.201304137

[9] Lannelongue, P., Bouchal, R., Mourad, E., Bodin, C., Olarte, M., Le Vot, S., Favier, F., & Fontaine, O. (2018). "Water-in-salt" for supercapacitors: A compromise between voltage, power density, energy density and stability. Journal of The Electrochemical Society, 165(3), A657–A663. https://doi.org/10.1149/2.0951803jes

[10] Amiri, M., & Bélanger, D. (2021). Physicochemical and electrochemical properties of water-in-salt electrolytes. ChemSusChem, 14, 2487–2500. https://doi.org/10.1002/cssc.202100550

[11] El Halimi, M. S., Poli, F., Mancuso, N., Olivieri, A., Mattioli, E. J., Calvaresi, M., Chafik, T., Zanelli, A., & Soavi, F. (2021). Circumneutral concentrated ammonium acetate solution as water-in-salt electrolyte. Electrochimica Acta, 389, 138653. https://doi.org/10.1016/j.electacta.2021.138653

[12] Gorji, S. A., Sahebi, H. G., Ektesabi, M., & Rad, A. B. (2019). Topologies and control schemes of bidirectional DC–DC power converters: An overview. IEEE Access, 7, 117997–118019. https://doi.org/10.1109/ACCESS.2019.2937239

[13] Etxeberria, A., Vechiu, I., Camblong, H., & Vinassa, J. M. (2010). Hybrid energy storage systems for renewable energy sources integration in microgrids: A review. Proceedings of IPEC 2010, 532–537. https://doi.org/10.1109/IPECON.2010.5697053

[14] Babu, T. S., Vasudevan, K. R., Ramachandaramurthy, V. K., Sani, S. B., Chemud, S., & Lajim, R. M. (2020). A comprehensive review of hybrid energy storage systems: Converter topologies, control strategies and future prospects. IEEE Access, 8, 148702–148721. https://doi.org/10.1109/ACCESS.2020.3015919

[15] Zheng, J. P., Jow, T. R., & Ding, M. S. (2001). Hybrid power sources for pulsed current applications. IEEE Transactions on Aerospace and Electronic Systems, 37, 288–292. https://doi.org/10.1109/7.913688

[16] Martellucci, L., Dell'Aria, M., & Capata, R. (2023). Experimental analysis and simulation of mixed storage with lithium-ion batteries and supercapacitors for a PHEV. Energies, 16, 3882. https://doi.org/10.3390/en16093882

[17] Palma, L., Enjeti, P., & Howze, J. W. (2003). An approach to improve battery run-time in mobile applications with supercapacitors. Proceedings of the IEEE PESC 2003, 918–923. https://doi.org/10.1109/PESC.2003.1218178

[18] Jørgensen, K. L., Mira, M. C., Zhang, Z., & Andersen, M. A. E. (2017). Review of high efficiency bidirectional DC–DC topologies with high voltage gain. Proceedings of the 52nd International Universities Power Engineering Conference (UPEC), 1–6. https://doi.org/10.1109/UPEC.2017.8231916

[19] Li, W., & Joós, G. (2008). A power electronic interface for a battery–supercapacitor hybrid energy storage system for wind applications. Proceedings of the IEEE Power Electronics Specialists Conference, 1762–1768. https://doi.org/10.1109/PESC.2008.4592198

[20] Jia, H., Fu, Y., Zhang, Y., & He, W. (2010). Design of hybrid energy storage control system for wind farms based on flow battery and electric double-layer capacitor. Proceedings of the

Asia-Pacific Power and Energy Engineering Conference (APPEEC), 1–6. https://doi.org/10.1109/APPEEC.2010.5448720

[21] European Parliament and Council. (2023). Regulation (EU) 2023/1542 concerning batteries and waste batteries. https://eur-lex.europa.eu/eli/reg/2023/1542/oj

[22] United Nations. (2024). 17 Sustainable Development Goals (SDG): 2030 Agenda for Sustainable Development. https://sdgs.un.org/goals

[23] United Nations. (2024). The Paris Agreement: International treaty on climate change. https://unfccc.int/process-and-meetings/the-paris-agreement

[24] Zhou, W., Zheng, Y., Pan, Z., & Lu, Q. (2021). Review on the battery model and SOC estimation method. Processes, 9(9), 1685. https://doi.org/10.3390/pr9091685

[25] Zhang, L., Hu, X., Wang, Z., Sun, F., & Dorrell, D. G. (2018). A review of supercapacitor modelling, estimation, and applications: A control/management perspective. Renewable and Sustainable Energy Reviews, 81, 1868–1878. https://doi.org/10.1016/j.rser.2017.05.283

[26] International Organization for Standardization. (2006a). ISO 14040:2006 – Environmental management: Life cycle assessment – Principles and framework. https://www.iso.org/obp/ui/

[27] International Organization for Standardization. (2006b). ISO 14044:2006 – Environmental management: Life cycle assessment – Requirements and guidelines. https://www.iso.org/obp/ui/

[28] Frischknecht, R. (2020). Lehrbuch der Ökobilanzierung. Springer Spektrum. https://doi.org/10.1007/978-3-662-54763-2

[29] Guinée, J. B., Gorrée, M., Heijungs, R., Huppes, G., Kleijn, R., de Koning, A., van Oers, L., Wegener Sleeswijk, A., Suh, S., Udo de Haes, H. A., de Bruijn, H., van Duin, R., & Huijbregts, M. (2002). Handbook on life cycle assessment: Operational guide to the ISO standards. Springer. https://doi.org/10.1007/0-306-48055-7

[30] Curran, M. A. (Ed.). (2012). Life cycle assessment handbook: A guide for environmentally sustainable products. Wiley. https://doi.org/10.1002/9781118528372

[31] Klöpffer, W., & Grahl, B. (2014). Life cycle assessment (LCA): A guide to best practice. Wiley-VCH. https://doi.org/10.1002/9783527655625

[32] Heigl, E.-M., Schäffer, M., Zeilerbauer, L., Zauner, A., Lindorfer, J., Ott, J., Fischer, P., Life cycle assessment of a novel hybrid energy storage system: Environmental hotspots and sustainability options based on experimental insights, Journal of Energy Storage, Volume 132, Part B, (2025), 117705, https://doi.org/10.1016/j.est.2025.117705

[33] Jiao, Y., & Månsson, D. (2023). Greenhouse gas emissions from hybrid energy storage systems in future 100% renewable power systems – A Swedish case based on consequential

life cycle assessment. Journal of Energy Storage, 57, 106167. https://doi.org/10.1016/j.est.2022.106167

[34] Sphera. (n.d.). LCA for Experts 10.7 software and professional database. https://sphera.com/software-fuer-die-lebenszyklus-beurteilung-lca

[35] Ecoinvent Association. (n.d.). Ecoinvent database: Sustainability assessment. https://ecoinvent.org/database/

[36] Blume, N., Becker, M., Turek, T., & Minke, C. (2022). Life cycle assessment of an industrial-scale vanadium flow battery. Journal of Industrial Ecology, 26, 1796–1808. https://doi.org/10.1111/jiec.13328

[37] Weber, S., Peters, J. F., Baumann, M., & Weil, M. (2018). Life cycle assessment of a vanadium redox flow battery. Environmental Science & Technology, 52, 10864–10873. https://doi.org/10.1021/acs.est.8b02073

[38] Huijbregts, M. A. J., Steinmann, Z. J. N., Elshout, P. M. F., & Stam, G. (2017). ReCiPe2016: A harmonised life cycle impact assessment method at midpoint and endpoint level. International Journal of Life Cycle Assessment, 22, 138–147. https://doi.org/10.1007/s11367-016-1246-y

[39] VDI. (n.d.). VDI 4600 – Kumulierter Energieaufwand: Begriffe, Definitionen, Berechnungsmethoden. https://www.vdi.de/

[40] Kupfer, T. (2021). GaBi Databases & Modelling Principles. Sphera. https://www.sphera.com

[41] Perry, R. H., Green, D. W., & Maloney, J. O. (Eds.). (1997). Perry's chemical engineers' handbook (7th ed.). McGraw-Hill.

[42] Peters, M. S., & Timmerhaus, K. D. (1991). Plant design and economics for chemical engineers (4th ed.). McGraw-Hill.

[43] Turton, R. (Ed.). (2018). Analysis, synthesis, and design of chemical processes (5th ed.). Prentice Hall.

[44] Weber, K. H. (2016). Engineering verfahrenstechnischer Anlagen: Praxishandbuch mit Checklisten und Beispielen (2nd ed.). Springer Vieweg. https://doi.org/10.1007/978-3-662-52897-6

[45] Zauner, A., et al. (2024). Deliverable D3.6 – Market potential analysis, HyFlow. https://cordis.europa.eu/project/id/963550/results

[46] da Silva Lima, L., Quartier, M., Buchmayr, A., Sanjuan-Delmás, D., Laget, H., Corbisier, D., Mertens, J., & Dewulf, J. (2021). Life cycle assessment of lithium-ion and vanadium redox flow batteries-based renewable energy storage systems. Sustainable Energy Technologies and Assessments, 46, 101286. https://doi.org/10.1016/j.seta.2021.101286

[47] Cossutta, M., Vretenar, V., Centeno, T. A., Kotrusz, P., McKechnie, J., & Pickering, S. J. (2020). A comparative life cycle assessment of graphene and activated carbon in a supercapacitor application. Journal of Cleaner Production, 242, 118468. https://doi.org/10.1016/j.jclepro.2019.118468

[48] Kamal Kamali, A., Glogic, E., Keppetipola, N. M., Sonnemann, G., Toupance, T., & Cojocaru, L. (2023). ACS Sustainable Chemistry & Engineering, 11(44), 15898–15909. https://doi.org/10.1021/acssuschemeng.3c04007

[49] Li, Y., Han, X., Nie, L., Deng, Y., Yan, J., Roumpedakis, T. C., Kourkoumpas, D.-S., & Karellas, S. (2024). Life cycle environmental hotspots analysis of typical electrochemical, mechanical and electrical energy storage technologies for different application scenarios: Case study in China. Journal of Cleaner Production, 466, 142862. https://doi.org/10.1016/j.jclepro.2024.142862

[50] Charvát, J., Pocedič, J., & Vrána, J. (2024, June 25–27). Detailed investigation of VFB stack with a focus on single cell. Paper presented at the International Flow Battery Forum, Glasgow, UK.

[51] BioLogic. (n.d.). Redox flow battery accessory. Retrieved from https://www.biologic.net/accessory/redox-flow-battery/

[52] Ceraolo, M., & Poli, D. (2014). Fundamentals of electric power engineering: From electromagnetics to power systems. John Wiley & Sons.

[53] Arena, N., Lee, J., & Clift, R. (2016). Life cycle assessment of activated carbon production from coconut shells. Journal of Cleaner Production, 125, 68–77. https://doi.org/10.1016/j.jclepro.2016.03.073

[54] PubChem. (n.d.). Ammonium acetate (compound). Retrieved from https://pubchem.ncbi.nlm.nih.gov/compound/Ammonium-acetate#Section=Household-Products

[55] Frischknecht, R., & Jungbluth, N. (Eds.). (2007). Ecoinvent report No. 1: Overview and methodology, Data v2.0. Swiss Centre for Life Cycle Inventories. https://inis.iaea.org/records/9306z-07798

[56] StoRIES Project. (2020–2025). StoRIES – Storage Research Infrastructure Ecosystem. Funded by the European Union's Horizon 2020 Research and Innovation Programme (Grant Agreement No. 101036910). Retrieved from https://www.storiesproject.eu

[57] Ceraolo, M., & Lutzemberger, G. (2014). Stationary and on-board storage systems to enhance energy and cost efficiency of tramways. Journal of Power Sources, 264, 128–139. https://doi.org/10.1016/j.jpowsour.2014.04.070

[58] Barelli, L., Bidini, G., Ottaviano, P. A., & Pelosi, D. (2019). Vanadium redox flow batteries application to electric buses propulsion: Performance analysis of hybrid energy storage system. Journal of Energy Storage, 24, 100770. https://doi.org/10.1016/j.est.2019.100770

[59] Pinflow Energy Storage. (n.d.). Pinflow Energy Storage – store and release energy with impact on safety, efficiency and durability. Retrieved October 13, 2025, from https://www.pinflowes.com/

[60] Chen, J.-Y., Hsieh, C.-L., Hsu, N.-Y., Chou, Y.-S., & Chen, Y.-S. (2014). Determining the limiting current density of vanadium redox flow batteries. Energies, 7(9), 5863–5873. https://doi.org/10.3390/en7095863

[61] Sezer, N., & Koç, M. (2021). A comprehensive review on the state-of-the-art of piezoelectric energy harvesting. Nano Energy, 80, 105567. https://doi.org/10.1016/j.nanoen.2020.105567

[62] Uzabakiriho, P. C., & Zhao, G. (2021). Recent progress in flexible pressure sensors based electronic skin. Advanced Engineering Materials, 23(5), 2001187. https://doi.org/10.1002/adem.202001187

[63] Gao, W., Ota, H., Kiriya, D., Takei, K., & Javey, A. (2019). Flexible electronics toward wearable sensing. Accounts of Chemical Research, 52(3), 523–533. https://doi.org/10.1021/acs.accounts.8b00500

[64] Wu, Y., Ma, Y., Zheng, H., & Ramakrishna, S. (2021). Piezoelectric materials for flexible and wearable electronics: A review. Materials & Design, 211, 110164. https://doi.org/10.1016/j.matdes.2021.110164

[65] Chen, B., Feng, Z., Yao, F.-Z., Zhang, M.-H., Wang, K., Wei, Y., Gong, W., & Rödel, J. (2025). Flexible piezoelectrics: Integration of sensing, actuating and energy harvesting. npj Flexible Electronics, 9, 58. https://doi.org/10.1038/s41528-025-00432-5

[66] Bae, J.-H., Lee, J., & Chang, S.-H. (2018). Characterization of low-velocity impact-induced damages in carbon/epoxy composite laminates using a poly(vinylidene fluoride–trifluoroethylene) film sensor. Composites Part B: Engineering, 135, 189–200. https://doi.org/10.1016/j.compositesb.2017.10.008

[67] Zhang, F., Gong, L., Wang, F., Zhou, H., He, W., Huang, Z., Peng, X., & Zhou, H. (2023). Embedded Pt-PVDF sensor without compromising mechanical properties of GFRP for on-line sensing. Thin-Walled Structures, 187, 110702. https://doi.org/10.1016/j.tws.2023.110702

[68] De Rosa, I. M., & Sarasini, F. (2010). Use of PVDF as acoustic emission sensor for in situ monitoring of mechanical behaviour of glass/epoxy laminates. Polymer Testing, 29(6), 749–758. https://doi.org/10.1016/j.polymertesting.2010.04.006

[69] Ahmed, O., Wang, X., Tran, M.-V., & Ismadi, M.-Z. (2021). Advancements in fiber-reinforced polymer composite materials damage detection methods: Towards achieving

energy-efficient SHM systems. Composites Part B: Engineering, 223, 109136. https://doi.org/10.1016/j.compositesb.2021.109136

[70] Mongioì, F., Selleri, G., Maccaferri, E., Fabiani, D., Zucchelli, A., & Brugo, T. M. (2025). CFRP laminate with autonomous sensing and enhanced impact resistance by P(VDF-TrFE) nanofibers interleaving. Composites Part B: Engineering, 293, 112143. https://doi.org/10.1016/j.compositesb.2025.112143

[71] Saghafi, H., Brugo, T., Minak, G., & Zucchelli, A. (2015). The effect of PVDF nanofibers on mode-I fracture toughness of composite materials. Composites Part B: Engineering, 72, 213–216. https://doi.org/10.1016/j.compositesb.2014.12.015

[72] Brugo, T., & Palazzetti, R. (2016). The effect of thickness of Nylon 6,6 nanofibrous mat on Modes I–II fracture mechanics of UD and woven composite laminates. Composite Structures, 154, 172–178. https://doi.org/10.1016/j.compstruct.2016.07.034

[73] Gasperini, L., Selleri, G., Pegoraro, D., Mariani, D., Rumi, A., Seri, P., & Fabiani, D. (2025). Corona triode poling of P(VDF-TrFE) nanofibers: Mechanisms and optimization strategies. Journal of Science: Advanced Materials and Devices, 10, 100870. https://doi.org/10.1016/j.jsamd.2025.100870

[74] Zanoni, M., Braidi, N., Selleri, G., Cavallo, D., Focarete, M. L., Fabiani, D., & Gualandi, C. (2025). Optimizing the piezoelectric response of poly(vinylidene fluoride-co-trifluoroethylene) electrospun mats: effects of copolymer composition, microstructure and thermal treatments. European Polymer Journal, 236, 114159. https://doi.org/10.1016/j.eurpolymj.2025.114159

[75] Manojkumar, K., Muthuramalingam, M., Sundamoorthy, A., Srinivasa Babu, P. S., Vamsi, R., Boominathan, J., Priyanka, S. G. S., Hajra, S., Panda, S., Kim, H. J., Dubal, D., & Vivekananthan, V. (2025). Revolutionizing energy storage: Self-charging supercapacitors toward self-powered micro and nano systems. Chemical Engineering Journal, 524, 168642. https://doi.org/10.1016/j.cej.2025.168642

[76] Selleri, G., Poli, F., Neri, R., Gasperini, L., Gualandi, C., Soavi, F., & Fabiani, D. (2023). Energy harvesting and storage with ceramic piezoelectric transducers coupled with an ionic liquid-based supercapacitor. Journal of Energy Storage, 60, 106660. https://doi.org/10.1016/j.est.2023.106660

[77] Soavi, F., Arbizzani, C., & Mastragostino, M. (2014). Leakage currents and self-discharge of ionic liquid-based supercapacitors. Journal of Applied Electrochemistry, 44(4), 491–496. https://doi.org/10.1007/s10800-013-0647-x

[78] Yang, Y., Li, L., Akhmedovich, M., Ma, W., & Xu, D. (2023). Design and machining applications of the piezoelectric vibration sensing system. Journal of Manufacturing and Materials Processing, 7(5), 166. https://doi.org/10.3390/jmmp7050166

[79] Tamilselvi, S., Gunasundari, S., Karuppiah, N., Abdul Razak, R. K., Madhusudan, S., Nagarajan, V. M., Sathish, T., Shamim, M. Z. M., Saleel, C. A., & Afzal, A. (2021). A review on battery modelling techniques. Sustainability, 13(18), 10042. https://doi.org/10.3390/su131810042

[80] Petri, E., Arnaiz, M., Gualandi, C., Soavi, F., & Ajuria, J. (2025). Scaling up pullulan-based supercapacitors: A sustainable approach to binder and separator integration in EDLCs. Journal of Power Sources, 657, 238177. https://doi.org/10.1016/j.jpowsour.2025.238177

[81] Poli, F., Momodu, D., Spina, G. E., Terella, A., Mutuma, B. K., Focarete, M. L., Manyala, N., & Soavi, F. (2020). Pullulan–ionic liquid-based supercapacitor: A novel, smart combination of components for an easy-to-dispose device. Electrochimica Acta, 338, 135872. https://doi.org/10.1016/j.electacta.2020.135872

[82] Spyker, R. L., & Nelms, R. M. (2000). Classical equivalent circuit parameters for a double-layer capacitor. IEEE Transactions on Aerospace and Electronic Systems, 36(3), 829–836. https://doi.org/10.1109/7.869502

[83] Kamel, T. M., & de With, G. (2007). Pyroelectricity versus conductivity in soft lead zirconate titanate (PZT) ceramics. Journal of Materials Research, 22(12), 3448–3454. https://doi.org/10.1557/JMR.2007.0438

[84] BlueUp S.r.l. (2025, March). Maxi BLE: Bluetooth Low Energy beacon (Version 2025/01) Data sheet. BlueUp S.r.l. https://www.blueupbeacons.com

Chapter 4: Experimental Analysis of Catholyte Carbon Ratios to Replace 3D RVC in Semi-Solid Lithium–Air Cells

4.1 Introduction

The University of Bologna spin-off BETTERY Srl [1], established in 2018, aims to scale up the concept of the Semi-Solid Lithium-Air Flow Battery (SLAFB), whose principle was outlined in Section 2.3.2 of the introduction. In summary, the SLAFB works as a partial redox flow battery because it employs metallic lithium as the anode, while the cathode consists of a liquid catholyte containing dispersed carbon particles in a solution of lithium salts within an organic solvent. The spin-off developed the first prototype, which featured a 12 cm^2 active surface, under the name NESSOX (New Semi-Solid Flow Lithium-Oxygen Battery) as part of the NESSOX project [2]. Preliminary tests indicate an energy density of approximately 950 Wh L^{-1} and a specific energy of 800 Wh kg^{-1}, excluding casing and control units [3]. NESSOX is a patented technology [4] that could offer both high energy density and improved safety, making it suitable for applications that demand high energy storage within a compact volume. First encouraging results have motivated further upscaling of the NESSOX technology, which requires advancements in all system components from both chemical and engineering perspectives. In particular, electrolyte formulation, separator design, cell frame and layout optimisation, and the integration of a management system represent crucial areas for improvement.

Carbonaceous suspensions should feature an efficient electronic percolating network. Once established, this network improves the kinetics of the faradaic process and facilitates electron transfer between the particles and the current collector, thereby reducing ohmic losses and increasing power output. However, incorporating carbon particles significantly affects the viscosity of the catholyte [5]. Literature indicates that the nature of carbon powder affects both the electrical properties and rheological behaviour of the slurries. Good results have been achieved using Pureblack fragmental particles in 0.5 m LiTFSI in TEGDME. This slurry features a not-Newtonian behaviour, i.e. it reduces viscosity as the shear rate increases [6]. Defining the optimal amount of carbon powder requires considering both electrical and fluid

dynamic benefits. Nevertheless, employing carbonaceous slurries demands considerable effort in designing the cell reactor and circuit to prevent clogging and ensure uniform flow.

A previous study conducted in our laboratory [7] investigated the effect of varying Pureblack carbon concentration (2-10%) in the 0.5 m LiTFSI in TEGDME catholyte on both electrical properties and mass flow. Electrochemical impedance spectroscopy (EIS) tests were performed using a small cell equipped with stainless-steel blocking electrodes, without lithium or graphite disks, thereby preventing any faradaic reactions. This configuration allowed the evaluation of the electronic resistance and the resistance of the percolating network. Following the model proposed by Youssry et al. [8] and depicted in Figure 4.1.1, a carbonaceous slurry can be modelled as two parallel branches: one branch contains the electronic resistance (R_e) associated with the carbon network, while the other comprises the ionic resistance (R_i) in series with a constant phase element (Q_{dl}), which represents the double-layer capacitance at the electrode/slurry interface. The high frequency intercept of the Nyquist plot provides R_{hf}, which is used to evaluate the electronic resistance R_e. The ionic resistance Ri is obtained by performing EIS on the electrolyte without carbon powder. Re is then calculated according to the Equation 4.1.1:

$$R_e = \left(\frac{1}{R_{hf}} - \frac{1}{R_i}\right)^{-1} \qquad 4.1.1$$

Electronic conductivity is evaluated using the Equation $\sigma_e = K\ R_e^{-1}$ where K is a geometric characteristic of the cell. The establishment of an effective percolating network is indicated in the EIS spectra by the appearance of a semicircle in the Nyquist plot. The diameter of this semicircle, measured along the real axis, corresponds to the percolating network resistance (R_{pn}). In the absence of carbon powder, the electronic resistance is extremely high, so the R_e branch can be considered open, and the Nyquist plot displays a straight-line characteristic of capacitive behaviour. The introduction of carbon powder decreases R_e, and the parallel configuration of the two branches produces a semicircle in the Nyquist plot, which reflects the contribution of the percolating network.

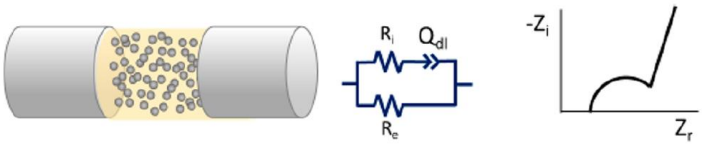

Figure 4.1.1 Homogeneous carbon distribution: slurry, equivalent circuit, and Nyquist plot adapted from [5]

Figure 4.1.2 illustrates the outcomes of the previous investigation [7]: in Figure 4.1.2a the electronic conductivity is reported showing that it increases with the highest proportion of carbon powder and declines with greater pump speed. At 10% carbon content, conductivity appears less affected by pump speed. The plot in Figure 4.1.2b presents the values of the percolating network resistance (R_{pn}), indicating that the lowest values for each pump speed occur at 8% carbon powder. The observed reduction in R_{pn}, together with the enhancement in electronic conductivity, demonstrates the effectiveness of the percolating network. Further investigations examined the rheological properties of slurries containing different proportions of PB within a 0.5 m LiTFSI in TEGDME catholyte. Figure 4.1.2c displays the mass flow for various carbon contents at different pump speeds. The data clearly indicate that the 6% and 8% catholytes correspond to the highest mass flow rates. When assessing the electronic conductivity across mass flow rate variations (Figure 4.1.2d), the highest conductivity values also occur at 6%, 8% and 10% carbon content. Several rheological investigations conducted on slurries with varying proportions of PB in 0.5 LiTFSI in TEGDME are presented in Figure 4.1.2e adapted from [5], which displays the corresponding viscosity–shear rate curves. These findings demonstrate that the slurries do not conform to Newtonian fluid behaviour: viscosity declined consistently as the shear rate increased, thereby indicating pseudoplastic behaviour across all formulations, although a higher carbon content generated greater viscosity values. The graphs further reveal that viscosity approached a plateau at elevated shear rates. The pseudoplastic behaviour can provide advantages by lowering pumping energy requirements during operation and minimising sedimentation under static conditions. This previous work demonstrates that, in terms of both electrochemical and fluid dynamic performance, the most favourable results are achieved with carbon amounts exceeding 6%. From a practical perspective, operating with more than 8% carbon introduces significant challenges in circuit management. Consequently, in the subsequent experimental tests, a carbon content of 7% was selected.

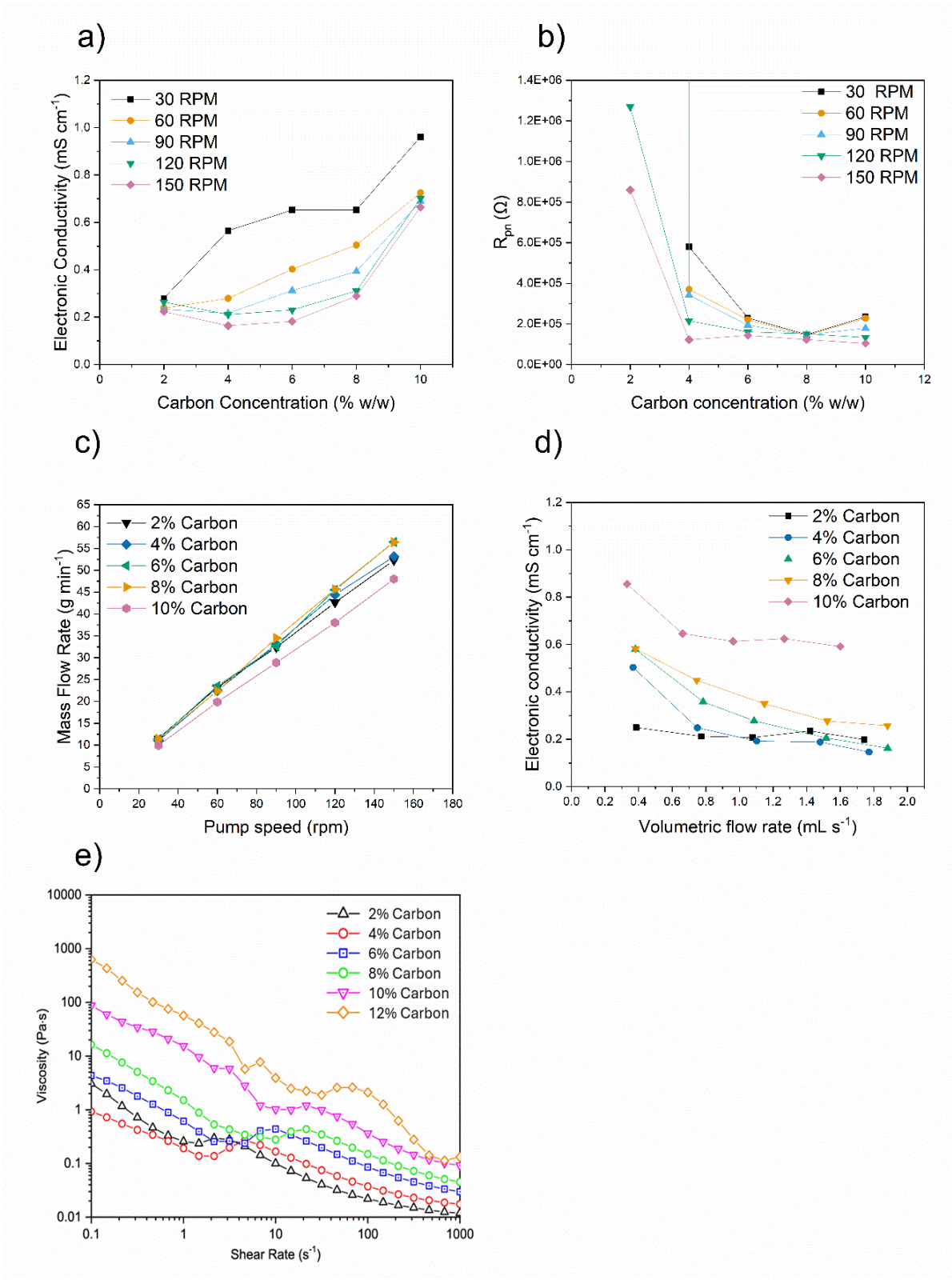

Figure 4.1.2 a) Electronic conductivity in relation to carbon content and pump speed; b) percolating network resistance (R_{pn}) for different carbon contents; c) mass flow rate for varying carbon content and pump speed; d) electronic conductivity at different mass flow rates; e) viscosity vs shear rate results for PB slurries, modified from [5].

The next phase of NESSOX development involves developing a cell with an active surface area of 200 cm^2. One of the most significant challenges in this prototype lies in the management and optimisation of the catholyte flow and the overall layout. Specifically, the cell currently incorporates a three-dimensional current collector composed of Reticulated Vitreous Carbon (RVC). RVC is a porous, conductive glassy carbon that is suitable for applications requiring high current densities, offering substantial chemical and thermal resistance and a high volume-to-area ratio. This material was selected because it provides a high surface area and a macroporous structure, which facilitate electron transfer, enhance oxygen diffusion within the cell, and reduce cathode passivation, thereby improving cycling performance [3]. However, disadvantages include its fragility, difficulties in establishing an adequate electrical connection, and, in the specific case of carbon suspension, its potential to cause obstruction [9].

In detail the new 200 cm^2 surface NESSOX prototype comprises two square Lithium electrodes with 10 cm edges. Figure 4.1.3 illustrates the assembled components of the cell, highlighting the presence of two Lithium housings. Indeed, a distinctive feature of NESSOX lies in its structure, which comprises two anodes and one circulating catholyte that flows in the middle of the cell (flow frame). While keeping the cathode inactivated, this configuration enables the pre-cycling of the two Lithium foils to form a controlled Solid Electrolyte Interface (SEI). Lithium square foils are positioned inside the Lithium housings and placed in contact with the Lithium current collector, which is manufactured from stainless steel. The catholyte circulates through the flow frame, situated at the centre of the cell following the shape of the inlet nozzle and spreading across a leaf-shaped flow guide. This new design is the results of a collaboration between the EStorage team [10] and Bettery with the objective of developing this design through fluid dynamic simulations to minimise pressure drops and ensure uniform flow velocity throughout the square section. The square cavity in the flow frame contains the 3D catholyte current collector consisting of a RVC mesh. The central position of the RVC within the cell represents a crucial issue in prototype development. The main challenge involves establishing contact without causing electrolyte leakage, while ensuring an effective electronic connection and considering the fragile nature of the RVC. Additionally, the porous structure should be designed in order to avoid the formation of agglomerates which could clog the current collector. To complete the assembly, separators are inserted on each side of the cell between the Lithium and the flow frame. Two Celgard® trilayer foils are positioned between

two gaskets to separate the Lithium and RVC components. The contacts with the current collector are established using the stainless steel tips on the Lithium current collector plates; the two tips are directly connected to each other. The contact with the RVC is achieved through two drilled holes positioned along the long edges of the flow frame, where stainless steel or graphite rods are inserted to extract the electrical connection.

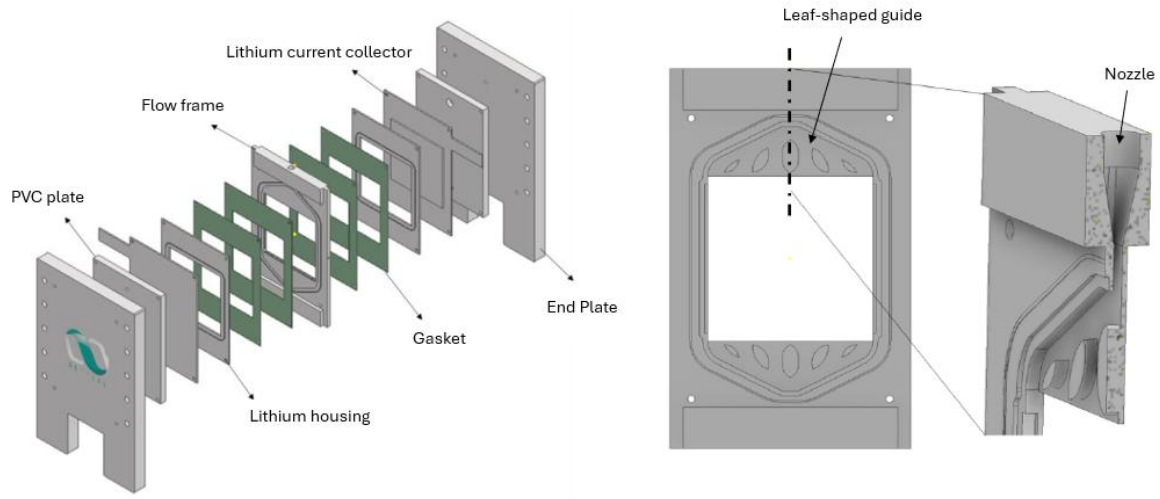

Figure 4.1.3 Assembled components of the fourth NESSOX prototype and a selected section of the flow frame.

The performance of the new NESSOX prototype are presented in terms of Power versus Current and Power density versus Current density in Figure 4.1.4. Two experimental tests are compared: the first one, shown in light blue (N_L_100rpm), demonstrates the results obtained using a small pump operating at 100 rpm, while the brown curve (N_B_228rpm) represents the data acquired when the catholyte was circulated with a larger pump at higher speed. In both tests, the catholyte consisted of Pureblack carbon at a concentration of 2% in 0.5 m LiTFSI in TEGDME and was circulated through the cell. As indicated in Figure 4.1.4a, in the first case (N_L_100rpm) the system achieved absolute current values exceeding 16 mA, which constitutes an outstanding result when compared with the data available in the literature. However, when the current is normalised by the surface area (Figure 4.1.4b), the current density reaches values below 0.20 mA cm^{-2}, which can be further improved for practical applications. One limiting factor of this performance could be the catholyte flow rate inside the cell, and for this reason Figure 4.1.4 also illustrates the data obtained using a larger pump with higher speed (N_B_228rpm), adjusted to achieve a speed of the order of magnitude of 10 cm s^{-1} which is the same order of magnitude of the flow speed in the previous study [3]. This

increased speed led to poorer performance, resulting in lower power and current values, as shown in the graphs, and is likely associated with the verified formation of agglomerates inside the RVC element, which are promoted by higher flow rates and clog the current collector. For this reason, the next Section presents a study on the formulation of a new catholyte designed to exploit the high conductivity and the formation of a percolating network that eliminates the need for the RVC.

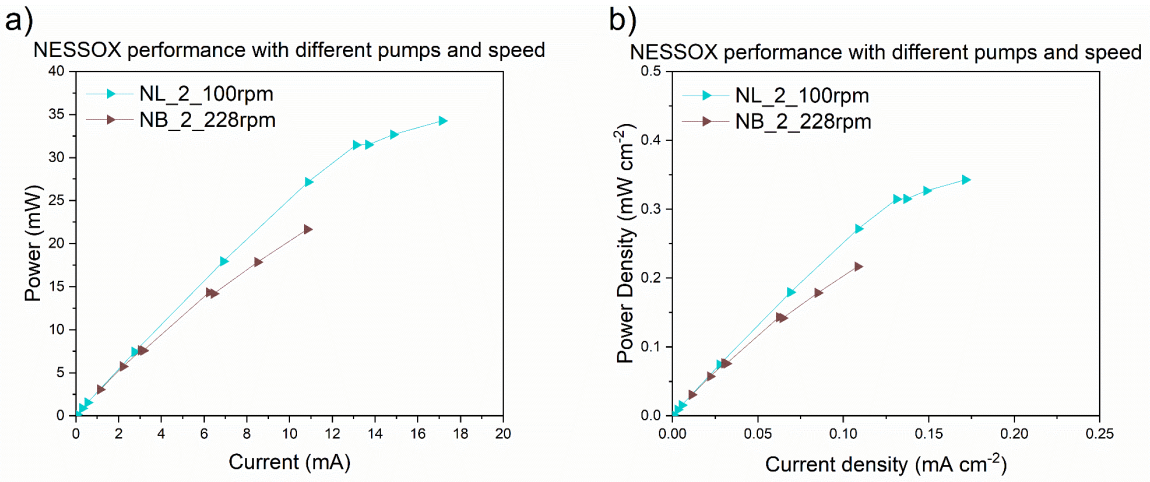

Figure 4.1.4 NESSOX prototype performance: a) Power vs. Current; b) Power density vs. Current density for N_L_100rpm and N_B_228rpm tests using 2% Pureblack carbon catholyte in 0.5 m LiTFSI in TEGDME

In summary, my collaboration with Bettery s.r.l. aimed at assessing the elimination of RVC by increasing the electronic conductivity of the semi-solid catholyte by increasing the concentration of carbon powder. Indeed, RVC is a critical component of the cell, as it is fragile and expensive, while its inherent tortuosity causes slurry agglomeration and clogging. RVC is employed because it provides a large surface area that facilitates electron transfer; however, this function can also be achieved by increasing the carbon content to ensure a continuous percolating network, as discussed above. Conversely, semisolid slurries require careful attention to viscosity adjustment and the formation of agglomerates caused by carbon particles [5]. Consequently, this Chapter focuses on testing a new catholyte formulation with a carbon content of 7% to evaluate the feasibility of removing RVC.

4.2 Materials and methods

To proceed with the investigation regarding the electrolyte formulation, a smaller cell was assembled. The Teflon-made cell adopts a Cross-type (CC) configuration, and its schematic representation appears in Figure 4.2.1 It is important to note that, in this simplified equivalent setup, the cell includes only one anode. This represents the main distinction from the Nessox prototype, along with the reduced size. On the anode side, the stainless steel cylinder was in direct contact with the lithium, which was then covered by two layers of Celgard® trilayer separator (Trilayer Microporous Membrane Polypropylene/Polyethylene/Polypropylene). On the cathode side, a graphite disk was used to improve the electronic contact between the stainless steel and the RVC. The catholyte flowed through the cell in the direction indicated by the arrow, passing through the disk holder, where the RVC could be inserted or excluded depending on the tested conditions. Electrical contact was established using stainless steel cylinders, covered with Kapton tape to prevent direct exposure to the catholyte. The design of the disk holder limited the active surface area to 0.4 cm^2, as shown in the detail of Figure 4.2.1.

The electrolyte used in all experimental tests consisted of a 0.5 mol kg^{-1} solution of lithium bis(trifluoromethanesulfonyl)imide (LiTFSI – Sigma Aldrich, purity ≥ 99%) in tetraethylene glycol dimethyl ether (TEGDME – Sigma Aldrich, purity ≥ 99%). Karl Fischer (756/831 KF Coulometer Metrohm) measurements on the purchased TEGDME revealed a water content of approximately 243 ppm, which was reduced to around 9 ppm by applying 50% by volume of molecular sieves for three days inside a glove box (MBraun LabMaster pro ECO, with concentration of O_2<0.01 ppm and H_2O < 0.1 ppm). The LiTFSI salt was dried overnight in a Büchi oven at 130 °C. The final catholyte was prepared by adding different percentages of PureBlack 315 (PB-Superior Graphite, BET=64 $m^2\ g^{-1}$) carbon powder, depending on the specific test condition. PB was dried overnight at 150 °C in the Büchi oven. After carbon addition, the dispersion underwent sonication at 450 W for 15 minutes using a 7-second on / 5-second off cycle to prevent excessive temperature rise. The final volume of electrolyte was estimated at approximately 50 mL. Pure oxygen was introduced into the catholyte at a point upstream of the cell inlet. Metallic lithium was laminated in a dry room (dry room purchased from Disgelo with a dew point of -40 °C) using a rolling press to achieve a thickness of 0.6 mm and then cut depending on the cell type. The RVC was dried overnight in an oven at 80 °C.

Figure 4.2.2 shows a simplified section of the setup in comparison with the NESSOX one: (a) illustrates the small CC cell, and (b) presents the NESSOX configuration with the double-sided lithium arrangement. In both cases, the RVC is included; however, in some tests, it was excluded to better evaluate the performance without it. The RVC employed was purchased from Goodfellow and had a porosity of 60 ppi (pores per inch) and a thickness of 6 mm.

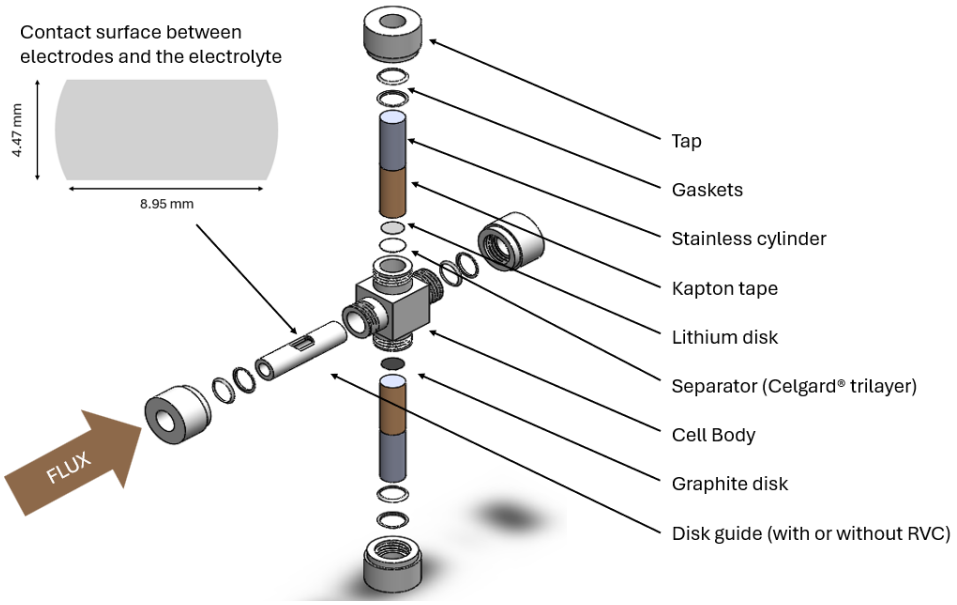

Figure 4.2.1 Exploded view of the cross-type cell showing the contact surface between electrodes and electrolyte

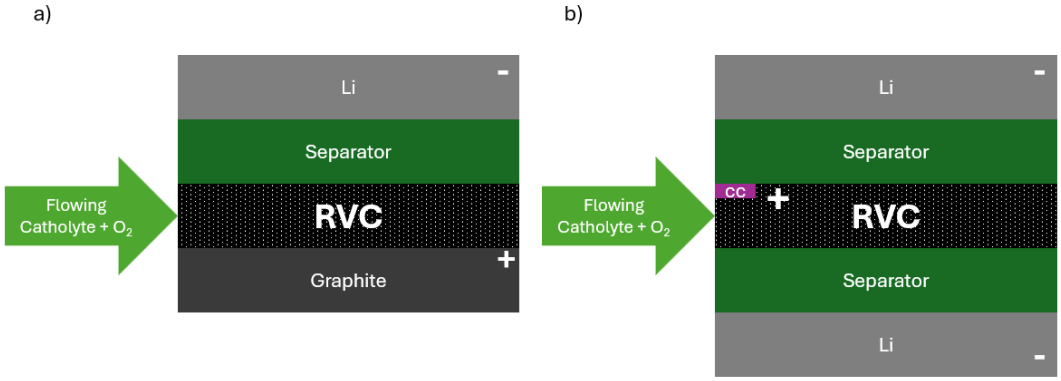

Figure 4.2.2 Simplified cross-sections of (a) the CC cell and (b) the NESSOX setup with double-sided lithium. RVC is shown in both, though omitted in some tests to assess its effect

The utilised pump is a Watson-Marlow 120DS/DV peristaltic one (24 W) paired with tubing of 4.8 mm internal diameter. For all experimental tests, the pump speed was determined to achieve a catholyte velocity inside the cell in the order of magnitude of 10 cm s^{-1}, a value extrapolated from [3]. The internal cross-sectional area was estimated according to the geometry illustrated in Figure 4.2.1, resulting in a crossing surface of A = 0.22 cm^2. The

volumetric flow rate of the pump operating at 100 rpm is Qv = 1.5 cm^3 s^{-1}. Using the Equation $v = Q_v A^{-1}$, which relates the internal flow velocity to the volumetric rate and the cross-sectional area, it can be extrapolated that the pump speed set at 100 rpm produces a velocity of approximately 7 cm s^{-1} inside the cell which is considerable a good value.

Three different configurations of CC cell were tested by varying the percentage of pure black powder and the presence or absence of RVC. Table 4.2.1 presents all the tested conditions with their corresponding abbreviations: CC denotes the Cross-Type Cell; Xww indicates the percentage of carbon powder in the catholyte; RVC and NORVC specify whether the RVC was included during the test; a pump speed of 100 rpm was applied for each configuration. With the intention of eliminating the RVC, the carbon powder content in the catholyte was increased up to 7%, in accordance with the results presented in the introduction from the study on the percolating network.

Table 4.2.1 Experimental tests conducted on the two cells with varied catholyte formulations and the presence or absence of RVC

	Pureblack Carbon	**RVC**	**Pump speed**
	%	*Y/N*	*rpm*
CC2wwRVC	2	Y	100
CC2wwNORVC	2	N	100
CC7wwNORVC	7	N	100

The electrochemical technique applied to assess the cell performance under different configurations was Chronoamperometry (CA) through a BioLogic VSP potentiostat. The cell was subjected to successive potential steps, starting from 3 V and decreasing to 2 V. Each potential step lasted for at least 30 minutes to allow monitoring of the current response. By recording the final current value (I) at the end of each voltage step (V), it was possible to construct a polarisation curve V *vs* I. Moreover, the power versus current graphs were developed by deriving the power (P) calculated through the product of current and potential, $P=VI$, and aligned with the relevant current rate. The power density versus current density graph was derived normalizing the power and the density by the active surface of 0.4 cm^2.

4.3 Results and discussion

Figure 4.2.3a illustrates the graph of the current density versus time, obtained by conducting the CA test described in Section 4.2 for the small CC cell featuring the RVC and 2% of carbon powder into the catholyte. The orange line denotes the current response to the potential steps, revealing three principal behaviours. Immediately after the potential change, the current exhibits a sharp increase followed by a decreasing trend which are attributable to the capacitive features of the system, which is enhanced by the carbon particles dispersed in the catholyte. At the longest times of the step, the current tends to a plateau, indicating that it is governed by reaction kinetics and O_2 mass transport that in turn depends on the slurry flow. Figure 4.2.3b reports the results obtained conducting the same experimental technique with the same amount of carbon but removing the RVC. The current density profile denotes really low values if compared with the previous graph indicating a poor performance. Figure 4.2.3c illustrates the same experiment conducted on the small CC cell containing 7% carbon powder without RVC. In this case, it is still possible to distinguish the capacitive, kinetic, and mass-transport controlled behaviours. However, the no-RVC system demonstrates a more stable current response, showing smaller fluctuations, and this could be associated with the absence of agglomerate formation, as observed by comparing Figures 4.2.3a and 4.2.3c. In the first case, the currents after approximately 5000 s are less regular and tend to decrease over time, whereas in the latter, the plateau currents are more defined, resulting in a more stable and reliable behaviour. However, the 7% system delivers lower current values compared with the 2%-RVC configuration. Nevertheless, the step-by-step current response is lower, although comparable, a trend that will be demonstrated more clearly in the polarisation curve.

Figure 4.2.4a illustrates the outcomes of the experiments described above through a polarisation curve, which presents the potential value of each step in relation to the average measured current density. The configuration labelled CC2wwRVC, referred to as the "benchmark" cell, achieved the highest current density (up to 3 mA cm^{-2}). This setup incorporated 2% carbon powder, RVC as the current collector, and a graphite disk. In contrast, the identical configuration without the RVC component (CC2wwNORV) generated a considerably lower current response as noticed in the previous paragraph. The cell without RVC but containing 7% carbon powder (CC7wwNORVC) reached 1.5 mA cm^{-2}.

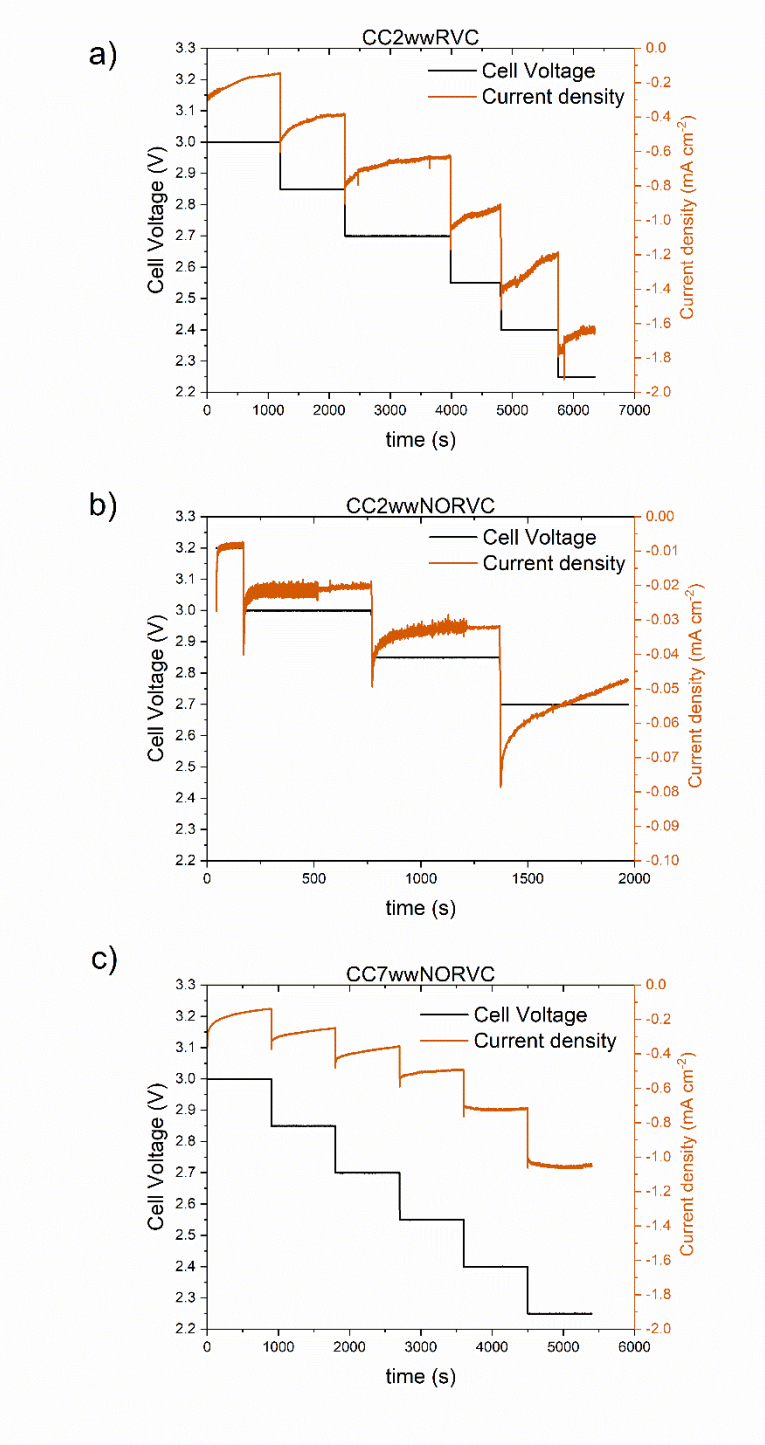

Figure 4.2.3 Current response of the small CC cell with a) 2% carbon powder and RVC , b) 2% carbon powder without RVC c) and 7% carbon powder without RVC under similar potential step test conditions.

The polarisation data were converted into a power density–current density graph, presented in Figure 4.2.4b, which confirms the previously discussed trends: the benchmark cell CC2wwRVC reports the best outcome, whilst the CC2wwNORVC the worst; medium performance was achieved by the CC7wwNORVC. These experimental results obtained with

the small cell demonstrate that eliminating the RVC can yield satisfactory performance when the carbon content is increased from 2% to above 7%, as it enables comparable outcomes even though it does not achieve the same benchmark performance. As explained in the introduction, one possible limitation of the NESSOX prototype is the accumulation of agglomerates around the RVC, which obstruct the flow. Indeed, the path length that the catholyte follows inside the RVC is greater compared to that in the small CC cell. This implies that employing a 7% carbon slurry in NESSOX could provide a considerable advantage.

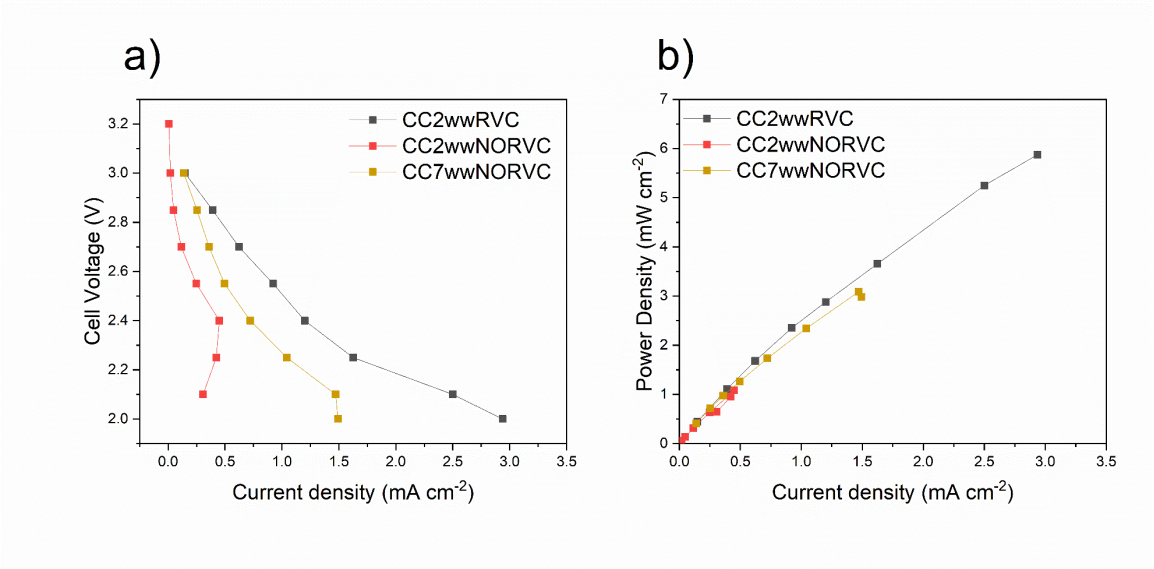

Figure 4.2.4 Comparison of a) polarisation and b) power density curves vs. current density based on test results

4.4 Conclusions

The present study aimed to investigate alternative formulations of the catholyte for an SLAFB prototype, specifically the NESSOX system developed by the University of Bologna spin-off Bettery. The prototype, with a surface area of 100 cm^2, represents one of the largest Li–air prototypes ever produced and achieved an absolute current of 16 mA, which constitutes an outstanding result. However, when the current is normalised to the surface area, it appears to be relatively low. One possible reason for this limitation is the formation of agglomerates inside a component of the cell: the RVC, which acts as the medium for catholyte flow, facilitates electron transfer, enhances oxygen diffusion within the cell, and reduces cathode passivation, thereby improving cycling performance. In addition for the current NESSOX set-up, RVC implies issues in taking the contact with it due to its fragile nature.

My investigation has contributed to the development of the NESSOX prototype by testing new catholyte formulations that vary the percentage of carbon, which, according to previous research, can decrease the electronic conductivity of the catholyte and establish an effective percolating network replacing the RVC's function. By incorporating 7% carbon into the TEGDME–LiTFSI electrolyte, it was demonstrated that the presence of the percolating network enables the achievement of current densities comparable to those obtained with the RVC configuration, although not superior (respectively 3 mA cm^{-2} vs 1.5 mA cm^{-2}) showing a more stable current probably related to the absence of agglomerates inside the cell. The elimination of the RVC and the use of a 7% slurry may provide advantages such as a reduced probability of agglomerate formation, which is likely to occur in the NESSOX prototype, since its large surface area produces a long path for catholyte transport through the RVC. Moreover, RVC is an expensive and fragile component, implying that its absence could decrease both cost and system complexity. Disadvantages related to high-percentage carbonaceous slurries concern circuit management because, as discussed in the introduction, slurries exhibit high viscosity. Nevertheless, they demonstrate pseudoplastic behaviour, which decreases the pumping energy required at higher speeds. Other potential limiting factors for NESSOX are associated with the lithium anode and the oxygen flow within the catholyte. These aspects require further investigation to optimise the prototype's performance, supported by a fluid-dynamic enhancement of the circuit.

Chapter 4 References

[1] Bettery. (n.d.). Better batteries for the future [Website]. Retrieved 17 October 2025, from https://www.bettery.eu/

[2] European Commission. (2022, September 4). Changing the electric-vehicle paradigm with green, long-lasting and fast recharge liquid batteries (Project No. 837041 – BETTERY SRL). CORDIS: EU Research Results. https://cordis.europa.eu/project/id/837041/results/it

[3] Soavi, F., Brilloni, A., De Giorgio, F., & Poli, F. (2022). Semi-solid lithium/oxygen flow battery: An emerging, high-energy technology. Current Opinion in Chemical Engineering, 37, 100835. https://doi.org/10.1016/j.coche.2022.100835

[4] Soavi, F., Arbizzani, C., & Mastragostino, M. (2017). Semi-solid lithium oxygen battery (WO2017021840A1). World Intellectual Property Organization. https://patentscope.wipo.int/search/en/detail.jsf?docId=WO2017021840

[5] Brilloni, A., Poli, F., Spina, G. E., Genovese, D., Pagnotta, G., & Soavi, F. (2021). Improving the electrical percolating network of carbonaceous slurries by superconcentrated electrolytes: An electrochemical impedance spectroscopy study. ACS Applied Materials & Interfaces, 13(11), 13872–13882. https://doi.org/10.1021/acsami.1c02439

[6] Ruggeri, I., Arbizzani, C., & Soavi, F. (2018). Carbonaceous catholyte for high energy density semi-solid Li/O_2 flow battery. Carbon, 130, 749–757. https://doi.org/10.1016/j.carbon.2018.01.056

[7] Mori, A. (2024). Studio della conducibilità elettronica di sospensioni carboniose per batterie a flusso semisolide [Bachelor's thesis, Università di Bologna]. Dipartimento di Chimica "Giacomo Ciamician"

[8] Youssry, M., Madec, L., Soudan, P., Cerbelaud, M., Guyomard, D., & Lestriez, B. (2013). Non-aqueous carbon black suspensions for lithium-based redox flow batteries: Rheology and simultaneous rheo-electrical behaviour. Physical Chemistry Chemical Physics, 15(27), 14476–14486. https://doi.org/10.1039/c3cp51371h

[9] Friedrich, J. M., Ponce-de-León, C., Reade, G. W., & Walsh, F. C. (2004). Reticulated vitreous carbon as an electrode material. Journal of Electroanalytical Chemistry, 561, 203–217. https://doi.org/10.1016/j.jelechem.2003.07.019

[10] eStorage Italia. (n.d.). Official website. Retrieved 17 October 2025, from https://www.estorageitalia.com/

Chapter 5: CO_2 Capture via Flow Supercapacitors

Section 2.4 introduced the concept of Supercapacitive Swing Adsorption (SSA) and reviewed the mechanisms currently under investigation in the literature. Numerous studies on SSA have been conducted worldwide, and a significant contribution has been attributed to Professor Forse's group at the Yusuf Hamied Department of Chemistry, University of Cambridge, UK. This Chapter presents the research I carried out as a visiting PhD student during my international period in Forse's group.

5.1 Introduction and objective

Different types of SSA cells have been developed to date. The first, reported by the Landskron Group in 2014 [1], consisted of an electrochemical cell with two cylindrical carbon electrodes immersed in an electrolyte [2]. Other research groups, such as Forse's, continued the investigation by employing coin-type cells where the negative electrode was exposed to a monitored pure CO_2 pressurised environment. This configuration provided additional flexibility for investigating the mechanisms involved in SSA by allowing variations in both the electrodes and electrolyte formulations [3]. Although these cell types are crucial for understanding and optimising SSA from a technological perspective, it remains necessary to develop a cell that interacts directly with a gas stream. For this purpose, Cong Liu and Kai Landskron designed an SSA module inspired by fuel cell architecture, integrating diffusion layers and flow channel technologies. The cell comprises two end plates in contact with two graphite plates. On the negative side, the graphite plate contains a serpentine channel in contact with a carbon cloth acting as a gas diffusion layer, which is then in contact with the electrode. On the positive side, the electrode is in direct contact with the graphite. An electrolyte-soaked separator is positioned between the two sides of the cell. The gas stream enters the cell from the positive side, flows through the serpentine, and diffuses into the gas diffusion layer [4].

The objective of my work is to assemble an electrochemical flow capacitor aimed at capturing CO_2 through SSA behaviour. This layout, which is describe in the next Section, differs from the fuel-cell-like design mainly in two aspects: the cell is symmetrical from a structural

perspective, and the electrolyte flows through the serpentine channels, driven by pumps and dedicated piping. The gas stream contacts the electrolyte upstream of the cell, allowing CO_2 to dissolve before entering. This configuration provides the advantage of testing different combinations of gas streams, with controlled variations in the flow on both the positive and negative sides of the cell.

5.2 Materials and methods

The study employed a Scribner flow cell, commonly utilised as a redox-flow battery (Figure 5.2.1). The device comprises several plates of different dimensions and materials. At both ends, two gold-coated copper current collectors were positioned, followed by two graphite blocks with serpentine channels functioning as flow fields. Two rubber gaskets with a square aperture were positioned between the graphite plates, providing sealing while simultaneously defining the space for the electrodes and the two separator foils. The assembly incorporated as electrodes two pieces of activated carbon cloth (ACC) with an area of 25 cm^2, and Table 5.2.1 presents the characteristics of the two different ACC employed. The separator was prepared by cutting two sheets of Whatman 1 glass-fibre filter paper.

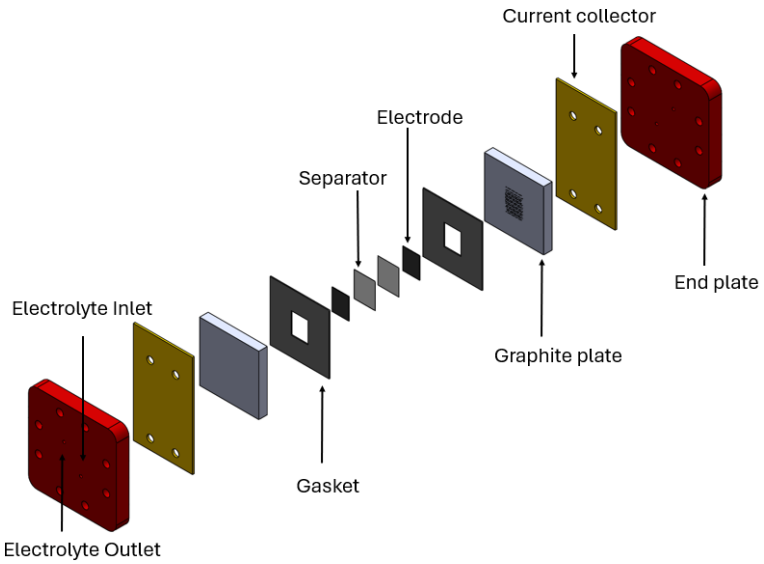

Figure 5.2.1 Scribner flow cell configuration with current collectors, graphite plates, gaskets, separators, and carbon cloth electrodes.

Table 5.2.1 Characteristics of the two activated carbon cloth (ACC) samples employed in the assembly.

	Weight	**Thickness**	**Specific Surface Area**
	g m^{-2}	*mm*	*m^2 g^{-1}*
Kynol ACC-507-20	90	0.43	>1800
Actitex	110	3.00	>1800

The first attempt to assemble the circuit employed a single pump for both sides of the cell; however, due to different pressure drops, the electrolyte did not flow evenly between the positive and negative compartments. The first configuration adopted, schematically shown in Figure 5.2.2a (SET-UP 1), uses two peristaltic pumps (Masterflex L/S model 77202-60), one dedicated to each side, paired with 1/8-inch tubing. The peristaltic pump compresses a flexible tube with an internal diameter of 3.1 mm (Masterflex L/S 16). The rotation speed was set to 20 rpm, corresponding to a volumetric flow rate of approximately 1.6 mL min^{-1}. An aqueous solution of 1 M Na_2SO_4 served as the electrolyte during each test. The electrolyte flows from the bottom of the reservoir, splitting into two circuits and driven by the pumps. Before entering the cell, it passes through a T-type connection designed to introduce the gas stream. Inside the cell, the flow follows the serpentine channel and exits on the same side as the inlet, mixing with the electrolyte from the opposite compartment before returning to the reservoir, where it drips back. The reservoir includes a tip at the top that enables the extraction of the headspace gas mixture, which is analysed to assess the adsorption and desorption of CO_2. The gas mixture passes from the headspace into a drying tube filled with $CaCl_2$ to reduce the water content that may interfere with CO_2 detection. The concentration of CO_2 in the gas stream, expressed as volume %, is monitored using a non-dispersive infrared (NDIR) sensor (SprintIR-6S by Gas Sensing Solution). After the drying tube the gas flows towards the CO_2 sensor, passes across it, and then moves outward into the atmosphere.

During the experimental test, a second version of the circuit was also employed, illustrated in Figure 5.2.2b (SET-UP 2). Dr Malina Seyffertitz (Alexander Forse's group member) designed this configuration to enhance the measurement of rapid CO_2 fluctuations. Indeed, the measurement of CO_2 concentration is affected by the variation of gas path cross-section. These variations occur when the gas moves from the tube into the reservoir headspace or into the drying tube, thus shifting from a narrow cross-section to a wider one where a larger gas volume with different concentration is present. This effect may reduce the peak measurement

of the CO_2 sensor due to the mixing of the gas in the wider volume areas. For this reason, the new arrangement excludes the drying tube from the system and switches the reservoir inlet and outlet to minimise the headspace volume, thereby reducing the cross-section variation. In addition, an Ag/AgCl reference was inserted between the two separator foils to evaluate the electrochemical behaviour of each electrode. SET-UP 2 can be considered an evolution of SET-UP 1, and this work presents results from both in order to enable comparison.

The gas supply can be adjusted to pure N_2 or to a mixture of CO_2 and N_2. Different proportions in volume of CO_2 were tested, but the 15–85 CO_2–N_2 ratio is the most relevant and serves as a simulated flue gas for point source carbon capture as described in Section 1.3.

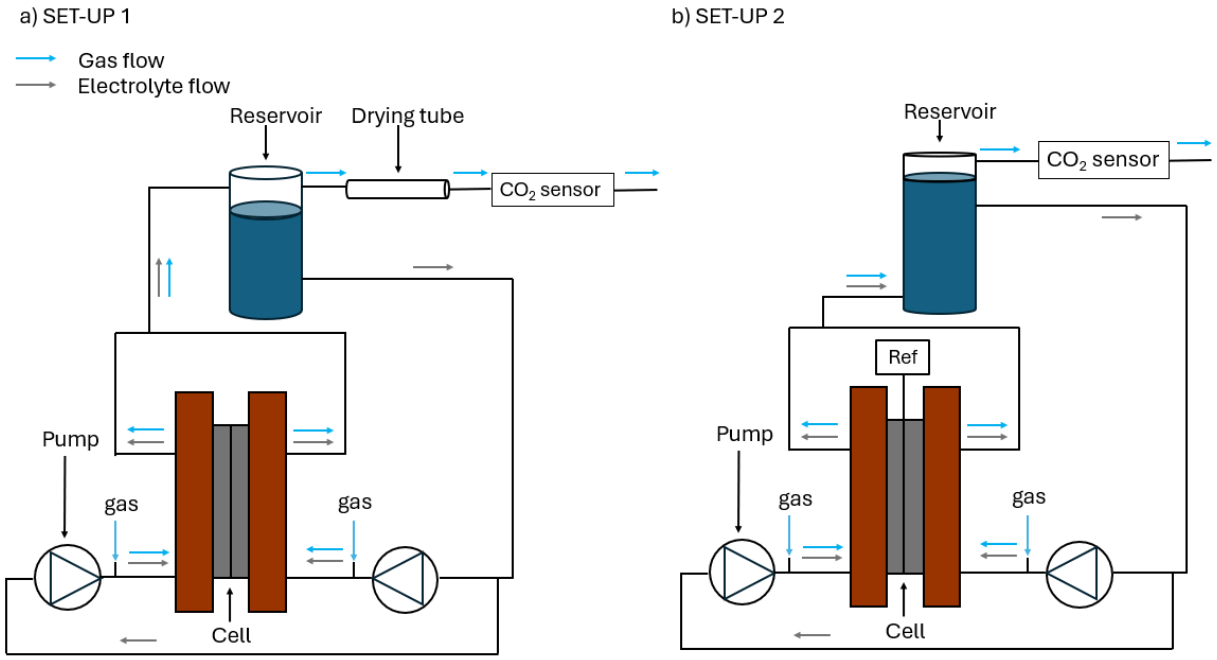

Figure 5.2.2 Circuit configurations: a) SET-UP 1 with two pumps and T-type gas connection; b) SET-UP 2 modified to reduce cross-section variation and including an Ag/AgCl reference.

As reported in previous studies, asymmetrically gas-exposed cells exhibit different results depending on whether the gas-exposed electrode is positively or negatively charged; in detail, the cell absorbs CO_2 when the gas-exposed electrode is negatively charged. In addition, the switching protocol, ranging from the negative potential value to the positive end, demonstrates the most effective adsorption results [3]. These findings emphasise the importance of exploring the negative and switching charging protocol as the cell undergoes a polarity shift between the two electrodes when the cell voltage is reversed; this process is enabled by the symmetry of the supercapacitor. The flow setup enables operation under both

symmetric and asymmetric gas-exposure conditions, permitting researchers to investigate various combinations of charging protocols and gas exposure. We employed Cyclic Voltammetry (CV) and Galvanostatic Cycling with Potential Limitation (GCPL) as electrochemical techniques. The cell underwent a preliminary procedure in which it completed 20 CV cycles at 20 mV s^{-1} within the potential range of –0.6 to 0.6 V. This range is consistent with the stability attained by pairing activated carbon cloth with 1 M Na_2SO_4.

Two different testing methods were applied: the first one (*continuous method*) involves a sequence of GCPLs assessing the positive, negative and switching protocols without introducing any rest period or voltage hold. In this case, as illustrated in Figure 5.2.3a, the GCPL procedure comprises five cycles with the negative charging (operating voltage from 0 to -0.6 V; legend: neg), followed by five cycles with the positive charging (operating voltage from 0 to 0.6 V; legend: pos), then five cycles with the switching charging (operating voltage from -0.6 to 0.6 V; legend: swi), and finally returns to the negative charging (legend: neg2). The second method (*rest method*) focuses on the negative and positive protocol and enabled the effect of a 15-minute rest period (zero current) after each voltage and peak valley and between protocols, as depicted in Figure 5.2.3b. This latter method was applied to the second cell set-up, which includes the reference electrode.

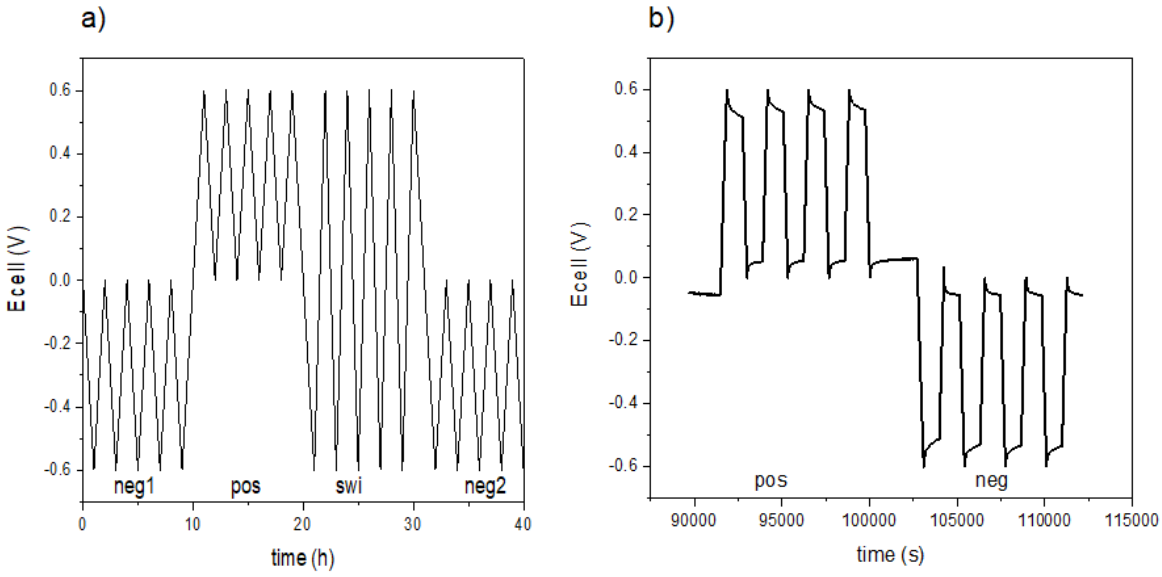

Figure 5.2.3 GCPL testing methodologies: a) continuous method (sequence without rest periods); b) rest method (sequence with 15-minute rest and reference electrode)

Tested current rates were evaluated according to the findings reported in research [3], where the highest adsorption rate was achieved at 30 mA g^{-1}. Consequently, the initial evaluated current rates were 2, 5, 10, 15, 20, 30, 40, 50, 60, 100, 150, 200, 250, 300 and 350 mA g^{-1}, calculated considering the average electrode mass. However, currents from 2 to 10 proved too low for the device because they were comparable to its leakage currents. Electrochemical tests were conducted within the range 15–350 mA g^{-1}, but from an SSA perspective the results were evident only in the range 50–350 mA g^{-1}.

The capacitance of each cycle was calculated by dividing the current rate by the average slope of the discharging voltage vs time profile: for the negative protocol, the segment from -0.6 to 0 V was assessed, and for the positive protocol, the segment from +0.6 to 0 V was examined; for the switching protocol, two segments were analysed, one from +0.6 to 0 and the other from -0.6 to 0 V. The mean capacitance was determined over 3 to 5 cycles, and the standard deviation was also considered.

The evaluation of the adsorption capacitance emerged as a challenging aspect of the research. In literature studies conducted on static SSA cells base the measurement of CO_2 fluctuations on pressure variations with a 100% CO_2 atmosphere [5] while other works on flow system measure the variation of CO_2 fraction [6]; the Landskron group reported the SSA metrics adopted in its flow SSA setup based on CO_2 concentration fluctuations, in a manner similar to the setup presented here with an atmosphere of 15% CO_2 and 85% N_2.[7] In this work, those Equations were adapted to the present configuration to account for the different flow measurement conditions; indeed in this setup, the gas flow was monitored only at the outlet by the NDIR sensor, whereas the inlet flow was determined by the flowmeter and considered constant throughout the experiments. Thus, the Equations reported in the paper were adapted to our setup as follows.

Since the CO_2 signal exhibits continuous oscillations due to adsorption and desorption around the 15 % fraction value, a baseline representing the mean trend around which these fluctuations occur, is needed. The employed baseline is a polynomial function with an order settable from 1 to 4, corresponding to the average y_{CO2} signal over time, as in ideal conditions this should maintain the same value throughout the examined period. The function is calculated as a polynomial regression using the least squares method. The number of moles

n_{CO2} is calculated according to Equation 5.2.1, where y_{CO2} indicates the measured CO_2 volume concentration and $y_{baseline}$ represents the baseline function; $\dot{n}_{TOT}$, which denotes the total flux of moles, is derived from the Ideal Gas Law (Equation 5.2.2) where P and T are the room pressure and temperature respectively; t_1, t_2 are the time coordinates where the baseline intercepts the y_{CO2} curve; Figure 5.2.4 illustrates, as an example, the integrated area obtained through Equation 5.2.1.

$$n_{CO_2} = \int_{t_1}^{t_2} [(y_{CO_2} - y_{baseline})\dot{n}_{TOT}]dt \quad 5.2.1$$

$$\dot{n}_{TOT} = \frac{P\dot{V}}{RT} \quad 5.2.2$$

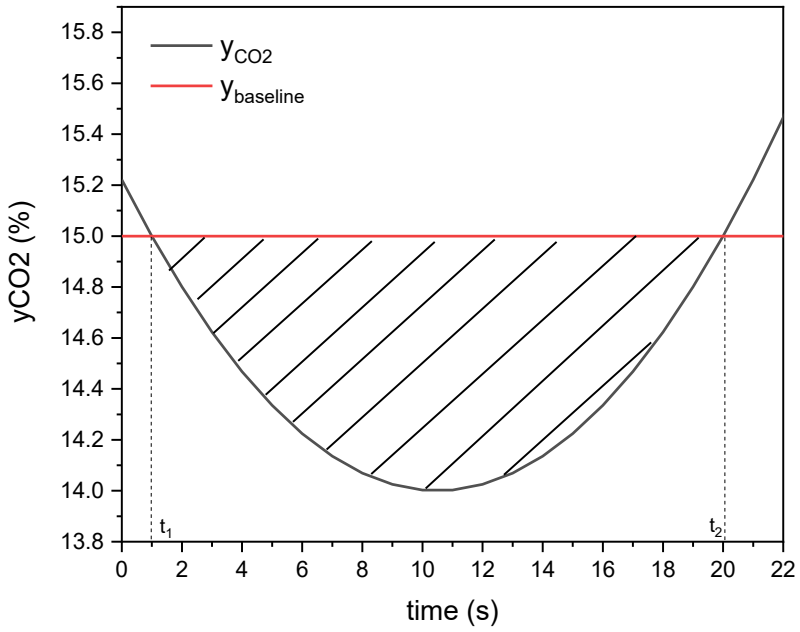

Figure 5.2.4 Example of CO_2 concentration profile (y_{CO_2}) and corresponding polynomial baseline ($y_{baseline}$). The shaded area between the measured signal and the baseline represents the integrated region used to calculate the amount of adsorbed CO_2 according to Equation 5.2.1.

The adsorption (AC) and desorption (DC) capacities (mol kg^{-1}) were calculated using Equation 5.2.3, where the moles were normalised by the average mass of the electrodes.

$$AC = \frac{n_{ads,CO_2}}{m_{avg,electrode}} \; ; \; DC = \frac{n_{des,CO_2}}{m_{avg,electrode}} \quad 5.2.3$$

In this context, the choice of the baseline strongly affects the AC and DC extrapolations and must therefore be selected appropriately. AC and DC were extrapolated for each cycle by calculating the mean (μ) for each protocol (μ_{AC} and μ_{DC}) as well as the standard deviation (SD). It is important to evaluate both AC and DC to verify whether they exhibit similar values, as literature evidence suggests that SSA adsorption is largely reversible [1]. This assumption implies that the baseline can be adjusted so that AC and DC are comparable; however, this approach may not take into account any CO_2 that is irreversibly captured. On the other hand, in some cases, the results demonstrated fluctuations in CO_2 concentration that appeared unrelated to the SSA behaviour, and the baseline function order was adjusted to disregard these trends. To assess the consistency of the extrapolated AC and DC rates, I proposed an approach derived from standard statistical error propagation principles [8]. A statistical indicator of the comparability between the AC and DC mean values was defined as the ratio between their difference and the propagated uncertainty on that difference, and denoted as R. R was calculated according to Equation 5.2.4, where $SEM = SD/n^{0.5}$ represents the standard error of the mean over the number of samples n. If $R < 1$, the two means are considered comparable because the difference is lower than the experimental error. If $R < 2$, the difference may be explained by experimental noise. If $R > 2$, the adsorption and desorption rates are considered not comparable. Varying the order of the polynomial baseline helped to obtain the most similar AC and DC mean rates; however, in some acquisitions, it was not possible to achieve low R values. Nevertheless, all AC and DC data reported in this Chapter underwent this analysis to be considered valid: mean values with R> 2 were discarded.

$$R = \frac{|\Delta|}{\sigma_\Delta} = \frac{|\mu_{AC} - \mu_{DC}|}{\sqrt{SEM_{AC}^2 - SEM_{DC}^2}} \qquad 5.2.4$$

Table 5.2.2 presents a summary of the tests conducted on the flow supercapacitor cell through different assemblies: three main assemblies were considered. F0 and F1 employed the ACC-507-20 carbon cloth and SET-UP 1, while F5 used a different carbon cloth and SET-UP 2. The continuous method was applied to all cells, whereas the rest method was applied only to F5. The gas mixture that flowed through the cell consisted of 15% CO_2 and 85% N_2 in every test, but the stream was directed in three different ways: it was supplied to both sides of the cell, to the positive side, and to the negative side, in order to assess the impact of the gas-exposed electrode on the results.

Table 5.2.2 Summary of the tests conducted on the flow supercapacitor cell under different assemblies and gas flow configurations.

	Configuration	ACC type	Electrochemical method	Exposed side of the cell		
				both	*pos*	*neg*
F0	SET-UP 1	ACC-507-20	continuous method	X	-	-
F1	SET-UP 1	ACC-507-20	continuous method	X	X	X
F5	SET–UP 2	Actitex	continuous/rest method	-	X	-

5.3 Results and discussion

This Section reports the electrochemical (Section 5.3.1) and SSA performance (Section 5.3.2) results obtained by the experimental tests conducted on the three cells F0, F1 and F5.

5.3.1 Electrochemical performances of the cells

Preliminary CVs at 20 mV s^{-1} were conducted on both F0 and F1 cells, and they displayed a box-shaped profile consistent with the behaviour of a symmetric supercapacitor, as illustrated in Figure 5.3.1.1a. Afterwards, we conducted GCPL experiments, according to the *continuous method*, at different current rates on F0, F1 and F5. As an example, Figure 5.3.1.1b presents some voltage profiles, which demonstrate a linear trend during both charge and discharge phases. All three cells exhibit triangular-shaped outcomes: in particular, F0 and F1 (containing the same ACC with 15% CO_2 flowing on both sides) almost coincide at the highest current (150 mA g^{-1}) and reveal very similar behaviour at the lowest (50 mA g^{-1}) with a small ohmic drop. F5, which employs a different ACC and receives the 15% CO_2 stream only on the positive side, indicates a lower capacitance and a larger ohmic drop that may be attributed to the greater electrode thickness and its lower wettability. We evaluated capacitance for each current rate, focusing especially on the results obtained with F0, where GCPLs were conducted both without and with gas flow to assess the impact of the stream on the electrochemical performance. Figure 5.3.1.1c reports mean capacitances for each current rate with no gas stream: mean capacitance across the different protocols remained consistent within the same current rate, while a slight decrease appeared when the current reached the highest values. Furthermore, Figure 5.3.1.1d compares the same no-gas-stream capacitance with that obtained

under the CO_2–N_2 mixture; we also reported the Mean Capacitance measured when a 100% N_2 stream flowed through the cell. The graph clearly demonstrates that mean capacitance increases of more than 10% at the lowest current rates when CO_2 enters the cell. This increase may be attributed to the dissolution of CO_2 in the electrolyte as HCO_3^-, which could enhance the conductivity of the electrolyte. As stated earlier, cell F5 was assembled according to SET-UP 2, which incorporates the reference electrode. Figure 5.3.1.1e illustrates the voltage profiles of the cell (E_{cell}), working electrode (E_{WE}), and counter electrode (E_{CE}) during the positive and negative protocols. It is important to emphasise that the two electrodes do not demonstrate symmetrical behaviour across the two protocols. Indeed, the potential windows attained by the single electrodes during the positive protocol are slightly different. When switching to the negative protocol, the potential windows of the electrodes interchange, demonstrating that the observed asymmetry is not related to the electrode material itself. This phenomenon can be interpreted by considering ion migration from one side to the other, which effectively reverses the polarity of the supercapacitor. In fact, Na^+ and SO_4^{2-} ions have different sizes and solvation properties, leading to electric double layers with distinct characteristics at negatively and positively polarized electrodes, respectively. The asymmetry is further confirmed by Figure 5.3.1.1f, which presents the mean capacitance extrapolated for the cell and single electrodes, indicating that the capacitance of the negatively charged electrode is higher. It is important to recall that F0 exhibited increased capacitance when the CO_2 mixture flowed inside the cell (Figure 5.3.1.1d). In F5 the gas stream passed through the positive side (WE) of the cell, yet this electrode did not display increased capacitance. These results suggest that the capacitance increases on both sides of the cell without any predominance of one side.

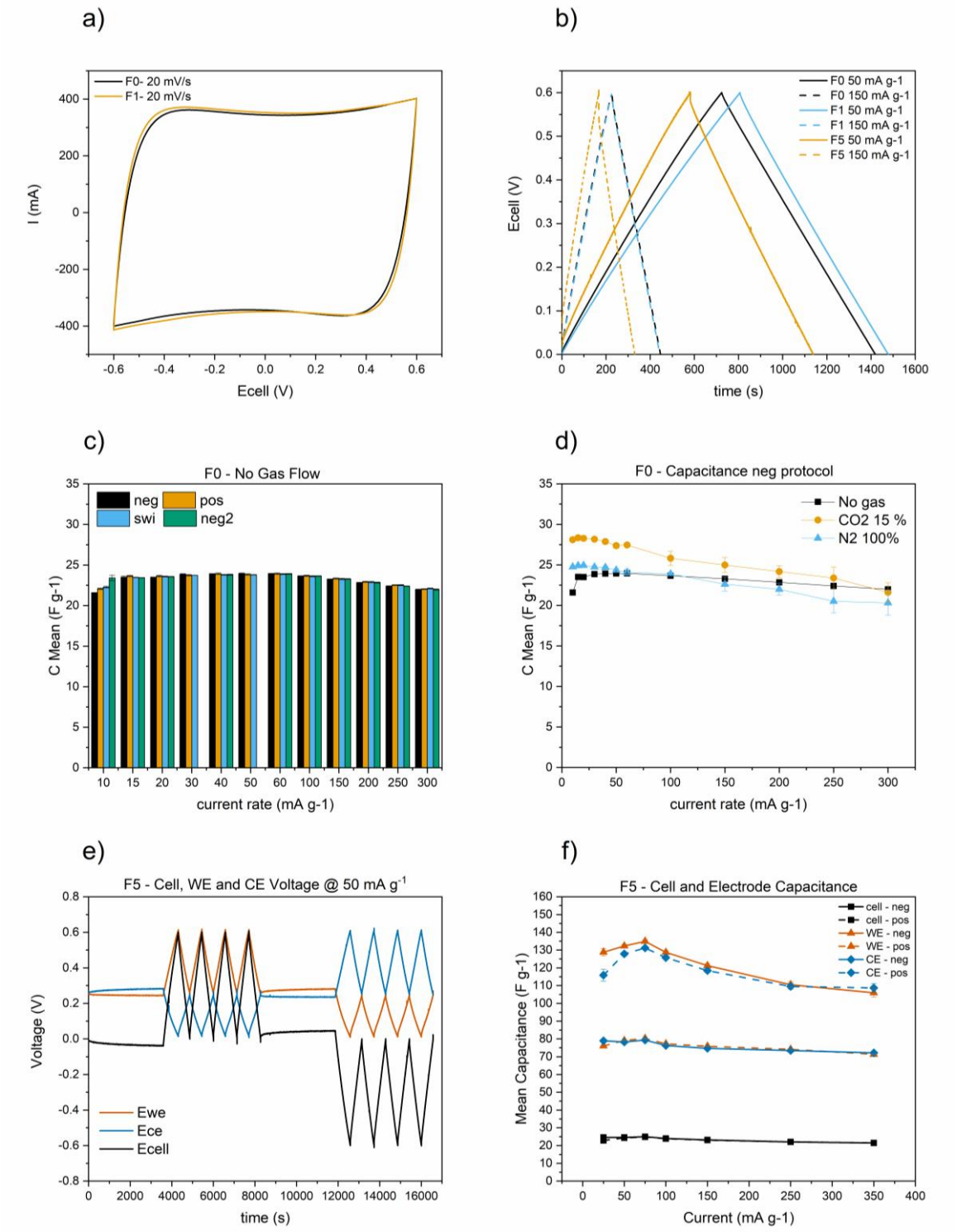

Figure 5.3.1.1 Electrochemical characterisation of F0, F1 and F5 cells: a) F0 and F1 CVs at 20 mV s^{-1}, b) GCPL profiles at different currents, c) mean capacitance of F0 without gas flow, d) mean capacitance comparison with CO_2–N_2 and N_2 streams, e) voltage profiles of E_{cell}, E_{WE} and E_{CE} for F5 under positive and negative protocols, f) mean capacitance values of F5 cell and individual electrodes

5.3.2 SSA performances

Continuous Method on Symmetric Gas Exposure Results

The first SSA studies were conducted on F0 using a CO_2 15% N_2 85% gas mixture flowing through both sides of the cell. Figure 5.3.2.1 illustrates the juxtaposition of the CO_2 concentration data with the GCPL profile at 50 mA g^{-1} obtained by applying the *continuous method*. The Figure highlights a correlation between the variation of CO_2 concentration with the voltage polarization. From a qualitative perspective there appears to be no preference regarding applied protocol, meaning that adsorption of CO_2 (negative peaks) seems to coincide both with the lowest or highest voltages achieved during polarization of the cell F0 (Figure 5.3.2.1 a-c-e). This trend is particularly evident in the switching protocol (Figure 5.3.2.1 e), where CO_2 adsorption is observable for each positive and negative polarization cycle. The same experimental procedure was undertaken on F1 but the SSA behaviour was different (Figure 5.3.2.1b-d-e). Results indicate that adsorption in this case favours the negative charging protocol, as no CO_2 adsorption is detected under the positive protocol (Figure 5.3.2.1d). Moreover, the switching protocol confirms that adsorption occurs exclusively when the polarity becomes negative (Figure 5.3.2.1f). However, the acquisitions on F0 and F1 were carried out in two-electrode mode without reference, and therefore the behaviour of F1 remains unclear.

The adsorption capacity of F0 is summarised in the bar chart presented in Figure 5.3.2.2a, which displays values derived at different current rates. This chart demonstrates that the positive protocol appears to generate the highest adsorption capacity, with approximately 40 mmol kg^{-1} at 50 mA g^{-1}. In addition, the adsorption capacity decreases as the current rate increases. Despite the unclear behaviour, the "asymmetry" of the cell F1 appeared to provide benefits in terms of adsorption. Figure 5.3.2.2b compares the adsorption capacity obtained through the negative protocol on F0 and F1, revealing higher values for F1 (around 40 mmol kg^{-1} at 50 mA g^{-1}). These results will be reconsidered in the next Section in comparison with those obtained with the *rest protocol* applied to F5.

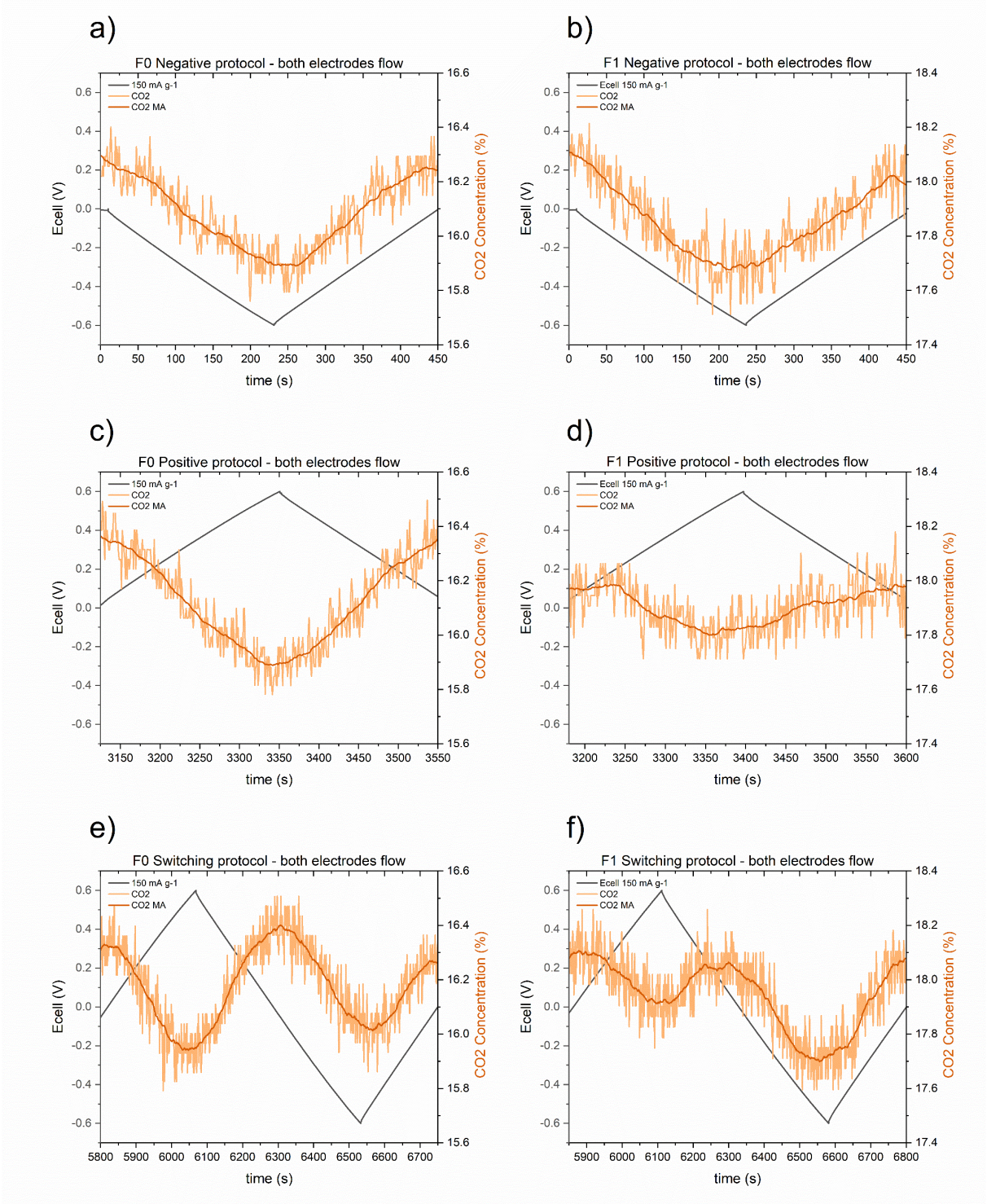

Figure 5.3.2.1 Comparison of SSA behaviour and CO_2 adsorption capacity for F0 and F1. Figures a, c, e) present the overlap of voltage profile, CO_2 concentration, and CO_2 moving average for cell F0 under the negative, positive, and switching protocols, respectively, all recorded at 150 mA g^{-1}. Figures b, d, f) show the corresponding data for cell F1 under the same conditions.

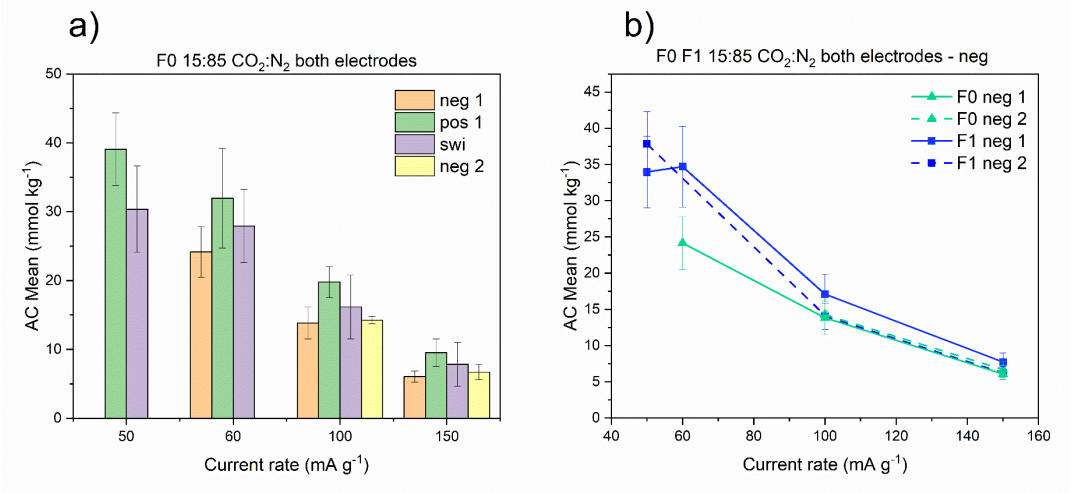

Figure 5.3.2.2 a) Adsorption capacity of F0 at different current rates, b) Adsorption capacity comparison between F0 and F1 under the negative protocol

Comparison of Continuous Method on Symmetric and Asymmetric Gas Exposure Results

F1 was evaluated under both symmetric and asymmetric gas exposure conditions. Figure 5.3.2.3a displays the AC Mean derived from data obtained by applying the continuous method, specifically presenting the negative protocol results. The gas stream was initially directed through the positive half-cell and subsequently through the negative half-cell. The reported outcomes indicate that the AC Mean is higher when the positive half-cell undergoes gas exposure. The results obtained with exposure of the negative half-cell demonstrated inconsistent SSA behaviour and, when available, lower values. The switching protocol produced noteworthy outcomes. Figure 5.3.2.3b compares the AC extrapolated from the F0 switching protocol (conducted under symmetrical gas exposure) with the same protocol applied to F1 under positive half-cell gas exposure; at 50 mA g^{-1}, F1 reached the highest AC of approximately 50 mmol kg^{-1}, which the CO_2 concentration fluctuation (reported in Figure 5.3.2.3c) also qualitatively confirmed. Indeed, in contrast to the behaviour illustrated in Figure 5.3.2.1e, where adsorption and desorption occur during each polarisation (whether positive or negative), leading to two desorption peaks and two adsorption peaks, a different pattern is observed in this case. Only one adsorption and one desorption appear to occur, with adsorption related to the negative polarisation and desorption to the positive one. Nevertheless, these outcomes obtained with the switching protocol were not further reproducible. Based on the acquired results, the investigation proceeded by considering only

the asymmetric gas exposure, using both the positive and negative protocols according to the *rest method*, which introduces a rest period after each voltage peak and valley, as explained in Section 5.2.

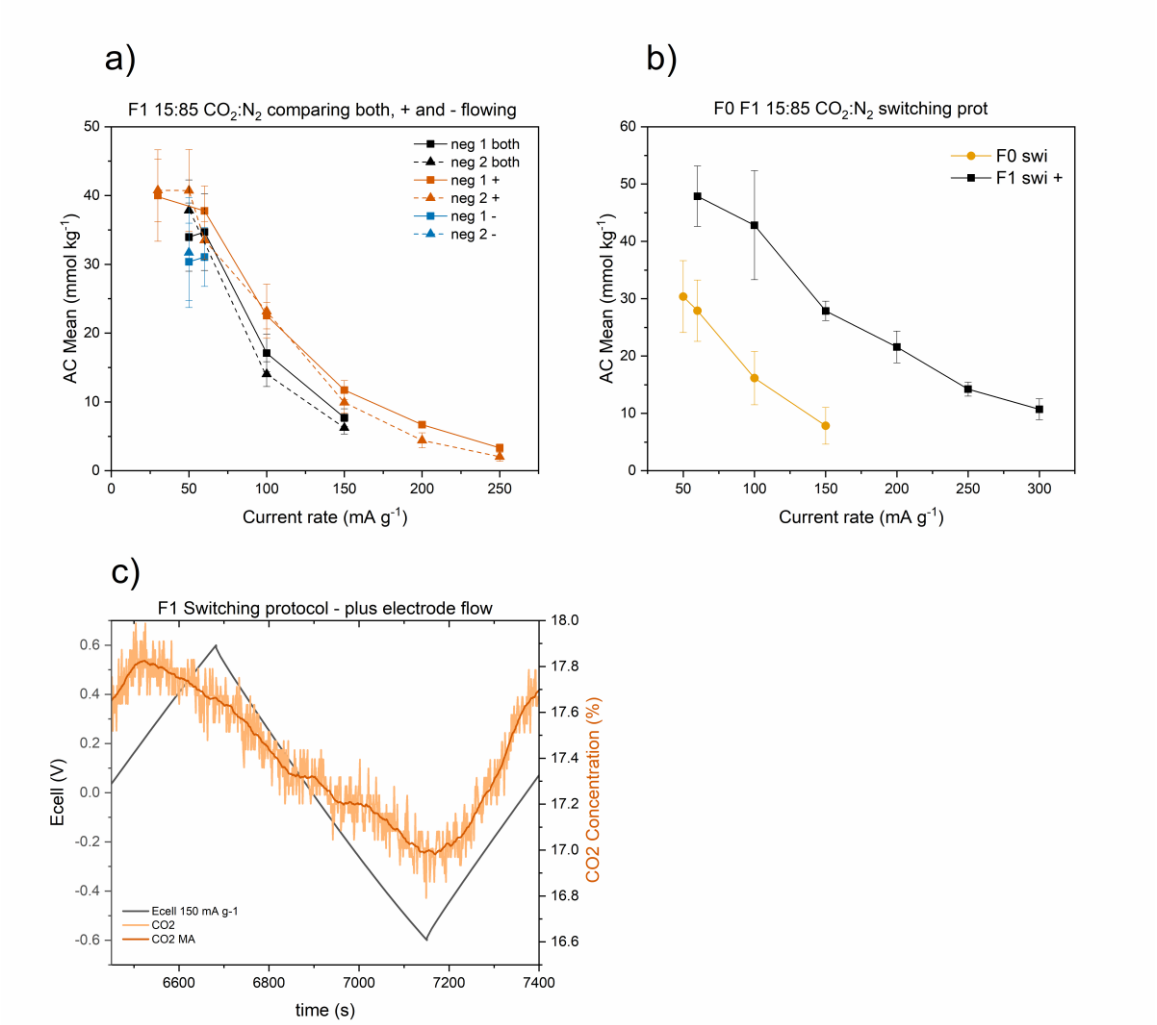

Figure 5.3.2.3 a) F1 AC Mean derived from the negatve protocol continuous method under symmetric and asymmetric gas exposure, b) Comparison between AC extrapolated from the F0 switching protocol with symmetric gas exposure and the same protocol applied to F1 with postivie half-cell exposure. c) CO_2 concentration fluctuation associated with the F1 switching protocol

Comparison between Continuous and Rest Method on Asymmetric Gas Exposure Set up

New experimental investigations concentrated on cell F5, which was assembled and tested by Dr Malina Seyffertitz, whereas my contribution focused on the analysis of the obtained data. The new configuration (SET-UP 2), combined with the *rest method*, enabled the achievement of clearer outcomes and an adequate baseline as a reference for numeric extrapolation. Figure

5.3.2.4 illustrates the CO_2 moving average chart adjacent to the voltage profile, comparing the negative protocol (a-c-e) outcomes with the positive ones (b-d-f) across different current rates (50, 150, 350 mA g^{-1}). In the negative protocol results, it appears evident that adsorption occurs when the cell receives a negative polarization; during the rest phase the CO_2 concentration returns to the baseline average value; CO_2 desorbs when the voltage returns to 0. Unfortunately, the positive protocol exhibits ambiguous fluctuations, since desorption appears in the positive phase when the voltage rises, but adsorption seems to occur during the rest period; moreover, a new small adsorption valley emerges during the discharge phase and a small adsorption peak during the subsequent rest phase. Because the positive protocol generated unclear outcomes, only the adsorption rates obtained through the negative protocol will be displayed in Figure 5.3.2.5.

F5 underwent both the *rest* and the *continuous method*, enabling a comparative analysis. Figure 5.3.2.5a illustrates the adsorption capacities obtained through the two methods and compares F5 with the results achieved by F1 under identical conditions. The *rest method* generated the highest AC, particularly at the fastest current rates. The *continuous method* applied to both F1 and F5 resulted in diminished adsorption when currents exceeded 100 mA g^{-1}. By examining Figure 5.3.2.4a-c-e, it is worth noting that the CO_2 adsorption peak is delayed in time in comparison with the end of the polarization; this phenomenon becomes more evident at the highest currents. This indicates that excluding the rest period would not allow the full exploitation of the adsorption attainable at that current. A similar outcome was identified by Mapstone et al. [3], where carbon adsorption, measured by pressure, exhibited a delay in the maximum CO_2 adsorption with respect the electrode polarisation, which they attributed to a mass-transport limitation. As an exploratory investigation, the adsorption test using a 30:70 CO_2:N_2 gas mixture was conducted: Figure 5.3.2.5b reports the AC values, highlighting an increased adsorption rate compared to the results achieved with the 15:85 CO_2:N_2 gas stream. This result could be attributed to a higher dissolution of CO_2 within the electrolyte. In addition, the 30% CO_2 adsorption value, reaching approximately 45 mmol kg^{-1} at 25 mA g^{-1}, constitutes a satisfactory outcome when compared with the performance of a static cell reported in [3], which operates at 30 mA g^{-1} under 100% CO_2 exposure and can attain around 60 mmol kg^{-1}.

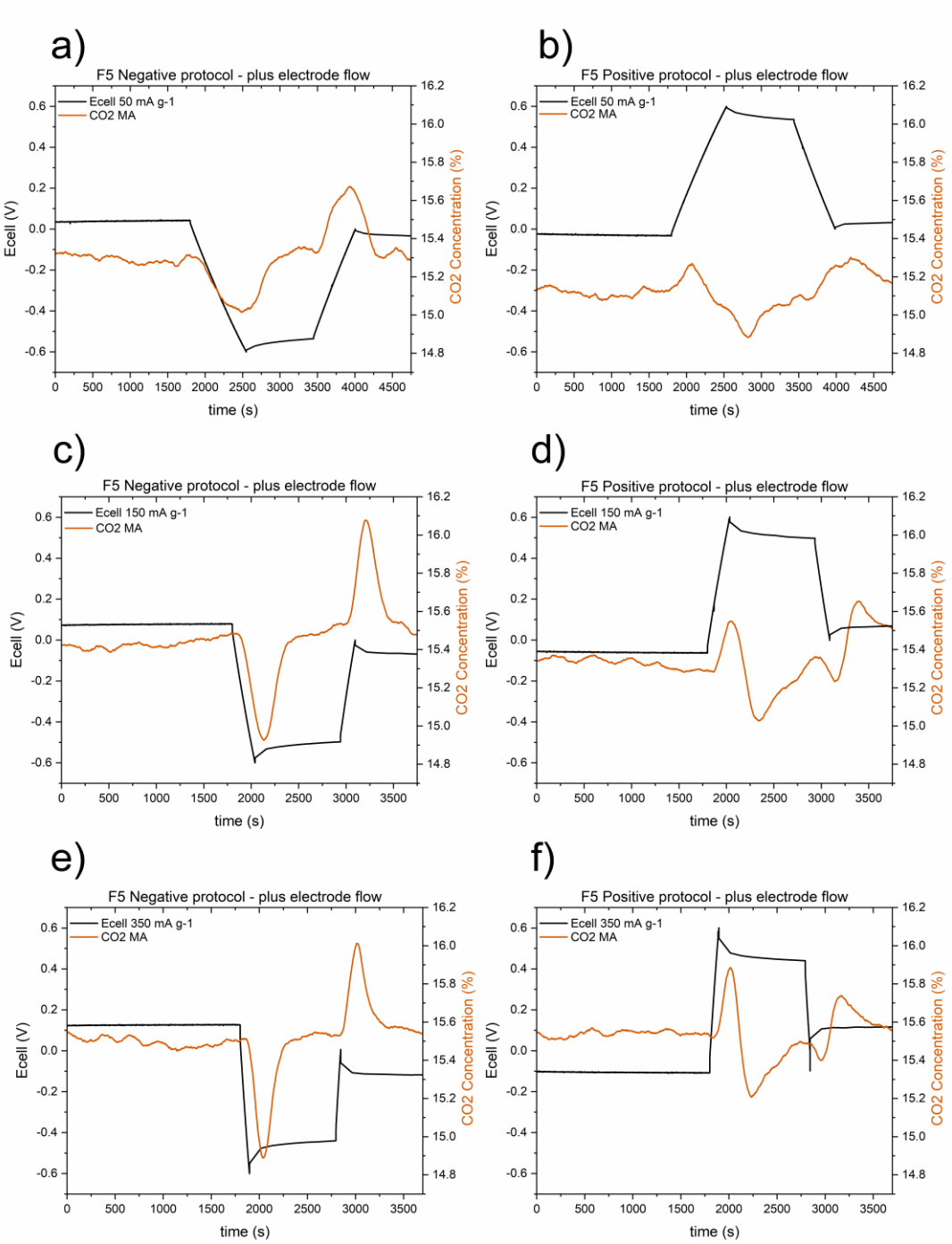

Figure 5.3.2.4 Moving average CO_2 concentration plot superimposed on the voltage profile, comparing outcomes of the negative protocol (a–c–e) and the positive protocol (b–d–f) at different current rates (50, 150, 350 mA g^{-1})

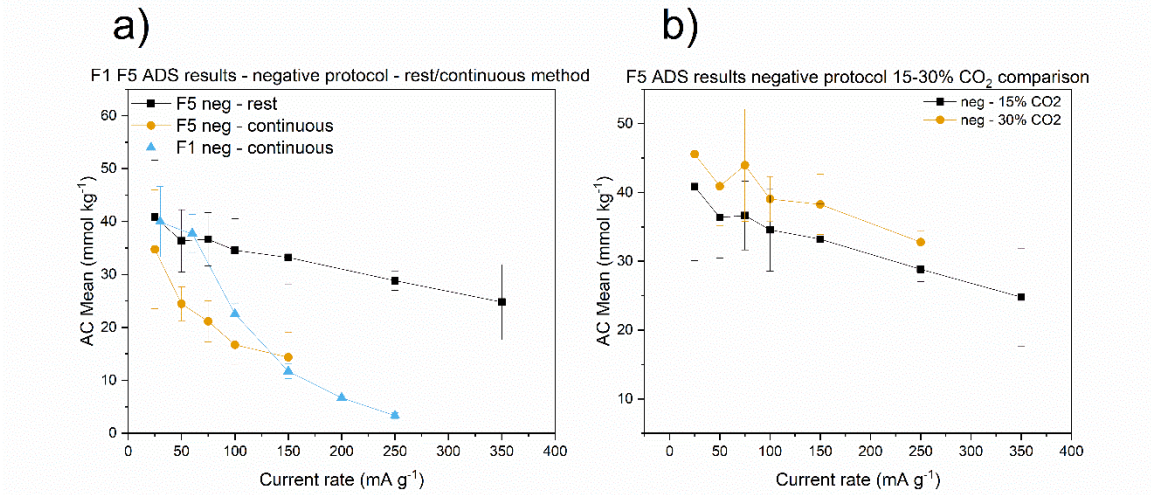

Figure 5.3.2.5 (a) Adsorption capacities (AC) mean of F1 and F5 obtained by rest and continuous methods. (b) AC values from adsorption tests with 30:70 and 15:85 CO_2:N_2 mixtures, showing enhanced adsorption at higher CO_2 concentration.

SSA Mechanisms analysis

The flow electrochemical supercapacitor system combined with the CO_2 gas stream generated fluctuations in the CO_2 fraction that are likely associated with the SSA phenomenon. At present, the mechanisms governing this behaviour remain unclear. During the experimental tests on F0, SSA-like behaviour was observed when the gas stream flowed through both sides of the cell, i.e. under completely symmetric conditions (Figure 5.3.2.1). Another possible explanation relates to the observation that, despite the symmetry of the system indicated by the reference electrode, the two electrodes exhibit different capacitances, which may enable differential adsorption when they are positively or negatively charged. These findings suggest that the mechanism responsible for CO_2 adsorption could involve either gas–solid or molecular liquid–solid interactions. Using the one-sided exposed set-up on F5 with the negative protocol (Figure 5.3.2.4) enabled a clearer observation of the behaviour, whereas inverting the polarity with the positive protocol produced inconclusive assumption.

5.4 Conclusions

The flow electrochemical supercapacitor configuration represents a valid system to investigate the SSA phenomenon and enables progress towards an effective CO_2 separation. The adopted arrangement permitted monitoring of SSA behaviour, although the mechanisms governing it remain unclear. Nevertheless, the present study constitutes a further step towards SSA comprehension due to the flexibility of the system. The opportunity to analyse symmetric and asymmetric cells and flows facilitates several possible configurations. For instance, one option is to assemble two circuits, one for each side of the cell, thereby completely separating the two sides. At present, this configuration was not attainable because the porosity of the glass-fibre separator allowed electrolyte to flow from one side to the other of the cell. The implementation of membranes could enable the investigation of different SSA behaviours that would consider ion mobility across the selected membrane.

One potential method to separate CO_2 involves employing carbon slurries instead of solid electrodes. The main limitation of SSA is that CO_2 becomes captured within the electrodes, which are not easily removed from the cell. Utilising carbon slurries could generate a "CO_2-charged" slurry that might be transferred to another facility for release. An example of a configuration that demonstrates this possibility is reported in [9] by Volker Presser et al.

Moreover, a comprehensive analysis of the system's energy consumption should be conducted, including the energy required for pumping. To compare results with alternative technologies, an upscaled estimation of the adsorption rate relative to the energy consumption is required. Indeed, it remains difficult to compare SSA performance, which is normalised by electrode mass, with, for instance, amine-based technologies, where results are normalised by solution mass.

5.5 Chapter 5 References

[1] Kokoszka, B., Jarrah, N. K., Liu, C., Moore, D. T., & Landskron, K. (2014). Supercapacitive swing adsorption of carbon dioxide. Angewandte Chemie International Edition, 53(14), 3698–3701. https://doi.org/10.1002/anie.201310308

[2] Wang, Y., Zhang, K., Feng, J., Sun, X., Li, C., Wang, K., Zhang, X., & Ma, Y. (2023). Supercapacitive swing adsorption of carbon dioxide: Current status and perspectives. Batteries & Supercaps, 6(12), e202300283. https://doi.org/10.1002/batt.202300283

[3] Mapstone, T., Ravi, S., & Suss, M. E. (2025). Understanding the mechanism of electrochemical CO_2 capture by supercapacitive swing adsorption. Energy & Environmental Science, 18(1), 123–135. https://doi.org/10.1021/acsnano.4c10931

[4] Liu, C., & Landskron, K. (2017). Design, construction, and testing of a supercapacitive swing adsorption module for CO_2 separation. Chemical Communications, 53(26), 3661–3664. https://doi.org/10.1039/c7cc01055a

[5] Xu, Z., Mapstone, G., Coady, Z., Wang, M., Spreng, T. L., Liu, X., Molino, D., & Forse, A. C. (2024). Enhancing electrochemical carbon dioxide capture with supercapacitors. Nature Communications, 15, 7851. https://doi.org/10.1038/s41467-024-52219-3

[6] Bilal, M., Li, J., & Landskron, K. (2023). Enhancing supercapacitive swing adsorption of CO_2 with advanced activated carbon electrodes. Advanced Sustainable Systems, 7(11), 2300250. https://doi.org/10.1002/adsu.202300250

[7] Zhu, S., Ma, K., & Landskron, K. (2018). Relationships between the charge–discharge methods and the performance of a supercapacitive swing adsorption module for CO_2 separation. The Journal of Physical Chemistry C, 122(32), 18476–18483. https://doi.org/10.1021/acs.jpcc.8b03968

[8] Taylor, J. R. (1997). An introduction to error analysis: The study of uncertainties in physical measurements (2nd ed.). University Science Books.

[9] Presser, V., Dennison, C. R., Campos, J., Knehr, K. W., Kumbur, E. C., & Gogotsi, Y. (2012). The electrochemical flow capacitor: A new concept for rapid energy storage and recovery. Advanced Energy Materials, 2(7), 895–902. https://doi.org/10.1002/aenm.201100768

Chapter 6: Conclusions

The European Green Deal defines the ambitious goal of reducing European emissions by 90% by 2040, aiming to make Europe the first climate-neutral continent. To reach this demanding objective, the energy sector must shift from fossil fuels to renewable alternatives and promote the electrification of transport and industry, while implementing CO_2 capture technologies. Within this framework, Energy Storage Systems play a crucial role: indeed, they can store energy derived from renewable sources characterised by intermittent and variable power, therefore improving the overall energy management efficiency In particular, Electrochemical Energy Storage Systems are suitable for these applications and for electrification. A significant degree of flexibility can be achieved by integrating different technologies to address the requirements of specific applications. Integration can occur at different levels, ranging from the System level to the Material level and, ultimately, the Functional level. This research examined the integration of different technologies at multiple levels, with a specific focus on flow systems and supercapacitors. In detail, this work investigated the design, development, and assessment of capacitive–flow hybrid systems as electrochemical solutions for clean energy and climate applications.

Chapter 3 focuses on the investigation of Supercapacitor-based Hybrid Storage Systems and Energy Harvesters describing two examples of System integration. The work reported in Section 3.1 explores the integration of a Vanadium Redox Flow Cell (VRFC) with a Supercapacitor (SC) in a passive configuration (avoiding DC–DC converters) under ideal operating conditions (Section 3.1.1) and realistic load scenarios (Section 3.1.2), together with a Life Cycle Assessment (LCA) and an economic evaluation of a potential upscaled hybrid system. The study highlights that the passive connection between the two systems is an effective strategy to exploit their combined benefits while reducing cost and environmental impact. The experimental analysis demonstrates that SC-VRFC coupling enables discharging at higher currents than those limited by the VRFC due to the contribution of the SC, thus increasing the energy delivered during short discharges. Furthermore, the direct connection of the VRFB with the SC is feasible when their cell voltages are comparable, which enables the use of water-based SC presenting similar operating voltage to that of the VRFC. A numerical

model was developed to predict the system's discharge and to provide a sizing tool capable of designing the capacitance according to the desired energy output. The model was later refined into a semi-empirical version, allowing simulation of real current loads, particularly the current profile of an electric city bus. This analysis revealed another benefit provided by the SC: the capacitance filters current peaks, thereby reducing fluctuations. This filtering effect can enhance the efficiency of the battery in practical applications. The LCA identified that the vanadium electrolyte represents the major contributor to the overall impact and that the passive configuration is more sustainable than the active one (with converters). Therefore, to further reduce the environmental burden of the HESS, alternative electrolytes for RFBs should be considered. The economic assessment confirmed that the passive configuration combined with the use of water-based electrolytes represents the most cost-effective solution. This study constitutes a step towards the practical implementation of such systems. Further experimental testing on an upscaled HESS is required to validate these results and to assess cycling stability, efficiency, and maintenance costs. The achieved results demonstrate that system integration can improve power performance compared with a single storage system, thereby expanding the application range while reducing economic and sustainability impacts.

Section 3.2 presents a study on the integration of a piezoelectric nanogenerator with a supercapacitor, where the first acts as an energy harvester from mechanical stress and the latter as a rapid energy storage device. My research concentrated on modelling the charging process of the previously tested supercapacitor. Two piezoelectric devices were assembled and employed to charge the SC: one made of lead zirconate titanate (PZT) and another obtained through polymer electrospinning (nanofibrous piezoelectric device, NF). The charging voltage profiles of the supercapacitor were recorded during both experiments, and the model aimed to reproduce these curves for validation purposes. The developed model predicted the charge curve of the PZT–SC system with a relative error of 9.4% and a 7% deviation in transmitted energy. In the case of the NF–SC system, replication of the curve was not achieved, likely due to the difficulty in characterising the NF piezoelectric device to obtain parameters required for model integration. However, the model serves as a valuable tool to estimate and predict system behaviour, which can be validated case by case. For the PZT–SC configuration, the model is validated for alike systems and applicable for evaluating charging times of systems with different nominal parameters (e.g., capacitance) and for use as a module when several

PZT–SC units are connected to harvest and store larger amounts of energy. This case of System integration enables the storage of energy harvested from a low-energy source, namely deformation energy, which cannot be effectively stored using alternative storage systems.

Chapter 4 presents my contribution to the development of a semi-solid lithium–air flow battery (SLAFB, NESSOX) prototype in collaboration with Bettery S.r.l. which employs carbon-based slurries as catholyte. The purpose of this research was to simplify the cell design, specifically by removing the three-dimensional current collector known as reticulated vitreous carbon. This component, due to its fragility and inner position within the cell, causes several assembly issues, such as slurry agglomerates formation and breakage during assembly, in addition to its relatively high cost. The study demonstrated that removing the RVC is feasible when employing a carbon slurry with a higher carbon concentration (from 2% to 7%). Although the current density provided by the 7% slurry cell (1.5 mA cm^{-2}) was lower than that of the RVC cell with 2% carbon (3.0 mA cm^{-2}), it exhibited a more stable current profile with fewer fluctuations, probably due to the absence of agglomerates within the reactor. Furthermore, the new catholyte displayed pseudoplastic behaviour, meaning its viscosity decreases with increasing speed, implying that less pumping energy is required. The findings indicate that the overall system cost and assembly procedure can be improved; however, further research is necessary to optimise circuit management because of the viscosity properties of the new catholyte. The solution presented in this Chapter provides an example of material integration, whereby carbon materials derived from supercapacitor technology are incorporated into a flow system in order to enhance power performance.

The final part of this thesis is devoted to the result of my work conducted during my research stay at the Department of Chemistry "Yusuf Hamied" of the University of Cambridge within the Alexander Forse group, where I investigated CO_2 capture through flow supercapacitors using the Supercapacitive Swing Adsorption (SSA) phenomenon. The specific aim of this study is to design an electrochemical flow cell capable of effectively separating CO_2 from a gas stream. The developed system enabled simultaneous control of liquid and gas streams, allowing the evaluation of the cell under various charging protocols, current rates, and gas compositions. The results indicate that the flow configuration is suitable for conducting SSA experiments under various parameters, enabling the capture of up to 40 mmol kg^{-1} and 45 mmol kg^{-1} of CO_2 when exposed to 15% and 30% CO_2 concentrations, respectively (with N_2 as

the remaining component). These outcomes are remarkable compared to the static setup, which achieved approximately 60 mmol kg^{-1} at 100% CO_2 exposure. From a practical perspective, the flow system requires further development to achieve effective CO_2 separation from gas streams. To achieve this primary purpose future work may include the incorporation of ion-exchange membranes and switching carbon electrodes with carbon slurries that could permit to "store" the CO_2 inside of them. Chapter 5 presents a case of functional integration, in which the adoption of a flow system may offer advantages for CO_2 capture performance compared with static SSA configurations.

Overall, this thesis contributes to the scientific and technological advancement of hybrid capacitive–flow systems through a multidisciplinary approach that combines modelling, experimentation, and sustainability assessment. The experimental investigations achieved promising outcomes across all tested systems, but this research underlines the importance of modelling methods that should be considered when designing HESS. Moreover, to meet sustainability goals, it is essential to conduct LCA analyses to identify the critical components within a system. Future studies should focus on testing upscaled versions of each system presented here, and the modelling approaches can be further refined to simulate HESS behaviour under more dynamic and realistic conditions.

My work has been carried out under national and international, collaborative projects that involved different research groups. These extremely fruitful collaborations were carried out under different national and international projects. The groups and projects with which I collaborated are detailed in Chapter 7 and in the Acknowledgements and Collaborations Section.

Chapter 7: Acknowledgments and Collaborations

7.1 National and International projects

During my Ph.D. I've been working under the following national and international projects:

[1] European Union within the Horizon 2020 Research and Innovation Programme (Grant No. 963550 HYFLOW project https://hyflow-h2020.eu/). All the Partners are acknowledged for the fruitful discussions.

Where I participated in diverse European project meetings:

- 6th Project Meeting of Hyflow – Fraunhofer Institute for Chemical Technology (ICT), Pfinztal, Germany – March 24, 2023, Presentation of WP1, Task 1.3: SC-VRFB integration
- 7th Project Meeting of Hyflow – Online – August 2, 2023
- 8th Project Meeting of Hyflow – Holiday Inn, Lisbon, Portugal – October 25–27, 2023, Presentation of WP1, Task 1.3: SC-VRFB integration
- 10th Project Meeting of Hyflow – CRAEM, Marina di Ravenna (Ravenna), Italy – February 12, 2024, Member of the Organizing Committee and presentation of achieved results by UNIBO WP1, Task 1.3

[2] Piano Triennale 2025-2027 della Ricerca di Sistema elettrico (ENEA 2025) – indetto con D.M. MASE n. 388 del 06/11/2024, dal titolo LA1.26 Approfondimento: Elettroliti redox a base di metalli multivalenti per nuove generazioni di sistemi di accumulo, CUP I53C24003300001, CUP I53C24003300001

7.2 Collaborations

The work presented in Section 3.1.1 was conducted within the framework of the HyFlow project, coordinated by Professor K.H. Pettinger (Landshut University of Applied Sciences), as the life cycle assessment and economic evaluation represent the outcomes of collaboration with Dr. Eva-Maria Heigl and Dr. Andreas Zauner from the Energie Institut of Linz; Professor Estanis Oyarbide (Epic Power Converters S.L.), Jiří Charvát (University of West Bohemia), and Pinflow Energy Storage s.r.o. also contributed to this Section.

The work described in Section 3.1.2 results from the Mentoring Programme for PhD students organised by the StoRIES Project, in which I participated and received guidance from Professor Linda Barelli (Department of Engineering – University of Perugia).

The research outlined in Section 3.2 was undertaken within the objectives of the THOR project (lighTweight self-cHarging piezO-supercapacitoR systems by nanotechnologies) in collaboration with Dr. Elisabetta Petri, Dr. Michele Zanoni, Dr. Federico Poli, and Professor Chiara Gualandi (University of Bologna: Department of Chemistry "Giacomo Ciamician") as well as Dr. Leonardo Gasperini, Dr. Giacomo Selleri, and Professor Davide Fabiani (Department of Electrical, Electronic, and Information Engineering "Guglielmo Marconi").

Chapter 4 presents my contribution to the upscaling of the Semi-Solid Lithium–Air Flow Battery prototype, NESSOX, developed by the University of Bologna spin-off Bettery S.r.l., in collaboration with Dr. Alessandro Brilloni and Professor F. Soavi.

Chapter 5 reports the results of my research activity carried out during my period abroad at the Yusuf Hamied Department of Chemistry, University of Cambridge, under the supervision of Professor Alexander Forse and in collaboration with Dr. Malina Seyffertitz and Dr. Jack Taylor.

Appendix

This Appendix reports the Supplementary Information related to Sections 3.1.1 and 3.1.2.

Supplementary Information of Section 3.1.1

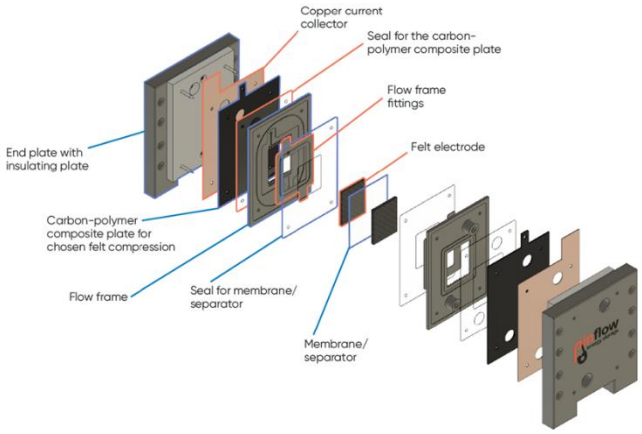

Figure S1 Exploded View Drawing of Pinflow VRFC.[1]

Table S1 Coulombic, energy and voltage efficiency of VRFC with N115 membrane at different current densities at 20°C and flow rate of 1 ml/min/cm²

current density mA cm-²	CE	EE	VE
50	94.48	84.14	89.05
100	96.13	79.15	82.34
150	96.74	73.56	76.03
200	97.17	66.64	68.58
250	97.63	57.66	59.06

a) b)

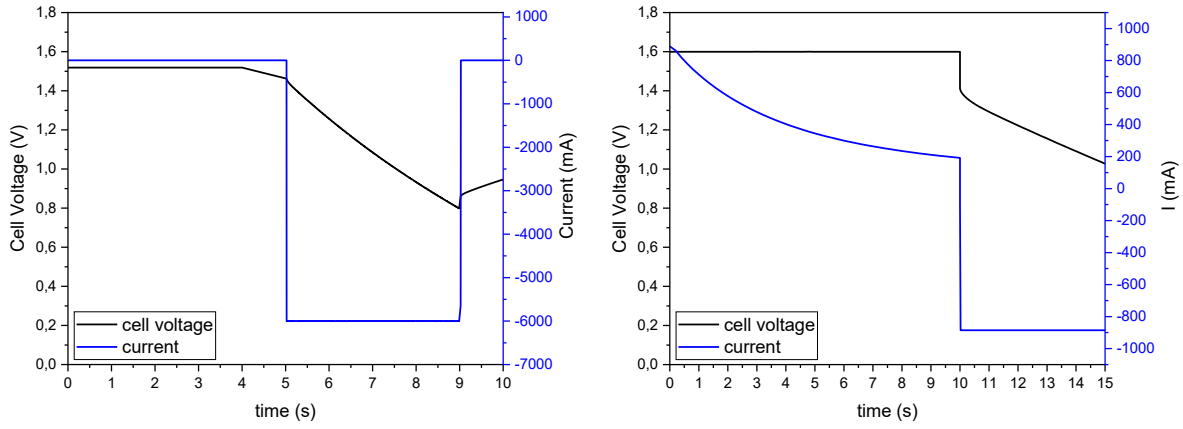

Figure S2 Examples of current and voltage profile during the test for a) VRFC and VRFC-SC and for b) SC.

Equivalent Electric Model

The Thevenin model approach is a method used in electrical engineering to simplify complex circuits for analysis and design purposes. It involves representing a part of a complex circuit as a reduced circuit consisting of a single voltage source (E_{Th}) and a single resistance (R_{Th}). This simplification allows to analyze the behavior of the original circuit more easily.

The theorem is reported from [2].

In a circuit composed of two parts, connected to each other by means of two wires, one part, if linear, can be substituted by the series of a voltage source and a resistor. The voltage source voltage is the voltage appearing across the two terminals of this part when disconnected from the other one; the resistor's resistance is the value "seen" from the terminals, when all the internal sources are deactivated.

The use of the Thevenin theorem requires the implementation of the rule of *Superposition principle in circuits* that here is a citation from [2].

Linear circuits can be solved by applying voltage and current sources one at a time, and partial summing results. It is possible to use them in groups. When a voltage or current source is not applied (or is deactivated), the corresponding branch is short- or open-circuited, respectively.

According to the *Thevenin Theorem* and the *Superposition principle*, the circuit is split in two parts: the SC branch is separated from the rest of the circuit (Figure S3). The voltage measured at the two open terminals (Figure S3) is the Thevenin Voltage source (E_{Th}). In Figure S4, the current source is open-circuited, and the voltage source short-circuited in order to find the Thevenin Resistance R_{Th}. The Equations of the Thevenin Voltage source and Thevenin Resistance are respectively: $V_{Th}=Vb-i_bR_b$ and $R_{Th}=R_{SC}+R_b$.

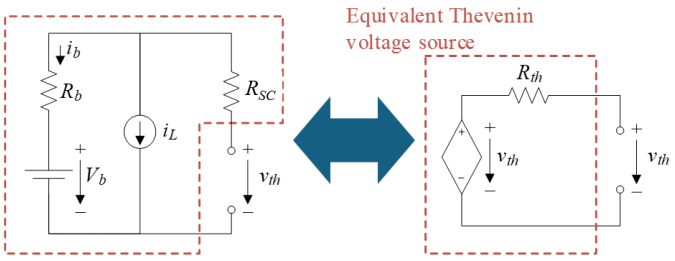

Figure S3 Equivalent Thevenin voltage source.

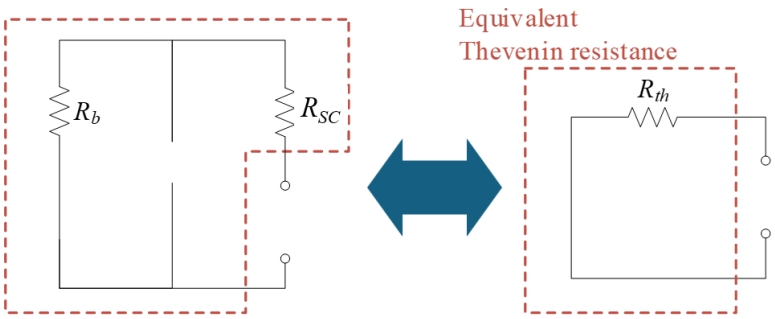

Figure S4 Equivalent Thevenin resistance

Once the Thevenin resistance and voltage source has been determined it is possible to compose the Thevenin circuit that is reported in Figure 3.1.1.2.4.1 b.

Kirchhoff's laws are implemented on the beginning equivalent circuit (Figure 3.1.1.2.4.1a). The Kirchhoff's current law is applied at one node to obtain the Equation 3.1.1.2.4.2. Instead, the voltage v_L (which is the corresponding voltage measured during the test and the same voltage applied at each branch of the parallel system) can be computed using the Kirchhoff's voltage law on the battery-load loop (Equation 3.1.1.2.4.3).

Life cycle assessment

The inventories for the production of the VRFB (Table S2) and the DC-DC converters (Table S4) were derived from HyFlow [3] and adapted to the new parameters of this study. The masses of the power components of the VRFB were linearly upscaled by the VRFB power and the masses of periphery components by the VRFB storage capacity. The required mass of electrolyte was calculated from the targeted storage capacity of the VRFB, which is determined by the energy density (1.6 M vanadium, 4M sulphate: 20 Wh L^{-1}) and the density (1.35 kg L^{-1}) of the electrolyte. The inventory for the production of vanadium pentoxide (V_2O_5), which is used as active component in the vanadium electrolyte, was derived from Blume et al. (2022) [4]. The mass of the electrolyte tank was adapted to the electrolyte's volume. The LCI for the DC-DC converter was directly provided by the manufacturer, who was a project partner in HyFlow, and linearly upscaled to the required conversion power. The inventories for the

inverter, EMS (control cabinet and computer) and cabling originate from the ecoinvent LCI database [5] and were also linearly scaled to the required parameters. For the commercial SC, we applied the LCI of the activated carbon-acetonitrile SC published by Jiao et al. (2023) [6] (Table S3). We are aware that, larger cells would be used to build large SCs as investigated in our study, which would probably result in a reduced relative mass of the aluminum cell cases. However, a comparison to real larger SC cells showed that Jiao et al. (2023) [6], who modelled a 1 kWh SC with these small cells, already provided a realistic mass for the cell cases of larger cells.

Table S2 Life cycle inventory of a 4 MWh/1MW VRFB, adapted from [3]

Function	Component	Material	Value [kg]	wt. %	Used dataset
Energy	Electrolyte	V_2O_5-based electrolyte	270 000	90.36	[3], adopted from [4]
	Electrolyte tank	PP tank with steel base	9 291	3.11	[3]
Power	Membrane	Nafion polymer ($C_7HF_{13}O_5S.C_2F_4$)	20	0.01	[3], dataset for Nafion adopted from [7]
	Electrodes	Raw carbon felt (PAN = polyacrylonitrile)	154	0.05	[3], dataset for PAN fibre adopted from [7]
	Bipolar plate	PPG86 composite (~88 wt.% synthetic graphite, ~12 wt.% PP)	1 023	0.34	[3], dataset for PPG86 adopted from [7]
	Cell frame (flow plates)	PVC	2 800	0.94	[3]
	Current collectors	Aluminum plate	283	0.09	
	Sealings/gaskets	PE	80	0.03	
	Bolts, nuts, pads (stack frame)	Steel	880	0.29	
	End plates (stack frame)	Aluminum	4 300	1.44	
Periphery	Pumps	PVC-coated steel	686	0.23	
	Pipes	HD-PE	3 518	1.18	
	Cables	Copper	1 268	0.42	
		PVC insulation	135	0.05	
	Heat exchangers	PE	1 286	0.43	
	Racks for stacks	Steel	3 084	1.03	
	Total		**298 808**	**100**	

Table S3 Life cycle inventory of a 1 kWh activated carbon-acetonitrile SC, adopted from [6]

Component	Material	Value [kg]	Unit	wt. %	Used dataset
Electrode	Activated carbon (AC)	155.2	kg	38	adapted from [8-13]; per 1kg AC: 9 t.km freight transport container ship sea (GLO), 1.2 t.km rail transport (RER), 0.2 t.km truck transport (RER), 1.5 kg deionized water (RER), 2.16 MJ electricity grid mix (IN), 4E-10 units chemical factory, organics (GLO)
Electrolyte	Acetonitrile	65.6	kg	16	DE: Acetonitrile Sphera
Collectors	Aluminum	12	kg	3	RER: Aluminium sheet ELCD/EAA
Separator	Paper	11.2	kg	3	EU-25: Graphic Paper Euro-graph/ELCD
	Rubber	22.8	kg	6	GLO: market for synthetic rubber ecoinvent 3.8
Case	Aluminum	112.5	kg	28	RER: Aluminium sheet ELCD/EAA
Others	n.a.	26.7	kg	7	
Energy	Electricity	5 204	kWh		RER: Electricity grid mix Sphera
	Diesel	263	L		RER: Diesel mix at filling station Sphera
Transport	Freight train	513	t.km		EU-28: Rail transport, average train, gross tonne weight 1 000 t / 726 t payload capacity Sphera
	Truck	19	t.km		RER: Truck transport incl. fuel, Euro 0-6 mix, 22 t total weight, 17.3 t max payload Sphera
Total		**406**	**kg**		

1**Table S4** LCI for production of a 6.2 kW bidirectional DC-DC converter, adopted from [6]

Process	Value	Unit	Used dataset
Inputs			
Galvanized steel	3 564	g	Steel hot dip galvanised, EU, Worldsteel
Aluminium	1 152	g	Aluminium sheet, RER, ELCD/EAA
Copper wire	1 011	g	Copper wire; technology mix; market mix, at plant; cross section 1 mm, EU-25, ECI/ELCD
Inductor THD	914	g	Market for inductor, ring core choke type, GLO, ecoinvent 3.8
Printed circuit board	608	g	Market for printed wiring board, surface mounted, unspecified, Pb free, GLO, ecoinvent 3.8
Nylon	198	g	Market for nylon 6, RoW, ecoinvent 3.7.1
Fan	83	g	Fan production, for power supply unit, desktop computer, GLO, ecoinvent 3.8
Inductor	78	g	Market for inductor, ring core choke type, GLO, ecoinvent 3.8
Paper	77	g	Graphic Paper, EU-25, Euro-graph/ELCD
Stainless steel	59	g	Stainless steel sheet (EN15804 A1-A3), RER, Sphera
THD integrated circuit (power semiconductor)	44	g	[3]
Film capacitor	36	g	Market for capacitor, film type, for through-hole mounting, GLO, ecoinvent 3.8
Power resistor	15	g	Market for resistor, surface-mounted, GLO, ecoinvent 3.8
Connector	14	g	Market for electric connector, wire clamp, GLO, ecoinvent 3.8
Electrolytic capacitor	12	g	Market for capacitor, electrolyte type, > 2cm height, GLO, ecoinvent 3.8
Fuse	11	g	Neglected: no dataset available, only 0.1 wt% of converter
Varistor	9	g	Neglected: no dataset available, only 0.1 wt% of converter
Diode	7	g	Market for diode, glass-, for surface-mounting, GLO, ecoinvent 3.8
SMD integrated circuit (power semiconductor)	4	g	[3]
Ceramic resistor	3	g	Market for resistor, surface-mounted, GLO, ecoinvent 3.8
Multi-layered ceramic capacitor (MLCC)	1	g	[3]
Electricity	0.299	kWh	Electricity grid mix, ES, Sphera
Transport raw materials, lorry	595	kg.km	Lorry transport incl. fuel, Euro 0-6 mix, 22 t total weight, 17.3 t max payload, RER, Sphera
Transport raw materials, rail	1 189	kg.km	RER: Rail transport incl. fuel, average train, gross tonne weight 1 000 t / 726 t payload capacity Sphera
Transport final product to customer, lorry	3 950	kg.km	Lorry transport incl. fuel, Euro 0-6 mix, 22 t total weight, 17.3 t max payload, RER, Sphera
Outputs			

DC-DC non-isolated converter (6.2 kW)	1	unit	6.2 kW converter = 9.74 kg
Electronic scrap (for recycling)	2.85	kg	
Aluminium scrap (for recycling)	1.15	kg	
Iron scrap (for recycling)	3.62	kg	

Table S5 LCI for production of 1 kg of activated carbon

Process	**Value**	**Unit**	**Used dataset**
Water, deionised	1.5	kg	RoW: market for water, deionised ecoinvent 3.8
Electricity	0.6	kWh	IN: Electricity grid mix Sphera (India)
Chemical factory	4E-10	units	GLO: market for chemical factory, organics ecoinvent 3.8
Transport, ocean ship	9	t.km	GLO: market for transport, freight, sea, container ship ecoinvent 3.8
Transport in Europe, rail	1 200	t.km	RER: Rail transport incl. fuel, average train, gross tonne weight 1 000 t / 726 t payload capacity Sphera
Transport in Europe, truck	200	kg.km	RER: Transport, truck (26 t total cap., 17.3 t payload) (A4) Sphera

Table S6 Energy efficiencies (EE) of HESS components

Component	**Energy efficiency (EE)**
VRFB (round-trip-efficiency)	75%[1)]
SC (round-trip-efficiency)	>95%[2)]
AC-DC inverter	97%[3)]
Battery converter (BC)	93%[1)]
Supercapacitor converter (SCC)	94%[1)]
System energy efficiency, converter-based HESS (storage pathway: slow charging via VRFB, fast discharging via SC)	51% $=EE_{inverter}*EE_{BC}*EE_{VRFB}*EE_{BC}*EE_{SCC}*EE_{SC}*EE_{SCC}*EE_{inverter}$
System energy efficiency, passive HESS (storage pathway: slow charging via VRFB, fast discharging via SC)	67% $=EE_{inverter}*EE_{VRFB}*EE_{SC}*EE_{inverter}$
[1)] values experimentally assessed in HyFlow WP1 and 2 [7] *[2)] value provided by manufacturer* *[3)] adopted from [11]*	
Component	**Energy efficiency (EE)**
VRFB (round-trip-efficiency)	75%[1)]
SC (round-trip-efficiency)	>95%[2)]

AC-DC inverter	97%[3)]
Battery converter (BC)	93%[1)]
Supercapacitor converter (SCC)	94%[1)]
System energy efficiency, converter-based HESS (storage pathway: slow charging via VRFB, fast discharging via SC)	51% $=EE_{inverter}*EE_{BC}*EE_{VRFB}*EE_{BC}*EE_{SCC}*EE_{SC}*EE_{SCC}*EE_{inverter}$
System energy efficiency, passive HESS (storage pathway: slow charging via VRFB, fast discharging via SC)	67% $=EE_{inverter}*EE_{VRFB}*EE_{SC}*\ EE_{inverter}$
[1)] values experimentally assessed in HyFlow WP1 and 2 [7] *[2)] value provided by manufacturer* *[3)] adopted from [11]*	

Table S7 Discharged energy and energy losses over HESS lifetime

[MWh]	**Converter-based connection**	**Passive connection**
Charged energy	105 960	95 808
Stored energy	80 000	80 000
Discharged energy	54 040	64 192
Losses	51 921	31 617

Table S8 LCI of production of ammonium acetate water-in-salt electrolyte (30 mol kg^{-1}), calculated based on stoichiometry of ammonia-acetic acid reaction and molality of electrolyte [9]

Process	Ref. value	Unit	Used background process
Inputs			
Ammonia (NH_3)	0.15	kg	RER: Ammonia (NH3) production mix, without CO_2 recovery (carbon dioxide emissions to air) Sphera
Acetic acid	0.54	kg	DE: Acetic acid from methanol (low pressure carbonylation) (Monsanto process) Sphera
Water, deionised	0.30	kg	RER: Water (deionised) Sphera
Chemical factory, organics	4E-10	kg	GLO: market for chemical factory, organics ecoinvent 3.8
Transport, lorry	100	kWh	RER: transport, freight, lorry 16-32 metric ton, EURO3 ecoinvent 3.8; transport distance according to [10]
Transport, rail	600	t.km	RER: Transportation by rail (EN15804 A4) Sphera; transport distance according to [10]
Outputs			
Ammonium acetate based "water-in-salt" electrolyte (30 mol kg^{-1})	1	kg	

Table S9 Investigated LCIA midpoint impact categories and related midpoint category indicators according to ReCiPe 2016 v1.1 [11]

Midpoint impact category	**Midpoint category indicator**	**Abbreviation**	**Unit**
Climate change, including biogenic carbon	Global warming potential	GWP	kg CO_2-eq
Fine particulate matter formation	Particulate matter formation potential	PMFP	kg PM2.5-eq
Fossil depletion / fossil resource scarcity	Fossil fuel potential	FFP	kg oil-eq
Freshwater consumption / water use	Water consumption potential	WCP	m^3
Freshwater ecotoxicity	Freshwater ecotoxicity potential	FETP	kg 1.4 DB-eq
Freshwater eutrophication	Freshwater eutrophication potential	FEP	kg P-eq
Human toxicity: cancer	Human toxicity potential, cancer	HTPc	kg 1.4-DB-eq
Human toxicity: non cancer	Human toxicity potential, non-cancer	HTPnc	kg 1.4-DB-eq
Ionizing radiation	Ionizing radiation potential	IRP	kBq Co-60-eq to air
Land use	Agricultural land occupation potential	LOP	m^2 × yr / annual cropland-eq
Marine ecotoxicity	Marine ecotoxicity potential	METP	kg 1.4-DB-eq
Marine eutrophication	Marine eutrophication potential	MEP	kg N-eq
Metal depletion / mineral resource scarcity	Surplus ore potential	SOP	kg Cu-eq
Photochemical ozone formation, ecosystems	Photochemical oxidant formation potential: ecosystems	EOFP	kg NOx-eq
Photochemical ozone formation, human health	Photochemical oxidant formation potential: human health	HOFP	kg NOx-eq
Ozone depletion	Ozone depletion potential	ODP	kg CFC-11-eq
Terrestrial acidification	Terrestrial acidification potential	TAP	kg SO2-eq
Terrestrial ecotoxicity	Terrestrial ecotoxicity potential	TETP	kg 1.4-DB-eq

Table S10 Investigated indicators for the primary energy demand (PED) [12-13]

PED category	**Abbreviation**	**Unit**
Primary energy demand from non-renewable resources (net calorific value)	PEDnr,n	MJ
Primary energy demand from renewable resources (net calorific value)	PEDr,n	MJ
Total primary energy demand (net calorific value) = PEDnr,n + PEDr,n	PEDn	MJ

Table S11 Surcharge factors for calculating the total costs of the HESS

Cost cluster	Parameter	Surcharge factor
Additional costs (direct surcharge factor f_d)	Material and services for civil engineering	15%
	Assembly of the main components	10%
	Process control technology (material and assembly)	5%
	Electrical engineering (material and assembly)	5%
	Site equipment	2%
	Safety test	3%
	Quality control	2%
	Engineering	10%
Indirect costs (indirect surcharge factors f_{id})	Construction and assembly monitoring	1%
	Commissioning	3%
	Approval	1%
	Other costs (e.g. size factor, contribution for the unforeseen, ...)	5% - 20%*

* … The factor diminishes over time, amounting to 20% in the year 2020 and decreasing to 5% by the year 2050. This alteration is attributed to the escalating number of installations, leading to an enhanced level of experience and consequently reducing unforeseen costs.

Table S12 VRFC Delivered Energy, Ohmic drop and R_b at each current extrapolated from pulsed discharge test data.

Current	*mA*	200	400	600	800	1 000	1 500	2 000
Delivered Energy	*Wh*	4.14E-04	7.82E-04	1.11E-03	1.41E-03	1.65E-03	2.11E-03	1.23E-03
Ohmic drop	*V*	0.07399	0.14479	0.21445	0.28005	0.33661	0.49661	0.650213
R_b	Ω	0.37	0.36	0.36	0.35	0.34	0.33	0.33

Non accessible energy (NAE) Equation:

$$\%NAE = \frac{V_{max}^2 - V_{opt}^2}{V_{max}^2} \quad \text{S1}$$

where V_{max} denotes the nominal voltage and V_{op} the operating voltage.

a)

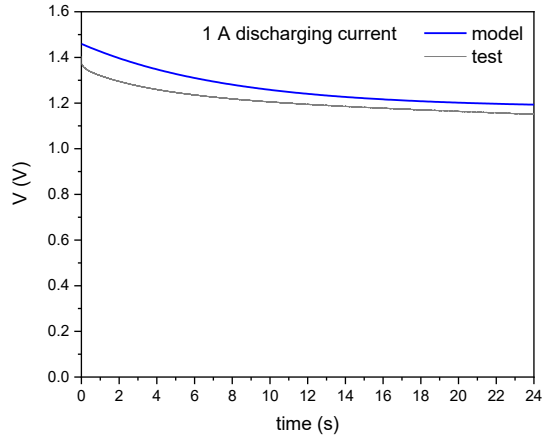

b)

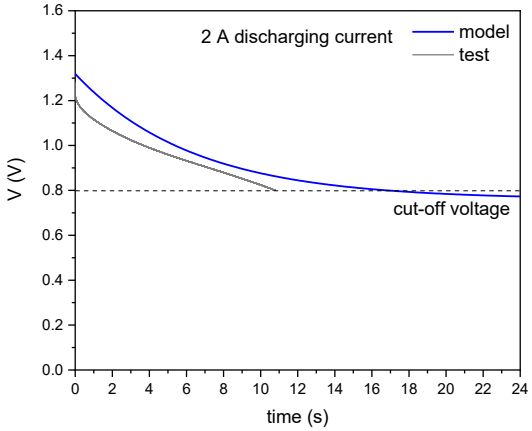

c)

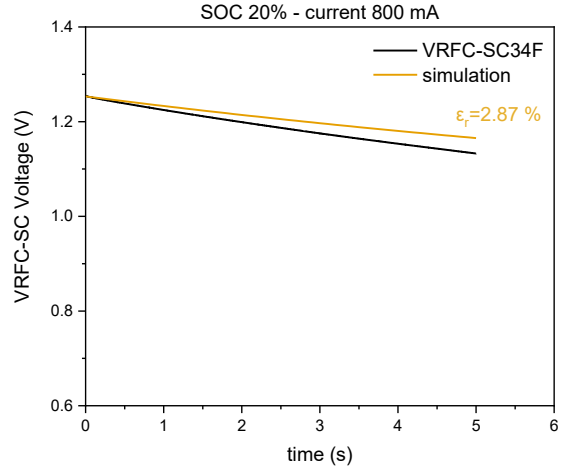

Figure S5 Examples of experimental and simulated discharge profiles of different VRFC-SC systems during discharges longer than 5 s at (a) 1 A and (b) 2 A for at 100 % SOC, and (c) for a short pulse at 800 mA and 20% SOC .for the VRFC-SC-34 F system

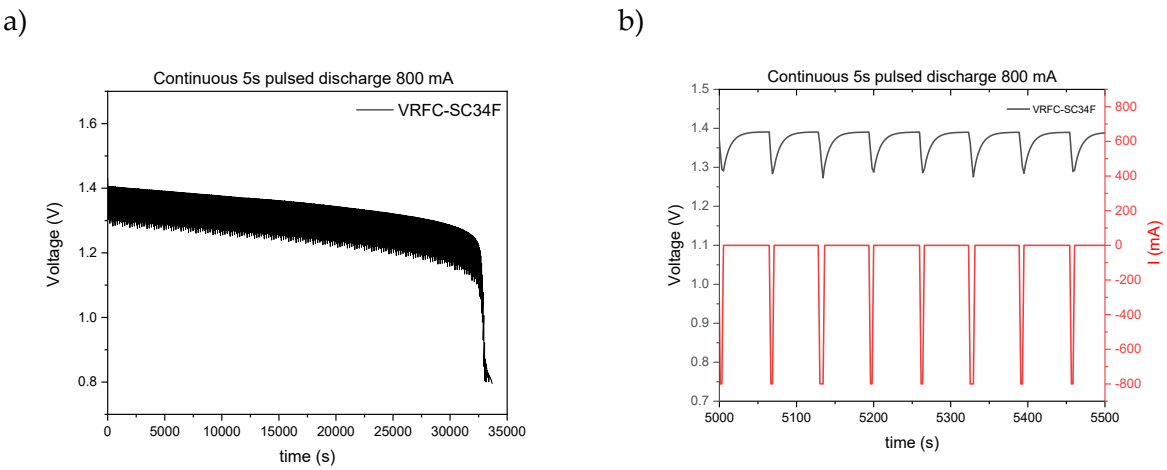

Figure S6 a)Voltage profile over a continuous pulsed discharge of the VRFC-SC34F by applying a current of 800 mA. The system is tested by 5 seconds pulses applied every 1 min of rest (I = 0 mA); b) detail of the voltage profile in a timeframe of 500 s.

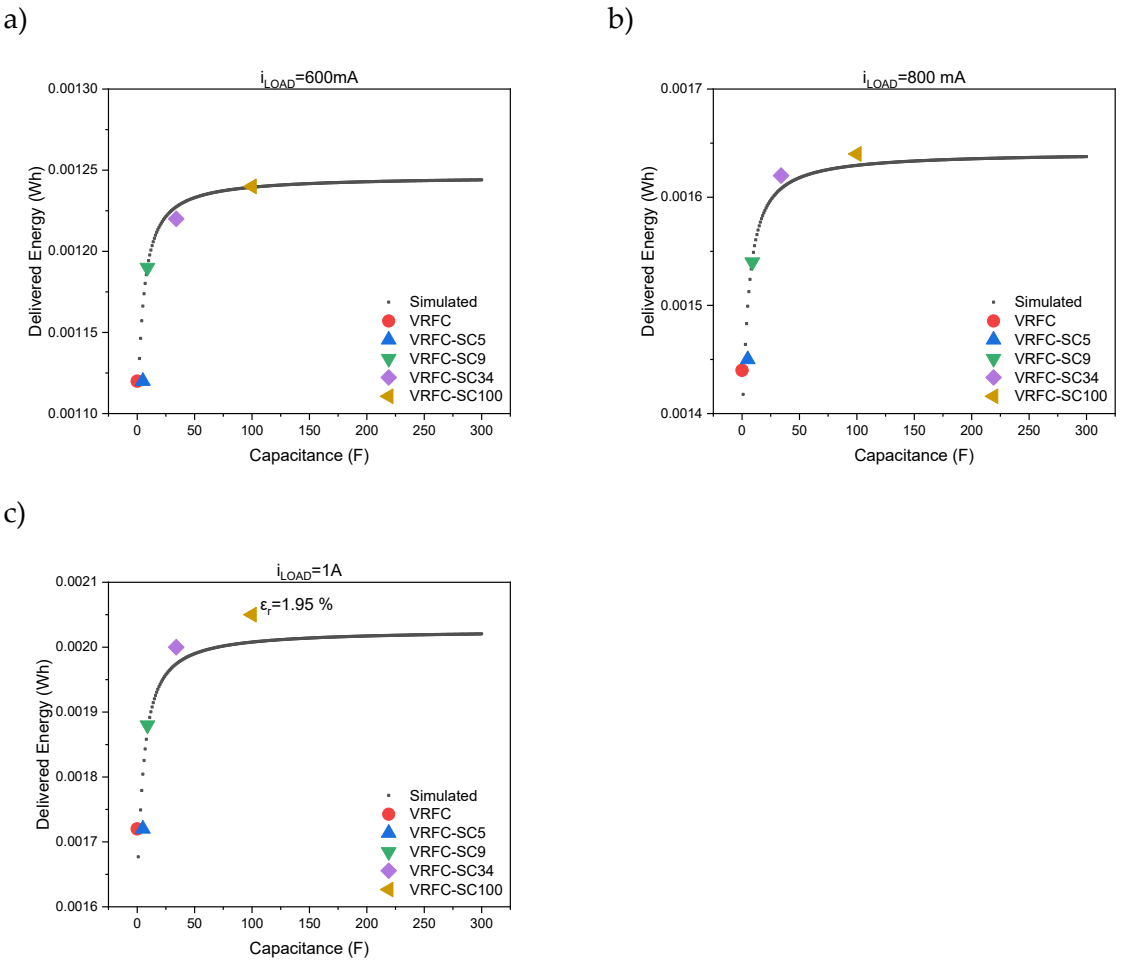

Figure S7 Energy delivered by the VRFC-SC hybrid system over 5-s pulses at a) 600 mA, b) 800 mA and c) 1 A vs SC Capacitance. The black dots are calculated using the model; coloured markers represent the results obtained during the parallel connection test between the VRFC and the commercial SCs.

Table S13 Input data implemented in the model to assess the effect of the SC ESR on the parallel system behaviour

	v_L	*ESR*	*C*
	V	*Ω*	*F*
VRFC	1.5	0.37	-
SC1	1.5	0.02	15
SC2	1.5	0.11	15

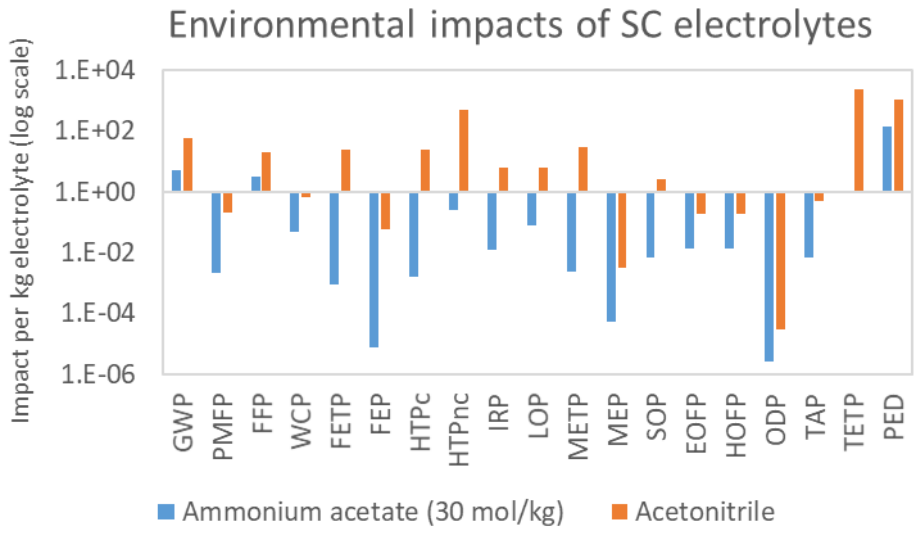

Figure S8 Environmental impacts of SC electrolytes (acetonitrile-based and aqueous)

Table S14 LCIA results for HESS production (absolute values for 1 HESS)

	Conf.	VRFB	SC (converter-based)	SC (passive)	DC-DC converters	AC-DC inverter + periphery	HESS (converter-based)	HESS passive
GWP	Base	3 170 414	2 588	7 765	69 493	124 906	3 367 402	3 303 085
	S1	3 170 414	5 176	15 529	119 131	205 457	3 500 179	3 391 401
	S2	3 170 414	10 353	31 059	218 407	366 107	3 765 281	3 567 580
	S3	3 170 414	20 706	62 117	416 959	698 142	4 306 221	3 930 673
	S4	3 170 414	41 411	124 234	814 063	1 361 758	5 387 647	4 656 407
	S5	3 170 414	82 823	248 468	1 608 271	2 688 539	7 550 047	6 107 421
PEDnr,n	Base	27 444 735	36 628	109 885	1 035 864	1 867 496	30 384 724	29 422 117
	S1	27 444 735	73 257	219 770	1 775 767	3 072 823	32 366 581	30 737 328
	S2	27 444 735	146 513	439 540	3 255 572	5 478 503	36 325 324	33 362 779
	S3	27 444 735	293 027	879 081	6 215 183	10 453 626	44 406 571	38 777 442
	S4	27 444 735	586 054	1 758 162	12 134 405	20 398 899	60 564 093	49 601 796
	S5	27 444 735	1 172 108	3 516 324	23 972 848	40 284 473	92 874 165	71 245 533
PEDr,n	Base	958 400	15 171	45 512	87 834	169 931	1 231 334	1 173 842
	S1	958 400	30 341	91 024	150 572	280 237	1 419 550	1 329 660
	S2	958 400	60 683	182 048	276 049	499 611	1 794 742	1 640 059

	S3	958 400	121 365	364 096	527 002	950 330	2 557 097	2 272 826
	S4	958 400	242 731	728 192	1 028 909	1 850 531	4 080 570	3 537 123
	S5	958 400	485 462	1 456 385	2 032 723	3 649 695	7 126 279	6 064 480
PEDn	Base	28 403 135	51 799	155 397	1 123 698	2 037 427	31 616 058	30 595 959
	S1	28 403 135	103 598	310 794	1 926 339	3 353 059	33 786 131	32 066 988
	S2	28 403 135	207 196	621 589	3 531 621	5 978 114	38 120 066	35 002 838
	S3	28 403 135	414 392	1 243 177	6 742 185	11 403 956	46 963 668	41 050 268
	S4	28 403 135	828 785	2 486 354	13 163 314	22 249 430	64 644 663	53 138 919
	S5	28 403 135	1 657 570	4 972 709	26 005 571	43 934 169	100 000 444	77 310 012
PMFP	Base	13 932	2	7	162	532	14 629	14 472
	S1	13 932	5	15	278	897	15 112	14 844
	S2	13 932	10	30	509	1 625	16 076	15 588
	S3	13 932	20	60	971	3 097	18 020	17 089
	S4	13 932	40	120	1 897	6 038	21 906	20 090
	S5	13 932	80	239	3 747	11 917	29 676	26 089
FFP	Base	620 556	848	2 543	23 903	43 132	688 439	666 231
	S1	620 556	1 695	5 086	40 977	70 930	734 159	696 573
	S2	620 556	3 391	10 172	75 125	126 411	825 483	757 140
	S3	620 556	6 781	20 344	143 421	241 209	1 011 968	882 109
	S4	620 556	13 563	40 688	280 012	470 689	1 384 820	1 131 933
	S5	620 556	27 125	81 376	553 194	929 533	2 130 408	1 631 465
WCP	Base	11 247	15	44	595	1 445	13 302	12 736
	S1	11 247	30	89	1 020	2 422	14 719	13 758
	S2	11 247	59	177	1 870	4 370	17 546	15 795
	S3	11 247	118	355	3 569	8 323	23 258	19 925
	S4	11 247	236	709	6 968	16 223	34 675	28 180
	S5	11 247	473	1 419	13 767	32 016	57 503	44 682
FETP	Base	9 344	5	14	9 465	86 014	104 827	95 372
	S1	9 344	9	28	16 226	146 950	172 529	156 323
	S2	9 344	19	56	29 747	268 715	307 825	278 115
	S3	9 344	38	113	56 790	512 579	578 750	522 035
	S4	9 344	75	226	110 875	1 000 197	1 120 491	1 009 767
	S5	9 344	150	451	219 046	1 975 326	2 203 865	1 985 121
FEP	Base	972	0	0	39	152	1 163	1 124
	S1	972	0	0	66	258	1 296	1 230
	S2	972	0	0	121	470	1 563	1 442
	S3	972	0	1	231	897	2 101	1 870
	S4	972	1	2	452	1 751	3 175	2 724
	S5	972	1	4	892	3 458	5 323	4 433
HTPc	Base	-1 380 737	24	73	3 912	46 277	-1 330 524	-1 334 387
	S1	-1 380 737	49	147	6 706	78 704	-1 295 278	-1 301 886
	S2	-1 380 737	98	294	12 295	143 532	-1 224 812	-1 236 911
	S3	-1 380 737	196	588	23 472	273 948	-1 083 121	-1 106 201
	S4	-1 380 737	392	1 175	45 827	534 755	-799 763	-844 806
	S5	-1 380 737	784	2 351	90 535	1 056 344	-233 074	-322 042
H	Base	2 427 349	152	455	223 582	1 509 344	4 160 427	3 937 148

	S1	2 427 349	303	910	383 284	2 572 711	5 383 648	5 000 970
	S2	2 427 349	607	1 820	702 688	4 696 808	7 827 451	7 125 977
	S3	2 427 349	1 213	3 639	1 341 494	8 956 989	12 727 045	11 387 977
	S4	2 427 349	2 426	7 278	2 619 108	17 474 711	22 523 594	19 909 338
	S5	2 427 349	4 852	14 556	5 174 336	34 507 517	42 114 054	36 949 422
IRP	Base	90 516	89	268	5 452	6 462	102 520	97 246
	S1	90 516	179	536	9 347	10 724	110 766	101 777
	S2	90 516	358	1 073	17 136	19 242	127 252	110 831
	S3	90 516	0	0	32 714	36 732	159 962	127 249
	S4	90 516	1 431	4 292	63 869	71 705	227 522	166 513
	S5	90 516	2 861	8 584	126 181	141 644	361 202	240 744
LOP	Base	17 917	89	268	1 336	5 948	25 290	24 133
	S1	17 917	179	536	2 290	9 782	30 167	28 234
	S2	17 917	357	1 072	4 198	17 366	39 839	36 355
	S3	17 917	715	2 144	8 015	32 895	59 542	52 956
	S4	17 917	1 429	4 288	15 648	63 871	98 866	86 076
	S5	17 917	2 859	8 576	30 915	125 741	177 431	152 234
METP	Base	6 577	7	21	12 287	106 551	125 422	113 149
	S1	6 577	14	42	21 063	182 011	209 665	188 631
	S2	6 577	28	84	38 615	332 786	378 007	339 448
	S3	6 577	56	169	73 720	634 751	715 105	641 497
	S4	6 577	112	337	143 930	1 238 535	1 389 155	1 245 449
	S5	6 577	225	674	284 350	2 445 955	2 737 107	2 453 206
MEP	Base	90	0	0	3	7	100	97
	S1	90	0	0	6	11	107	101
	S2	90	0	0	11	20	121	111
	S3	90	0	1	21	39	150	130
	S4	90	1	2	40	76	207	168
	S5	90	1	4	79	150	320	243
SOP	Base	168 143	4	11	1 306	6 407	175 860	174 561
	S1	168 143	8	23	2 239	10 751	181 140	178 916
	S2	168 143	15	45	4 105	19 288	191 551	187 476
	S3	168 143	30	90	7 836	36 292	212 302	204 526
	S4	168 143	60	181	15 299	70 151	253 654	238 475
	S5	168 143	121	362	30 226	137 719	336 208	306 224
EOFP	Base	19 190	9	27	207	441	19 847	19 658
	S1	19 190	18	54	355	738	20 301	19 982
	S2	19 190	36	107	650	1 331	21 207	20 629
	S3	19 190	72	215	1 241	2 538	23 042	21 943
	S4	19 190	143	430	2 424	4 952	26 709	24 571
	S5	19 190	286	859	4 788	9 777	34 042	29 827
HOFP	Base	19 717	9	26	188	415	20 329	20 159
	S1	19 717	18	53	323	694	20 752	20 464
	S2	19 717	35	106	592	1 251	21 595	21 074
	S3	19 717	71	212	1 129	2 386	23 303	22 315
	S4	19 717	141	423	2 205	4 654	26 717	24 794

	S5	19 717	282	847	4 356	9 189	33 544	29 753
ODP	Base	3	0	0	0	0	3	3
	S1	3	0	0	0	0	3	3
	S2	3	0	0	0	0	3	3
	S3	3	0	0	0	0	3	3
	S4	3	0	0	1	1	4	3
	S5	3	0	0	1	1	5	4
TAP	Base	59 388	6	18	345	1 444	61 184	60 851
	S1	59 388	12	37	592	2 431	62 423	61 856
	S2	59 388	24	73	1 085	4 397	64 895	63 859
	S3	59 388	49	147	2 071	8 375	69 883	67 910
	S4	59 388	98	293	4 044	16 323	79 853	76 005
	S5	59 388	195	586	7 989	32 213	99 786	92 188
TETP	Base	6 308 880	1 712	5 136	1 748 038	7 317 590	15 376 220	13 631 606
	S1	6 308 880	3 424	10 273	2 996 637	12 470 392	21 779 332	18 789 544
	S2	6 308 880	6 849	20 546	5 493 834	22 738 729	34 548 292	29 068 155
	S3	6 308 880	13 697	41 092	10 488 229	43 279 168	60 089 974	49 629 139
	S4	6 308 880	27 395	82 184	20 477 018	84 322 779	111 136 072	90 713 843
	S5	6 308 880	54 789	164 368	40 454 597	166 372 736	213 191 002	172 845 984

Supplementary Information of Section 3.2.1

Table S15 Measured d_{33} values for each stack component. The data includes three measurements for each of the two sides of the samples.

Sample	d33 up 1	d33 up 2	d33 up 3	d33 down 1	d33 down 2	d33 down 3	**media tot**
1	-26,7	-25,5	-27,3	-27,3	-26,2	-27,5	**-26,8**
2	-30,4	-29,5	-29,5	-30,7	-31,5	-31,5	**-30,5**
3	-29,9	-30,3	-30,6	-31,3	-31,2	-30	**-30,6**
4	-29,2	-29,8	-29,3	-30,6	-29,8	-30	**-29,8**
5	-29,5	-28,8	-28,5	-28,3	-28,3	-28,9	**-28,7**
6	-30,1	-30,8	-29,6	-30,7	-30,2	-31,1	**-30,4**
7	-31,8	-31	-32,2	-32,3	-29,9	-32,4	**-31,6**
8	-28,6	-28,6	-29,1	-28,8	-28,7	-28,7	**-28,8**
9	-28,4	-27,4	-28,8	-29	-28,8	-29	**-28,6**
10	-26,6	-26,2	-26,2	-27	-26	-26,9	**-26,5**
11	-26,3	-27,2	-27,7	-27,2	-26,9	-28,1	**-27,2**
12	-26,3	-25,1	-26,5	-26,7	-26	-26,6	**-26,2**
13	-28,9	-29,5	-28,9	-29,9	-30,4	-31,1	**-29,8**
14	-28,8	-29,3	-28,2	-30,5	-30,7	-28,9	**-29,4**
15	-30,9	-31,7	-31	-30,6	-29,5	-30,3	**-30,7**
16	-26,4	-28,7	-27,7	-27,7	-26,3	-29,1	**-27,7**
17	-30,8	-30,5	-31,1	-31,6	-31,5	-31,5	**-31,2**
18	-27,1	-27,6	-27,5	-27,3	-27,7	-27,6	**-27,5**
19	-28,6	-29,3	-29,6	-28,7	-29,7	-28,8	**-29,1**
20	-25,7	-25,7	-26,7	-25,9	-27,8	-26,5	**-26,4**
21	-29,9	-29	-30,9	-30,1	-30,2	-30,8	**-30,2**
22	-29,9	-30,7	-30	-27,5	-30,1	-29,3	**-29,6**
23	-31,8	-31,5	-29,4	-31,9	-31,4	-31,7	**-31,3**
24	-25,7	-24,8	-24	-25,1	-25,3	-25,6	**-25,1**
25	-30,8	-32,1	-28,5	-32,1	-32,3	-32,6	**-31,4**
26	-28,7	-27	-28,7	-28,7	-28,5	-27,6	**-28,2**
27	-28,8	-29,3	-28,7	-29,6	-27,8	-29,5	**-29,0**
28	-31,6	-30,4	-29,3	-31,8	-30,7	-27	**-30,1**
29	-26,2	-26,9	-26,8	-24,6	-24,1	-26,5	**-25,9**
30	-27,9	-28,9	-30,5	-30,7	-31,4	-30,8	**-30,0**
						Average	**-29**
						Dev.St	**2**

Appendix References

[1] Picture from https://www.biologic.net/accessory/redox-flow-battery/]

[2] Ceraolo Massimo and Poli Davide, Fundamentals of Electric Power Engineering: From Electromagnetics to Power Systems, 2014th ed. John Wiley & Sons.

[3] E.-M. Heigl, M. Schäffer, L. Zeilerbauer, A. Zauner, J. Lindorfer, J. Ott, P. Fischer, Life cycle assessment of a novel hybrid energy storage system: Environmental hotspots and sustainability options based on experimental insights, *Journal of Energy Storage*, Volume 132, Part B, (2025), 117705, https://doi.org/10.1016/j.est.2025.117705

[4] N. Blume, M. Becker, T. Turek, C. Minke, Life cycle assessment of an industrial-scale vanadium flow battery, *Journal of Industrial Ecology*, 26, (2022), 1796–1808, https://doi.org/10.1111/jiec.13328

[5] Ecoinvent Association, ecoinvent database: sustainability assessment, https://ecoinvent.org/database/

[6] Y. Jiao, D. Månsson, Greenhouse gas emissions from hybrid energy storage systems in future 100% renewable power systems – A Swedish case based on consequential life cycle assessment, *Journal of Energy Storage*, 57, (2023), https://doi.org/10.1016/j.est.2022.106167

[7] S. Weber, J. F. Peters, M. Baumann, M. Weil, Life Cycle Assessment of a Vanadium Redox Flow Battery, *Environmental Science & Technology*, 52, (2018), 10864–10873, https://doi.org/10.1021/acs.est.8b02073

[8] N. Arena, J. Lee, R. Clift, Life Cycle Assessment of activated carbon production from coconut shells,
Journal of Cleaner Production, Volume 125, (2016), pp. 68-77,
https://doi.org/10.1016/j.jclepro.2016.03.073

[9] Ammonium Acetate (compound), https://pubchem.ncbi.nlm.nih.gov/compound/Ammonium-acetate#section=Household-Products

[10] R. Frischknecht, N. Jungbluth (Eds.), ecoinvent report No. 1, Overview and Methodology, Data v2.0 (2007), Swiss Centre for Life Cycle Inventories, Dübendorf, December 2007, https://inis.iaea.org/records/9306z-07798

[11] M. A. J. Huijbregts, Z. J. N. Steinmann, P. M. F. Elshout, G. Stam, ReCiPe2016: a harmonised life cycle impact assessment method at midpoint and endpoint level, *International Journal of Life Cycle Assessment*, 22, (2017), 138–147, https://doi.org/10.1007/s11367-016-1246-y

[12] VDI, VDI 4600 Kumulierter Energieaufwand - Begriffe, Definitionen, Berechnungsmethoden, VDI, https://www.vdi.de/

[13] T. Kupfer, LCA for Experts (formerly GaBi) Databases & Modelling Principles, (2021), [Online], www.sphera.com

Acronyms

AC – Alternating Current or Adsorption capacity (only Chapter 5)

ACC – Activated Carbon Cloth

AC/DC – Alternating Current to Direct Current (converter)

BC – Battery Converter

C – Capacitance

CAPEX – Capital Expenditure

CE – Counter Electrode

CRM – Critical Raw Material

CV – Cyclic Voltammetry

CVS – Controlled Voltage Souce

DAC – Direct Air Capture

DC – Direct Current or Desorption Capacity (only Chapter 5)

DC/DC – Direct Current to Direct Current (converter)

DOD – Depth of Discharge

eCCC - electrochemical Carbon Capture and Concentration

ECM – Eqiovalent Circuit Model

EDL – Electrical Double Layer

EDLC – Electrical Double Layer Capacitor

EE – Energy Efficiency

EESS – Electrochemical Energy Storage System

EFC – Electrochemical Flow Capacitor

EGD – European Green Deal

EIS – Electrochemical Impedance Spectroscopy

EMS – Energy Management System

EOFP – Photochemical Oxidant Formation Potential: Ecosystems

EPR – Equivalent Parallel Resistance

ESR – Equivalent Series Resistance

ESS – Energy Storage System

ESW – Electrochemical Stability Window

FETP – Freshwater Ecotoxicity Potential

FEP – Freshwater Eutrophication Potential

GCPL - Galvanostatic cycling with potential limitation

GHGs - GreenHouse Gases

GWP – Global Warming Potential

HESS – Hybrid Energy Storage System

HOFP – Photochemical Oxidant Formation Potential: Human Health

HTPc – Human Toxicity Potential, Cancer

HTPnc – Human Toxicity Potential, Non-Cancer

IL – Ionic Liquid

IPCC - Intergovernmental Panel on Climate Change

IRP – Ionizing Radiation Potential

KPI – Key Performance Indicator

LCA – Life Cycle Assessment

LCI – Life Cycle Inventory

LCIA – Life Cycle Impact Assessment

LCOS - Levelized Costs of Storage

LIB – Lithium-ion battery

LOP – Agricultural Land Occupation Potential

MEP – Marine Eutrophication Potential

METP – Marine Ecotoxicity Potential

MLCC – Multi-Layered Ceramic Capacitor

NDIR – Non-Dispersive InfraRed

NF - Nanofibrous

NPV - Net Present Value

OCV – Open-Circuit Voltage

ODP – Ozone Depletion Potential

ORR/OER – Oxygen Reduction/Oxygen Evolution Reactions

PCS – Power Conversion System

PED – Primary Energy Demand

PEDn – Total Primary Energy Demand (net calorific value)

PEDnr,n – Primary Energy Demand from Non-Renewable Resources

PEDr,n – Primary Energy Demand from Renewable Resources

PENG – Piezoelectric nanogenerators

PZT – Lead Zirconate Titanate

RFB – Redox Flow Battery

RMS – Root Mean Square

RT – Room Temperature

RTE – Round-Trip Efficiency

RVC – Reticulated Vitreous Carbon

SC – Supercapacitor

SD – Standard deviation

SEM – Scanning Electron Microscopy

SI – Supplementary Information

SDG - Sustainable Development Goal

SLAFB – Semi-Solid Lithium–Air Flow Battery

SPSC – Self-powered supercapacitors

SOC – State of Charge

SRFB – Semi-Solid Redox Flow Battery

SSA – Supercapacitive Swing Adsorption

TAP – Terrestrial Acidification Potential

TETP – Terrestrial Ecotoxicity Potential

VC – Variable Capacitor

VR – Variable Resistor

VRFC – Vanadium Redox Flow Cell

VRFB – Vanadium Redox Flow Battery

WE – Working Electrode

WiSE – Water in Salt Electrolyte

Personal Acknowledgements

The first acknowledgment goes to my mentor and professor, Francesca Soavi, who has believed in me since our first contact. Undertaking a PhD in electrochemistry as an automotive engineer represented a genuine challenge, yet her guidance and support ensured that the path remained illuminated by a constant light. Her passion for this field and her profound expertise encouraged me to appreciate the electrochemistry domain and to perceive myself as a new kind of hybrid researcher, similar to the hybrid systems we study. I am sincerely grateful for all the opportunities she provided, which I will always remember.

I would also like to thank all the people who contributed to my research, beginning with my group members, who created an inclusive and comfortable environment while sharing insightful scientific ideas. In particular, I wish to thank Elisabetta Petri, who supported me considerably, especially at the beginning, when I was an engineer lost into a chemistry laboratory. My appreciation also goes to Alessandro Brilloni, who introduced me to several topics and consistently assisted me during experimental activities. I would also like to thank Antunes Staffolani for dedicating his time to my occasional technical and scientific questions.

I also wish to thank Karl-Heinz Pettinger for including me in the ambitious European project HyFlow. This opportunity enabled me to collaborate with universities and companies across Europe, thereby enhancing my knowledge through various international conferences and extending my scientific network.

I would like to acknowledge Professor Alexander Forse, who offered me the chance to experience life at the University of Cambridge, and I am thankful to all the Forse Group members who created an inclusive and reliable atmosphere. Malina and Jack were the best supervisors I could have imagined.

I wish to express my gratitude to all the researchers who contributed to this work from different institutions and organisations, starting from the HyFlow members, such as Eva Heigl and Andreas Zauner, as well as Estanis Oyarbide and Jiří Charvát. My thanks also go to Leonardo Gasperini, Giacomo Selleri, and Michele Zanoni, together with Professor Chiara Gualandi and Professor Davide Fabiani.

My appreciation also extends to Professor Linda Barelli for her mentorship, which allowed me to envision new applications for my research.

Finally, I wish to thank all the supporting structures that enabled me to complete these three years, beginning with my new family and my old one, who believed in my decision to change my career path. I am also deeply grateful to all my friends, who have been my source of energy and confidence, constantly reminding me to trust myself.

In case I have inadvertently forgotten someone, please accept my sincere apologies and gratitude.

To everyone, thank you.